Swimming through spherical shell buckling

Abderrahmane Djellouli

Communauté
UNIVERSITÉ Grenoble Alpes

THÈSE

Pour obtenir le grade de

DOCTEUR DE LA COMMUNAUTÉ UNIVERSITÉ GRENOBLE ALPES

Spécialité : PHYSIQUE APPLIQUEE

Arrêté ministériel : 25 mai 2016

Présentée par

Abderrahmane DJELLOULI

Thèse dirigée par **Catherine QUILLIET** et
co-encadrée par **Gwennou COUPIER**

préparée au sein du **Laboratoire Interdisciplinaire de Physique**
dans **l'École Doctorale de Physique**

Nage par flambage de coque sphérique

Thèse soutenue publiquement le **15 juin 2017**
devant le jury composé de :

Monsieur Philippe Peyla
Professeur des universités, Université de Grenoble Alpes et Laboratoire Interdisciplinaire de Physique, Examinateur et président du jury

Monsieur Médéric Argentina
Professeur des universités, Université de Nice et Institut non linéaire de Nice, Rapporteur

Monsieur Douglas Holmes
Professeur assistant, Boston University, Rapporteur

Monsieur Ramiro Godoy-Diana
Chargé de recherche CNRS, Laboratoire physique et mécanique des milieux hétérogènes, Examinateur

Monsieur Arnout Imhof
Professeur des universités, Utrecht University, Examinateur

Swimming through shell buckling

Abstract

0.1 Abstract in English

Microswimmers, and among them aspirant microrobots, are generally bound to cope with flows where viscous forces are dominant, characterized by a low Reynolds number (Re). This implies constraints on the possible sequences of body motion, which have to be nonreciprocal. Furthermore, the presence of a strong drag limits the range of resulting velocities.

Here, we propose a swimming mechanism which uses the buckling instability triggered by pressure waves to propel a spherical hollow shell. The particularity of this mechanism is that it fulfills naturally the necessary condition of swimming at low Re. In addition, the swiftness of the instability might produce inertial effects even at the microscopic scale.

With a macroscopic experimental model we show that a net displacement is produced at all Re regimes. We put in evidence the role of geometrical parameters, shell material properties and rheology of the surrounding fluid on the swimming efficiency.

An optimal displacement is reached at intermediate Re. Using time-resolved PIV measurements, we explain that non-trivial history effects take place during the instability and enhance net displacement.

Thesis advisor: Maitre de conférence Catherine Quilliet Adel Djellouli

Using a simple model, validated by the study of shell dynamics, we show that due to the fast activation induced by the instability, this regime would be reachable by microscopic shells. The rapid dynamics would also allow high frequency excitation with standard traveling ultrasonic waves. Scale considerations predict a swimming velocity of order 1 cm/s for a remote controlled microrobot, a suitable value for biological applications such as drug delivery.

0.2 Résumé en Français

Les déplacements des micronageurs, et parmi eux les micronageurs artificiels, sont généralement associés à des écoulements dominés par des forces visqueuses. Ces écoulements sont caractérisés par un bas nombre de Reynolds (Re). Cela impacte la stratégie de nage et plus particulièrement les séquences de forme possibles, qui doivent nécessairement être non-réciproques dans l'espace de déformation pour espérer induire un déplacement net non-nul. De plus, à cause des forts effets de traînée, les vitesses de nage sont limitées à des valeurs faibles.

Dans cette thèse, nous examinons la possibilité d'utiliser un mécanisme de nage basé sur l'instabilité de flambage d'une sphère creuse. Cette instabilité est provoquée en soumettant la sphère à une onde de pression. La particularité de ce mécanisme est qu'il satisfait la condition nécessaire de nage à bas Reynolds exposée précédemment. De plus, la rapidité de la déformation lors de l'instabilité pousse à prévoir l'apparition d'effets inertiels, et ce même à l'échelle microscopique.

Une étude expérimentale a été conduite à l'échelle macroscopique dans le but de comprendre la dynamique de l'instabilité et son impact sur le fluide qui entoure la coque creuse. Ces expériences nous permettent de montrer qu'un déplacement net non-nul est produit pour tous les régimes d'écoulement. Nous mettons en évidence le rôle des paramètres géométriques, des propriétés du matériau composant la coque creuse et de la rhéologie du fluide sur l'efficacité de la nage.

Nous montrons l'existence d'un optimum de déplacement net pour des valeurs intermédiaires du nombre de Reynolds. Pour expliquer cela, nous nous servons de mesures de PIV résolues temporellement pour mettre en évidence la présence d'effets d'histoire non-triviaux qui augmentent le déplacement net.

Enfin, nous développons un modèle simplifié de la dynamique de flambage basé sur les observations expérimentales pour montrer que ce régime optimal de nage est atteignable pour des sphères microscopiques. Ceci est possible grâce à l'activation rapide de l'instabilité. Cette propriété permet aussi une excitation à haute fréquence en utilisant des ultrasons. Une étude d'échelle nous permet de prédire une vitesse de nage de 1 cm/s pour un micro-robot contrôlé à distance. Cet ordre de grandeur de vitesse est idéal pour des applications biologiques comme la distribution ciblée de médicaments.

Contents

To the three women of my life.

Acknowledgments

First, I would like to thank my team: Gwennou, Catherine and Philippe, with whom I spent amazing three years of my life. Through their generosity, their dedication and good spirits, they provided ideal conditions for me to thrive, to feel fulfilled and to enjoy my work. Gwennou, with his patience and pedagogy always listened to me and my ideas even the most extravagant, he never made me feel rejected and was always honest. Catherine, always managed to find time when needed, always happy and joyful, and it was great to learn from her and work with her. Philippe, was always open for our needs and helped with his never fading wits, to solve problems. I admire his curiosity and extensive knowledge. Second, I would like to thank Salima Rafai, Thomas Podgorski, Philippe Peyla for their wise counsel and their availability to help. I would like to thank Olivier Stephan who helped me numerous times, always lifted my spirits when they were down. I would like to thank the technical team and especially David Terrier and Patrice Ballet who were always there to help me with my infinite requests. I would like to thank my interns for their devoted work and optimism, especially Clement Gregoire. In a more general way, I would like to thank all the people of LiPhy who welcomed me and made me one of theirs. I would also like to thank our collaborators from LEGI who made possible PIV measurements, especially Henda Djeridi who always stood by me. Finally, I would like to thank my mother and my grand mother who raised me to be the man I am, and Fanny who accepted who I am.

La dernière chose qu'on trouve en faisant un ouvrage est de savoir celle qu'il faut mettre la première.

Blaise Pascal, 1662

1 Introduction

1.1 Context

A growing interest in understanding locomotion of microorganisms in fluids and identifying efficient propulsion mechanisms has given birth to a new field: artificial microswimmers. Besides their playful aspect, artificial microswimmers present undeniable fundamental and practical interests, mostly driven by a constant race toward increasing miniaturization with potential applications in numerous fields like medicine, biology, material and enviromental sciences. Active control of these microswimmers can have them being used as locomotives to transport cargo for a targeted drug delivery, which increases drug's efficiency, allows to reduce dosage and avoid undesirable side-effects. They can also serve in microfluidic

chips, perform operation in cells until now impossible to do, modify viscoelastic properties of a material or collect toxic material in human bodies or clean water streams.

The main challenge comes from the nature of the flow regime they inhabit. Indeed, microscopic swimmers live in a world where viscous forces are dominant, which is characterized by a low Reynolds number (Re). Their relationship with the surrounding liquid is equivalent to that of a human being trying to swim in a pool filled with honey. Before looking at which strategies can be used at such scales to achieve efficient swimming, let us first define what is swimming.

1.2 Definition of swimming

If we stick with the strictest definition, swimming would be defined as a set of time-dependent shape deformation that a body applies to a fluid region, inducing a flow [Lauga & Powers, 2009] . In turn, this flow exerts stress on the body boundary. If the resulting force on the body is not zero, it will cause locomotion. This definition excludes bodies that move thanks to an external force, or bodies that are drifting with the fluid flow through advection [Childress, 1981].

The motion of the surrounding fluid is described by the Navier-Stokes equations, that simplify if the fluid is incompressible and Newtonian to[*]:

$$\frac{\partial \mathrm{u}}{\partial t} + (\mathrm{u}.\nabla)\mathrm{u} = -\frac{1}{\rho}\nabla p + \frac{\mu}{\rho}\nabla^2 \mathrm{u} + f \tag{1.1}$$

$$\nabla u = 0 \tag{1.2}$$

The fluid is characterized by a constant density ρ, and a constant viscosity μ [†]. The state of the fluid is described at any given instant by the pressure field $p(\mathrm{x}, t)$ and by the velocity field $\mathrm{u} = (u(\mathrm{x}, t), v(\mathrm{x}, t), w(\mathrm{x}, t))$,

[*]The symbol '.' is the scalar product.

[†]The second viscosity effect λ that appears in more generalized Navier-Stokes equations is supposed equal to zero.

where ($\mathrm{x} = x_i, i \in 1,2,3$) are the spatial coordinates and t is time. f represents volume forces that may include gravitational acceleration g.

1.3 Swimming strategies

In Nature, swimmers range from microscopic organisms such as bacteria to macroscopic organisms that can reach up to 30 m. Within this realm, several locomotion strategies exist, based on three dimensionless numbers:

1. Froude number: $F = \frac{U^2}{Lg}$ which describes the relative importance of fluid kinetic energy compared to gravitational potential energy.
2. Strouhal number: $St = \frac{\omega L}{U}$ which allows to describe oscillating flow mechanisms.
3. Reynolds number: $Re = \frac{\rho U L}{\mu}$ that compare inertial forces to viscous forces.

These numbers are derived from the Navier-Stokes equations (eq.1.1 and eq.1.2) written in dimensionless variables, by supposing that L is the characteristic length of the swimmer's body, ω the oscillation frequency, U a characteristic speed. We define then:

$\tilde{t} = \omega t$, $\tilde{\mathrm{x}} = \mathrm{x}/L$, $\tilde{\mathrm{u}} = \mathrm{u}/U$,$\tilde{p} = p/(\rho U^2)$,$\tilde{\nabla} = L\nabla$.

Equations 1.1 and 1.2 become:

$$St\frac{\partial \tilde{\mathrm{u}}}{\tilde{t}} + \tilde{\mathrm{u}}.\tilde{\nabla}\tilde{\mathrm{u}} = -\tilde{\nabla}\tilde{p} + \frac{\tilde{\nabla}\tilde{\mathrm{u}}^2}{Re} + \frac{1}{F} \tag{1.3}$$

$$\tilde{\nabla}.\tilde{\mathrm{u}} = 0 \tag{1.4}$$

A fourth number called Womersley number, can be derived to describe the relative importance of transient inertial forces compared to viscous forces, defined as: $Wo^2 = \frac{\rho\omega L^2}{\mu} = ReSt$

In Nature, Strouhal number varies at most by 1 order of magnitude[Gazzola et al., 2014, Childress, 1981], however Reynolds number may vary over 15 orders of magnitude[Gazzola et al., 2014, Brennen,

1977]. This implies that Re is overwhelmingly important in the construction of swimming models for living organisms.

Based on Reynolds number, we can separate the realm of swimming into two categories (see fig.1.1):

- Case where $Re << 1$ (called Stokesian regime). This regime is associated with micro-organisms but can also describe swimming in a very viscous fluids, or very slow motions.
- Case where $Re >> 1$ (called Eulerian regime, or inertial regime). In such a regime, inertia dominates viscous drag. Three sub-regimes exist within this category that influence the flow structures. For moderate values of Re, we speak about laminar flow where a fluid flows in parallel layers with no perturbation between streamlines. When Re is high, we speak about turbulent regime where the flow is characterized by chaotic changes in flow velocity and pressure. In between, flow is transitional, partly laminar and partly turbulent.

Associating a Reynolds number to a swimmer can prove to be a delicate matter. For example, we can associate two Reynolds number to a tail beating fish: one for the tail beating taking into account the amplitude and the velocity of oscillation, and a second to the overall swimmer body with its characteristic length and mean velocity.

In the case of a low Re number, Navier-Stokes equations become linear (called Stokes equations) in respect with u^* when considering the case of a swimmer with a St=1, in the absence of volume forces. $Re \to 0$ may be taken and it reduces the system to the formal limit:

$$\nabla p - \nabla^2 \mathrm{u} = 0 \tag{1.5}$$

$$\nabla . \mathrm{u} = 0 \tag{1.6}$$

In this case, time does not play a role in fluid dynamics even though body deformation is time-dependent.

*If the body deformation depends on u, nonlinear effects might subsist.

Re	animal
62,000	seagull
50,000	large fish
3,900	butterfly
1,000	honeybee
300	african frog tadpole
120	housefly
15	chalcid wasp
0.2	paramecium
0.025	dinoflagellate
0.0035	spermatozoa, sea urchin
0.000,01	bacterium

Figure 1.1: Reynolds numbers associated to animals, source The Physics Hypertextbook

In the case of $Re >> 1$, fluid motion exhibits nonlinear effects and is in most cases not solvable analytically.

In nature, swimmers at high Re have evolved to have a slender-body shape defined in [Lighthill, 1960] as a fish or a swimming mammal, whose dimensions and movements at right angles to its direction of locomotion are small compared with its length, while its cross-section varies along it only gradually. Self-propulsion is generated by a response that arises from the acceleration of fluid opposite to the swimming direction [Childress, 1981]. High Re swimmers present high swimming efficiency, due to the fact that the effects of viscosity are confined to thin boundary layers, and also due to optimized flow control mechanisms of the vortex shedding. This is made possible by a well synchronized body motion, avoiding uncontrolled separation [Triantafyllou, 2002]. The efficiency of such a mechanism decreases drastically with Re [Walker, 2002].

Inhabitants of smaller scales have a Reynolds number that ranges from 10^{-4} for bacteria up to $10^{-2}$for mammalian spermatozoa [Brennen, 1977], inertial thrust then cannot be produced. Furthermore, a *sine qua non* condition to fulfill in order to achieve propulsion is to undertake a non-reciprocal path in the

deformation space [Purcell, 1977]. This is known as the "'scallop theorem"'. The underlying mechanism is that time being out of the equation, a reciprocal sequence of movements cannot result in net displacement for a swimmer operating at a low *Re* regime in a Newtonian fluid. This concept can be demonstrated with a theoretical three-link swimmer [Purcell, 1977] illustrated in figure1.2. In this configuration, two degrees of freedom are allowed, the swimmer can undergo a series of angle configuration. The sequence **ABCDA** (Fig.1.2-(a)) is non-reciprocal, therefore a net displacement is achieved after one cycle. On the other hand, the sequence **ABCBA** (Fig.1.2-(b)) is reciprocal, therefore no net displacement is produced after one cycle.

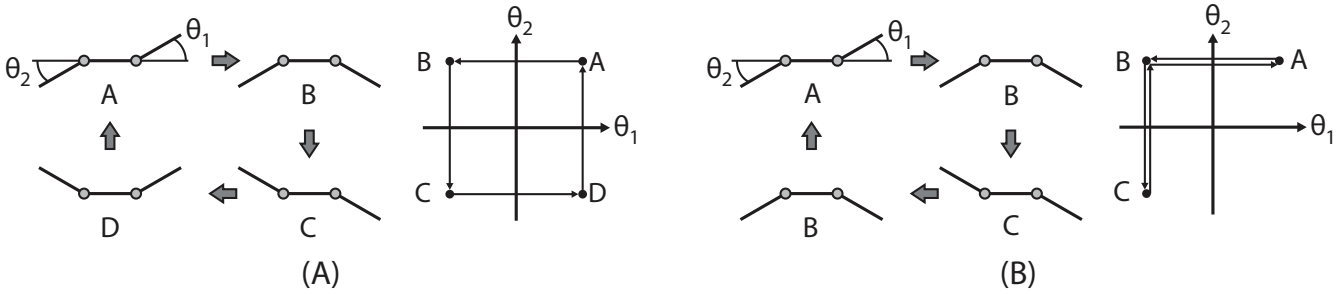

Figure 1.2: Theoretical three-link swimmer. Left sequence (A) represents a non-reciprocal series of angles, the right sequence represents a reciprocal series of angles. Image from [Peyer et al., 2012].

If the fluid is non-Newtonian, however, symmetry breaking can be obtained by viscous effects [Qiu et al., 2014].

1.4 Microswimmers

1.4.1 Biological microswimmers

In nature, microorganisms such as bacteria, algae, and spermatozoa, have developed through evolutionary process, propulsion strategies that are driven (most of the time) by a gradient of some sort: either a gradient in nutriment concentration (chemotaxis), light (phototaxis) or gravity (gravitaxis). Most of these gradient-driven swimmers exhibit a"'run and tumble"' motion: for a given direction,

when the environmental conditions are improving, the swimmer continues to swim in that direction, and that's what is called run. When the conditions are worsening, the swimmer changes its course randomly, looking for better conditions. Two main categories of swimming microorganisms can be distinguished in Nature:

1. Passive deformation swimmers[Pande et al., 2017]: these organisms move different parts of their body in coordinated yet asymmetric ways. We can distinguish pushers that achieve forward motion by wiggling or rotating a flagellum (see fig.1.3-(a)), Squirmers such as cilia-covered swimmers which swim forward by a stroke-like wiggling of the cilia on their body (see fig.1.3-(b)) and pullers, such as *Chlamydomonas* which use two frontal flagella-like arms to swim by a breast-like pattern (see fig.1.3-(c)).

2. Amoeboid swimmers: these organisms employ pronounced changes of the membrane shape to achieve propulsion. *Eutreptiella gymnastica* represent illustration of such swimmers in nature (see fig.1.3-(d)).

All these swimmers have drag-based propulsion. They exploit the viscous drag to achieve swimming.

1.4.2 Artificial microswimmers

The design of artificial microswimmers is a technological challenge due to the difficulty of satisfying the necessary condition imposed by the scallop theorem previously introduced. Two branches in design strategies are currently followed. The first one relies on mimicking design principles found in Nature. Among many realizations, a classical example is a swimmer which imitates the propulsion mechanism of a sperm cell [Dreyfus et al., 2005, Zhang et al., 2009]. It consists of rotating a part of their body which creates a forward propulsion. Actuation is realized by application of a strong enough magnetic torque. Typical velocities are of the order of 10 μm/s [Peyer et al., 2012]. Maneuverability on the other hand is achieved by orienting the magnetic fields in 3D. In the presence of a swarm, magnetic torque affects all micro-robots in the same manner and selective control is not possible. There are also examples of biomimetic microswimmers with acoustically activated flagella [Ahmed et al., 2016, Kaynak et al.,

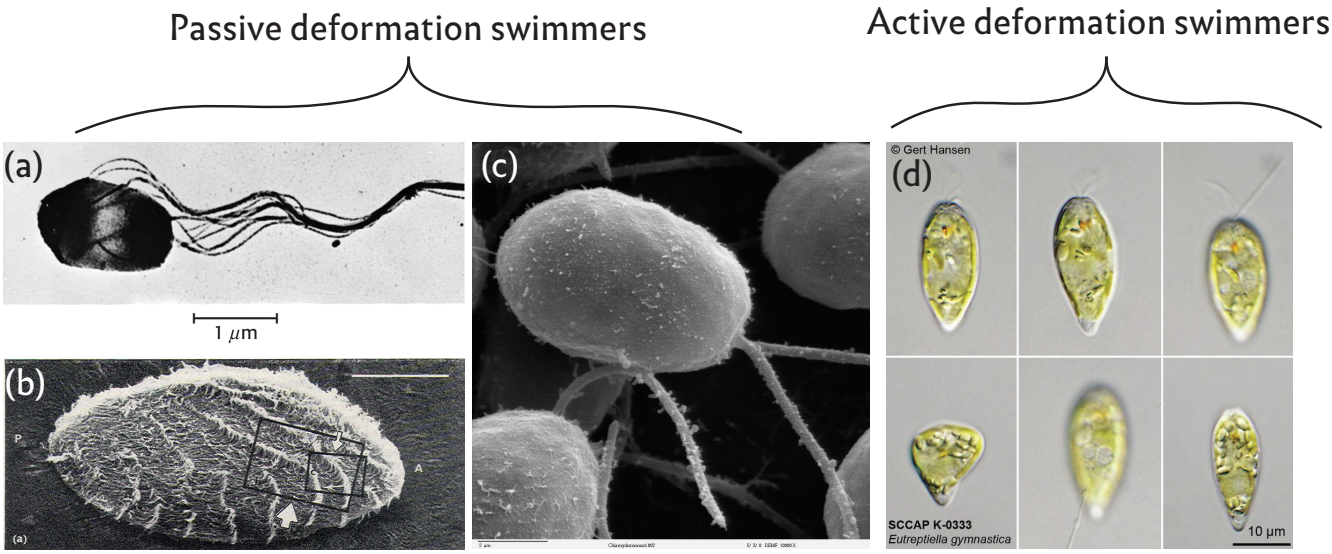

Figure 1.3: Categories of natural microswimmers: (a) Example of a pusher, image displaying Salmonella swimming by a bundle of rotating helical flagella, picture taken from [Brennen, 1977]; (b) Example of a squirmer, picture displays the cilia present on the of *Opalina*, the scale bar is 100μm, picture taken from [Tamm & Horridge, 1970]; (c) Example of a puller, image displaying a *Chlamydomonas* algae, picture taken from Dartmouth college emf; (d) Example of an Amoeboid swimmer, image represents *Eutreptiella gymnastica*, taken from Nordic micro algae.

2017]. The second branch contains novel construction principles, with simpler designs more practical to realize. Most famous category are Janus particles that rely on different types of gradient to achieve propulsion such as bimetallic nanorods and microspheres [Paxton et al., 2004] which use a chemical reaction to induce a surface tension gradient linked to the body which leads to propulsion. Other examples rely on catalytic chemical reactions to create an asymmetric, non-balanced distribution of reaction products to induce phoretic forces [Golestanian et al., 2005, R, 2009]. Such microrobots have limited fuel and/or require specific environment conditions to operate. Furthermore, they cannot be maneuvered. Therefore, they cannot be used in biological environments such as the human body. In biocompatible family, we can find accoustic microswimmers that move thanks to ultrasonically powered bubble oscillation engines [Ahmed et al., 2015, Bertin et al., 2015], which can achieve high velocity motion (1 mm/s) and are to some extent selectively manipulable. Their production in large number is limited, however.

From previous examples, we can draw a sketch of an ideal artificial microswimmer requirements:

1. It should have a simple geometry.

2. It should use a propulsion mechanism that fulfills the scallop theorem requirements, or generate inertial thrust.

3. The mechanism should not require fuels.

4. The mechanism principle can be employed in biological environments.

5. It should use a simple actuation method that allows for selective activation in a group of swimmers.

6. 3D maneuverability should be possible.

7. It should reach high velocities and overcome gravitational forces.

8. High throughput production should be possible.

We suggest to fulfill these conditions with simple spherical colloidal shells, that are microscopic objects quite easy to manufacture using common physico-chemical tricks [Zoldesi & Imhof, 2005, Pisani et al., 2009].

The swimming mechanism relies on a buckling instability that triggers brutal deflation from a spherical geometry to a concave shell configuration. When re-inflating the shell, a deformation hysteresis "'naturally"' occurs.

Practically, buckling can be experienced when playing with a jumping popper toy for example. Such mechanism can be observed in Nature, with a species of aquatic carnivorous plants called *Utricularia* which trap their preys through a sudden opening of the trap door (buckling) [Vincent et al., 2011]. However, no known biological microswimmer uses such a mechanism. The closest biological example would be amoeboid swimmers, because of the pronounced shape deformation. Details concerning the buckling mechanics will be provided in the chapter the shell dynamics.

Deflation/re-inflation cycles are driven by a single scalar control parameter (inner volume, or outside pressure). It has already been shown that classical ultrasound waves can effectively trigger buckling in such colloidal shells [Marmottant et al., 2011a]. In a group of swimmers heterogeneous in terms of radius and thickness, pressure waves with specific frequency and amplitude would be used to target individuals or a sub group separately, with strong nonlinear on/off response*. To avoid liquid cavitation in biological environments, pressure wave amplitude should be kept between -1 and 1 bar.

1.5 Motives for the up-scaling

To investigate swimming through shell buckling, we opted for a macroscopic scale study, using objects of a few centimeters in diameter while varying viscosity, so that relevant dimensionless numbers can be kept unchanged. This allowed us to access a larger set of control parameters, such as the external radius R and thickness d of the shell, the material rigidity E, and dissipation coefficients. As a consequence, a more accurate visualization of the buckling dynamics is obtained, that is not reachable at the microscopic scale.

This strategy also allows a broader choice of experimental setups, giving access to quantities and time scales hardly reachable for a microscopic study.

For all these reasons, the up-scaling was required and a technique was developed to manufacture shells.

*We will see later that buckling occurs if a critical pressure is reached. This critical pressure depends — among other parameters— on the thickness/radius ratio.

The Secret of Happiness lies in looking at all the wonders of the world and never forgetting the two drops of oil in the spoon.

The alchemist, Paulo Coelho

2

Materials and methods

To investigate the physics of swimming through shell buckling, a technique to realize the shells and three experimental setups were fully developed: an experiment where shells are attached to a spring used as a force sensor while controlling the pressure externally, another experiment where shells are linked to a freely moving frictionless rail, and to study the flow in different configurations, particle-image velocimetry (PIV) experiments were conducted where shells are kept attached to a rigid support and immersed in a liquid seeded with tracer particles. In the following chapter, the experimental methodology followed in each case will be exposed.

2.1 Shell fabrication

2.1.1 Motivations

Studying swimming through shell buckling requires a full control over the geometry, the material and the manufacturing process, to ensure the reproducibility of the experiments.

Furthermore, two constraints were to be taken into account: the ability to induce the buckling within a relative pressure range of -1 bar and 2 bar (see section 2.1.3) and the ability to apply several cycles without damaging the shell.

This implies that the material to be used has first, a high tensile strength to withstand the deformation cycle without entering the plastic domain and, second, a rigidity small enough to trigger a buckling in the imposed pressure range. Visco-elastic polymers called elastomers qualify to these prerequisites and have been chosen for the shell manufacturing.

Before deciding to manufacture spherical hollow shells, we tried different kind of commercial "'balls"' such as beach balls, squash balls and so on. It was not conclusive because the process of fabrication was not intended to be reproducible in terms of material composition, thickness or outer radius. This is why it was decided to manufacture shells.

Several techniques were considered to manufacture polymer-based spherical hollow shells, including 3D-printing, rotational molding, processes involving high-pressure vulcanization. These techniques would have required either buying expensive equipments or subcontracting to a company with inconveniences of time delay, loss of control over the process and expensive cost of prototyping. The most suitable solution was the more common bi-molding process where the two halves of an object are cast and then assembled. The main advantages are the cost and the low-time consumption, plus a total control over the process, which includes the choice of materials, the reproducibility and more freedom over the geometry. This adds a constraint to the shell manufacturing: a thickness $d > 1$ mm and an external radius $R < 50$ mm. With a thickness lower than 1 mm, it becomes hard to manipulate the cast half capsules during the gluing step. A radius larger than 50 mm would be inconvenient because it would require larger experimental setups.

The material used for the molding is detailed in the appendix A.3.1.

2.1.2 Materials and protocols

Three materials were chosen to produce the shells used in the experiments done during this study: "'Dragon Skin®30"' manufactured by "'**Smooth-on©**"' which has a specific molding protocol and AJO 121 and AJO 122 manufactured by "'**BLUESTAR silicones©**"' which have a common molding protocol. In each case, two half sphere are cast and glued together using the same material. Details of the protocol developed can be found in appendix A.2 and A.3.

2.1.2.1 Dragon skin®30

This material is typically used to make special effects. In the case of our study, it was used to investigate the effect of the $\frac{d}{R}$ parameter on the swimming mechanism. The exact chemical constitution of this so-called "'cure liquid silicone compound"' could not be provided by its manufacturer. It consists of two liquid components named A and B, highly viscous. Component A represents the silicon polymer chains, with the presence of fillers designed to enhance the mechanical properties of the final material. Component B is the cross-linking agent providing bonds that link one polymer chain to another, decreasing the flexibility of the polymer chain and increasing its rigidity. Mixing these two components at room temperature creates a semi-transparent solid that takes the shape of the container it was poured in. The typical mechanical properties of the resulting rubber -given by the manufacturer- are:

- 100% elastic modulus : 0.6 MPa
- Elongation at break : 364%
- Shore A Hardness : 30
- Specific gravity : 1.08
- cure time (at room temperature) : 16 hours

2.1.2.2 AJO121/122

The two materials *AJO 121* and *AJO 122* were samples kindly supplied by "'**BLUESTAR silicones©**"'. Both are hot curing silicone rubbers obtained after addition of a vulcanization agent. The

typical applications of these materials are molding and injection molding process for technical parts. They were chosen to investigate the effect of solid dissipation, characterized by the rebound resilience property. This pair of materials present the particularity of sharing the same value for what concerns the elastic modulus, which means that the elastic energy stored when a stress is applied is exactly the same. Both materials present a soft white paste-like texture. The vulcanization process is temperature-controlled and is induced at 115°C.

The typical mechanical properties of the resulting rubbers -given by the manufacturer- are:

- 100% elastic modulus AJO121 / AJO122 : 2.2 MPa / 2.3 MPa
- Rebound resilience AJO121 / AJO122 : 45% / 65%
- Elongation at break AJO121 / AJO122 : 560% / 366%
- Shore A AJO121 / AJO122 : 60 / 59
- Specific gravity : 1.16
- cure time (at 115°C) : 10 minutes

2.1.3 Spherical shells

The spherical shells used in the different experiments are (i) a set of 3 shells cast in the 'Dragon skin ®30' material, with three thicknesses: 2 mm, 5 mm and 6.5 mm and (ii) a set of two 2mm thick shells, cast in the "'AJO 121"' and "'AJO 122"' materials. All the shells have an external radius of 25 mm.

The choice of the thicknesses of the first set is primarily directed by the fact that we wanted to explore the effect of stored elastic energy on the buckling mechanism and on the thrust induced during the deflation and the re-inflation of the capsule. Taking into account that the theoretical critical pressure P_c that triggers the buckling instability scales like $\frac{d}{R})^2$ [Landau & Lifshitz, 1986, Marmottant et al., 2011b], the resulting range of variation of the geometric ratio $\frac{d}{R}$ is 6.4 10^{-3} to 6.8 10^{-2}, hence one decade in d/R. A lower value of this parameter was tried (taking a thickness of 1 mm) but it resulted in a spontaneous buckling when the shell was immersed, due to the static pressure gradient. A

higher value of this parameter was tried (taking a thickness of 7.5 mm) but it was not possible to produce a buckling in the range of the operable relative pressure [0, 2] bars.

The second set of shells cast in the "'AJO 121"' material and the "'AJO 122"' is intended to study the effect of material dissipation over the swimming, taking into account that the two materials used have, approximately, the same elastic modulus.

Theoretically, the buckling instability nucleates randomly on the surface of the shell. Practically when the boundary conditions are not changed [*], this instability always occurs at a specific spot of the elastic shell which represent its weak spot. Hence during the manufacturing, an imperfection was introduced over the shells, by locally reducing the thickness by 0.2 mm over a disk of 10 mm diameter. This imperfection is introduced in order to impose the location of the buckling spot, which allows a better control of the orientation of the ball in the different experimental setups. This imperfection affects the theoretical critical buckling pressure[Lopez Jimenez et al., 2017]. However, the reduction of thickness is relatively small and its effect is negligible.

For the frictionless rail and PIV experiments, a 2 mm hole is drilled in each shell and a nozzle is plugged in it, to connect the inner volume to the pressure controller through a flexible tube.

For the PIV measurement experiments, the shells are dyed in black (matt paint) to absorb the laser light and avoid strong refraction on the surface which can damage the camera pixel sensors.

2.1.4 Buoyancy

Ideally, we wanted to study the swimming of a spherical shell in the bulk fluid, which can move in all directions. But since we opted for shells at the macroscopic scale, a buoyancy problem rose: the overall density of the spherical shells is small compared to the density of the liquids in which we wanted to conduct our experiments. One can propose to ballast the shell to match the liquid's density, but during

[*]Experimentally, when the shell is in contact with a wall, the buckling spot locates at the contact point, due to some change in the shell stress.

the deflation, there is a drastic drop in the volume which would increase the "'shell+ballast"' system's density. Taking into account that the typical period of the pressure cycles is around 15 s, this would have been enough time to make the swimmer sink. Hence, we cannot study the swimming of a **free** spherical shell in the bulk. Practically, this means that the shell needs to be kept immersed in the liquid by some means. This was the main constraint to take into account when designing the experimental setups that will be presented next.

2.2 Spring experiment

2.2.1 Brief introduction and motives

The purpose of this experiment is to quantify different relevant quantities such as volume, shell deformation and thrust, during the buckling and unbuckling phases when the pressure cycle is imposed externally. In order to prevent the shells from floating (due to buoyancy effects), we attached them to a spring fixed to the bottom of the tank, by the intermediate of a suction cup. The spring keeps the shells immersed, but also, if well designed, plays the role of a force sensor. The buckling spot is directed in the vertical direction, to get a 1-D displacement.In theory, the buckling can happen anywhere randomly on the capsule. In practice, the buckling happens at the same spot if the boundary conditions are not changed [Lee et al., 2016, Zhang & Ru, 2016]. This is due to the presence of a localized weakness in the material which determines the buckling spot.

Pressure cycles are applied by pressurizing the air above the liquid in which the shell is immersed. Figure 2.1 is a representation of the spring experiment.

The advantages of this method is that all the forces that are involved can be quantified using the recording images of the experiment.

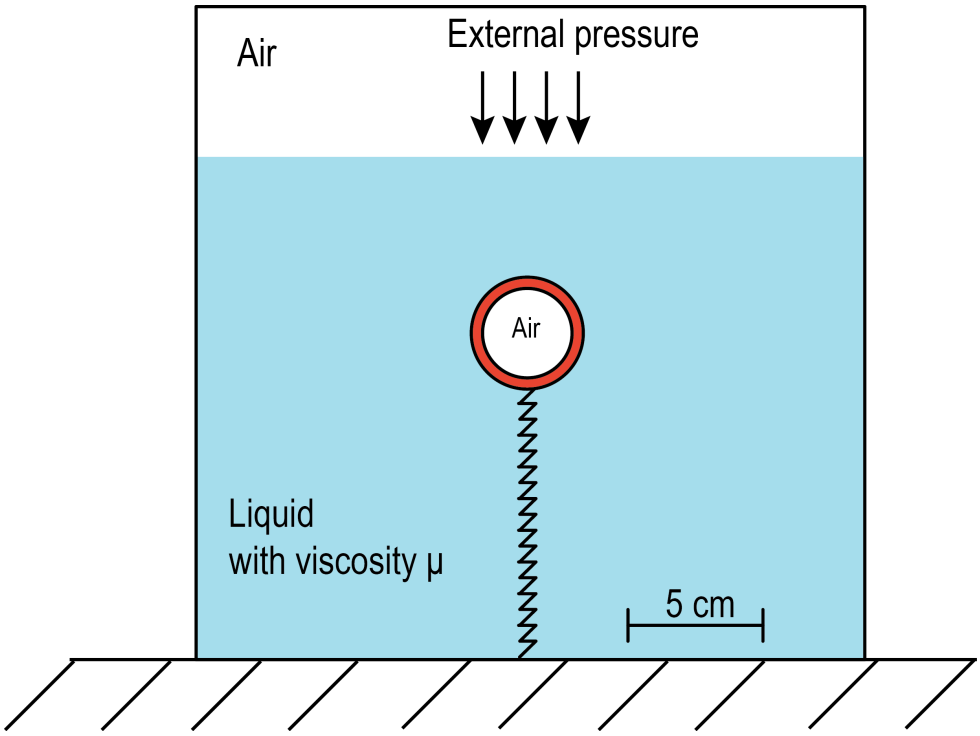

Figure 2.1: Schematics of the spring experiment. The liquid can be considered as Newtonian and incompressible.

2.2.2 Equipment

2.2.2.1 Tank

It consists of a cubic tank (see fig.2.2) made of anodized Aluminum supplied with windows made of polycarbonate polymer. It is dimensioned to withstand an absolute pressure of $3.10^5 Pa$. Its dimensions are consistent with the non-confinement conditions where the characteristic length of the container is close to 10 times the characteristic length of the object to be studied.

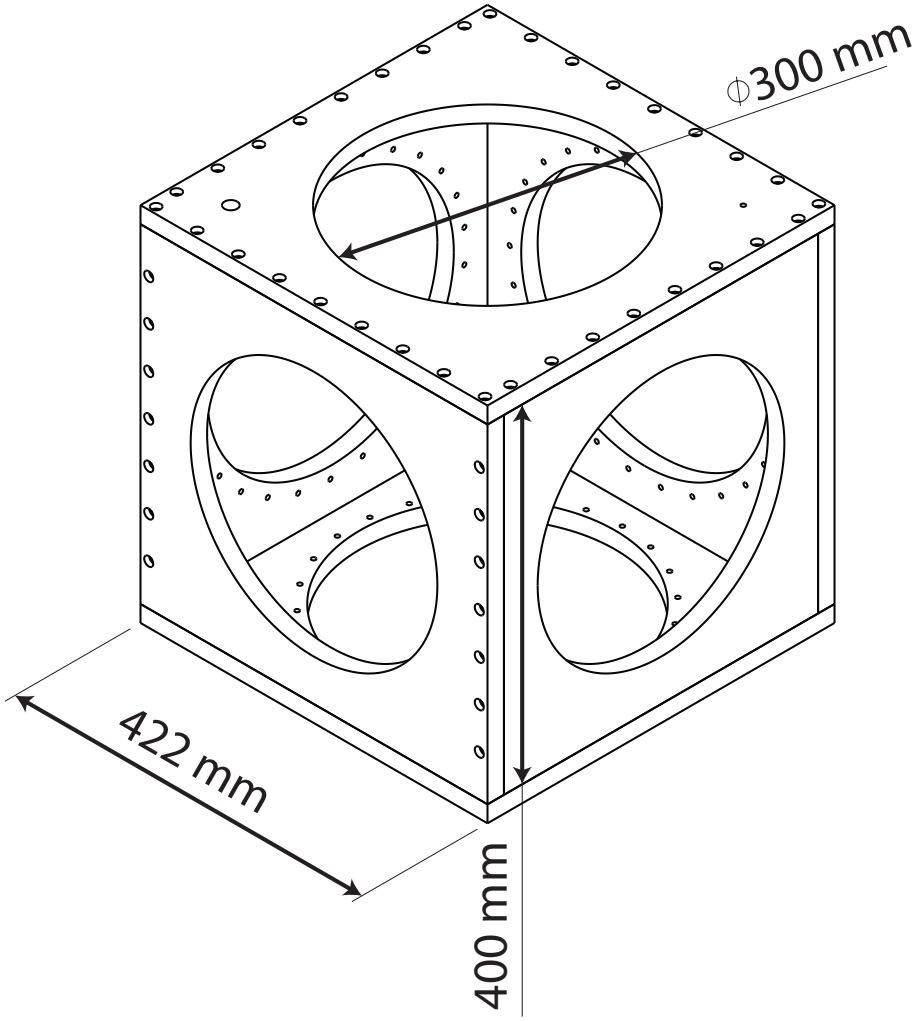

Figure 2.2: Schematics of the pressurizeable tank

2.2.2.2 Spring

As described earlier, the spring is used as a force sensor. When the system "'shell-spring"' is static, its elongation is directly proportional to the tension force $k\Delta x$, where k is the stiffness coefficient. In the case of our study, the spring is solicited in traction*. The spring also allows to keep the spherical shell immersed in the liquid.

*At any moment, during the experiment, the elongation of the spring is bigger than the length at rest with no mass attached.

Taking into account that the outer radius for all the capsules studied was fixed at 25 mm and that the buoyancy force is significantly larger than the weight, only one spring stiffness was needed to carry out all the experiments. The spring-shell system was dimensioned to have a total length of 200 mm, at rest, in water. Knowing that after the buckling, the equilibrium state reached is lower due the decrease in volume (by $\approx$ 20%, determined by preliminary results), a constraint was added to avoid the case where the spring rings would be in contact with each other, which would bias the force measurement.

The characteristics provided by the manufacturer concerning the spring used in this experiment are:

- Stiffness coefficient : 7 N/m
- Length at rest : 100 mm
- Material : EN 10270-3 stainless steel
- Wire diameter : 0.5 mm
- External diameter: 7.93 mm

It was also provided with threaded ends to fit M6 and M4 screws. The M6 end is designed to link the spring to a fixed base at the bottom of the tank. The M4 end is designed to support a suction cup provided with a M4 screw. This suction cup is used to attach the spherical capsule to the spring.

2.2.2.3 Pressure controller

Since deflation and re-inflation cycles are actuated by applying a difference of pressure between the inside of the shell and the outside, it was necessary to use a pressure controller (an instrument that allows to regulate pressure set by the operator in an enclosed environment).

The equipment used during this experiment is the OB1 flow control system manufactured by Elveflow©. This system is supplied with channels which operate between 0 and 2 bars (relative pressure); one channel operates between -1 and 1 bar and requires a vacuum pump to reach -1 bar, in addition to a pressure source. In the spring experiment, the external pressure is the control parameter, therefore only a 0-2 bar channel was used.

The pressure is controlled thanks to a graphical interface, which allows to apply different kind of pressure signals such as: constant, ramp, sinusoidal, square signals. It also allows programing sequences using the previously stated signals, but also wait time, triggers and loops. This particular function was helpful to implement reproducible pressure cycles during the spring experiment [*].

2.2.2.4 Camera, lenses and light sources

Camera: Taking into account the fast nature of the instability, where the shells undertakes a deformation of almost a radius in less than 5 ms, it was necessary to use a high-speed camera. The camera used for this purpose is the Phantom©Miro 310, its main characteristics are the following:

- Resolution: One megapixel, 1280x800.
- Full resolution speed: 3260 frame per second (FPS).
- Sensor: CMOS sensor with 20 μm pixel size, 12-bit depth gray-scale colors.

It is supplied with a software which allows the control of these parameters and also triggering and storing images.

Lenses: A lens with high iris opening value is necessary to capture images at high speed with low light exposure. It was necessary to capture a large field which contains an object of 50 mm plus part of a spring which moves during the process. This is why a fixed focal length $f = 50$ mm with a maximum aperture of f/1.4 was selected.

Light source: Three parameters were to take into account for the choice of light sources:

[*]This pressure controller is not supposed to be used in such conditions, operating on rather large air volumes. One of its inconveniences was its time response with a max air-flux dimensioned for micro-fluidic experiments. We bought a pressure controller intended to work with large volumes but it was not supplied with neither any power supply nor any software and necessary electronics to control it with a computer. The fact that we were not investigating the actuation frequency role in the physics and the impossibility to control negative relative pressures, comforted us into using the plug and play solution "'OB1"'.

1. A stable source of light with no variation of light intensity was required to be able to use the 2D image registration algorithm "'UnwrapJ"', to correct the deformation of the tank windows, due to pressure.

2. A powerful intensity is required to be able to record at high speed.

3. A homogenous light source is needed to be able to correctly extract the edges of the shell from the images (no light gradient).

To do so, two 30x30 daylight balanced led-based panels were used providing 6560 lumen, disposed as shown in figure 2.3. The one at the back is tuned at full power to highlight the complete ball-spring system and a filter is added to diffuse light and avoid seeing the individual leds. The one upfront is used with 25% of its power, in order to see the concavity, once the shell is buckled.

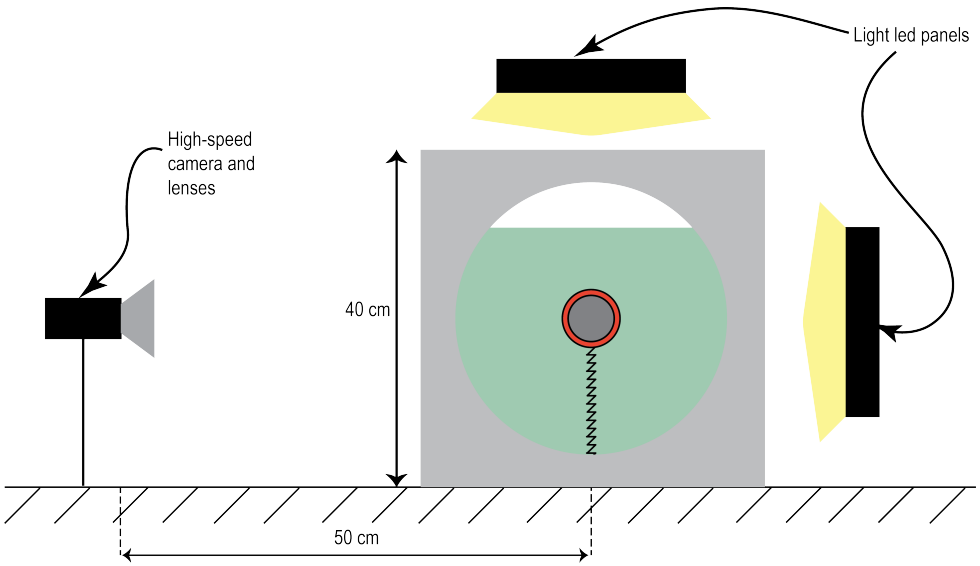

Figure 2.3: Representation of the light and camera disposition for the spring experiment

2.2.3 Experimental process

2.2.3.1 Experimental protocol

We used three fluids in this experiment, and in each fluid, three capsules were investigated varying the relative thickness $\frac{d}{R}$ (see sec.2.1.3). The main characteristics of the fluids used are shown in table 2.1.

Fluid	Density (Kg.m^{-3})	Viscosity (Pa.s)
Glycerol	1250	1
Water	1000	10^{-3}
Air	1.2	10^{-6}

Table 2.1: Fluids used in the experiments and their main properties at room temperature.

The following experimental protocol is applied for each fluid.

First, an image is recorded at (P=0), then the pressure is increased by a pressure step and an image is recorded. This process is repeated until nearing the pressure at which the buckling occurs, which can slightly vary from an experiment to another; the pressure is then gradually increased by smaller steps* and when arriving to a critical pressure where the buckling occurs, the camera is triggered and a movie is recorded at 5000 FPS. An image is taken at the end of the buckling phase, in order to record the state to which the capsule has relaxed to, following the buckling. The pressure is decreased with a certain depressurization rate α until nearing the critical pressure at which the unbuckling occurs and the same procedure is followed for the buckling phase. After that, the pressure is decreased down to zero.

*The smaller steps are necessary in order to keep the pressure constant at the buckling and unbuckling phases, to independently study the buckling and unbuckling dynamics.

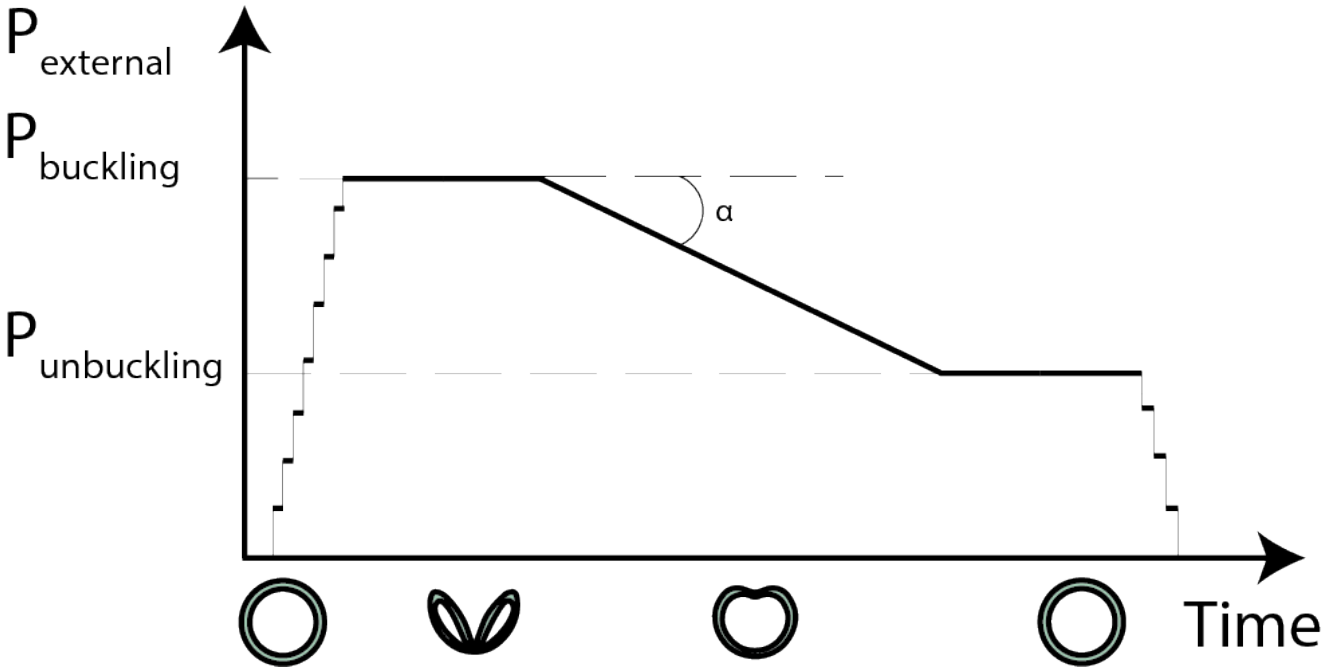

Figure 2.4: Qualitative representation of pressure cycles applied during the experiments

The temperature of the fluid is measured at the beginning of the pressure cycle, and at its end. These temperature measurements are then used to properly characterize the viscosity of the medium, by taking a sample and perform rheological measurements, thanks to a rheometer.

The tables 2.2, 2.3 and 2.4 summarize the control parameters of the pressure cycle for each $\frac{d}{R}$, in each fluid.

Capsules	Buckling pressure (mbar)	Unbuckling pressure (mbar)	Depressurization rates α(mbar.s^{-1})	Temperature (Celsius)
$\frac{d}{R} = 0.08$	100	[70,80]	-1, -10, -20	[20,21.5]
$\frac{d}{R} = 0.22$	[780,790]	[380,390]	-1, -10, -15	[24.5,26]
$\frac{d}{R} = 0.30$	[1350,1450]	[620,660]	100 mbar steps, -1, -10	[25,26]

Table 2.2: Experimental pressure cycle parameters in glycerol

Capsules	Buckling pressure (mbar)	Unbuckling pressure (mbar)	Depressurization rates α (mbar.s^{-1})	Temperature (Celsius)
$\frac{d}{R} = 0.08$	[100,110]	[75,85]	-1, -10, -20	[23,23.5]
$\frac{d}{R} = 0.22$	780	[360,370]	-1, -10, -20	[20,23.2]
$\frac{d}{R} = 0.30$	Experiments were not possible due to the non visibility of the buckling concavity in water.			

Table 2.3: Experimental pressure cycle parameters in water

Capsules	Buckling pressure (mbar)	Unbuckling pressure (mbar)	Depressurization rates α (mbar.s^{-1})	Temperature (Celsius)
$\frac{d}{R} = 0.08$	[100,110]	[70,80]	-1, -1, -2	[23.5,25]
$\frac{d}{R} = 0.22$	[850,900]	[380,480]	-1,-2,-2.5	[24.5,26]
$\frac{d}{R} = 0.30$	1570	790	-1	23

Table 2.4: Experimental pressure cycle parameters in air

2.2.4 Image treatment

Image treatment is the basis of the measurements extracted from the spring experiment, since every physical quantity of interest is extracted from the images. But before quantitaively recording position data from the images, a correction of the distortion (due to windows curving during the pressurization of the tan)k was necessary.

2.2.4.1 Image calibration due to window distortion

When static pressure is applied inside the tank used for the experiment, its ploycarbonate windows, bend. This bending induces a barrel distortion which intensity depends on the pressure applied inside the tank (fig.2.5). Distortion alters the images recorded during the experiment and ultimately any distance measurements extracted from them. The error depends on the camera position in regard to the window, the spring-ball position in regard to the window and the pressure inside the tank. For example, an estimation of this deformation at (P = 1000 mbar), by measuring a horizontal central line between the image at (P=0) and at (P=1000 mbar) yields an elongation of $\epsilon_{horizontal} = \frac{\Delta L}{L_0} = 2\%$

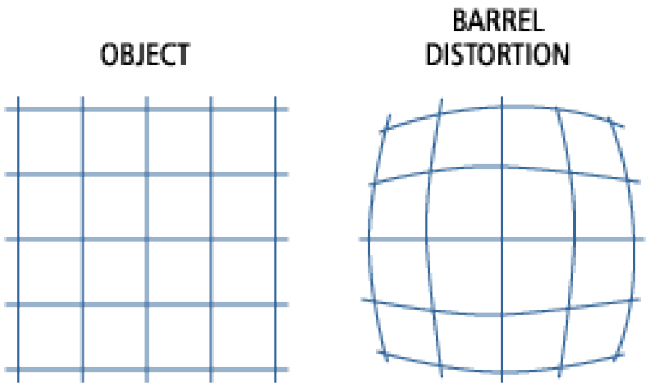

Figure 2.5: Qualitative representation of a barrel distortion

To correct this effect, a numerical method is applied to find the deformation of the image between the rest state (where the relative pressure is zero) and a state at pressure P. Once found, this deformation matrix is inverted and we can transform a distorted image to a non-distorted one. To calibrate the correction, the spring-ball system is removed and a damier is placed at the place of the spring-ball system. Images are recorded for each one of the pressure steps used during the experiments in one fluid. From each damier image, we extracted a deformation matrix that links the rest state at (P=0) to the damier image at (P=p_{image}) and the deformation matrix is inverted to get the transformation needed to transform the damier image at (P=p_{image}) into the damier image at (P=0), using an algorithm implemented in the registration plugin category of ImageJ, called "'bUnwrapJ"'.

"'bUnwarpJ"' is an algorithm for elastic and consistent image registration developed as an ImageJ plugin. It performs a simultaneous registration of two images, A and B. Image A is elastically deformed in order to look as similar as possible to image B, and, at the same time, the "inverse" transformation (from B to A) is also calculated so a pseudo-invertibility of the final deformation could be guaranteed.

This image registration algorithm is based on the minimization of an energy functional that includes the dissimilarity between the source and target images -in both directions- E_{img}, an optional landmark constraint E_{μ}, a regularization term ($E_{div} + E_{rot}$), and an energy term E_{cons} that accounts for the geometrical consistency between the elastic deformation in both directions. Namely, the energy function is given by:

$$E = w_i E_{img} + w_\mu E_\mu + (w_d E_{div} + w_r E_{rot}) + w_c E_{cons}$$

Where the weights of every term are set by the user in the main window of the plugin. The optimization process is a Levenberg-Marquardt minimization enhanced by a Broyden-Fletcher-Goldfarb-Shanno (BFGS) estimate of the local Hessian of the goal function, and both, images and deformations are represented by cubic B-splines [Arganda-Carreras et al., 2006, Sorzano et al., 2005].

Once the deformation matrix and its inverse extracted from the calibration step, each inverse transformation matrix $A(P)$ is applied to the $image(P)$ recorded during the spring experiment. The result-

ing image corresponds to an image recorded using a non-deformed tank window.

All this process was automatized, using a script written in ImageJ macro language.

2.2.4.2 Contour extraction algorithm

Once the distortion corrected, we needed to extract from each image three physical quantities:

1. Elongation of the spring.
2. Shape and volume of the capsule.
3. Gravity center of the capsule.

An algorithm was written in Python, based on an image treatment library called "'Opencv"', to automatically extract the three quantities for each image. The steps followed will be presented accompanied with an illustration for each step, depicting the case of a deflated shell (fig.2.6):

Figure 2.6: Raw image used for the illustrations

First, the image is cropped and filtered, using two types of filters: a Gaussian filter where each point in the input array is convolved with a Gaussian kernel and then summing them all to produce the output array. Gaussian blurring is highly effective in removing Gaussian noise from the image. The second, is a median filter, which runs through each element of the image and replaces each pixel with the median of its neighboring pixels. It is highly effective against salt-and-pepper noise in the images. The filtering kernel sizes were kept to a low level, to avoid dilatation of the pixels and an alteration of the capsule's contour.

Second, Canny edge detector algorithm[Canny, 1986] is used to find the edges on the image (fig.2.7). Briefly, this algorithm relies on finding the intensity gradients of the image, thinning the edge, by using the "'non-maximum suppression"' technique, and then applying a double threshold to get rid of the noise.

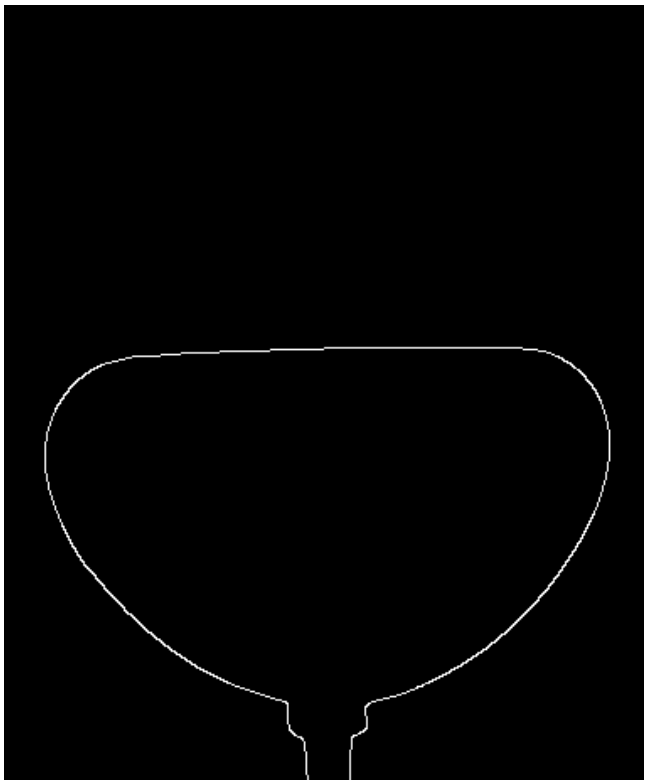

Figure 2.7: Canny edge detection

From the Canny image (fig.2.7), the white pixels are extracted, providing the general contour. Then, the capsule shape is extracted, by setting a threshold on the horizontal distance between two white points.

Once the ball shape defined, its outer contour is fitted with a parametric curve (see fig.2.8), defined in the polar coordinates system as such:

$$\tilde{R}(\theta)_i = \sum_{k=0}^{M} a_k \sin(\theta_{exp_i} - \theta_0)^k$$

The algorithm followed can be found in appendix A.4.

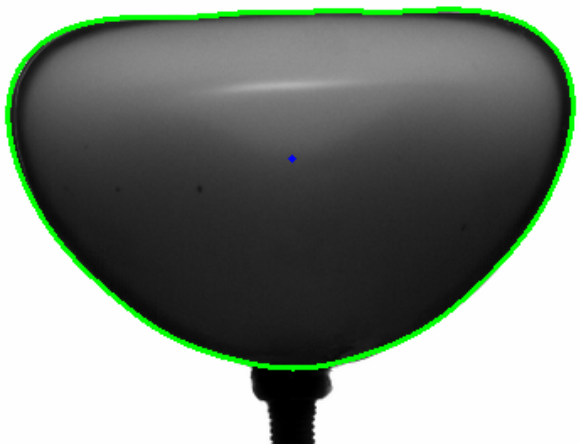

Figure 2.8: Fitted outer contour in green, and center of the parametric curve in blue

Once the outer contour fitted (fig.2.8), the experimental points defining the concavity are extracted from the image automatically. A region of interest (ROI) where the concavity occurs is defined around the maximum diameter region (fig2.9). Canny edge detector, is then applied to the ROI.

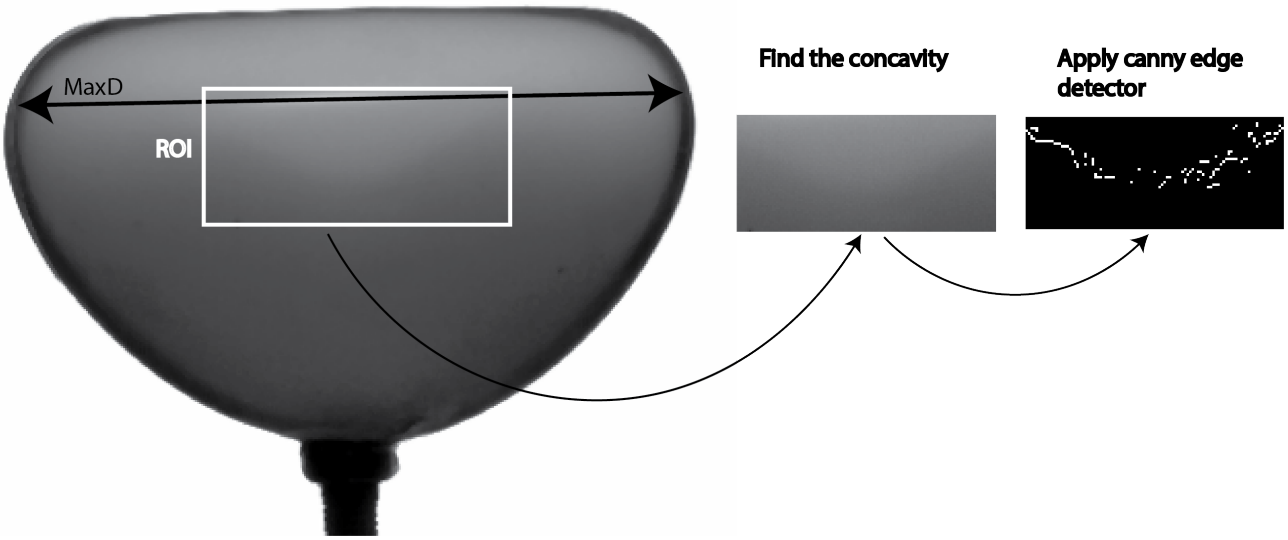

Figure 2.9: Extraction of the concavity experimental points

To create a complete fit between the outer contour and a fit of the concavity, we need first to cut the outer contour where it ceases to belong to the shape generatrix, which generates the physical surface of the concave capsule, when integrated around the y-axis. This limit is set by the point of the parametric outer curve where the tangent is almost horizontal (numerical threshold sets the angular limit to 5.10^{-2} rad). Practically, it means, find the point $M(R_h, \theta_h)$, such as the the following condition is respected:

$$\tan(\theta + \alpha) = 0 \tag{2.1}$$

Where α is the angle defined between the tangent line T with the vector $\vec{OM}$ (see fig.2.10), such as:

$$\tan(\alpha) = |\frac{\tilde{R}(\theta)}{\tilde{R}'(\theta)}| \tag{2.2}$$

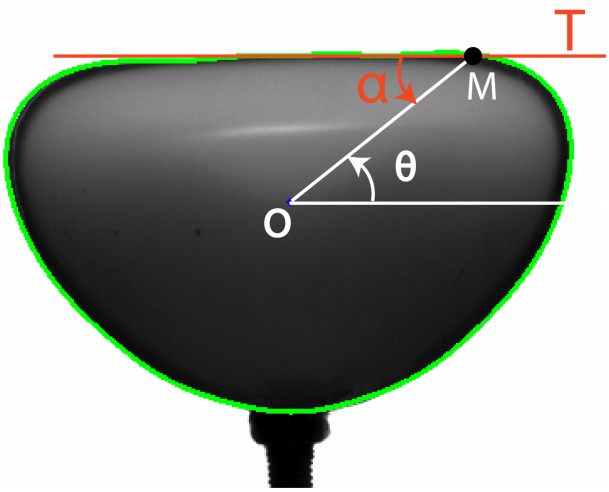

Figure 2.10: Definition of the horizontal tangent

The outer contour belonging to the shape generatrix is defined as:

$$\tilde{R}(\theta) = \sum_{k=0}^{M} a_k \sin(\theta)^k$$

With $\theta \in [-\pi - \theta_h, \theta_h]$

The concavity experimental points with a polynomial which guaranties the continuity and differentiability at the $M(R_h, \theta_h)$ point.

The combination of the two fits determines an analytical description of the generatrix (fig.2.11), allowing the analytical calculation of the volume and the center of gravity of the capsule.

As precised earlier, the example treated here is the most complex. In the case of a convex shape (non-buckled shape), only the outer contour fit is considered, and θ_h is equal to $\frac{\pi}{2}$.

The estimation of the error over the shape detection is set to the pixel level, and is around 0.1mm

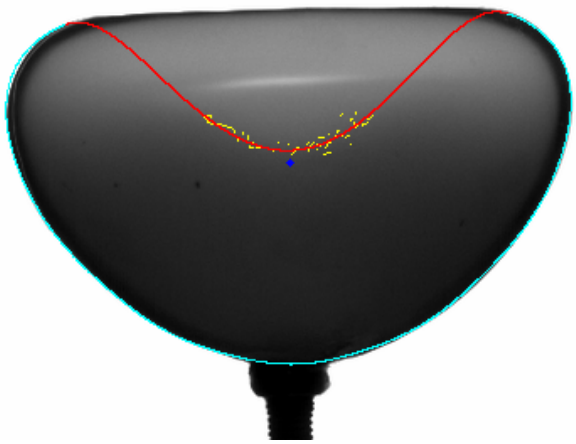

Figure 2.11: Fitted outer contour in blue, fitted concavity in red, and experimental concavity points in yellow

2.3 Frictionless rail

2.3.1 Brief introduction and motives

The spring experiments allows us to quantify —among other quantities— the thrust induced by the buckling and unbuckling phases, in a situation where the shells are attached to a spring, but we wanted to go further by studying the shell dynamics and its interaction with the surrounding fluid in a configuration that allows more freedom. Keeping in mind that shells are light and float to the surface when left free of any attach, we needed to design an experimental setup which keeps the shell immersed and allows it to move freely at the same time. One of the most elaborate attempts [*] was to attach the shell to a support, itself fixed to a large plastic disc. The plastic disc/shell system is trapped between two non-miscible liquids[†] designed to present a large difference of density, which increases the stability when the pressure is eventually applied. This setup would have allowed to study the 2-D motion of a spherical shell submitted to external pressure cycles, but unfortunately stability issues rose during the buckling and unbuckling phases. Buckling increases the density of the system due to the strong deflation, but also shifts the center of gravity of the system and tilts the disc, preventing from having controlled and reproducible experiments.

To characterize the swimming, we kept the idea of a free swimmer but constrained the degrees of freedom to only one. The setup we used consists in a spherical capsule attached to a support, itself mounted on an frictionless air bearing which can slide horizontally on a rail, allowing a 1-D translational displacement. The shell is immersed in a liquid, as represented in figure 2.12. Contrary to the spring experiment where the shell deformation is actuated through application of a positive relative

[*] 3 other experimental setups were tried: The first based on ballasting the shell to have the same density with the surrounding liquid, but the volume change during the buckling and unbuckling is too brutal to find a ballast that works in all deformation configurations. The second is based on using a splined shaft, implying a solid friction and a threshold to overcome in order to move. A displacement was observed during the buckling but not during the unbuckling, which could not allow us to conclude on the net displacement for a free spherical shell. The third experimental setup developed relied on using a magnetic long shaft surrounded by a thin magnetic envelop, oriented in a way to have a repulsion and thus, levitate. Unfortunately, it was too unstable to produce reproducible experiments.

[†] This condition comes from the fact that when pressurizing the tank, air is blown inside the tank creating a flow which may move the disc. To avoid this bias, a liquid is added on top of the disc, lighter than the system, allowing to damp the flow generated by the pressurization.

pressure inside a tank, this option was not chosen in the frictionless rail experiment, due to the complexity of the experimental setup it would have required: Building a bigger tank designed to host a 600 mm long rail, and apply two different pressure ranges, one to supply the truck with a 5-6 bar pressure, and another range between 0 and 2 bar applied inside the tank, and most importantly, find a way so that when pressurizing the tank, the air flow doesn't move the frictionless rail and pollute the displacement measurement. Instead, the shape deformation cycles are induced by applying negative pressure cycles to the volume of air enclosed in the spherical capsule. This is done by connecting the enclosed volume to a pressure controller, through a flexible pipe. The buckling spot is oriented in a direction parallel to the rail, to ensure the capture of the full displacement during the buckling and unbuckling phase. The position of the support and the shell deformation are captured using a high-speed camera.

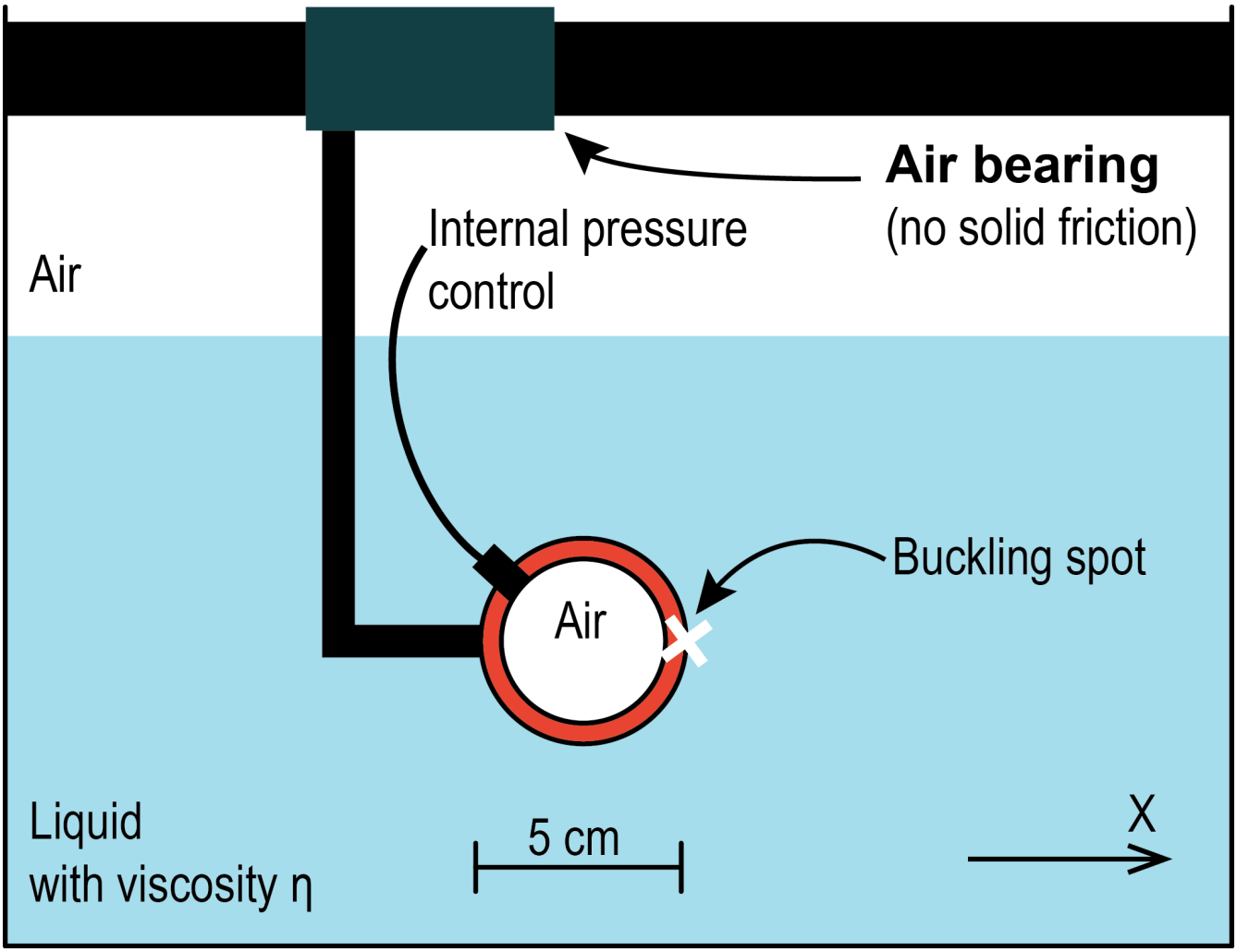

Figure 2.12: Schematic representation of the frictionless rail experimental setup

2.3.2 Equipment

2.3.2.1 Air bearing system

The air bearing rail system manufactured by "'Air Way ™"' (fig.2.13), is constituted of two main parts made of black anodized aluminum. The first component is a 600mm long and 75mm large T-shaped rail, which serves as a guide to the second component, which the truck. The truck is designed to slide along the guide without solid friction. This is possible thanks to microscopic holes present in the inner surface of the truck. These holes allow pressurized air to stream on the surface of the guide

and create a cushion air, which prevents the surfaces of the guide and the truck from being in contact. The air pressure which is provided to the truck through its inlet, sets the load capacity.

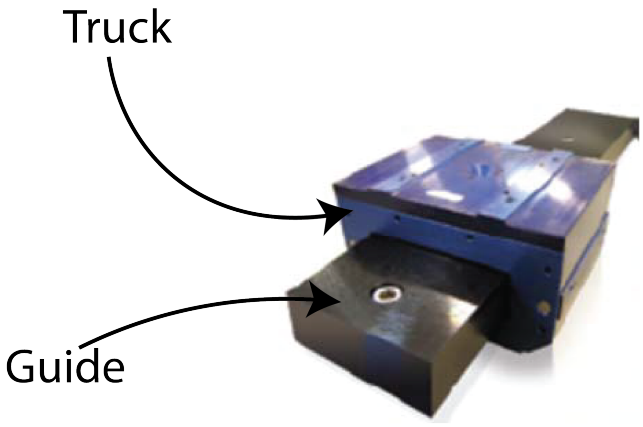

Figure 2.13: Illustration of the air bearing system

In the case of the experiment, the input pressure was of 5 bars. This pressure allows the loads precised in table 2.5. These maximum loads are big compared to the forces involved in the experiment. For example, the max buoyancy force plus the weight of the truck give a total of 11N.

A flexible tube is used to link the air pressure source to the truck pressure input. The tube is suspended at a 2m height and left loose, to avoid any bending or tension force which might displace the truck and lead to a measurement error.

Input pressure (bar)	horizontal load (N)	Vertical load (N)	maximum moment force in the three directions (Nm)
6	473	709	2.8

Table 2.5: Load capacity for a 5 bar pressure

The rail is mounted on two slides, which can translate vertically on two rigid extruded aluminum profiles(fig.2.14). This allows to set the rail at the horizontal plane, using an electronic spirit level. This operation is necessary to ensure that no drift is produced, which may lead to unsatisfactory measuring precision.

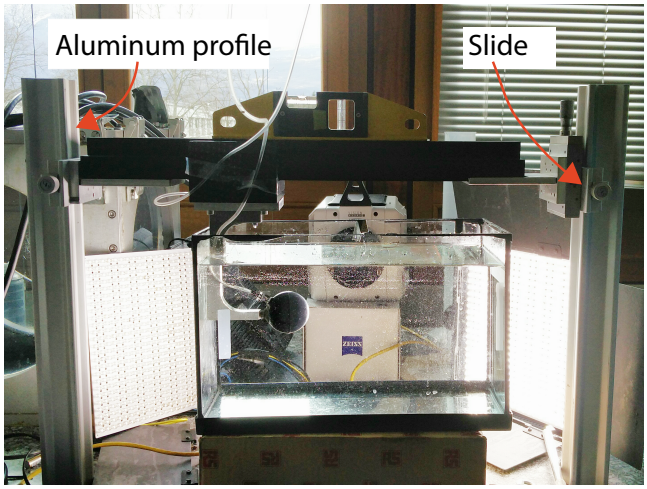

Figure 2.14: Picture representing the experimental setup to mount the rail

2.3.2.2 Mounting support

To link the spherical shell to the truck, a L-shaped mounting support was realized made of Aluminum (fig.2.15). This support is supplied with a tapped hole to fix it to the truck and a tapped hole to connect it to the spherical shell, through a suction cup. The support weighs 250g, in addition to the 1300 g of the truck. Other materials and designs were considered to make a lighter support, but we found out that the thrust produced during the buckling phase, was able to bend the support, which alters the displacement produced and introduces a bias in the experiment and its physical interpretation.

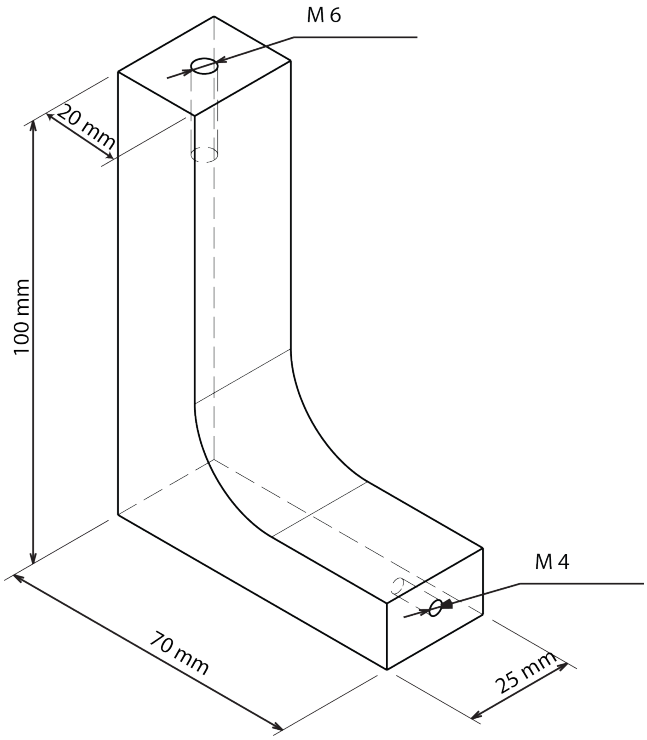

Figure 2.15: Schematics of the mounting support

2.3.2.3 Pressure controller

The pressure controller used in this experiment has been presented earlier in the spring experiment (2.2.2.3). This time, it is operated on the [-1,1] bar channel and required the use of a vacuum pump to reach -1 bar.

2.3.2.4 Tank

The tank used in this experiment is an open recipient, with 340mm by 170mm rectangular base and 250 mm height, made out of glass.

2.3.2.5 Camera, lenses and light sources

The equipment used for the experiment is the same as in the spring experiment (2.2.2.4). In addition, a macro lens with a fixed focal length $f = 100$ mm with a maximum aperture of f/2.0 was used to zoom over a region of interest, without losing spatial resolution.

2.3.3 Experimental process

Experimental investigations were focused on the effect of primary physical quantities over the swimming. The quantities explored are:

1. The effect of the amount of elastic energy stored prior to buckling on the swimming efficiency. This is done by varying the thickness of the shell, keeping the outer radius constant, and this is performed with the set of three shells cast out of "'Drangon skin"'®material.

2. The effect of solid dissipation on the swimming efficiency, by varying the rebound resilience of the material in which the shell is cast. This quantity refers to the restitution rate of the stored elastic energy. To isolate its effect, two materials were chosen with the specificity of sharing the same elastic modulus, and two shells with an identical thickness were cast.

3. When at proximity to a wall, with the buckling spot facing it, the swimming induced by the buckling and unbuckling phases is modified. To study this effect, two series of experiments are conducted, one far from the wall, to characterize the swimming in the bulk, and the second one near the wall to study the effect of directional confinement*.

All the enumerated experiments above are conducted for different viscosities of the swimming medium, to vary the *Re* number characterizing the flow regime. To do so, seven "'water-glycerol"' solutions were prepared, with viscosities ranging from 0.001 Pa.s with (100% Water-0% glycerol) solution to 1.3 Pa.s with a (0% Water-100% glycerol) solution, with a targeted viscosity step of half a decade, taking advantage of the miscibility of the (water-glycerol) couple. To target the desired viscosity, the volume fraction of each liquid needs to be calculated precisely, because the viscosity of a water-glycerol solution evolves in a non-linear way[Cheng, 2008]. To approach the targeted viscosity, the volume fractions were calculated using an empirical formula found in the literature[Cheng, 2008]. A sample is collected at the end of the experiment and its viscosity is measured at the experiment temperature range.

*Only the frontal wall proximity is investigated, the lateral, rear or any other angular configurations are to be studied in the future

In addition, experiments are conducted in a liquid called "'UCON Lubricant 75-H-90,000 "', which has a viscosity of 37 Pa.s at room temperature, providing another decade to the viscosity range explored. All the water-glycerol solutions are transparent, and the "'UCON Lubricant"' presents a yellowish coloration which does not impede the visualization during the experiment. Table2.6 summarizes the solutions in which the experiments are conducted.

Solution number	liquid volume fractions	targeted viscosity at 20°C (Pa.s)
1	100% Water-0% glycerol	0.001
2	59% Water-41% glycerol	0.005
3	47% Water-53% glycerol	0.01
4	26% Water-74% glycerol	0.05
5	19% Water-81% glycerol	0.1
6	6.4% Water-93.6% glycerol	0.5
7	0% Water-100% glycerol	0.5
8	100% Ucon oil	37

Table 2.6: Summary of the solutions prepared.

2.3.3.1 Experimental protocol

Once the volume fractions for a targeted viscosity are calculated, a 20L solution is prepared, and an experimental protocol is followed for each one of the 5 shells to be studied:

Preliminary settings First, the spherical shell is connected to the mounting support via a suction cup that is, on one hand, glued to the spherical shell and on the other hand screwed to the M4 tapped hole in the mounting hole.

The system "'support-shell"' is immersed at the liquid's mid height. This step is followed by a horizontality check of the frictionless rail, using a spirit level that allows a 0.001 rad precision.

Then, rail pressure inlet is supplied with a 5 bar air pressure, and the truck is positioned at the middle of the 340 mm long tank.

Multiple pressure cycles To study the displacement produced by the shape deformation, 20 successive pressure cycles (each one lasting 15 s) are applied to the volume enclosed in the spherical shell,

and images of the "'support-shell"' system are recorded at 24 FPS (fig.2.16).The pressure cycles applied begin by a 5s descending pressure ramp until ΔP reaches the buckling critical value, followed by a plateau at a the same pressure for 2.5s. The pressure is increased through a 6.5s ascending pressure ramp, until reaching the unbuckling ΔP^* and is followed by a 1s plateau (fig.2.17).

Temperature measurements are performed at the beginning and at the end of the pressure cycles.

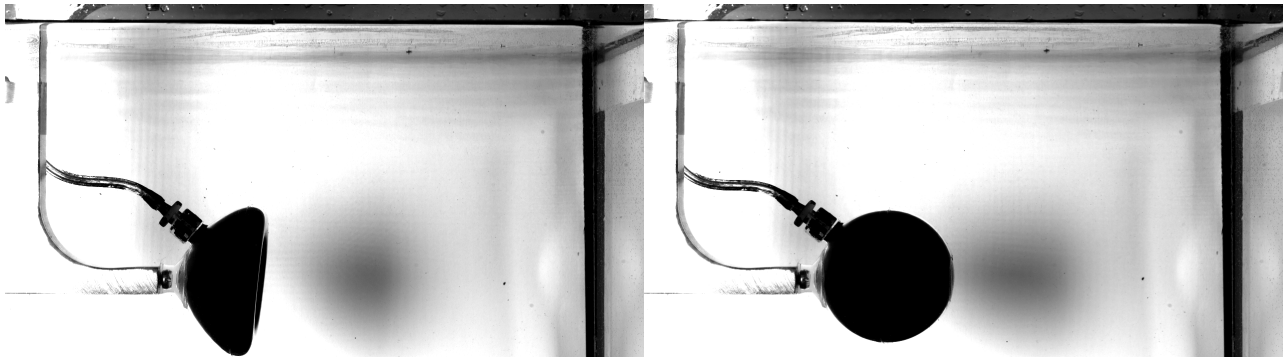

(a) Deflated state **(b)** Inflated state

Figure 2.16: Illustration of the recorded images during the two plateaus of the pressure cycle

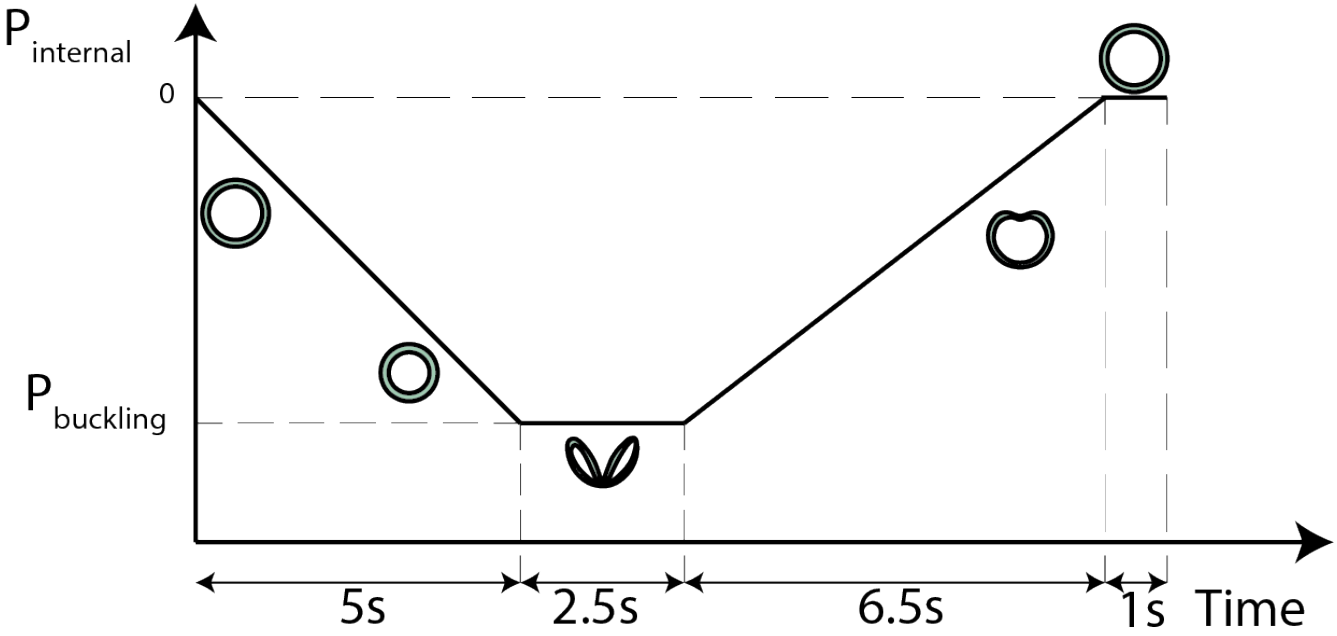

Figure 2.17: Qualitative representation of the pressure cycles

*The unbuckling ΔP, can be negative sometimes for small thicknesses, due to the fact that the shell collapses completely on itself and obstructs the hole which communicates with the pressure controller. To force the shape to unfold, pressurized air is injected inside the shell inner volume.

To study the displacement produced by the shape deformation near a wall, the "'support-shell"' is brought at a distance where the tip of the spherical shell is at 25 mm from the wall, and the same process stated previously is followed.

High temporal resolution recordings In order to quantify the shape deformation cycle, a high temporal resolution is needed. To do so, the truck is positioned at the middle of the tank, a pressure cycle is applied (with the same settings as in the previous step), and images are recorded at 600FPS. This operation is iterated three times to provide an estimation of the error.

Temperature measurement are performed at the beginning and at the end of the each iteration.

Drag-coefficient measurements In order to extract the thrust produced during the buckling and unbuckling phases, it is necessary to measure the drag force, independently. To do so, the truck is brought to the middle of the tank and is given an initial velocity. Images are recorded at 600 FPS. This is done in two constant deformation configurations: a spherical shape configuration to account for the drag coefficient when the shell is unbuckled, and a collapsed concave configuration to account for the drag coefficient when the shell is buckled.

Temperature measurement are performed at the beginning and at the end of the each iteration.

Table2.7 summarizes the pressure cycle settings for all the studied spherical shells.

Shells	Buckling pressure (mbar)	Unbuckling pressure (mbar)	period (s)
$\frac{d}{R} = 0.08$	-100	100	15
$\frac{d}{R} = 0.22$	-600	0	15
$\frac{d}{R} = 0.30$	-1000	0	15
"'AJO 121"'	-200	100	15
"'AJO 122"'	-350	100	15

Table 2.7: Experimental pressure cycle parameters for the frictionless rail experiment

2.3.4 Image treatment

The image treatment needed for the frictionless rail is relatively lighter compared to the one needed for the spring experiment, because the gravity center of the shell was impossible to extract. It can be summarized as follows:

1. From the multiple cycles set of experiments, the successive positions of the system after buckling and unbuckling phases are retrieved, by detecting the edge of the support, using the Canny edge detector algorithm.

2. From the high-resolution set of experiments, the temporal evolution of the height of the convex envelop $H(t)$ (see fig.2.18) is retrieved, using the Canny edge detector algorithm.

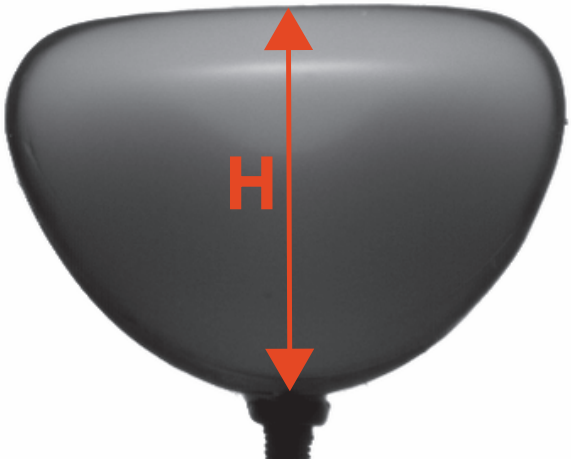

Figure 2.18: Illustration of the height of the convex envelop

3. From the drag-coefficient measurements set of experiments, the position of the support is tracked through time.

2.4 Particle-image velocimetry measurements

2.4.1 Brief introduction and motives

To understand the evolution of the displacement obtained through the deflation and the re-inflation of the spherical shell, and how it is affected by the viscosity of the surrounding medium, it was necessary to understand the flow generated during both phases and how this flow changes with the fluid viscosity.

To do so, particle-image-velocimetry measurements (PIV) were performed in two distinct viscosities: water and glycerol.

Particle-image-velocimetry measurement method is a non-intrusive method which simultaneously provides the instantaneous spatial flow field description and a quantitative result. Its principle is based on the measurement of the displacement of small tracer particles that are carried by the fluid during a short time interval. The tracer particles need to be sufficiently small and neutrally buoyant in order to accurately follow the fluid motion and not alter the fluid properties or flow characteristics. Tracer particles are illuminated by means of a thin light sheet generated from a source light plus an adequate lens and the light they scatter is recorded onto two successive image frames by a high-speed camera. The recorded images are processed offline on a computer to extract the Eulerian velocity field. Figure 2.19 schematically describes the principle of the PIV measurement.

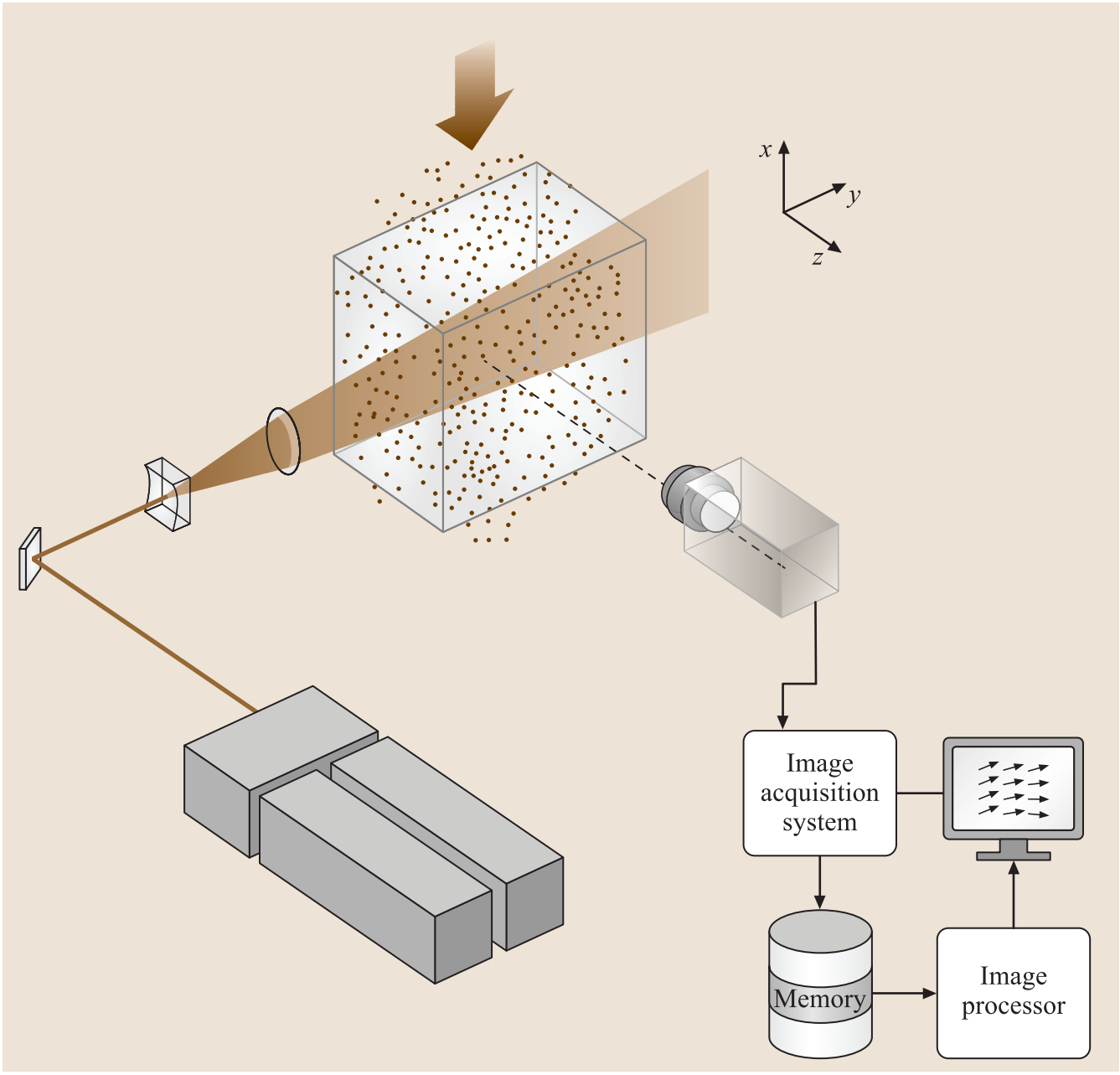

Figure 2.19: Principle of Particle Image Velocimetry

The experimental setup (fig.2.20) used to investigate the flow produced during the buckling and unbuckling phases consists of attaching the spherical shell to a fixed support, orienting the buckling spot vertically. The system was immersed in a glass tank of 50x50x50 cm tank, filled by either water or glycerol, previously seeded with 10-30 μm particles. A 1 mm vertical thin light sheet was produced with a

continuous laser source running through an tunable optical system. Just like for the frictionless rail experiment, pressure cycles were applied to the air volume enclosed in the spherical shell by connecting it to the pressure controller through a flexible tube. A high-speed camera was carefully aligned in the direction normal to the light-sheet plane*.

The experiments were conducted in collaboration with Henda Djeridi at the LEGI laboratory, who has a solid experience in PIV measurements and the adequate equipment to realize it.

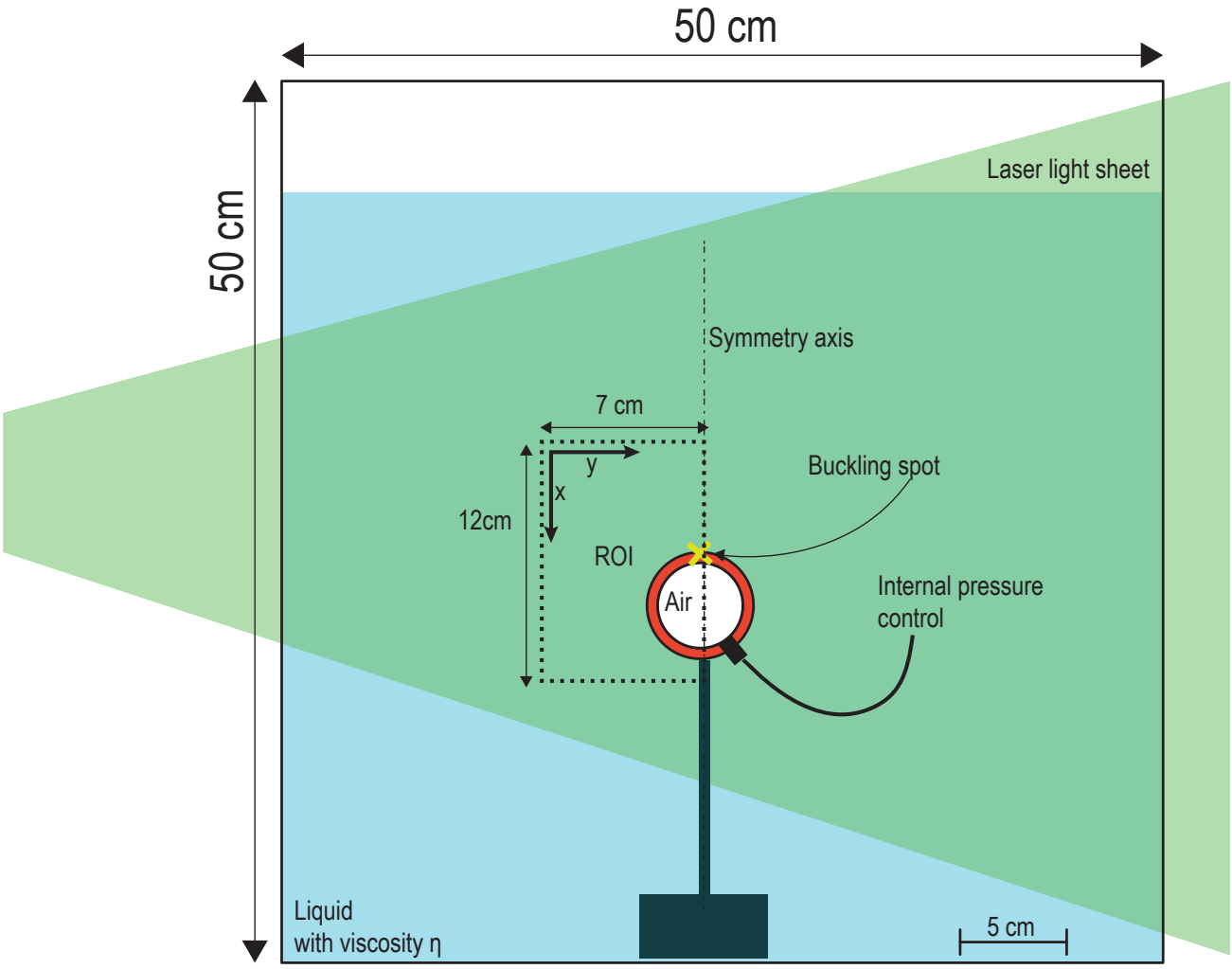

Figure 2.20: Schematics of the PIV experimental setup

*Only one high-speed camera was needed because we assumed that the flow is axisymmetric and has negligible out-of-plane velocity component, hence, two velocity components are enough to characterize the flow. If out-of-plane velocity component would not be negligible, stereo-PIV measurement would need to be performed, which requires two cameras with an angle $\neq 90$ in order to have the 3 velocity components.

2.4.2 Equipment

The complexity of the flow generated by the buckling and unbuckling phases lies in its highly unsteady nature. When the instability occurs, the flow goes from a rest state to an unsteady state with different relevant characteristic times which span from the 10^{-5} s to few seconds.

This is why it was critical to choose the right equipment to study it.

2.4.2.1 Laser source, light sheet generator and camera

In order to investigate the short unsteady flow generated during the deflation and re-inflation, a good temporal resolution is needed to capture the physics of the flow. Two optical systems were considered: a high-frequency* pulsed laser system coupled with a triggable camera, and a continuous laser source coupled with a high-speed camera. The latter system was chosen, due to the availability of the equipment at the LEGI laboratory. A 5 W continuous laser source which emits at a wavelength of 532 nm was used. It was necessary to operate at such a high power, in order to collect a satisfying light scattering from the tracer particles during a period of 50 μm.

To generate a thin light sheet, the laser source was guided inside an optical arm which is basically an assembly of hollow metal tubes provided with mirrors at the joints, allowing to direct the beam (see fig.2.21). The optical arm ends with an optical system composed of a set of lenses that generate the thin light sheet, making possible to rotate and to thin the resulting light sheet. It was positioned at 1m from the position of the spherical shell, to have a homogenous thickness of the light sheet.

*Common pulsed laser sources such as "'Nd:YAG-based"' have a frequency that ranges between 10 and 50 Hz, which is the major downside of Nd:YAG-based systems when performing time-resolved experiments except for very low-speed flows ($v < 0.2$m/s)[Tropea et al., 2007].

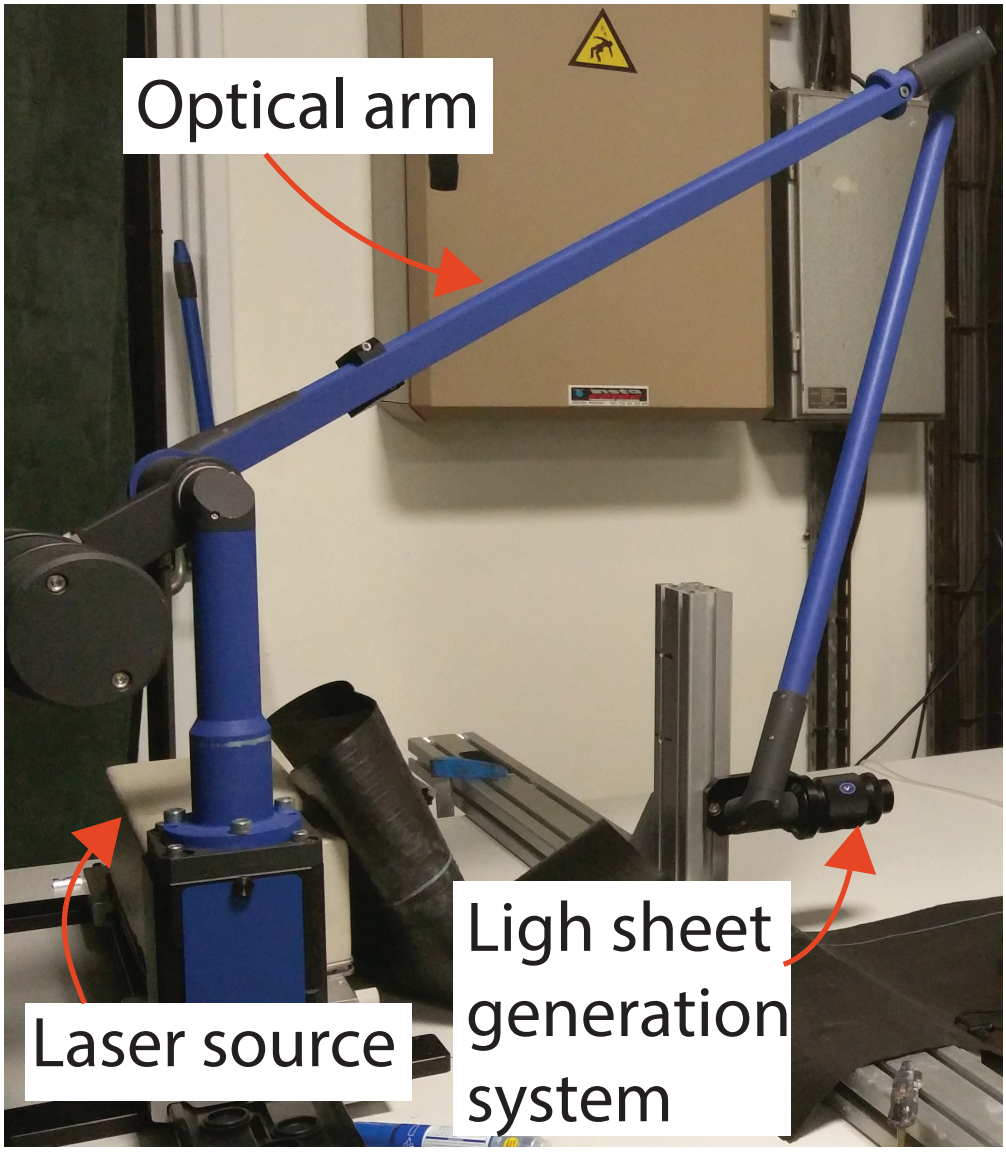

Figure 2.21: Picture of the laser and optical system used for the PIV measurements

A high-frequency camera Phantom©V2511 was used to capture the PIV image frames, its main characteristics are:

- Resolution: One Megapixel, 1280x800.
- Full resolution speed: 25000 frame per second (FPS).
- Sensor: CMOS sensor with 28 μm pixel size, 12-bit depth gray-scale colors.

The camera was coupled with a macro lens "'Milvus 2/100M"' ZEISS in order to have a satisfying spatial resolution, and was positioned at 45 cm from the shell, providing a field of view of 12cm x 7cm.

2.4.2.2 Tracer particles

The tracer particles used for the PIV measurements are spherical hollow glass particles coated with silver, with a density of 1050 Kg/m^3, with a diameter ranging between $10 - 30$ μm. To choose the right tracer particles, we minimized the slip velocity which corresponds to the difference between the particle velocity and the flow velocity[Tropea et al., 2007], expressed as:

$$v_p - U = \frac{2}{9}\frac{a^2(\rho_p \rho_f)}{\mu}\frac{dv_p}{dt}$$

Where a corresponds to the diameter of the particle, ρ_p to the density of the particle, ρ_f to the density of the fluid, μ to the viscosity of the fluid and $\frac{dv_p}{dt}$ to the acceleration of the particle. To minimize this expression, we focused on minimizing the diameter and the difference of densities. In the case of water, $\max(v_p U) = 15.10^{-5}$ m/s, and in the case of glycerol, $\max(v_p - U) = 7.5.10^{-6}$ m/s, these values are negligible compared to the experimental velocity range $U \in [0.1, 3]$ m/s.

Another requirement to take into account when choosing the seeding particles is that they should scatter enough light in order to be visible. The particle scattering cross section depends on the particle diameter a, the wavelength of the light λ, and the refractive index of the particle (relative to the refractive index of the surrounding medium)[Tropea et al., 2007]. In order to maximize the light scattering, we chose a particles with a diameter ($a > \lambda$) in order to be in the Mie regime, which yields a scattering cross section roughly proportional to a^{2*}. We also chose particles made of hollow glass coated with silver, which increase the intensity of the reflected light by an order of magnitude compared to solid beads such as polystyrene[Boutier, 2013].

*when the particle diameter becomes less than the wavelength of light, the scattering cross section is proportional to a^4

2.4.3 Experimental protocol

Laser sheet and camera alignment PIV measurement were conducted in water and glycerol. Each time we filled the tank with a new liquid, preliminary steps were performed to set the camera optical axis normal to the light sheet plane. To do so, a low power light sheet was turned on, and a uniformly spaced dot grid was introduced in the liquid. We brought the grid tangentially to the light sheet, then we focused the camera on the grid and we tuned its position to have all the dots of the grid in the focus plane, which means that the camera optical axis is normal to the light sheet. We captured an image frame of the grid used later to calibrate distance conversion.

Seeding A solution of 10 g of tracer particles diluted in 100 ml of water is prepared to seed the 110 l of liquid present in the tank. This yields roughly 200 particles in an area of 100x100 px. A surfactant is added to the solution to decrease the clustering of particles, by reducing their cohesiveness.

The seeding solution is poured in the liquid, along the light sheet plane, then it is mixed locally to homogenize the distribution along the plane.

The experimental protocol is fairly simple and follows these steps for each shell:

1. The shell is attached to the fixed support and positioned in a way that the sheet line crosses it in the middle. It is also positioned along the light sheet plane so that only half of the shell is visible to the camera in the ROI frame shown in figure 2.20. This strategy is adopted to increase the spatial resolution, by assuming an axisymmetry of the flow.

2. When the flow comes back to rest, the laser sheet is turned on, operating with a source at 3W.

3. Pressure inside the shell is dropped to the critical pressure of buckling and the camera is triggered just before the instability, operating at 20khz. The image frames are then saved into the computer.

4. Pressure inside the shell is increased to the critical pressure of unbuckling and the camera is triggered just before the instability, operating at 20khz.

Note In water, experiments are also conducted at 1khz, because the flow continues to evolve after the end of the deformations.

2.4.4 Image processing

A commercial software "'Lavision"'©"'Davis"' was used to extract the time resolved velocity fields from the recorded image frames. The processing principle is based on cross-correlation analysis of the particle-image patterns in small sub-domains between two successive image frames. The following steps summarize the basic operations performed to extract the velocity field:

1. To convert the pixel space into the physical space, a calibration is performed by using the dot grid image captured at the beginning of the experiments.
2. Images set is imported into the software and the time step is set.
3. Since the geometry of the shells evolves through time, a dynamical masking of the non-fluid domain is performed by using a sequence of image treatment operations to identify and mask the deforming shell, followed by a geometrical masking of the rigid non-fluid domain.
4. Then, cross-correlation analysis parameters are entered, setting the size of the interrogation windows, the number of passes to perform in order to increase precision*.
5. Finally, a post-processing step is performed to filter aberrant vectors, using statistical tools and thresholds specified by the user.

Details about the image processing settings can be found in the appendix A.5.

2.5 Summary of the experimental setups

Spring experiment The purpose of this experiment is to quantify several relevant quantities during the buckling and unbuckling phases when the pressure cycle is imposed externally. The shell is attached to a spring and immersed in a tank filled with a liquid. A spring plays the role of a force sensor

*Perform analysis on large-sized interrogation windows and re-iterate on smaller ones, with window overlapping.

and prevents the spherical shell from floating to the surface due to buoyancy effects. The buckling spot is directed in the vertical direction, to get a 1-D displacement. The shell is submitted to external pressure cycles, and images are recorded capturing the shell's shape and the spring position, which gives access to all the forces involved in the phenomenon, through extensive image treatment. Two parameters were explored, the relative thickness $\frac{d}{R}$ which translates the shell's ability to store elastic energy, and the viscosity and density of the surrounding medium.

Frictionless rail experiment The purpose of this experiment is to characterize the swimming induced by the shell deformation. The shell was attached to a support itself mounted on an air bearing frictionless rail, and immersed in a fluid which is a water/glycerol or water/Ucon oil (Dow chemicals) mixture. The air volume it encloses was connected to a pressure controller through a flexible pipe, allowing cycles in the inside-outside pressure drop ΔP with an amplitude ± 1 bar. In order to ensure a 1-D problem, the shell was oriented so that the buckling spot pointed in a direction parallel to the rail. Position of the moving support on the rail and shell deformation were recorded using a fast camera. Four parameters were explored: first, the relative thickness $\frac{d}{R}$. Second, the viscosity of the surrounding medium. Third, the effect of the dissipation in the material. And finally, the proximity to the wall.

PIV measurements To understand the evolution of the displacement obtained in the deflation and the re-inflation of the spherical shell, and how it is affected by the viscosity of the surrounding medium, it was necessary to first, characterize the flow generated during both phases, and to understand how this flow changes with the fluid viscosity. To do so, particle image velocimetry measurements were conducted on a shell attached to a rigid support, and immersed it in a large tank filled with either water or glycerol. The fluid is seeded with tracer particles, which are lighten by a laser thin sheet. Images are recorded during the buckling and unbuckling phases, with a high-speed camera, positioned in the direction normal to the light sheet.

This sums up the material and methods developed for this study. In the next chapter, results extracted from the experimental setups will be exposed and discussed.

En este mundo traidor, nada es verdad ni mentira, todo es según el color, del cristal con que se mira.

Ramón de Campoamor

3

Shell dynamics

3.1 Introduction

When a homogeneous elastic spherical hollow shell is submitted to a uniform inside-outside difference of pressure $\Delta P = P_{ext} - P_{int}$, it first shrinks isotropically, keeping its spherical symmetry. Then, when a certain critical pressure difference is reached, it undergoes a symmetry breaking which relaxes the elastic energy to a lower energy state, by a sudden inward snap of a spherical cap, through a sub-critical instability called *buckling*.

The classical buckling theory of elastic thin shells [Landau & Lifshitz, 1986, Pogorelov, 1988, Knoche & Kierfeld, 2011] predicts a critical pressure at which the buckling should occur:

$$\Delta P_c = \frac{2}{\sqrt{3(1-\nu^2)}} E (\frac{d}{R})^2 \tag{3.1}$$

where E is the Young modulus, ν the Poisson ratio, d the shell thickness, and R the shell radius based on its midplane surface. Furthermore, the nature of buckling in spherical shells is very sensitive to imperfection [Libai & Simmonds, 1998], which means that experimentally, buckling should occur at a lower ΔP [Drmota et al., 1987, Gräff et al., 1985, Hutchinson, 1967, Lopez Jimenez et al., 2017].

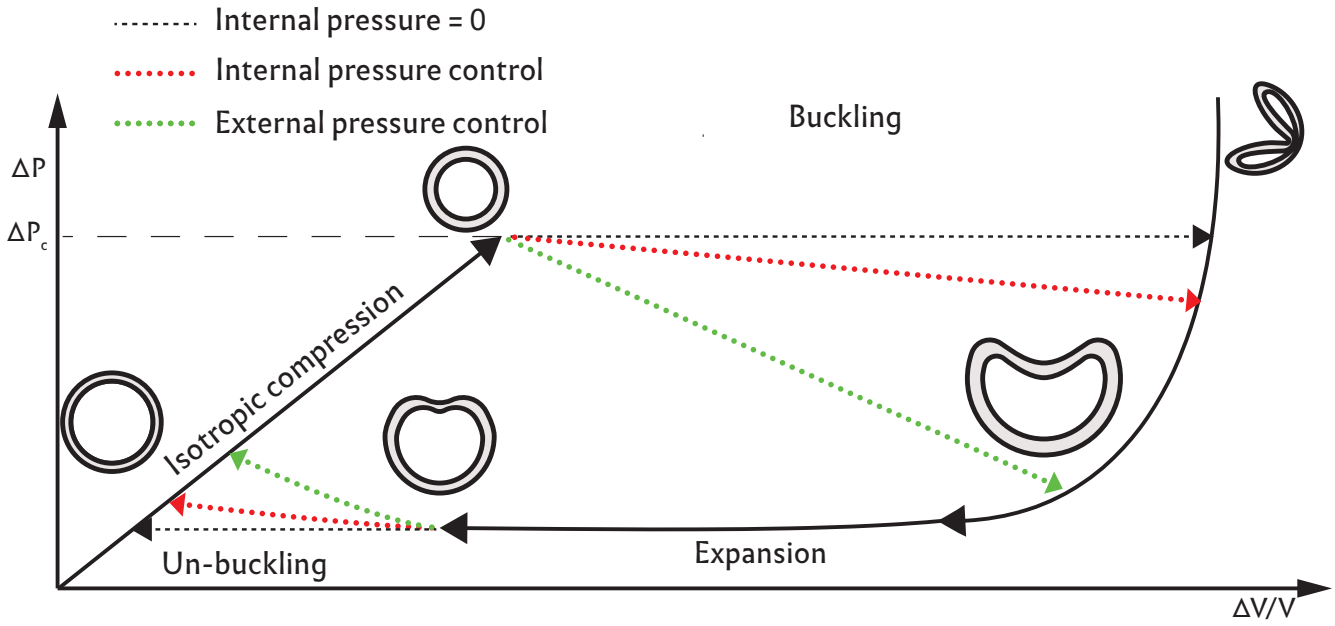

Figure 3.1: Qualitative Pressure-Volume diagram of a shell submitted to a cycle of pressure. Solid lines show stable configurations and dashed lines show transient unstable shape configurations

A thorough work has been performed to predict the stable equilibrium states of the shell deformation under pressure difference or by reducing volume[Knoche & Kierfeld, 2011, Quilliet, 2012].

Their results in the ideal case of completely hollow shell ($P_{int} = 0$) are translated qualitatively in figure 3.1, where we can see that when reaching a critical ΔP_c, the shape transits from a compressed

spherical shape to a highly deflated configuration through the buckling instability. When decreasing back the ΔP, the shell re-inflates following a different deformation path, until it reaches a pressure threshold where the shell jumps back to the spherical symmetry configuration, through another sub-critical instability that we call *Unbuckling*. The instability transitions in such an ideal case happen at constant pressure. However, these transitions in the case of an enclosed shell (filled with air) and submitted to external pressure are different from the ideal case, due to the fact that during the transition a change in volume implies a change in the internal pressure and we cannot be at $\Delta P = const$ during both transitions. In the case of an internal pressure control, we are somewhat in the middle because there is still air inside the shell during deflation but less air than in the case of an enclosed shell, which means that change in internal pressure is less impacted by volume changes.

In both pressure control scenarii, the deformation path presents an hysteresis and such mechanism would naturally fulfill the sine qua non condition for swimming at low Re.

In this chapter, we will present experimental results related to the deformation path, but we will mainly focus on the dynamics of the instability which has not been studied before, neither theoretically nor experimentally.

3.2 Deformation cycle

3.2.1 Shape evolution

We submitted elastic shells made of an elastomer material characterized by a Young modulus 0.5MPa and a Poisson's ratio of $\nu = 0.5$ (measured by traction experiments at 5% elongation) to external pressure cycles as well as internal pressure cycles. In both cases we recorded the evolution of the shape, summarized in figure 3.2. We notice that the shapes obtained confirm qualitatively the theoretical predictions (fig.3.1), except for the state just before the buckling marked as (B) in the figure, where the shape reaches a stable convex state but loses its spherical symmetry. In this state, the shell flattens around the area where the buckling later nucleates when ΔP is increased further.

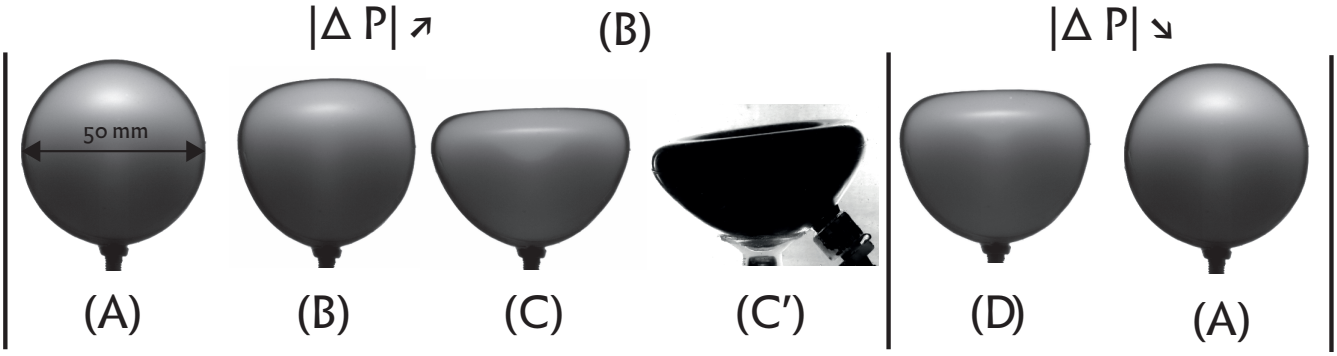

Figure 3.2: Shape configurations encountered when submitting a shell to a ΔP cycle, where (A) is the original spherical shape, (B) corresponds to a convex shape just before the buckling, (C) to the concave shape when controlling external pressure, (C') to an almost completely collapsed concave shape when internal pressure is controlled and (D) to the concave shape just before the unbuckling. The initial external diameter of the shell is 50 mm.

Varying the reduced thickness ($\frac{d}{R}$), we obtain different buckled shapes as shown in figure 3.3.

Figure 3.3: Shape after buckling for different $\frac{d}{R}$ parameters, when submitted to external pressure variations. C extracted from connection points between external fit of the shape and fit of the concavity (see sec.2.2.4.2).

We clearly see that the diameter C of the concavity increases when we increase ($\frac{d}{R}$) (see fig.3.4) for an external pressure control. We notice that when the internal pressure is controlled, the shell is fully collapsed with a concavity size $C \approx 2R_{ext}$.

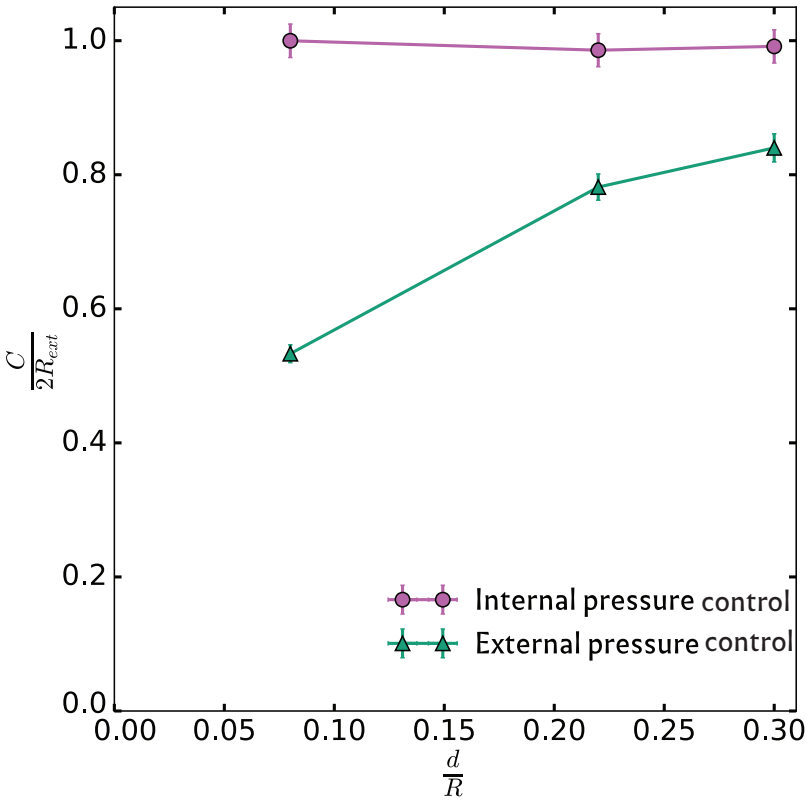

Figure 3.4: Evolution of the concavity size as a function of $(\frac{d}{R})$ when controlling pressure externally and internally. For internal pressure control, measurements performed by manual image treatment.

If ΔP is increased further, a self-contact configuration is reached. Numerical simulations [Quilliet, 2012] predict the apparition of wrinkles with a typical spacing of $\sqrt{dR}$.

3.2.2 Pressure-Volume relationship for external pressure control

In the case of external pressure control, we were able to measure the volume of the shell by fitting the external shape of the shell, which allowed to calculate the internal pressure, based on the hypothesis of the perfect gas submitted to an isothermal process*.

*This hypothesis is valid for the convex path and the plateau, but can be questioned in the case of the transitions, since they occur in few milliseconds and lead probably to an adiabatic process instead, which would shift down the values of ΔP by increasing the temperature of the gas, temperature which would require a certain time to diffuse through the shell material, a rubber material known to be a heat insulator, making the adiabatic hypothesis to be more realistic. Estimations of the temperature rise are $\Delta T(\frac{d}{R} = 0.22) \approx 30$ C, and $\Delta T(\frac{d}{R} = 0.30) \approx 70$ C. but unfortunately, no temperature measurements could be performed yet to confirm that.

We then built the pressure-volume diagram shown in figure 3.5. We see that the pressure-volume diagram is qualitatively comparable to the theoretical predictions shown earlier (see fig.3.1), and confirms the existence of an hysteresis in the deformation path. Quantitatively, the theoretical pressure threshold as defined in equation (3.1)— which is supposed to be an upper limit— is exceeded experimentally for all $(\frac{d}{R})$ (see table 3.1a). When it comes to the reduced volume threshold defined theoretically[Quilliet, 2012, Hutchinson, 1967] as:

$$\frac{\Delta V_c}{V_0} = \frac{V_0 - V(\Delta P_c)}{V_0} = \sqrt{3(\frac{1-\nu}{1+\nu})}\frac{d}{R} \tag{3.2}$$

With V_0 the volume at $\Delta P = 0$, and $V(\Delta P_c)$ volume at ΔP_c. We observe that the reduced volume preceding the experimental buckling is close to the theoretical predictions as shown in table 3.1b .

We notice also a plateau for the difference of pressure during the re-inflation (deflated branch) which confirms the theoretical predictions[Knoche & Kierfeld, 2011, Quilliet, 2012] even though it was not characterized explicitly in the case of a pressure controlled deformation. As for the unbuckling pressure and volume, no prediction exists in the literature. The experimental values obtained for the different $\frac{d}{R}$ are summarized in table 3.2. The convex branch during the deflation and re-inflation shows a linear trend and share the same slope, even though the re-inflation branch does not coincide exactly with the deflation branch, meaning for the same difference of pressure, we obtained a different deformation. This later point is probably due to the visco-elastic nature of the material used (creep and memory effects).

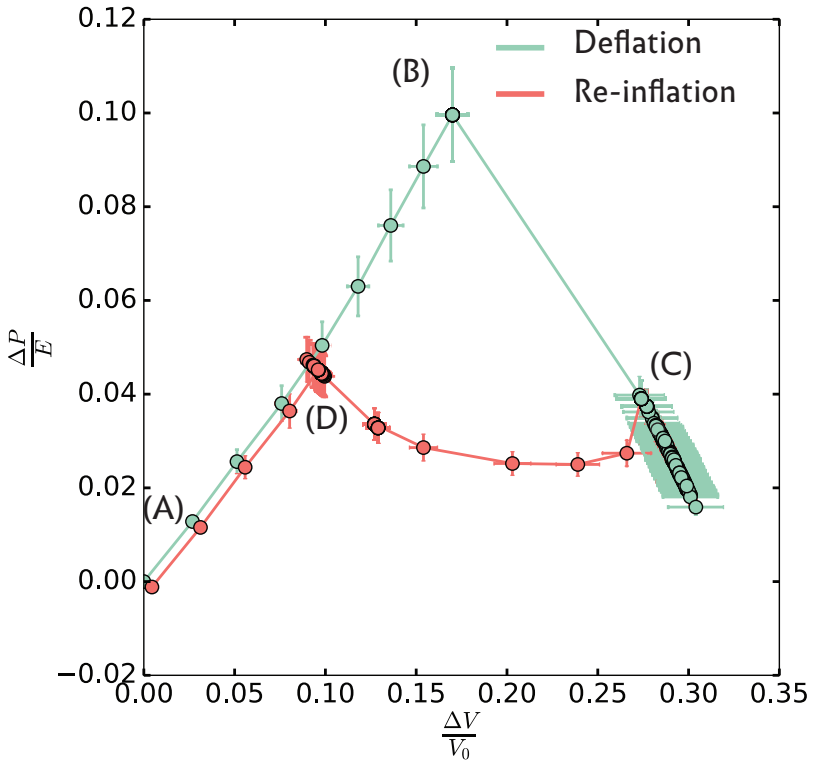

Figure 3.5: A dimensionless representation of a pressure-volume diagram corresponding to a shell with $\frac{d}{R}$=0.22 in glycerol. The x-axis corresponds to a reduced volume defined as $\frac{\Delta V}{V_0} = \frac{V_0 - V(\Delta P)}{V_0}$, with volumes defined at the midplane. The y-axis corresponds to the difference of pressure $\Delta P = P_{ext} - P_{int}$ reduced by the Young modulus. Deflation marked with the green line (light) corresponds to an increase of the external pressure until buckling, re-inflation corresponds to a reduction of the external pressure until reaching the atmospheric pressure. The letters correspond to the shapes presented in figure 3.2.

$\frac{d}{R}$	ΔP_c (th) (KPa)	ΔP_c (exp) (KPa)
0.08	4.3	4.9
0.22	32.3	49.7
0.3	60.0	104.

(a) Comparison between the theoretical and experimental buckling pressure.

$\frac{d}{R}$	$(\frac{\Delta V_c}{V_0})$ (th)	$(\frac{\Delta V_c}{V_0})$(exp)
0.08	0.08	0.05
0.22	0.22	0.17
0.3	0.3	0.21

(b) Comparison between the theoretical and experimental buckling reduced volume.

Table 3.1: Buckling pressure and volume characteristics

$\frac{d}{R}$	ΔP_{exp} (KPa)	$(\frac{\Delta V}{V_0})_{exp}$
0.08	3.34	0.035
0.22	22.5	0.095
0.3	40.0	0.115

Table 3.2: Difference of pressure and reduced volume corresponding to the unbuckling transition.

Figure 3.6 shows that the values of ΔP_c and $\frac{\Delta V_c}{V_0}$ at the buckling transition increase with $(\frac{d}{R})$. The slope of the convex path increases with $(\frac{d}{R})$ [*]. The proportionality of the slope with $(\frac{d}{R})$ has been predicted theoretically [Quilliet, 2012]:

$$(\frac{\Delta P}{E}) = \frac{2}{3(1-\nu)}(\frac{d}{R})(\frac{\Delta V}{V_0}) \tag{3.3}$$

Figure 3.7 confirms the linear increase of the convex path's slope, but the prefactor is ≈ 3 to be compared to $\frac{2}{3(1-\nu)} = 1.33$ in the case of the material used. This may be due to the fact that we used a thin shell theory for relatively thick shells.

[*] the convex path looses its linearity for high $(\frac{d}{R})$ values [Knoche & Kierfeld, 2011].

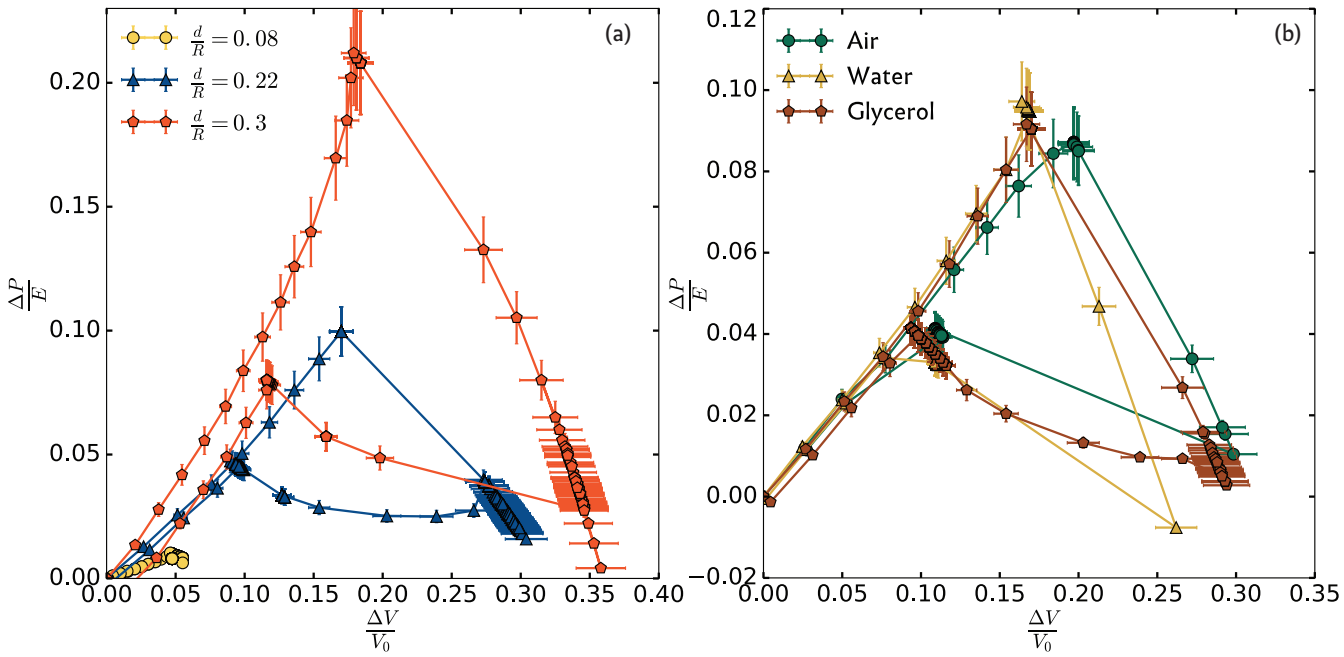

Figure 3.6: (a) shows the P-V diagram for different $(\frac{d}{R})$. (b) shows the P-V diagram for different fluids for a shell with a $(\frac{d}{R}) = 0.22$, Air ($\eta = 10^{-6}$ Pa.s Water ($\eta = 10^{-3}$ Pa.s), Glycerol ($\eta =$ 0.9 Pa.s).

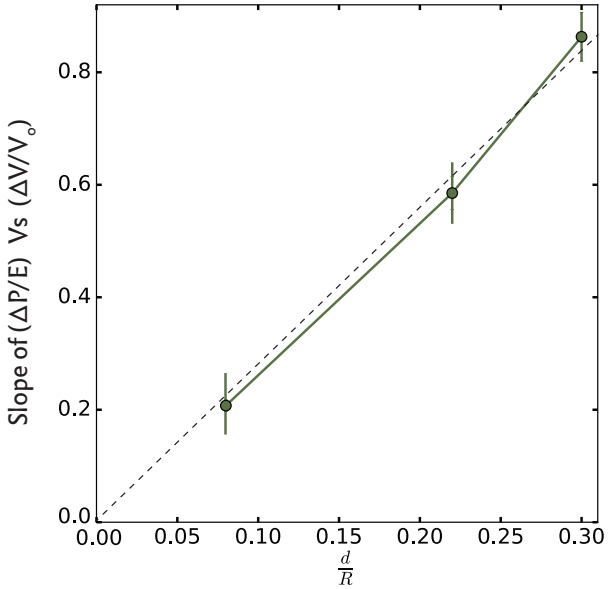

Figure 3.7: Evolution of the convex path's slop with $(\frac{d}{R})$. Dashed lines represent a linear fit with a slope of ≈ 3.

From figure 3.6(b), we observe that the diagram P-V does not seem to be affected by the surround-

ing fluid viscosity or density.

Note The volume could not be measured for the case of internal pressure control, and this is why we could not construct the P-V diagram. In order to compare shape hysteresis in both cases of pressure control, we used geometrical quantities that are related to the variation of the volume, as we will see in section 3.2.4.

3.2.3 Final volumes after buckling

The volume change during buckling is an interesting quantity as it will control the volume of the displaced fluid.

For a volume between $\simeq 0.2V_0$ and the critical volume V_c, the pressure difference is expected to plateau [Knoche & Kierfeld, 2011, Quilliet, 2012]. For smaller residual volume, a highly deflated configuration is reached, and the pressure difference increases. This configuration is unlikely to occur in the case of shells with remaining gas inside.

The plateau pressure difference has been determined by numerical simulations:

$$\Delta P_p = \delta E(\frac{d}{R})^{5/2} \text{ with } \delta = 0.75(1-\nu^2)^{-0.733} \tag{3.4}$$

External pressure control

The relationship between inner pressure P and V depends on the heat exchange across the shell material. We assume that PV^γ is a constant, where $\gamma = 1$ for an isothermal transform and $\gamma = 7/5$ for an adiabatic transform. At rest the shell has a volume V_0 and an inner pressure P_0 equal to the outside pressure.

Right before buckling the internal pressure is $P_{int} = P_0(\frac{V_0}{V_c})^\gamma$ and the external pressure that has to be applied is $P_{ext} = P_{int} + \Delta P_C$. After buckling, the final volume V_f is given by $V_f/V_0 = (P_0/P_f)^{1/\gamma} =$

$[P_0/(P_{ext} - \Delta P_p)]^{1/\gamma}$ so finally:

$$\frac{V_f}{V_0} = \Big[\frac{1}{\frac{1}{(1-\beta\frac{d}{R})^\gamma} + \alpha\hat{E}(\frac{d}{R})^2 - \delta\hat{E}(\frac{d}{R})^{5/2}}\Big]^{1/\gamma} \tag{3.5}$$

with $\hat{E} = E/P_0$, $\alpha = 2[3\,(1-\nu^2)]^{-1/2}$, $\beta = (3\,\frac{1-\nu}{1+\nu})^{1/2}$

Internal pressure control

The inner pressure is controlled until buckling, *i.e* during the initial slow isotropic deflation, while during buckling, because of the typical response time of the pressure controller (10 ms), the inner pressure is transiently not controlled and the shell can be considered as closed. Thus we first observe buckling to a moderate final volume V_f, followed by oscillations. Then the volume slowly decreases down to the very deflated conformation that is expected for buckling instability at fixed pressure difference. This 2 step sequence is all the more pronounced as d/R is small, because the volume is then still high.

We consider here that the outside pressure is always equal to P_0. Right before buckling the internal pressure is $P_{int} = P_0 - \Delta P_C$ and the volume is V_b. Right after buckling the final pressure is $P_f = P_0 - \Delta P_p$ and the final volume is such that $V_f^\gamma P_f = V_b^\gamma P_{int}$, so finally:

$$\frac{V_f}{V_0} = (1-\beta\frac{d}{R})\Big[\frac{1-\alpha\hat{E}(\frac{d}{R})^2}{1-\delta\hat{E}(\frac{d}{R})^{5/2}}\Big]^{1/\gamma}, \tag{3.6}$$

with $\hat{E} = E/P_0$.

d/R	V_c/V_0	V_f/V_0 - P_{ext}		V_f/V_0 - exp	V_f/V_0 - P_{int}	
		$\gamma = 1$	$\gamma = 7/5$	$\gamma = 1$	$\gamma = 1$	$\gamma = 7/5$
0.08	0.92	0.89	0.90	0.94	0.89	0.9
0.22	0.78	0.67	0.70	0.70	0.59	0.64
0.30	0.70	0.56	0.61	0.64	0.36	0.44

Table 3.3: Final volumes after buckling for a shell with $\hat{E} = 5$ and $\nu = 0.5$ according to equations 3.5 and 3.6 and experimental data with external pressure control.

Conclusion

Numerical application of equations 3.5 and 3.6 for our macroscopic shell with $\hat{E} = 5$ is shown in table 3.3. We observe that experimental measurements of $\frac{V_f}{V_0}$ validate our theoretical estimations.

Note eventually that in both pressure control configurations explored here, the power series for $\frac{V_f}{V_0}$ as a function of d/R are identical for the first terms:

$$\frac{V_f}{V_0} = 1 - \beta\frac{d}{R} + \frac{\alpha}{\gamma}\hat{E}(\frac{d}{R})^2 - \frac{\delta}{\gamma}\hat{E}(\frac{d}{R})^{5/2} + O\big((\frac{d}{R})^3\big). \tag{3.7}$$

3.2.4 Shape hysteresis

An effective and straightforward way to observe and quantify the shape hysteresis is to look at the apparent maximum height and maximum width. Figure 3.8 shows examples in the case of an external pressure control and an internal pressure control. We notice that the paths *(A-B)* and *(D-A)* show a regular tendency between the height and width, whereas the *(B-C)* and *(C-D)* paths show a non-monotonic relationship with oscillations. The oscillations that can be observed at the unbuckling transition are less pronounced compared to the one observed during the buckling.

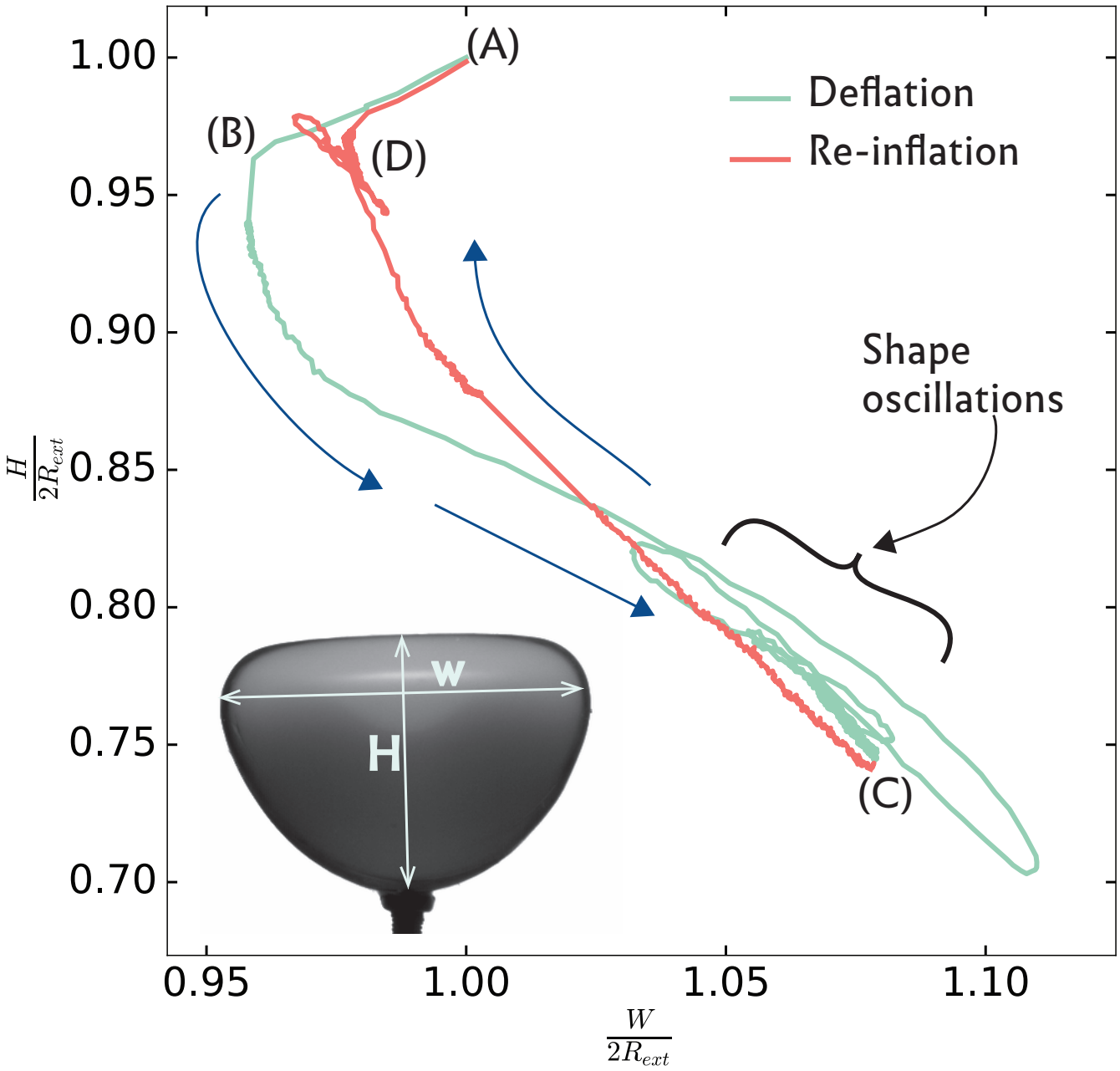

Figure 3.8: Evolution of the reduced height $\frac{H}{2R_{ext}}$ as a function of the reduced width $\frac{W}{2R_{ext}}$ during a pressure cycle controlled externally, for a shell of $(\frac{d}{R}) = 0.22$, in glycerol. The letters refer to the shapes presented in figure 3.2.

We measured the height and width for different $(\frac{d}{R})$ and in different liquids, as shown in figure 3.9. To allow comparison between different configurations, the area enclosed by the path (A-B-C-D-A) was measured. We observe that the shape hysteresis area drastically increases when we pass from a low

$(\frac{d}{R}) = 0.08$ to $(\frac{d}{R}) = 0.22$ and then stabilizes for a larger $(\frac{d}{R})$. A possible explanation may be that for a low $(\frac{d}{R})$, the buckling affects the shape locally by creating a small concavity and does not modify the shell's shape outside its immediate neighborhood, hence, values of H and W are less impacted. As for the influence of the surrounding fluid, we see that the shape hysteresis tends to become smaller when the viscosity increases, but the dependency is weak.

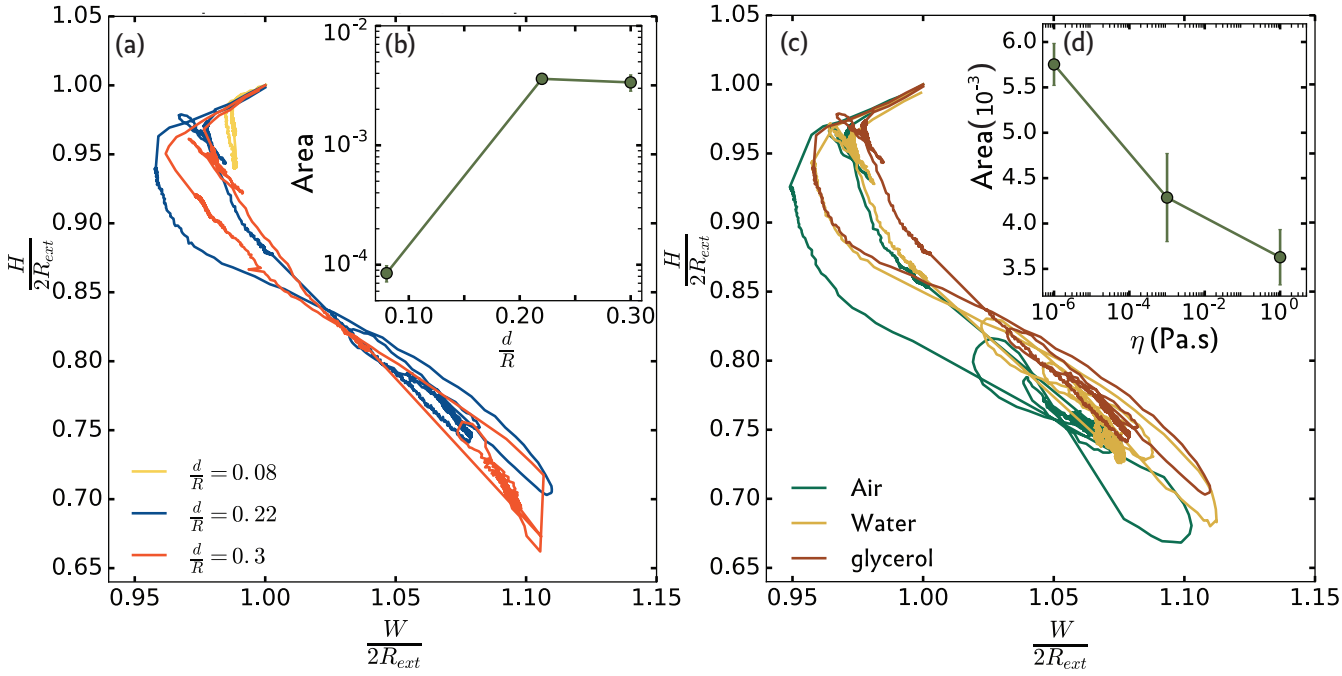

Figure 3.9: (a) presents H(W) reduced by the external diameter for different $(\frac{d}{R})$. (b) is the evolution of the area enclosed inside the H(W) deformation path as a function of $(\frac{d}{R})$. (c) Shows the H(W) path for a shell of $(\frac{d}{R}) = 0.22$ in different fluids, accompanied by the evolution of the area as a function of the reduced thickness, shown in (d).

We measured the height and width for a shell deformed by control of the internal pressure, and compared it with results obtained through external pressure control (see fig.3.10). We observe similar (A-B) and (D-A) paths —which are the convex shape paths—, but for an internal control which induces a complete collapsed configuration, the shape deforms further by getting wider and flatter. Measurements performed in the case where pressure is controlled internally were noisy and the signal was smoothed. A quantification of the area is not relevant in this case. We can observe that qualitatively, the difference in the area is not significant.

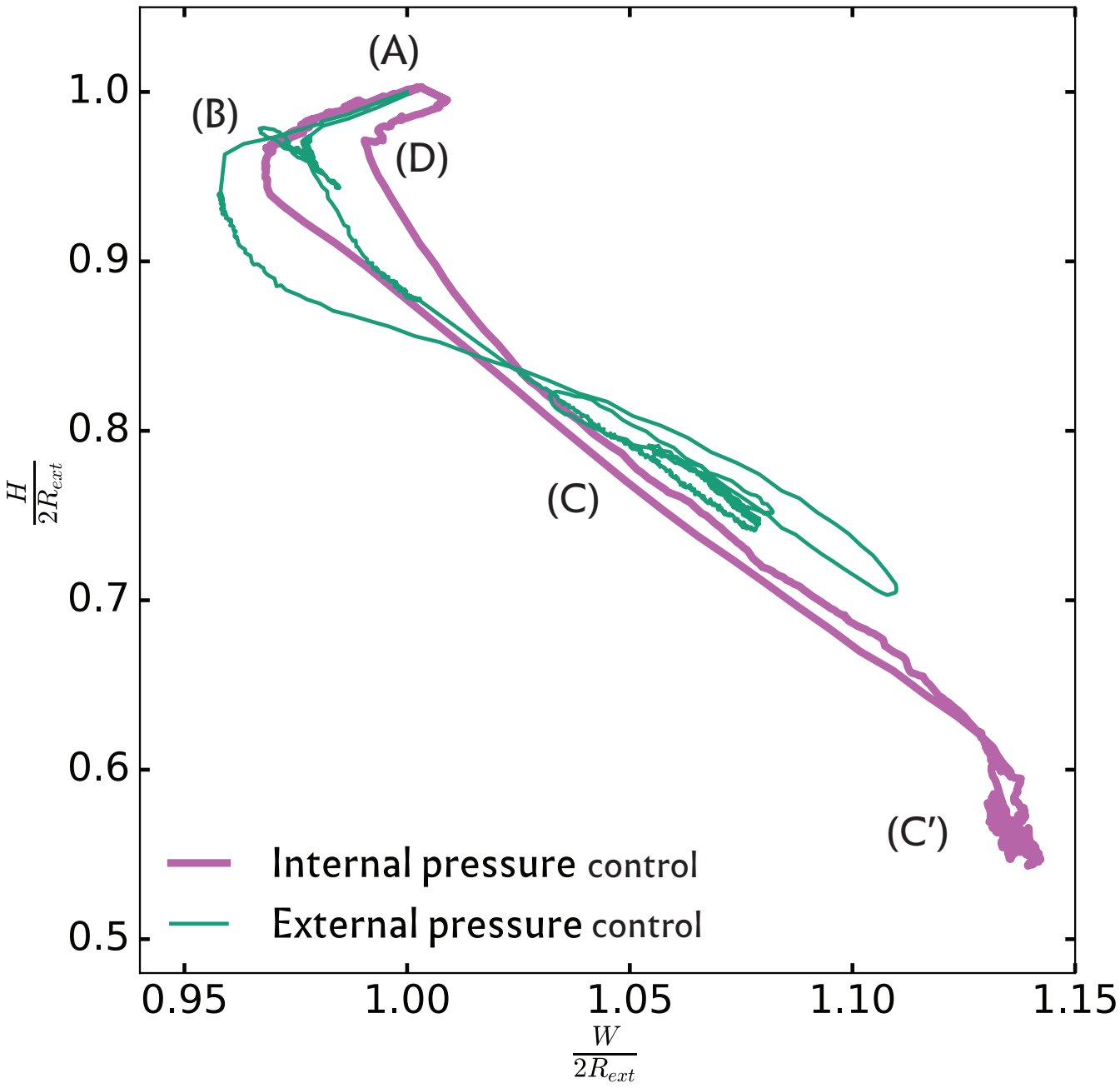

Figure 3.10: Comparison of the shape hysteresis between and external and internal pressure control for a shell of $(\frac{d}{R}) = 0.22$, in glycerol.

3.2.5 Summary

We compared experimental results about pressure and volume to the theoretical predictions. They show a qualitative agreement but also some discrepancies with the theory: the shape looses its spherical

symmetry before reaching critical pressure, but remains stable. When it comes to the critical thresholds, we achieved buckling at substantially higher pressures than what is presented in the literature [Drmota et al., 1987, Gräff et al., 1985, Hutchinson, 1967]. We also provided new experimental input to re-inflation, namely the critical threshold allowing a return to the spherical branch.

To quantify the shape deformation, we measured the maximum apparent height and maximum width of the outer shell and we observed that the $(\frac{d}{R})$ parameters plays an important role in determining the extent of the deformation path described during a pressure cycle. We also noticed that the viscosity of the surrounding fluid has no notable effect on the shape deformation path. Besides, internal control of the pressure allows to increase substantially the extent of the deformation path.

Let us take a look now at the dynamics of the instability and how it is affected by the geometry, the surrounding fluid rheology and the way the pressure is imposed.

3.3 Instability dynamics

3.3.1 Introduction

In the previous section, we showed experimentally that when an elastic hollow shell is submitted to a pressure cycle, it deforms following a non-reciprocal path in the deformation space, as predicted by the classical buckling theory. This condition is necessary to swim using shape deformation in a low Reynolds regime. But the Reynolds number is likely to jump when buckling occurs. Furthermore, the volume decreases significantly in the matter of a few milliseconds, accelerating a comparable volume of the surrounding fluid, and this might induce inertial effects and ultimately another swimming mechanics. To be able to use it, a thorough understanding of the shell dynamics during the instabilities needs to be conducted. In this section, we will present experimental results that might shed light on the dynamics of the buckling a spherical shell.

To quantify the instability dynamics, we have access to spatial and temporal evolution of the shell's external shape during the instability. We chose to follow the evolution of the maximum of apparent height and the maximum width (as represented in figure 3.8) during the instabilities. The typical evolution of these two quantities in the case of an external pressure control is shown in figure 3.11. At the beginning of the transition, we observe a rapid change in both quantities; followed by oscillations damped in time where the first amplitude of the height is twice as big as the amplitude of the width. We observe that H and W share the same period highlighted by the dashed lines with a phase shift close to π.

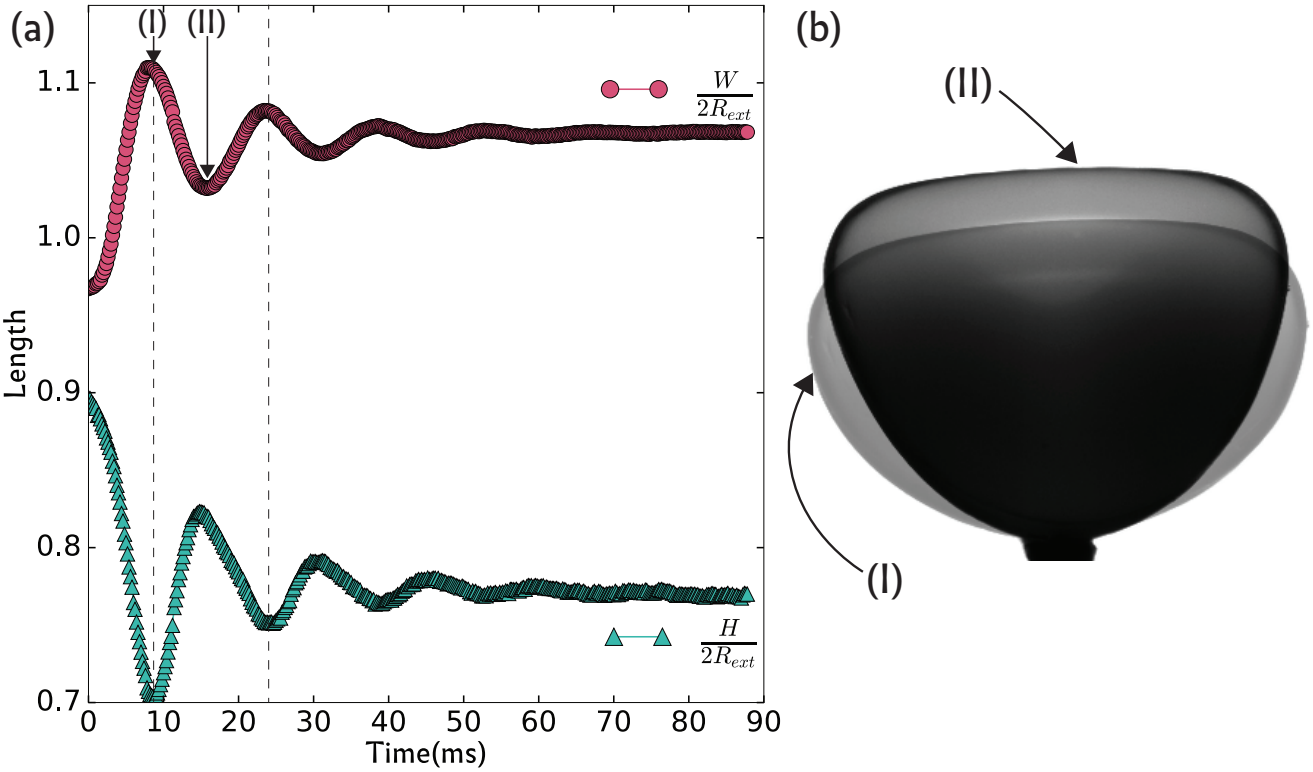

Figure 3.11: (a) Shows the evolution of reduced H and reduced W as a function of time during the buckling instability ($\frac{d}{R} = 0.22$ in glycerol, external pressure control). The dashed lines mark the times where H is at minimum amplitude. (b) represents the state of deformation marked as *(I)* and *(II)* in figure (a), where *(I)* corresponds to a minimum value of H and a maximum value of W, and *(II)* corresponds to a maximum of H's amplitude and a minimum of W's amplitude.

Repeating the same exercise for the case of an internal pressure control yields a different result as shown in figure 3.12. We notice that at the beginning of the instability these two quantities change

rapidly, and this time the height oscillates but the width seems to converge quickly to the equilibrium. Consequently, the deformation mode in the case of an internal pressure is different form the external pressure case. The difference lies in the fact that in the case of the internal pressure control, it's the rolling and unrolling of the rim (edge) of the concavity that produces the post-buckling oscillations. In the case of the external pressure control, artificial rigidity due to air compressibility seems to change the deformation mode.

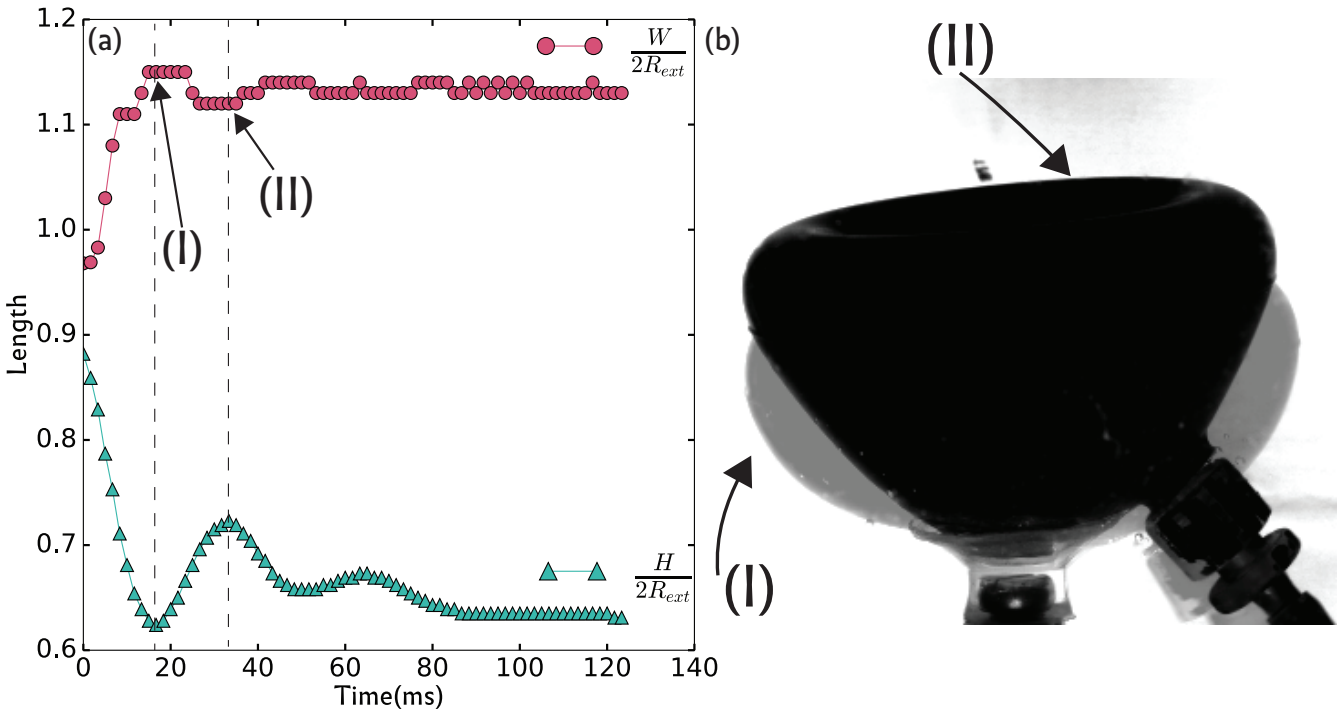

Figure 3.12: (a) Shows the evolution of reduced H and reduced W as a function of time during the buckling instability ($\frac{d}{R} = 0.22$ in glycerol, internal pressure control). The dashed lines mark the times where H is at minimum amplitude. (b) represents the state of deformation marked as *(I)* and *(II)* in figure (a), where *(I)* corresponds to a minimum value of H and a maximum value of W, and *(II)* corresponds to a maximum of H's amplitude and a minimum of W's amplitude.

Let us now compare the buckling and unbuckling deformations when the pressure is controlled externally and internally. To do so, we compare the measured height over time as shown in figure 3.13. In the case of an external pressure control, the amplitude of the height during buckling is larger than during the unbuckling by a factor ≈ 2.5. In the case of an internal pressure control, the amplitude of deformation is twice larger during the buckling compared to the unbuckling. Furthermore, the sharp

deformation during the unbuckling is not followed by oscillations, but instead, undergo a sort of a "*belly dance*"' where an undulation travels along the shell's surface. Figure 3.14 shows clearly a contrast between the deformation obtained during the unbuckling by an external pressure control –where we see a similar deformation at the tip and the flank (see fig.3.14)— and by an internal pressure control where we see that the undulation at the tip does not show a regular periodic pattern, compared to the flank which shows such pattern.

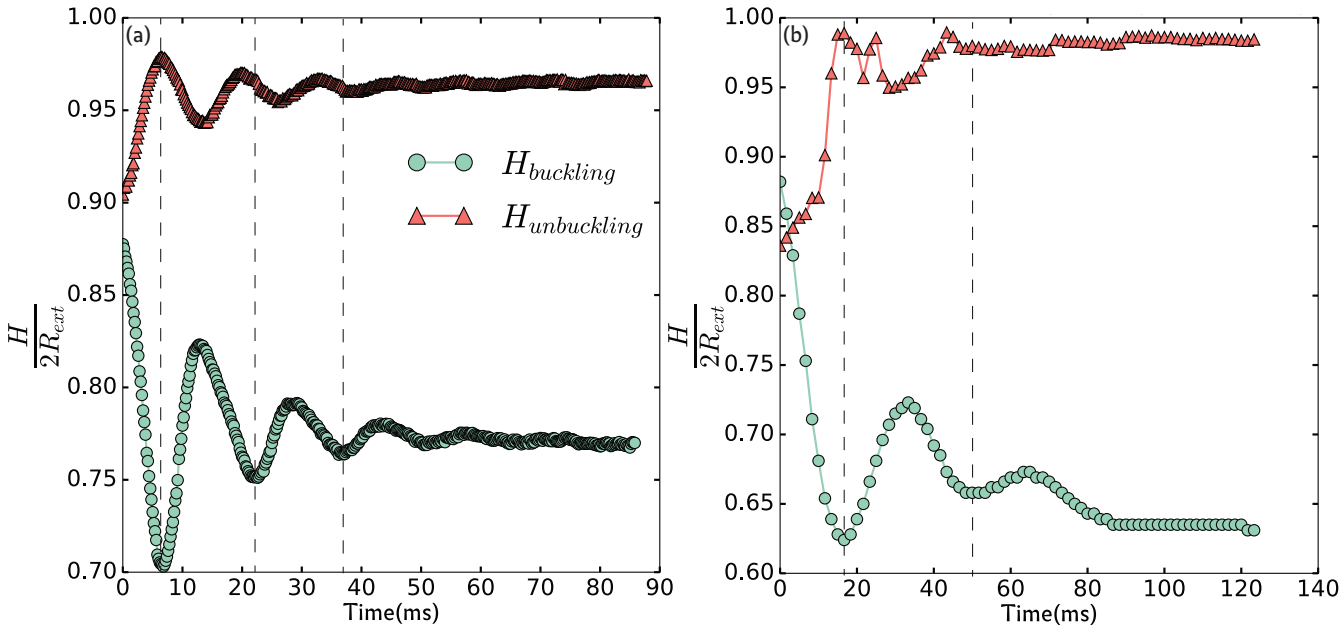

Figure 3.13: (a) shows the evolution of the reduced height in time during the buckling and unbuckling transitions, in the case of a shell of $\frac{d}{R} = 0.22$ in glycerol and an external pressure control. (b) shows the evolution of the height in time during the buckling and unbuckling transitions, in the case of a shell of $\frac{d}{R} = 0.22$ in glycerol and an internal pressure control. Dashed lines mark the times where H is at minimum amplitude.

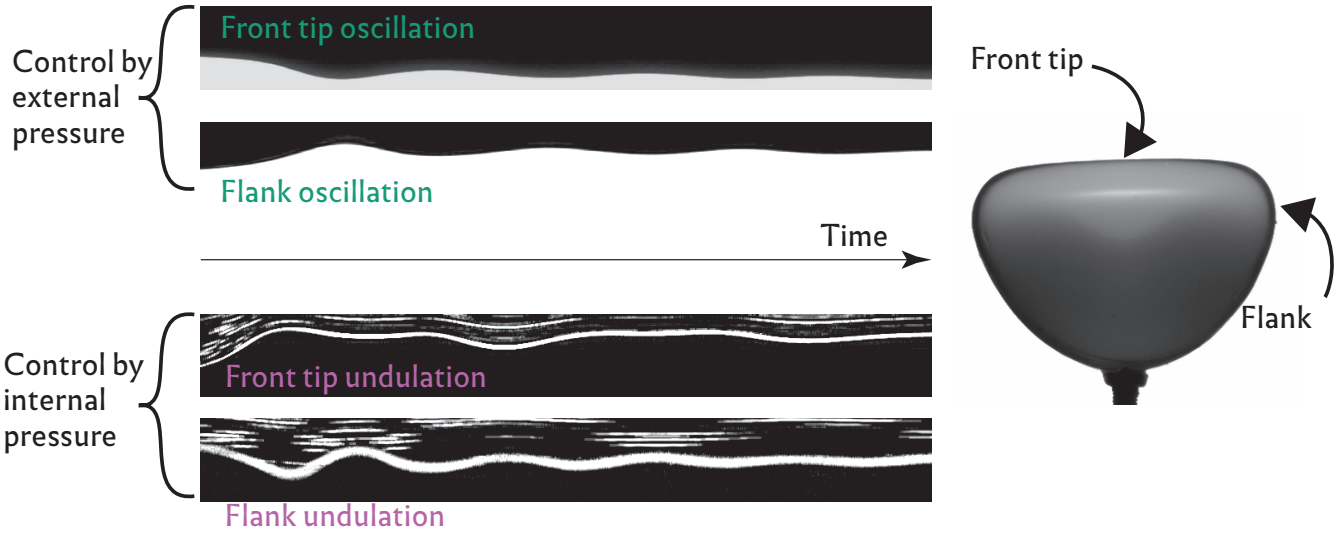

Figure 3.14: Illustration of the unbuckling oscillations in the case of external pressure control (up) and internal pressure control (down) by re-slicing the recorded images vertically at the front tip and at the flank.

3.3.2 Evolution of the dynamics with respect to the reduced thickness and the fluid viscosity

Now that we introduced the relationship between the height and width during the buckling and unbuckling transitions, for both methods of pressure control, we can focus on how the height evolves when varying the geometrical parameter ($\frac{d}{R}$) and rheological parameter η.

First, we begin by the influence of the reduced thickness ($\frac{d}{R}$), illustrated in figure 3.15.

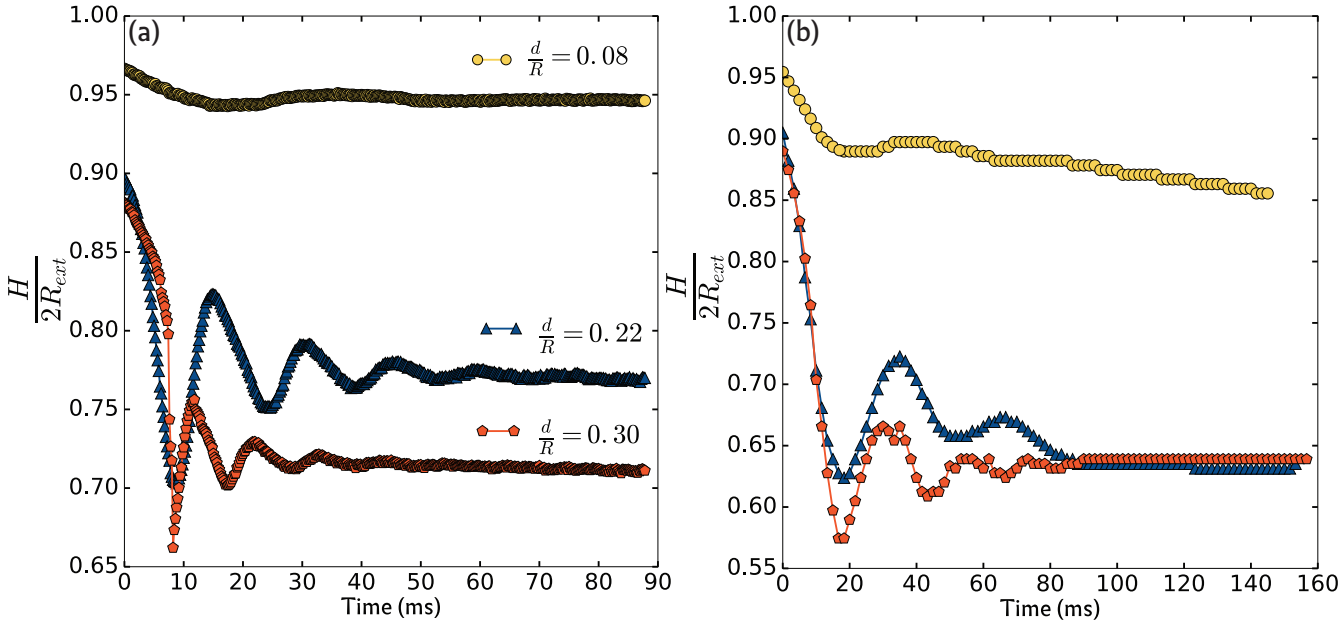

Figure 3.15: (a) shows H(t) for different $(\frac{d}{R})$ during the buckling transition, in glycerol. (b) its equivalent with an internal pressure control. Height difference between low and high d/R will be explained in the text.

We observe that independently from pressure controls, the initial amplitude of the oscillation increases with $(\frac{d}{R})$. When reaching the equilibrium, the final height decreases with increasing $(\frac{d}{R})$ in the case of external pressure control. When pressure is controlled internally, the final height at equilibrium converges to a value independent from $(\frac{d}{R})$. For small $(\frac{d}{R})$, the shell does not transit directly to a highly deflated configuration, as discussed in section 3.2.3. Instead, it buckles while still having air inside. The buckling in this case is equivalent to buckling with external pressure.

We observe that the period and damping of the oscillations are influenced heavily by the $(\frac{d}{R})$ parameter. In figure 3.17 (a), we show that the period decreases when increasing $(\frac{d}{R})$. When comparing the results for internal pressure and external pressure (see fig.3.17 (a)), we notice that the period of oscillations is larger —with a ratio between 2 and 3— in the case of the internal pressure control compared to external pressure control, while the amplitudes of deformation remain very comparable. This confirms that the air entrapped inside the shell increases the shell's effective rigidity, when controlling pressure externally, and this extra rigidity depends strongly on $(\frac{d}{R})$.

The effect of the fluid viscosity is now studied in the case of both pressure controls (see fig.3.16) . We notice that in both cases of pressure control, the dynamics is affected but a little by the viscosity of the fluid. Except for large viscosities (Ucon©oil $\eta = 37$ Pa.s), where the regime of deformation is over-damped and no oscillations are observed. This can be verified by looking at the evolution of the period over the viscosity (see fig.3.17 (b)) and we see that the period is at most doubled when varying the viscosity over several orders of magnitude.

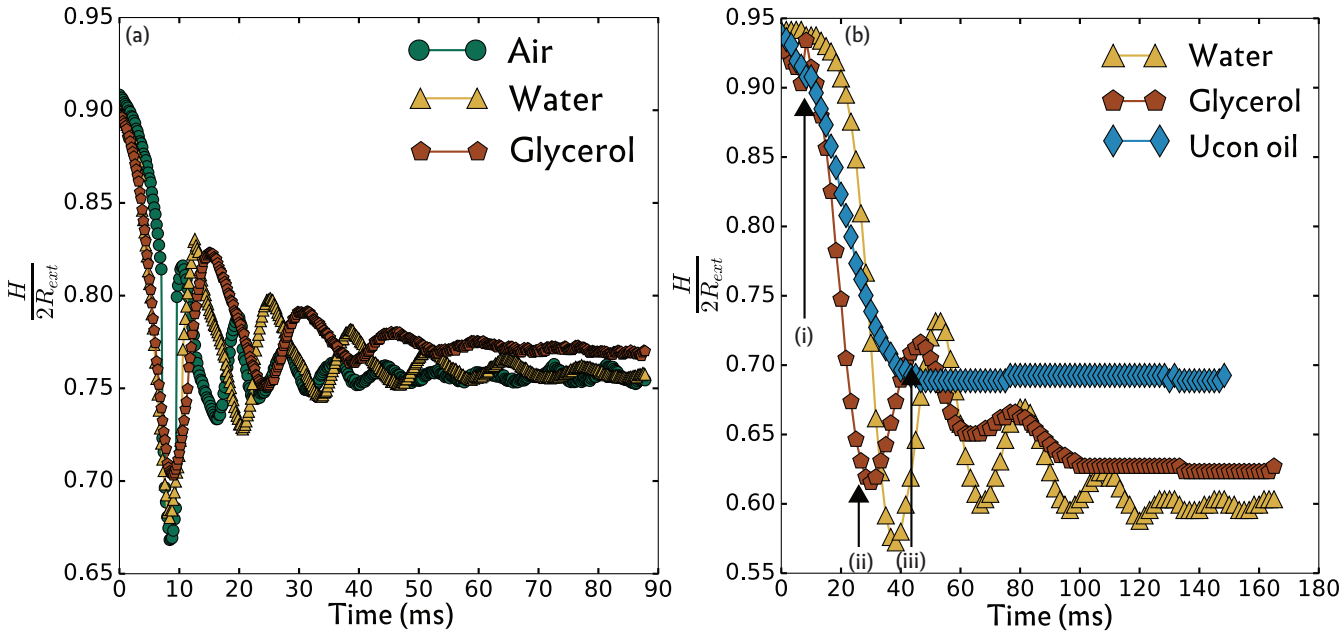

Figure 3.16: (a) Time evolution of the height right after buckling in three different fluids for a shell of $\frac{d}{R} = 0.22$ in the case of an external pressure control. (b) its equivalent with internal pressure control. Air ($\eta = 10^{-6}$ Pa.s Water ($\eta = 10^{-3}$ Pa.s), Glycerol ($\eta = 0.9$ Pa.s), Ucon©oil ($\eta = 37$ Pa.s). Labels (i) to (iii) refer to sequences that will be discussed within the swimming chapter.

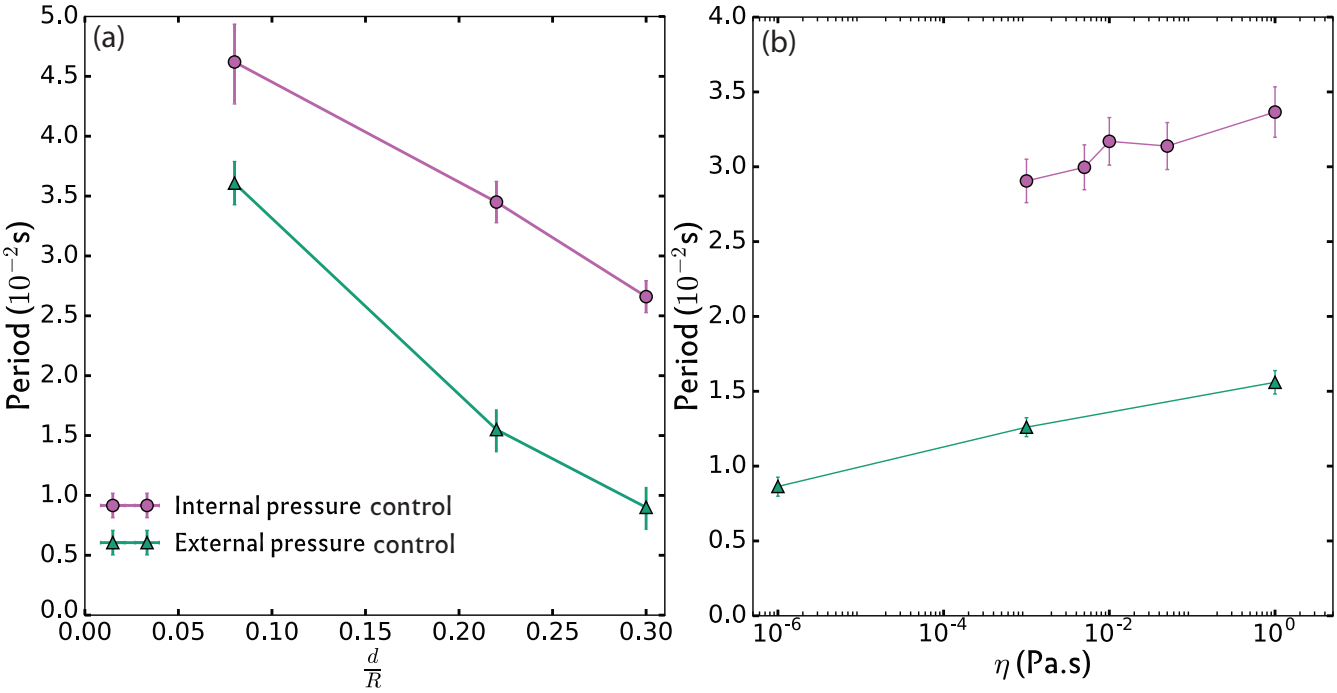

Figure 3.17: (a) is the evolution of the oscillation period as a function of $(\frac{d}{R})$. (b) represents the evolution of the oscillation period as a function of the fluid viscosity.

Figures 3.15 and 3.16 show another interesting aspect, the damping of the oscillations seems to vary with $(\frac{d}{R})$ and η. Assuming that we can model the height by:

$$H(t) = Ae^{-\frac{t}{\tau}} \cos(\omega t + \phi) \tag{3.8}$$

where $\omega = \sqrt{\omega_0^2 - \frac{1}{\tau^2}}$, ω_0 the natural frequency and τ the relaxation time. We measured the logarithmic decay defined as:

$$\psi = \ln\left(\frac{A(t_n)}{A(t_n + T)}\right) \tag{3.9}$$

Where $A(t_n)$ and $A(t_n + T)$ represent the amplitude at the instant t_n and $t_n + T$ respectively and T is the period of the oscillation.

In this case, the logarithmic decay is linked to the period and to the damping characteristic time by:

$$\frac{1}{\psi} = \frac{\tau}{T} \tag{3.10}$$

When the $\frac{\tau}{T}$ ratio decreases, it means that the damping increases. The evolution of this quantity in the different configurations is shown in figure 3.18.

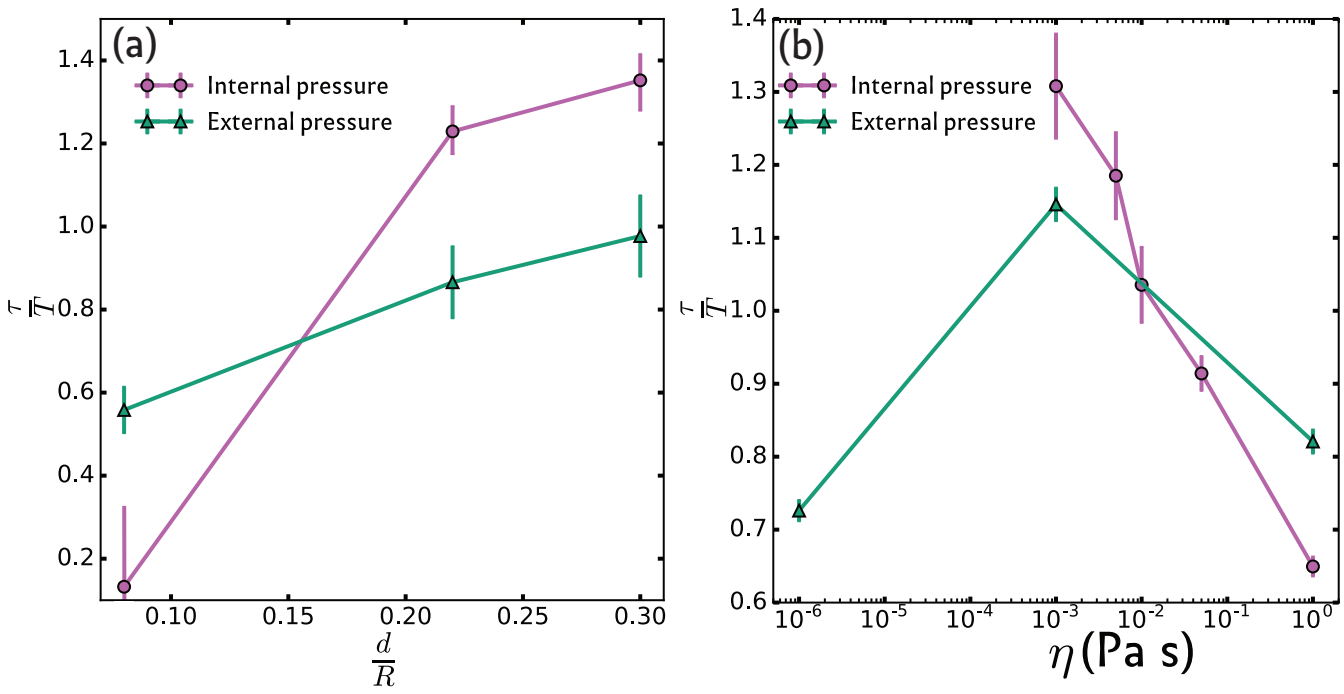

Figure 3.18: (a) Evolution of $(\frac{\tau}{T})$ as a function of $(\frac{d}{R})$ in glycerol for both methods of pressure control. (b) Evolution of $(\frac{\tau}{T})$ as a function of the surrounding fluid viscosity for a shell of $\frac{d}{R} = 0.22$ for both methods of pressure control.

First, we notice that independently from how the pressure is controlled, when $(\frac{d}{R})$ increases, damping decreases. Dependency with the reduced thickness is stronger in the case of an internal pressure control. Damping is more important in the case of external pressure control, except for small $(\frac{d}{R})$.

Second, the damping increases when the viscosity of the surrounding medium increases, but the dependency remains weak.

To complete the presentation of the experimental results concerning the shape dynamics, let us take a look at the deformation rate extracted from the $H(t)$. Deformation rate is defined as the absolute value of the highest slope of $H(t)$ (which corresponds to the slope of the first quarter of the first oscillation period).

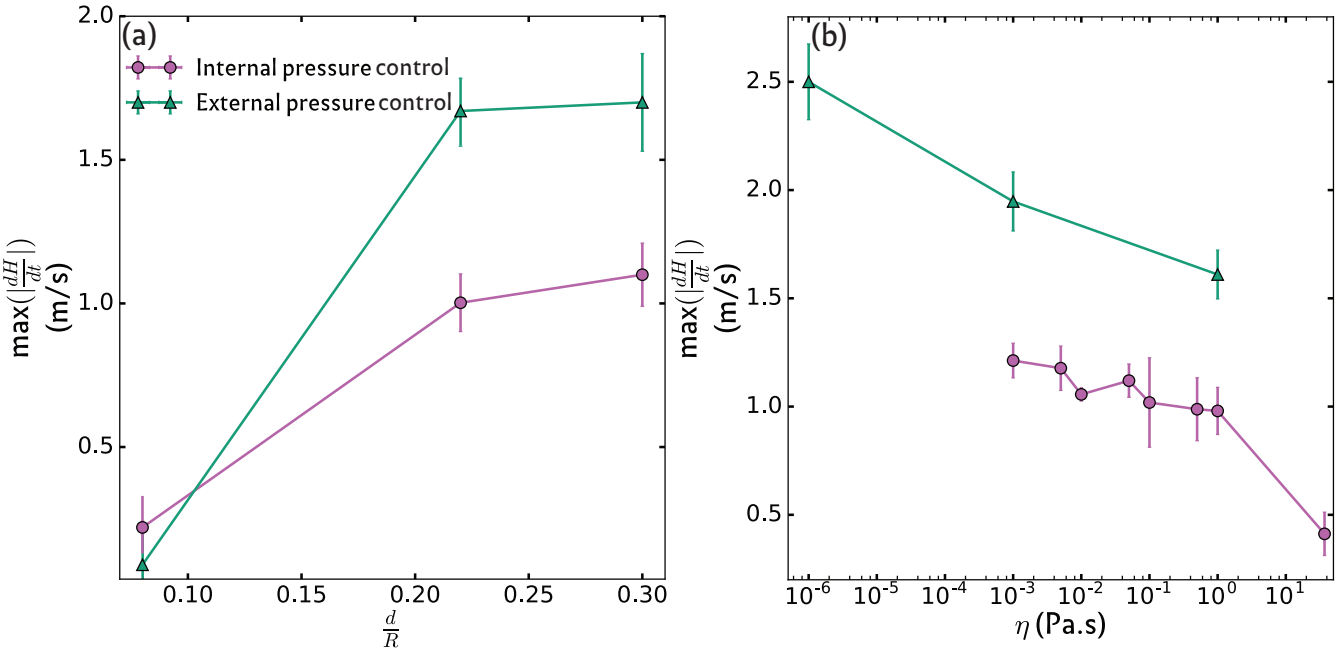

Figure 3.19: (a) Evolution of $\max(|\frac{dH}{dt}|)$ in regard to $(\frac{d}{R})$ in glycerol for both methods of pressure control. (b) Evolution of $\max(\frac{dH}{dt})$ as a function of the surrounding fluid viscosity for a shell of $\frac{d}{R}$=0.22, for both methods of pressure control.

As shown in figure 3.19, we notice that the deformation rate depends strongly on the parameter $(\frac{d}{R})$. The rate increases rapidly for small enough $(\frac{d}{R})$ but then reaches a limit for high values of $(\frac{d}{R})$, in both cases of pressure controls. Deformation rate achieved with external pressure control has a plateau ≈ 1.7 times higher than the deformation rate obtained when the pressure is controlled internally. This can be explained by the fact that the shell deforms with comparable amplitude between the two methods while it has a period at least 2 times smaller when the pressure is controlled externally.

When looking at the evolution of the rate of deformation in regard to the medium viscosity, we notice that the rate decreases when the viscosity increases. Dependency of $\max(|\frac{dH}{dt}|)$ with η is weak for $\eta \leq 1$. It decreases by 60% at 37 Pa.s.

From these elements, we can consider that the deformation of the shell is independent from the viscosity of the surrounding fluid when its buckling is followed by an oscillatory regime.

3.3.3 Summary

First, we notice that the nature of the pressure control (external/internal) produces different modes of deformation, either during the buckling or during the unbuckling instabilities. However, the spatial and temporal relevant quantities remain very comparable. Most importantly, these quantities are very sensitive to $(\frac{d}{R})$ and depend weakly on the viscosity of the surrounding fluid, which means that the buckling imposes a rate of displacement to the fluid, independently from its viscosity. This is true in a wide range of viscosities as long as the dissipation in fluid remains smaller than the dissipation in the material.

To understand the role of the material's viscosity, experiments were conducted on shells made of rubber-like polymers that share the same elastic modulus but have a different a rebound resilience, a property that denotes the damping of the material. The results are exposed in the following section.

3.4 The role of the material viscosity on the buckling dynamics

3.4.1 Introduction

Rubber-like materials are viscoelastic materials, which means that they exhibit a viscous and elastic behavior when being deformed. Furthermore, such materials tend to have a large elastic domain, which means that they can be submitted to large deformations and recover their original state.

To characterize simply such materials, a complex modulus $E*$ is used to characterize both the elastic and the viscous behavior

$$E* = E' + iE'' \ , \tag{3.11}$$

where E' is called the storage modulus (elastic recovery) and E'' the loss modulus (viscous damping)[*]. The ratio between the loss modulus and the storage modulus is called the *loss tangent*:

$$\tan\delta = \frac{E''}{E'} \tag{3.12}$$

A perfect elastic material would have a phase shift δ of 0°, and a purely viscous material would have a phase shift δ of 90°. Viscoelastic materials lie in-between. $E*$ can be measured experimentally by at least two means: the first one is *dynamic mechanical analysis* (DMA), which consists in applying a small oscillatory stress and measuring the resulting strain. The phase shift between applied stress and resulting stress provides the loss tangent. This is the most commonly used test. The second is the rebound resilience test where a small spherical steel ball is dropped on a well-clamped rubber sample from a height L and a rebound height L' is measured, the ratio $\frac{L'}{L}$=C_{rr} is called the rebound resilience (see fig. 3.20). The loss tangent $\tan\delta$ in this case is approximated as $\frac{L''}{L'}$. The relationship between these two quantities is:

$$\tan\delta = \frac{1}{C_{rr}} - 1 \tag{3.13}$$

[*]In reality, these quantities depend in a complex way on the temperature and the excitation frequencies.

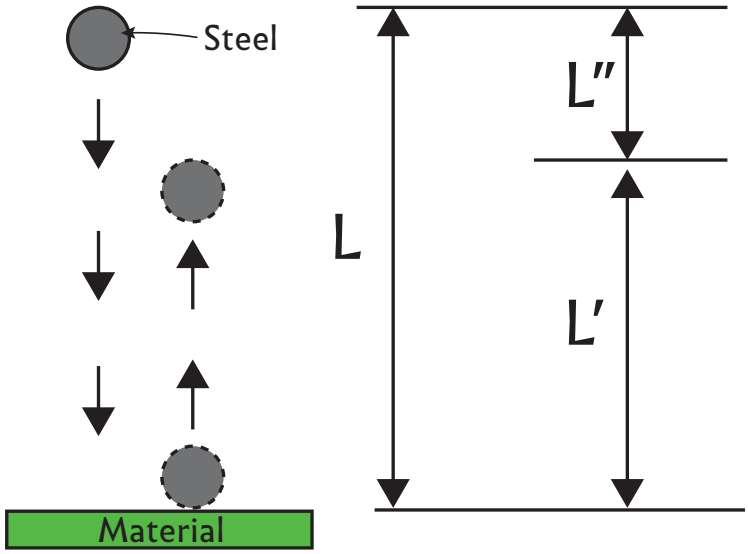

Figure 3.20: Schematic principle of rebound resilience test: $C_{rr}=\frac{L'}{L}$

3.4.2 Results

Two shells of relative thickness $\frac{d}{R} = 0.08$ made of two distinct elastomer materials "'AJO 121"' and "'AJO 122"', that present a comparable Young modulus ≈ 2 MPa, but differ by their rebound resilience of 0.45 ($\tan\delta = 1.22$) and 0.65 ($\tan\delta = 0.54$) respectively [*], were used to study the effect of the solid viscosity on the buckling dynamics.

[*]Data provided by the manufacturer.

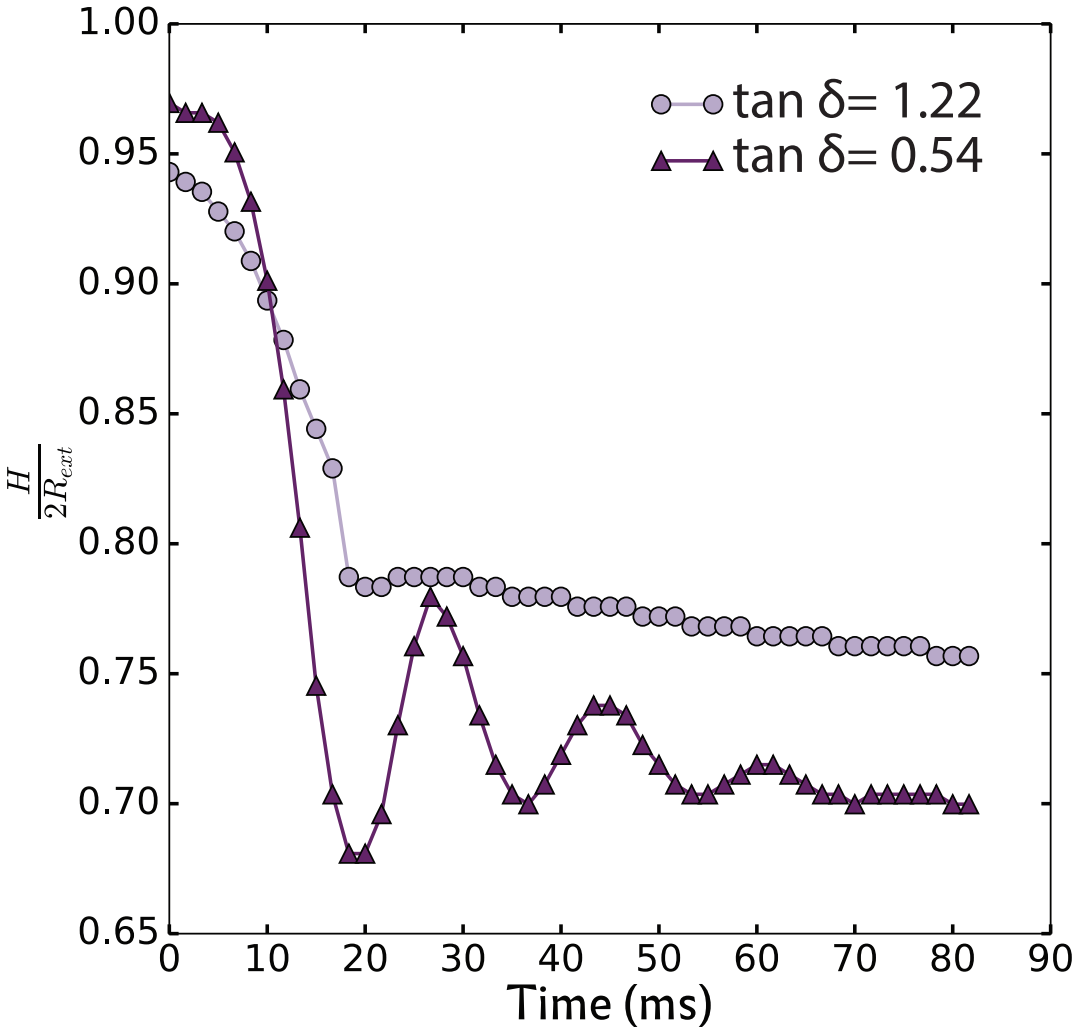

Figure 3.21: H(t) during the buckling transition, in water when pressure is controlled internally. d/R=0.08.

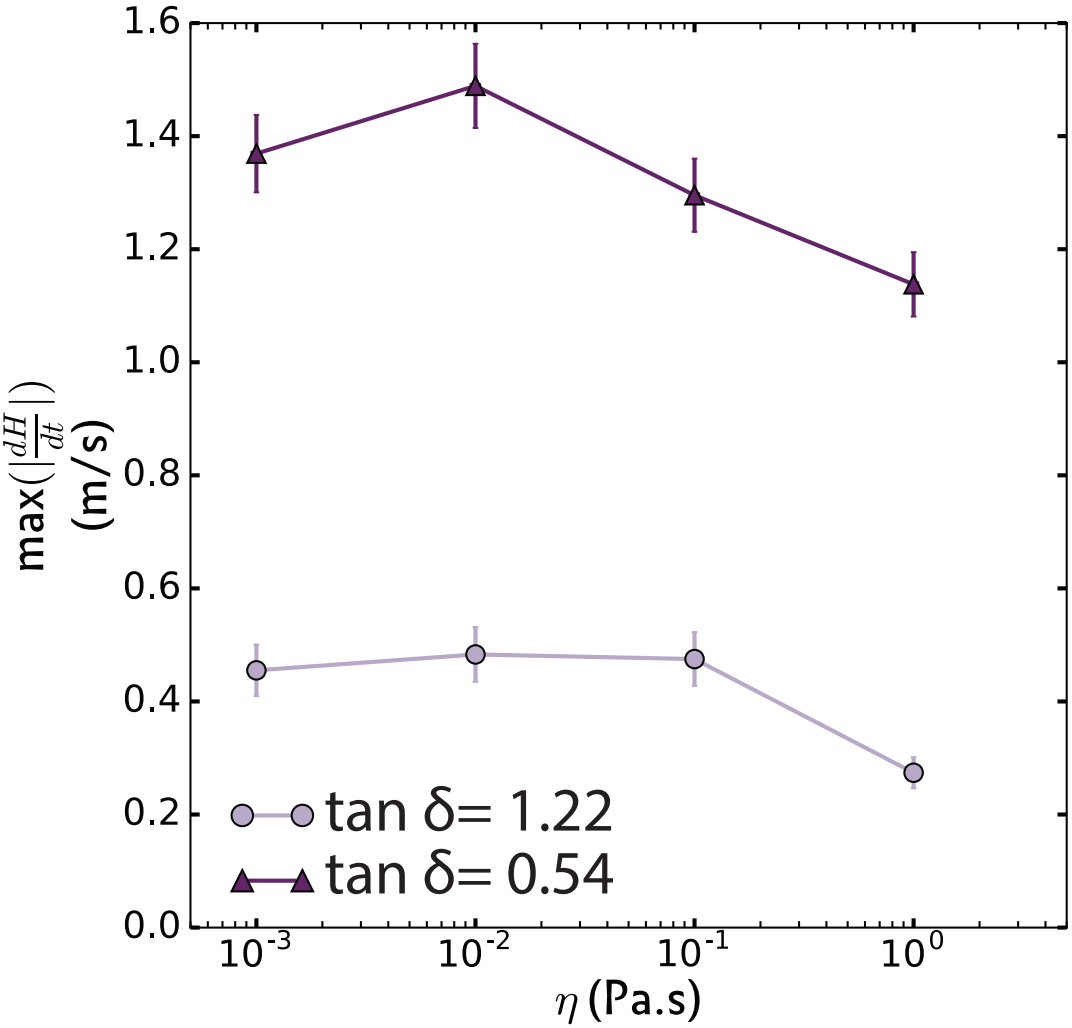

Figure 3.22: Evolution of $\max(|\frac{dH}{dt}|)$ as a function of the surrounding fluid viscosity.

Figure 3.21 shows the evolution of the apparent height over time during the buckling transition. We observe that the initial drop in amplitude of the height for the shell with $\tan\delta = 0.54$ is almost twice the initial drop of amplitude for the shell with $\tan\delta = 1.22$.

While we observe an oscillatory regime for the shell with $\tan\delta = 0.54$, no oscillations are observed for the shell with $\tan\delta = 1.22$, which means that the $H_{\tan\delta=1.22}(t)$ is in an over-damped regime. The typical values of the period for the shell with $\tan\delta = 0.54$ is $T = 17.5$ ms, and the relaxation time $\tau = 25$ms. The definition of the relaxation time, as the intersection between the initial tangent of $H_{\tan\delta=1.22}(t)$ with the time axis in the case of an over-damped regime, provide a typical value of τ which is is approximately 14 ms, for the shell with $\tan\delta = 1.22$.

We also notice that the deformation rate is different between the shell with $\tan\delta = 1.22$ and the shell with $\tan\delta = 0.54$. The maximum deformation rate was measured for various viscosities of the surrounding fluid. Figure 3.22 shows that the deformation rate stays relatively constant over three decades of viscosity and drops in glycerol by 40% for the shell with $\tan\delta = 1.22$ and 20% for the shell with $\tan\delta = 0.54$ compared to their respective plateau. The deformation rate plateau is 3.5 times higher for shell with $\tan\delta = 0.54$ compared to the shell with $\tan\delta = 1.22$.

In the light of these results, we can deduce that the buckling dynamics depends strongly on the rebound resilience coefficient.

These results helped us to identify what are the important factors (reduced thickness, loss tangent) to be taken into account for a theoretical interpretation and the building of a model, which is the subject of the next section.

3.5 A simple model for buckling dynamics

As we said earlier, the full buckling dynamics of an elastic shell of radius R and thickness d (such that its external radius is $R + d/2$) has never been studied theoretically and is out of the scope of this study. Nevertheless, we propose here a simple model —developed collectively with G. Coupier and C. Quilliet— that turns out to account for the observed dynamics in our macroscopic experiment. This model is based on the following consideration: we consider the hemispherical cap which will revert its concavity during buckling as a set of thin rods of length $\pi R/2$ going from the equator to the pole where buckling will take place. Buckling can be seen as the release of the thin rods far from their equilibrium position where the two poles touch each other, with 0 initial velocity and initial release position of order $2R$ (See Fig. 3.23).

We then first consider the problem of the oscillation of a thin rod, then we use the results to determine the typical buckling velocity and post-buckling oscillation frequency. We will first consider the case with no fluid around the shell, then we will consider the coupling with a fluid. We shall neglect in all cases the problem of inner gaz compressibility.

3.5.1 Thin rod dynamics

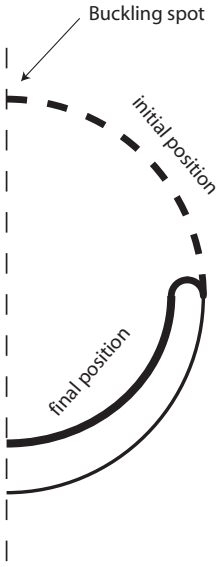

Figure 3.23: Principle of the beam model. The initial (unstable) position of each meridian of the top cap corresponds to the sphere. At buckling, the equilibrium position is that which corresponds to a buckled shell. The buckling dynamics is described by the release of the beam from the initial position.

We consider a thin rod of viscoelastic material described by Voigt law, characterized by a storage modulus $E'(w)$, a loss modulus $E''(w)$ and density ρ, $E'(0) = E$ is the Young modulus. The rod has a length L and a thickness d (in the direction of motion). The width does not come into play in the following equations. By extension of the equation 21 of Ref. [Baker et al., 1967], where constant Young modulus and viscosity are considered, the dynamics of the free end of the rod with the other end fixed can be described by the equation $\ddot{y} + \frac{2}{\tau_n}\dot{y} + \omega_n^2 y = 0$, where $\omega_n^2 = (\beta_n/L)^4 d^2/(12\rho)E'(\omega)$ and $\frac{2}{\tau_n} = \omega_n^2 E(\omega)/(\omega E'(\omega))$. The first mode frequency is given by $\beta_0^2 = 3.52$.

Looking for an oscillating solution $y(t) \propto e^{i(\omega+i\alpha)t}$ one finds that $\alpha = \chi_n E(\omega)/(2\omega)$ and

$$\omega^4 - \omega^2 \chi_n E'(\omega) + (\chi_n E(\omega)/2)^2 = 0, \tag{3.14}$$

with $\chi_n = (\beta_n/L)^4 d^2/(12\rho)$. There is a real root of the latter equation for ω^2 iff $E'(\omega) > E(\omega)$, which

is most often the case for solids [Lakes, 2009], whatever ω. This means that the beam motion is always a quasi periodic motion. E'/E is the inverse of the loss factor often written $\tan\delta$. In that case, ω is solution of the equation $\omega^2 = \frac{\chi_n E'(\omega)}{2}(1 \pm \sqrt{1-(E(\omega)/E'(\omega))^2})$. The solution with minus sign is not physical as it implies increasing frequency with increasing damping. The equation for ω is thus

$$\omega^2 = \frac{\chi_n E'(\omega)}{2}\xi(\omega)^2 \tag{3.15}$$

$$\text{with} \qquad \xi(\omega)^2 = 1+\sqrt{1-(E(\omega)/E'(\omega))^2} \tag{3.16}$$

The exact solution for ω depends on the functions $E'(\omega)$ and $E(\omega)$ but remarkably, as $1 < \xi(\omega)^2 < 2$,

$$\frac{\chi_n E'(\omega)}{2} < \omega^2 < \chi_n E'(\omega). \tag{3.17}$$

In addition, $\omega/\alpha = 2\omega^2/(\chi_n E(\omega)) = \frac{E'(\omega)}{E(\omega)}\xi(\omega)^2$, which is comprised between 1 and $+\infty$.

From this we can estimate the maximum of the absolute value of the velocity V of the endpoint of the beam (reached around its first passage close to equilibrium position). It can be shown numerically that, because $1 < w/\alpha < \infty$, if the beam is released at position $y_0 > 0$ with zero velocity, we have:

$$0.6\, y_0\omega < V < y_0\omega \tag{3.18}$$

3.5.2 Shell dynamics

From the preceding calculations on beam — equation for ω (Eq. 3.15) and inequality for the maximum velocity (Eq. 3.18)—, we find that the motion of the buckling spot will be quasi periodic and that the post-buckling frequency and the buckling velocity $V_b \equiv V$ obey:

$$\omega \simeq \frac{3.5d}{\sqrt{2}(\pi R/2)^2\sqrt{12}} \times \sqrt{E'(\omega)/\rho} \times \xi(\omega) \tag{3.19}$$

$$\simeq 0.3\,\frac{d}{R^2} \times \sqrt{E'(\omega)/\rho} \times \xi(\omega) \tag{3.20}$$

$$\text{with} \qquad 1 < \xi(\omega) < 1.4, \tag{3.21}$$

$$\tag{3.22}$$

and

$$V_0 < V_b < 2.3V_0 \tag{3.23}$$

$$\text{with } V_0 = 0.6\,\frac{2R \times 3.5d}{\sqrt{2}(\pi R/2)^2\sqrt{12}} \times \sqrt{E'(\omega)/\rho} \tag{3.24}$$

$$\simeq 0.4\,\frac{d}{R}\sqrt{E'(\omega)/\rho}, \tag{3.25}$$

with ω being the solution of Eq. 3.20.

An important control parameter is the buckling pressure ΔP_c, which scales like $E(\frac{d}{R})^2$ (see eq.3.1)

Equation 3.20 can be rewritten:

$$w \simeq 0.3R^{-1}\sqrt{\frac{\Delta P_C}{\rho}}\sqrt{\frac{E'(\omega)}{E}} \times \xi(\omega), \tag{3.26}$$

.

with $1 < \xi(\omega) < 1.4$.

As for the buckling velocity, one gets

$$0.4\sqrt{\frac{\Delta P_C}{\rho}}\sqrt{\frac{E'(\omega)}{E}} < V_b < 0.9\sqrt{\frac{\Delta P_C}{\rho}}\sqrt{\frac{E'(\omega)}{E}} \tag{3.27}$$

Since E' is often an increasing function of ω, this implies first that

$$V_b > 0.4\sqrt{\frac{\Delta P_C}{\rho}}. \tag{3.28}$$

and that V_b for a microscopic system will be higher than for a macroscopic system made with the same material.

Those inequalities allow to estimate the buckling velocities from the sole knowledge of E' without that of E. As they are quite tight they allow to discuss the possible scalings between microscopic systems and macroscopic ones without bothering too much with the question of where the solutions ω and V lie exactly in the established ranges.

Note that the minimal buckling velocity is only set by the buckling pressure and the density of the

material, whatever the considered scale but that the exact value of the velocity depends on the scale through the factor $E'(\omega)$, where ω is the solution of Eq. 5.3.

We validate Eqs. 5.3 and 5.4 through our macroscopic shells.

For our $d/R = 0.22$ shell with $\rho = 1060\text{kg/m}^3$, if we assume that $E'(\omega) = E'(0) \equiv E$, we find $\omega \simeq 64$ Hz, which first is of the same order of magnitude as the measured pulsation $\omega \simeq 150$ Hz and second validates the above assumption since for elastomeric materials the stiffness $E'(\omega)$ is almost constant up to the kHz [Lakes, 2009]. Defining V_b as $V_b = 2\text{max}(\frac{dH}{dt})$, we find $V_0 = 1.9$ m/s, hence a buckling speed V_b comprised between 1.9 and 4.4 m/s, which perfectly surrounds the experimental value of $V_b \simeq 2.4$ m/s in water.

The preceding considerations are valid if the fluid does not influence the shell deformation characterized by a quality factor $Q_f = \omega\tau > 1$. The typical time associated with the damping of membrane motion due to fluid viscous friction can be calculated as follows: the mass of the moving material is that of the hemisphere $m = \rho \times 2\pi R^2 d$. The moving material has a diameter $2R + d$ so in a first approximation the viscous damping coefficient should be close to $\alpha_f = 3\pi\eta(2R + d)$ (because, as will be consistently checked in the next paragraph, we expect the fluid to influence the shell deformation at low Reynolds number). This leads to a typical time $\tau_f = m/\alpha_f = \rho R^2 d/[(R + d/2)3\eta]$.

The damping in the fluid will influence the shell dynamics when $\omega\tau_f < 1$. For our macroscopic shell, this leads to a crossover viscosity $\eta^* \simeq 2$ Pa.s, in agreement with experimental data (Fig. 3.19-(b)) showing an experimental crossover between between 1 and 37 Pa.s.

The only true wisdom is in knowing you know nothing.

Socrates

4

Flow dynamics

4.1 Introduction

We exposed in the previous chapter the dynamics of shell buckling where we saw that it depends strongly on the reduced thickness (d/R) and on the loss tangent $\tan\delta$, but weakly on the surrounding fluid viscosity up to a certain point.

The next questions we needed to answer is about what kind of flow is generated during deflation and re-inflation, and how does this fluid flow depend on the shell dynamics, that imposes specific boundary conditions?

To answer these questions, we developed an experimental setup exposed in section 2.4 and performed time-resolved particle-image velocimetry measurements. These latter allowed to get the temporal and spatial evolution of the Eulerian velocity field during the instabilities in two liquids: water and glycerol.

We will begin first by illustrating the flow patterns step by step in both liquids for a shell of (d/R)=0.22. The flow structures we describe from here on are to be considered independent from (d/R) or $\tan\delta$ unless explicitly stated otherwise.

Note A reminder for the reader:

Water is is a Newtonian liquid, with a density of $\approx$ 1000 kg/m3 and a dynamic viscosity $\approx 10^{-3}$ Pa.s. Glycerol is also a Newtonian liquid, with a density of $\approx$ 1250 kg/m3 and a viscosity 1000 times the viscosity of water*.

Note We focused here solely on the description of the flow. We will establish the causal relationship with shell deformation thoroughly in the chapter dealing about the swimming.

4.2 Flow during deflation

For what concerns the flow, we separated the time of the deflation into 3 sub-phases based on shell deformation phases: Buckling nucleation flow, Shape oscillations flow and Post-deformation flow.

In the following, we will use a certain nomenclature to point to regions surrounding the shell, or to directions, when alluding to figures. Vocabulary is made explicit on figure 4.1.

*At room temperature.

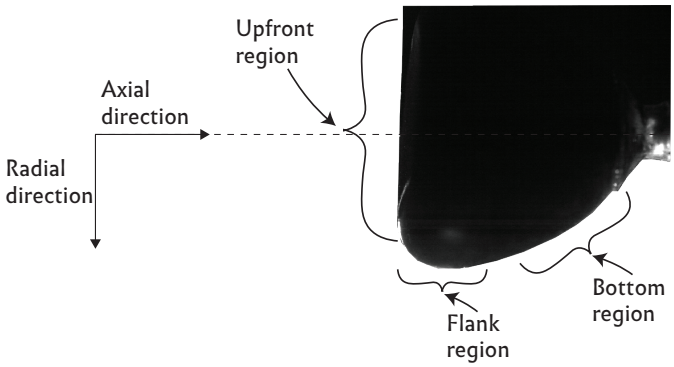

Figure 4.1: Schematics representing the vocabulary used in comment text.

4.2.1 Buckling nucleation

Buckling nucleation phase corresponds to the creation of the concavity and its radial/axial propagation, and it lasts $\approx$ 20 ms. During this phase, we observe a similar flow in water and in glycerol: upfront, an axial flow (along the symmetry axis of the concavity) converges toward the concavity. In the bottom region, a flow converges toward the shell. A flow escapes from the flank region, some of it converges toward the upfront region and some of it toward the bottom regions as illustrated in figure 4.2.

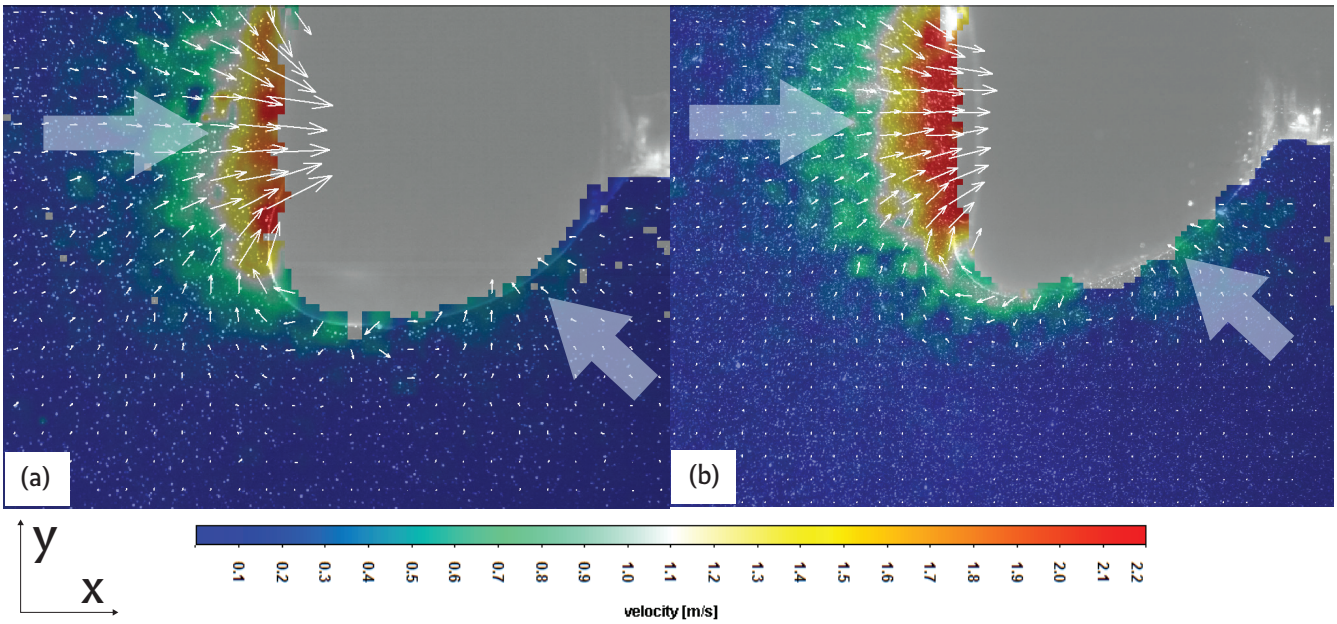

Figure 4.2: Typical instantaneous velocity field during buckling nucleation: (a) in water ($\eta \simeq 10^{-3}$Pa.s);(b) in glycerol ($\eta \simeq 1$Pa.s). Results for a shell of (d/R)=0.22.

Upfront, flow accelerates from rest to velocities that can attain 2.5 m/s for shells of (d/R) of 0.22 and 0.3, and reaches at most 0.5 m/s for a shell of (d/R)=0.08. At the bottom, typical velocities are around 0.5 m/s for (d/R) of 0.22 and 0.3, and are negligible for (d/R)=0.08. Note that the maximum of the velocity intensity is to be found during this phase, and acceleration can overcome 300 m/s^2.

We averaged the velocity components over the buckling nucleation period and results are shown in figure 4.3 and 4.4. Time-averaged x-component of velocity (axial) is characterized by a unique positive frontal lobe in both water and glycerol, while there are two frontal lobes with opposite signs in the time-averaged y-component of velocity (radial), in agreement with the axial symmetry of the shell deformation*.

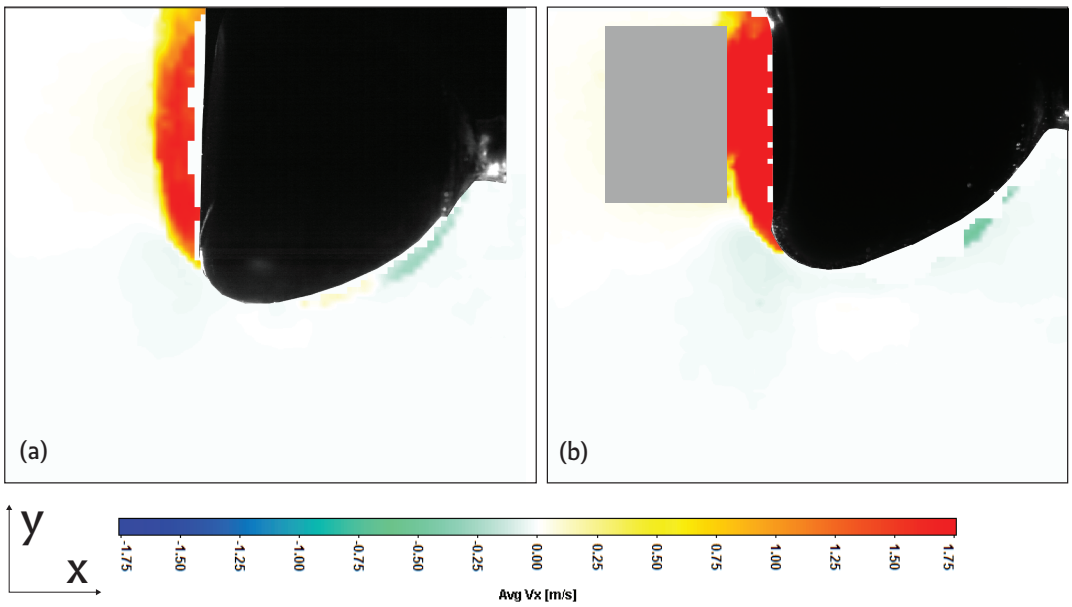

Figure 4.3: Buckling nucleation time-averaged x-component of velocity: (a) in water;(b) in glycerol, (d/R)=0.22 shell.

*Gray rectangle was added to mask regions where measurements were polluted by too much light reflection when the shell's shape was convex.

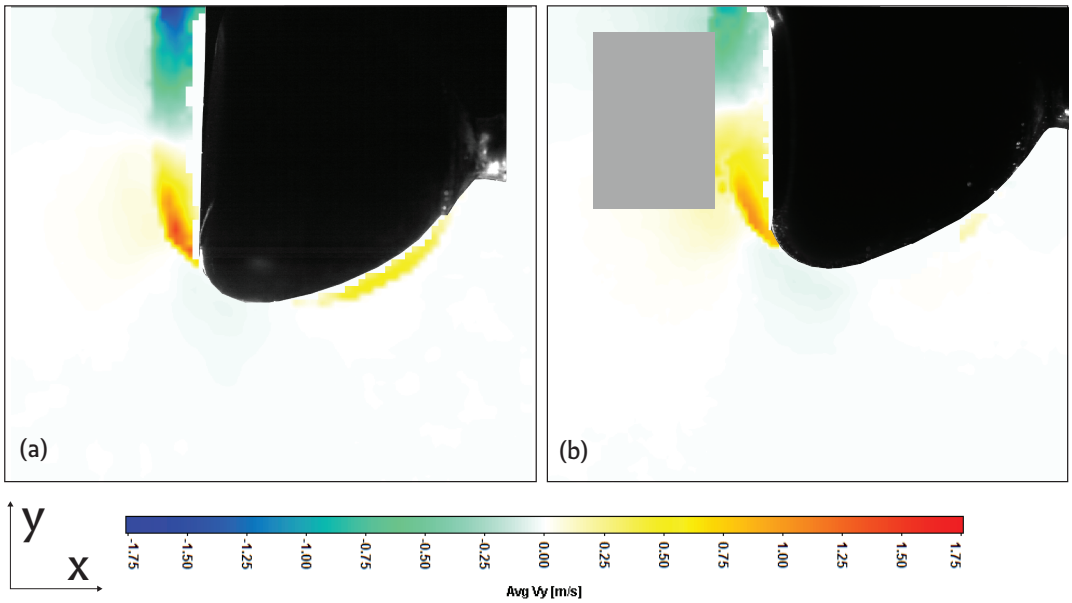

Figure 4.4: Buckling nucleation time-averaged y-component of velocity: (a) in water;(b) in glycerol. (d/R)=0.22 shell.

4.2.2 Shape oscillations

Once the concavity reaches its critical radial size, the buckling evolves into shape oscillations which consist in a succesion of inward-outward axial translation of the concavity without significant radial motion of the flanks. We will describe the flow during the first inward and first outward shell oscillations.

4.2.2.1 Inward deformation

During this phase, the concavity is decelerating along the x-axis until it reaches a stop point. For a shell of (d/R)=0.22, this step lasts 22 ms and 28 ms in water and glycerol respectively. Typical velocities are smaller (1.5 m/s for (d/R)=0.22) than velocities encountered during buckling nucleation as a consequence of the decelerating motion.

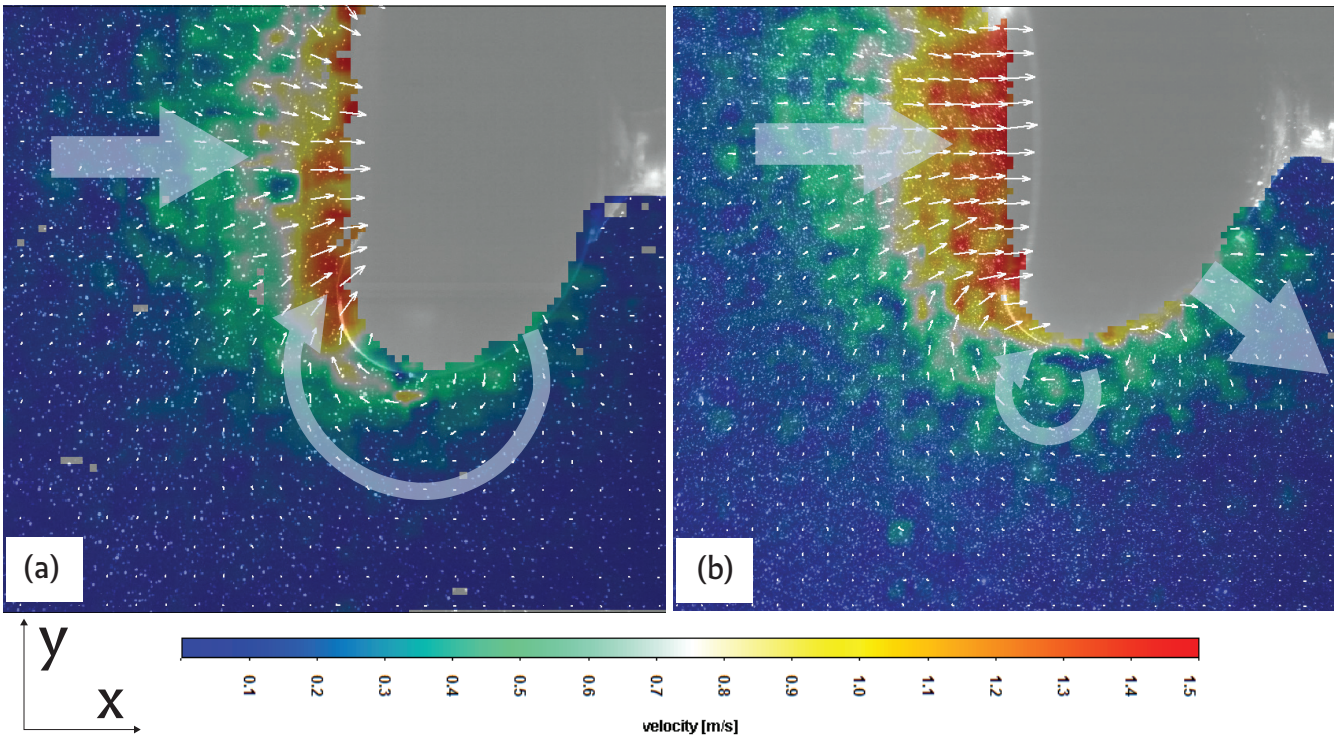

Figure 4.5: Typical instantaneous velocity field during first inward deformation: (a) in water ($\eta \simeq 10^{-3}$Pa.s);(b) in glycerol ($\eta \simeq 1$Pa.s). Results for a shell of (d/R)=0.22.

Figure 4.5 shows the typical structure of the flow in water and glycerol during the inward deformation.

The fluid keeps following the displacement of the concavity upfront with a flow characterized by an axial velocity where maximum velocity intensity is encountered. Meanwhile, at the bottom region, the flow is accelerated away from the shell. These observations are common to water and glycerol. However at the flanks, in water the fluid rotates from the bottom toward the concavity (compression-depression sources respectively) with a virtual center of rotation situated inside the shell, while in glycerol, a vortex nucleates at the flank with a real center of rotation*, in the fluid domain. It moves away from the flank toward the front, while a frontal flow penetrates between the flank and the vortex. The penetrating flow is then tangential to the boundary. The direction of the frontal flow combined with the direction of rotation of the vortex explains the direction of displacement of the center of the vortex. The vortex dissipates after less than $15ms$. We will provide complementary observations later in this chapter

*In the frame we used, the vortex that forms at the flank has a clock-wise rotation.

(sec. 4.6).

These observations and differences are confirmed by the time-averaged velocity field components shown in figures 4.6 and 4.7, where we see that a the positive frontal lobe in water is narrower than the one in glycerol which envelops the shell. This is compatible with the presence of a vortex in glycerol that does not exist in water.

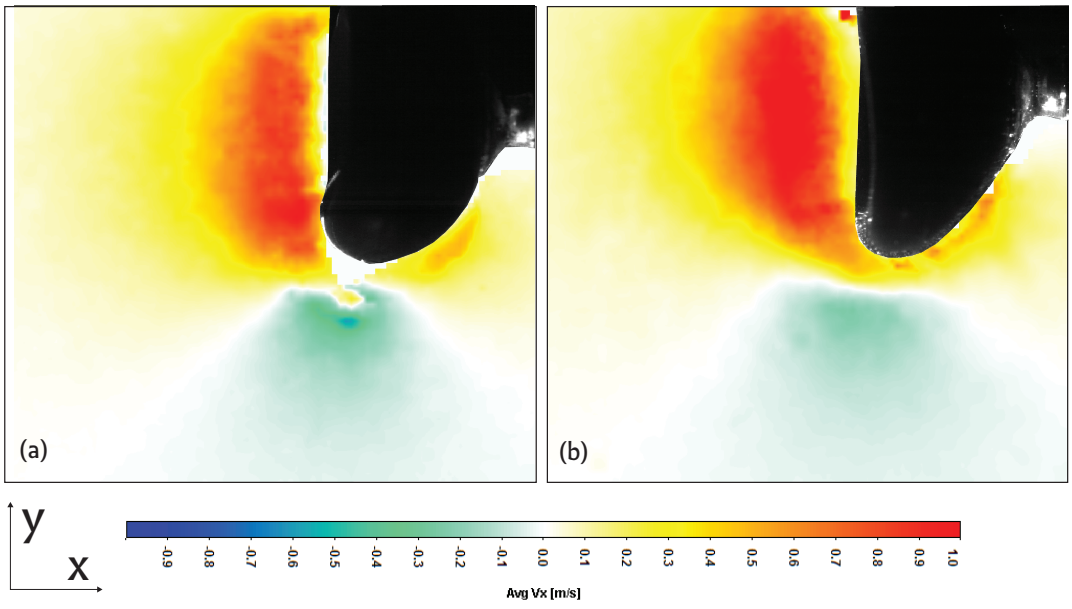

Figure 4.6: Time-averaged x-component of velocity during post-buckling first inward deformation: (a) in water;(b) in glycerol. (d/R)=0.22 shell.

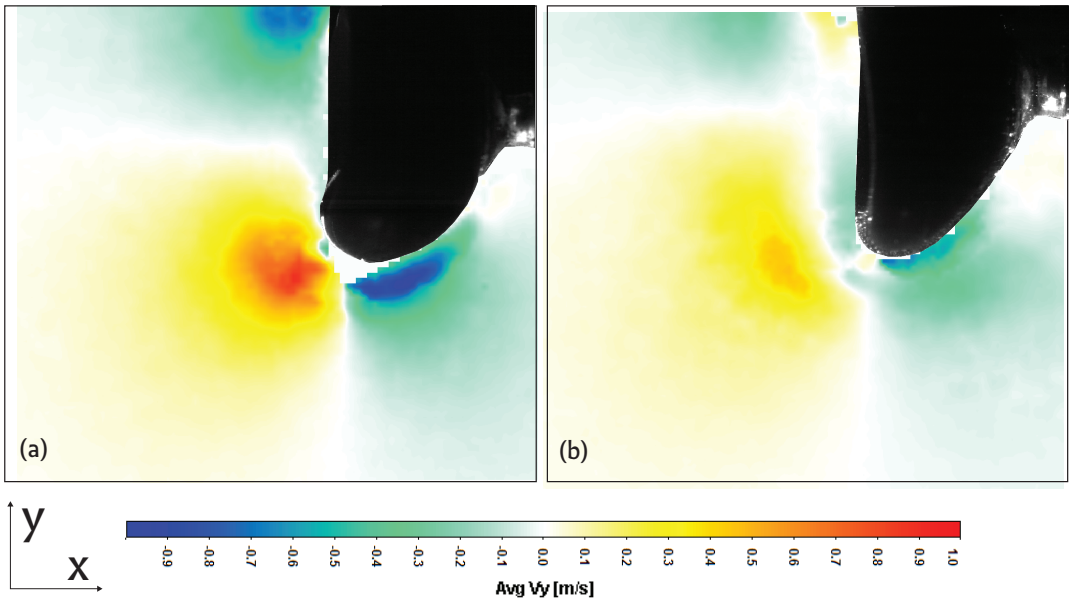

Figure 4.7: Time-averaged y-component of velocity during post-buckling first inward deformation: (a) in water;(b) in glycerol. (d/R)=0.22 shell.

4.2.2.2 Outward deformation

Once the inward deformation reaches a stop point, it starts moving outward (negative direction along x-axis) with a duration of the outward deformation estimated at approximately 14 ms.

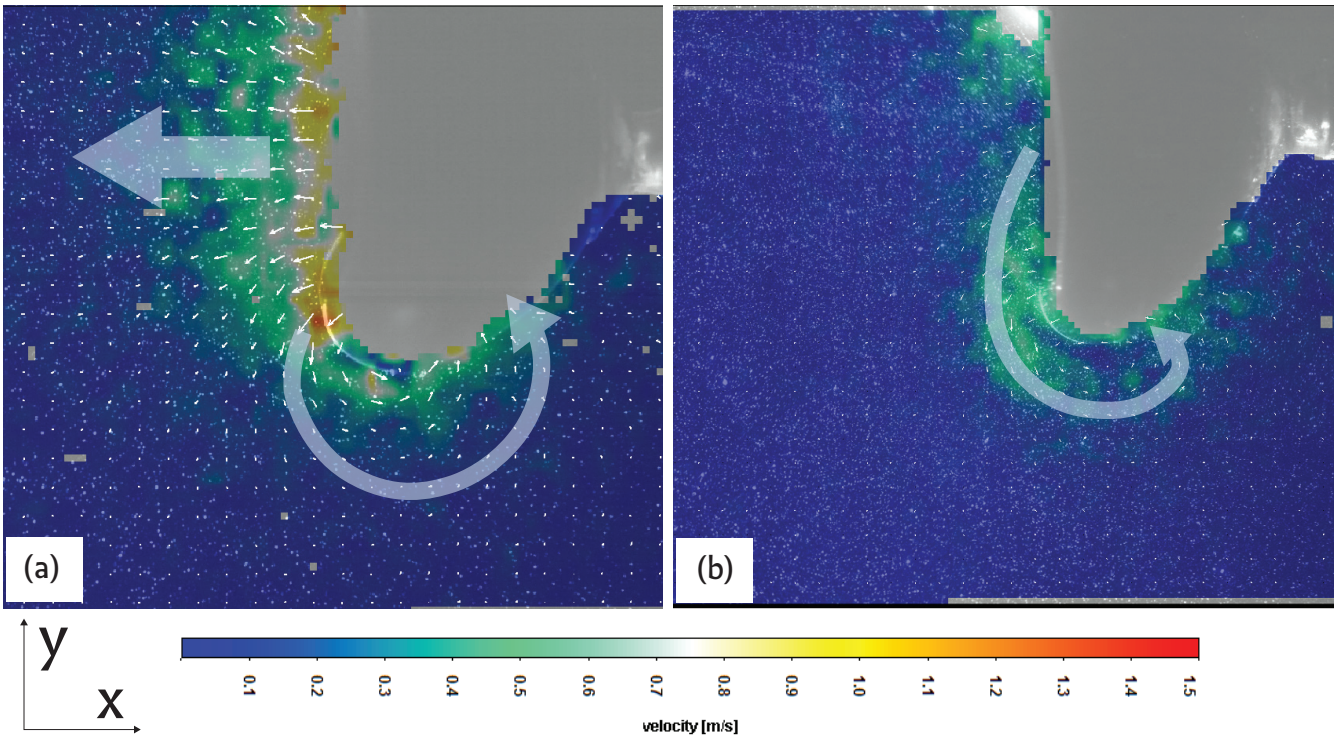

Figure 4.8: Typical instantaneous velocity field during first outward deformation: (a) in water ($\eta \simeq 10^{-3}$Pa.s);(b) in glycerol ($\eta \simeq 1$Pa.s). Results for a shell of (d/R)=0.22.

Two distinct flow structures can be observed in water and glycerol as illustrated in figure 4.8: In water, we clearly see that the flow reverts between the inward and outward deformation, with a slight decrease in the maximum velocity reached during the outward deformation. In opposition, the flow in glycerol does not simply revert: the frontal flow is mainly radial this time. It rotates around the flank and comes back at the bottom. This difference is highlighted in the time averaged velocity fields illustrated in figures 4.9 and 4.10. They shows the clear change of flow structure between water and glycerol.

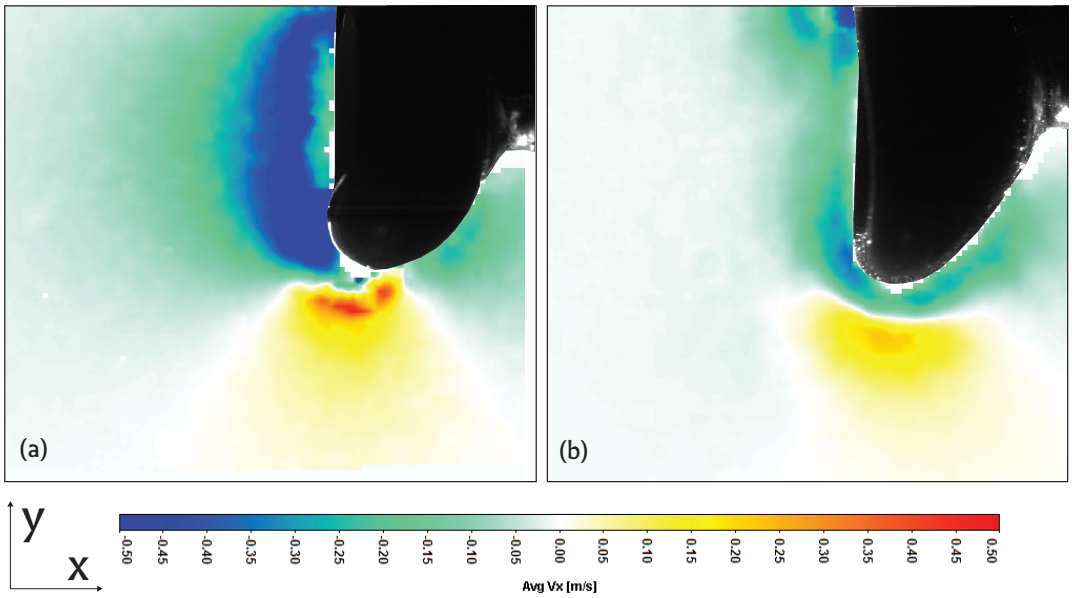

Figure 4.9: Time-averaged x-component of velocity during post-buckling first outward deformation: (a) in water;(b) in glycerol. (d/R)=0.22 shell.

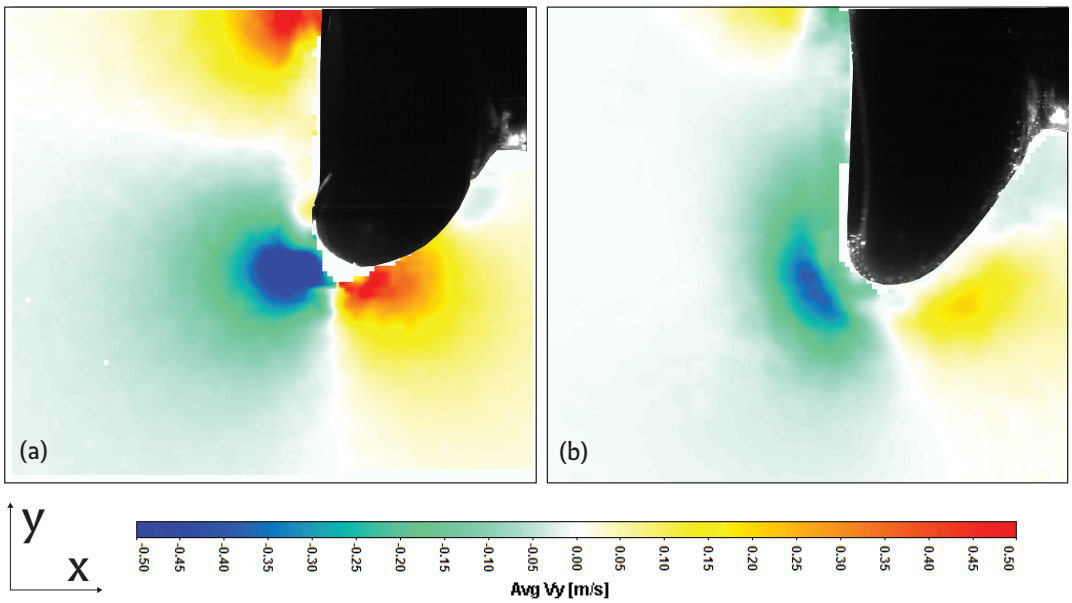

Figure 4.10: Time-averaged y-component of velocity during post-buckling first outward deformation: (a) in water;(b) in glycerol. (d/R)=0.22 shell.

The flow structures shown earlier appear periodically —with decreasing intensity— as long as the post-buckling shape oscillations take place. In glycerol however, after the first outward deformation,

frontal flow converges axially toward the concavity even when the shell is undergoing an outward oscillation.

To highlight the impact of the asymmetry of the flow in glycerol compared to the symmetry of the flow in water, we averaged the velocity field over the duration of the shell deformation (slightly longer in water) as shown in figures 4.11 and 4.12. We observe that in total, the frontal flow converges toward the concavity in both liquids with an average value 5 times higher in glycerol.

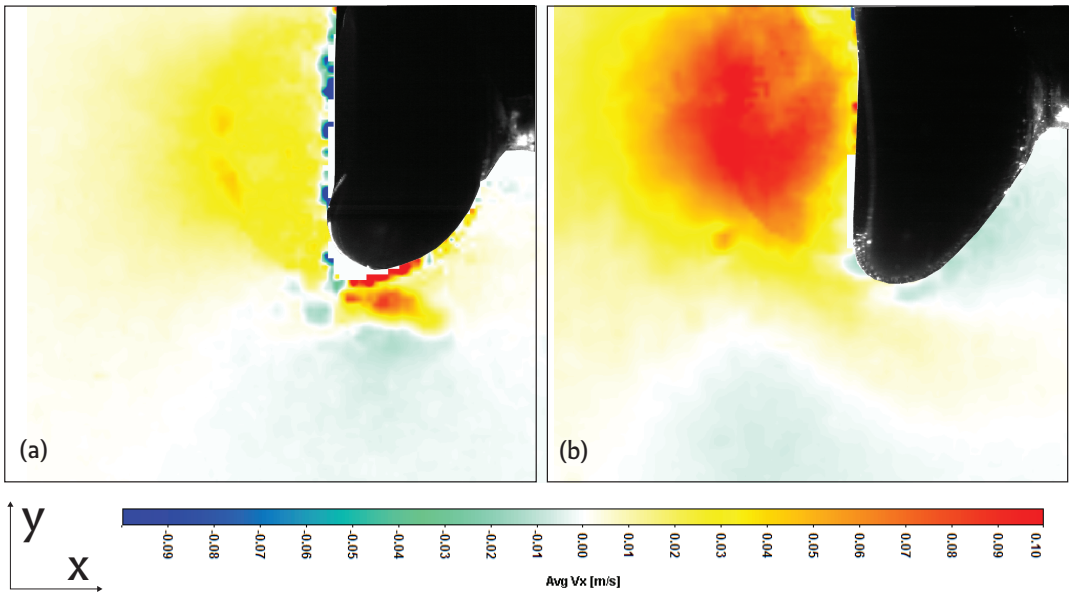

Figure 4.11: Time-averaged x-component of velocity during all deformation phases: (a) in water, averaging done over a duration of ≈ 132 ms;(b) in glycerol, averaging done over a duration of ≈ 110 ms. (d/R)=0.22 shell.

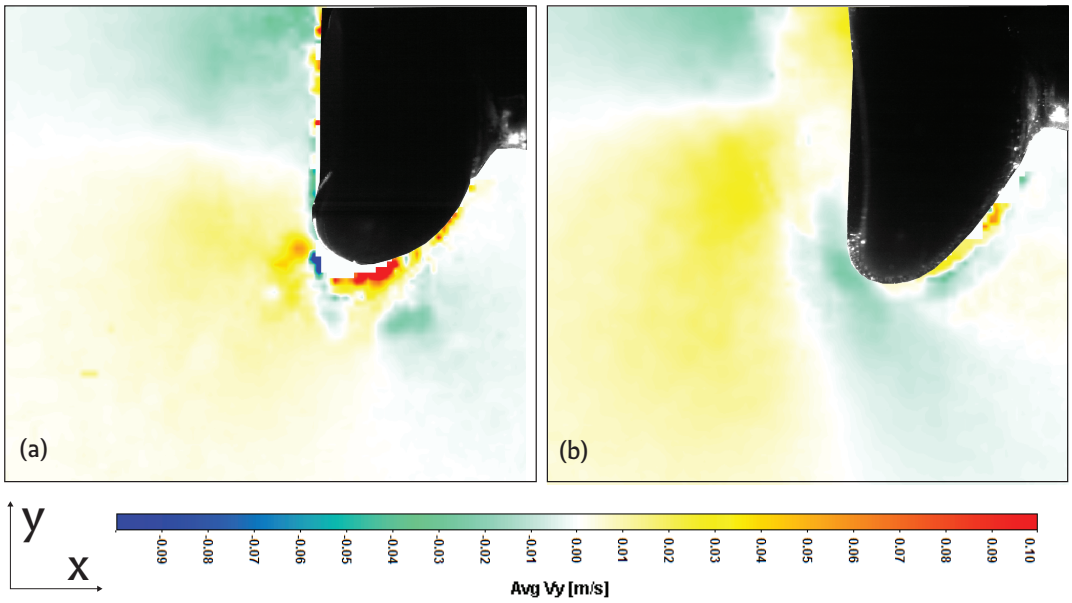

Figure 4.12: Time-averaged y-component of velocity during all deformation phases: (a) in water, averaging done over a duration of ≈ 132 ms;(b) in glycerol, averaging done over a duration of ≈ 110 ms. (d/R)=0.22 shell.

Finally, let us remark that the structures and velocity fields observed earlier lead us strongly to validate the assumption of existence of 3D axi-symmetry of the flow.

Note— A water flow with velocities reaching 2.5 m/s ($Re \approx 10^4$) around a spherical object should exhibit flow separation. In the flow region we explored, none of these effects were observed. The creation of a circulation that comes from the bottom of the shell toward the frontal region may be responsible. When measuring the fluctuations of the velocity field in water, during deflation phase, the root mean square of the velocity, defined as:

$$v'_x = \sqrt{< V_x^2 > -(< V_x >)^2} \tag{4.1}$$

where <> defines a time average.

can reach values of 0.5 m/s in the frontal regions and at the flanks. It is however hard to assess if this value expresses only the turbulence present in the flow or if it is coupled with the unsteady nature of the flow. Further investigations are required. For now, turbulent effects will not be taken into ac-

count.

4.2.3 Post deformation flow

The fluid does not return to equilibrium directly after the end of shape deformation, especially in water. An estimation of the duration of the flow perturbation is given by:

$$\tau_{perturbation} = \frac{L^2}{\nu} \tag{4.2}$$

with L being the characteristic length of the perturbation (R in our case) and ν the kinematic viscosity. This gives a dissipation time of 625 s (resp.0.8 s) in water (resp. glycerol) which are in agreement with experimental observations.

An important qualitative observation in that in water, a vortex* develops at the flanks just after the buckling, that travels toward the bottom and then detaches after 4 s. Such structure is not observed in glycerol.

4.3 Flow during re-inflation

We saw in the chapter about shell dynamics that re-inflation is not just the inverse of deflation in terms of deformation. Consequently, this will impact the flow generated. During re-inflation, we can distinguish two phases: in the first one, the shell snaps back to a convex configuration (unbuckling), and the second it undergoes undulations which damp into the initial spherical configuration. For both phases, time-resolved PIV measurements were also conducted in water and in glycerol.

4.3.1 Unbuckling

In the first phase, the outward rolling of the fold that circles the concavity pushes the liquid immediately in front of it, with no noteworthy deformation localized at the back of the shell. Unbuckling lasts approximately 15 ms.

*Vortex direction of rotation in the frame we used is clock-wise.

Flow during the unbuckling is localized at the front of the shell as shown in figure 4.13; we observe that the fluid is diverging away from the shell frontal region but is clearly less axial than in the buckling phase. We also observe that no significant flow is produced elsewhere. These observations are common to both liquids.

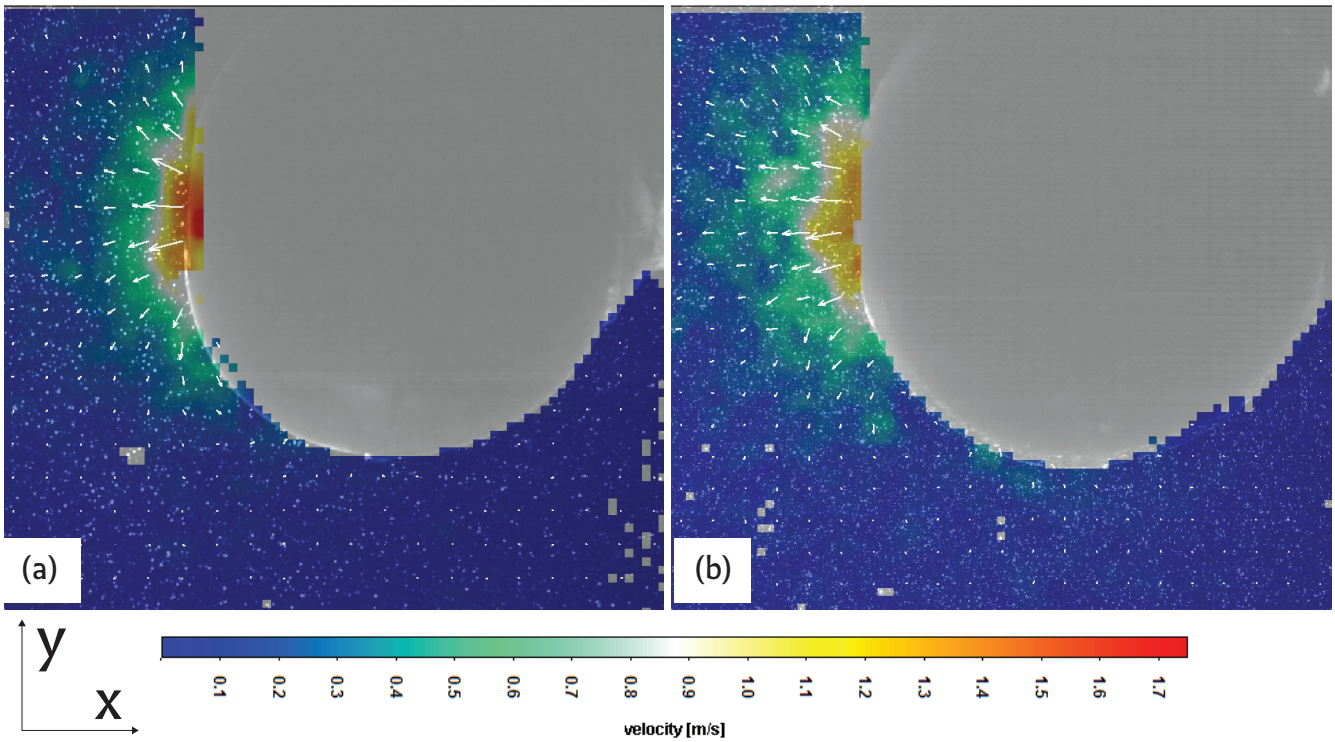

Figure 4.13: Typical instantaneous velocity field just after the transition to the convex shape: (a) in water ($\eta \simeq 10^{-3}$Pa.s);(b) in glycerol ($\eta \simeq 1$Pa.s). Results for a shell of (d/R)=0.22.

The maximum velocity reached during this phase for a shell of (d/R)=0.22 is around 1.8 m/s, lower than the 2.4 m/s reached during the buckling phase. But remarkably, both phases exhibit sensitively the same absolute value in acceleration, estimated about 300 m/s^2.

Figures 4.14 and 4.15 show that the intensity of the frontal lobe velocity is 10 times smaller than the intensity of the mean velocity components encountered in the buckling nucleation phase. We observe also that the region of maximum velocity is significantly smaller during this phase, compared to the buckling phase.

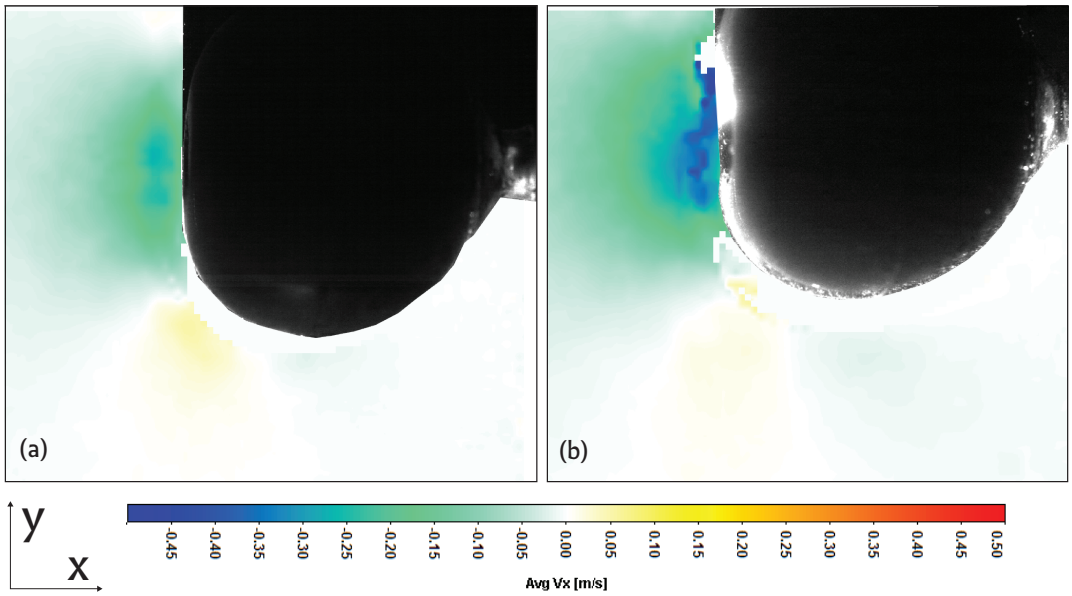

Figure 4.14: Time-averaged x-component of velocity during unbuckling phase: (a) in water;(b) in glycerol. Averaging done over a duration of $\approx$ 15 ms, (d/R)=0.22 shell.

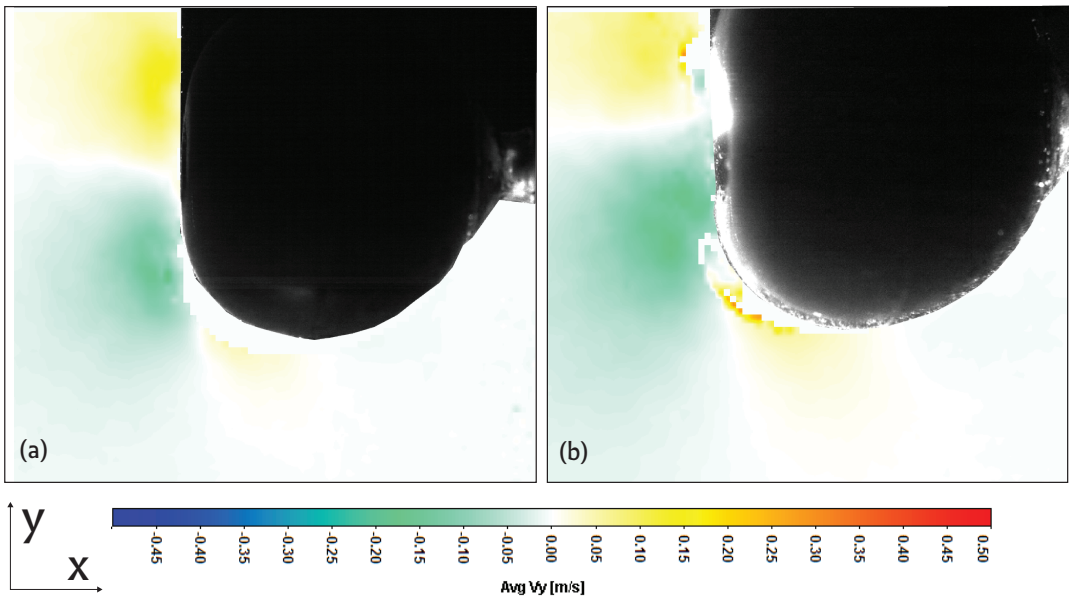

Figure 4.15: Time-averaged y-component of velocity during unbuckling phase: (a) in water;(b) in glycerol. Averaging done over a duration of $\approx$ 15 ms. (d/R)=0.22 shell.

4.3.1.1 Undulation phase

Unlike the buckling where we clearly see a periodic deformation of the membrane after the buckling, the unbuckling is followed by a phase where the front of the ball stretches forward, triggering a wave created at the bottom that travels forward then comes back as we showed in figure 3.14, in the chapter about shell dynamics. This undulation creates moving sources of compression and depression which induce a complex non-periodic flow, but overall, velocities encountered during this process stay very low with an order of magnitude of cm/s.

4.3.2 Summary

We will end this section by reminding the key observations:

1. Buckling nucleation phase produces similar flows in water and glycerol and induces the highest velocities. Flow is mainly axial during this phase.

2. It is followed by shell oscillations which produce synchronous axial flow during inward and outward shell deformation, in water. In glycerol, flow is axial during inward deformation and radial during outward deformation. Overall, this asymmetry makes more fluid converge toward the shell in glycerol compared to water.

3. Re-inflation induces a diverging flow concentrated on a narrow frontal region synonym of small accelerated fluid mass.

4. Results show the 3D axis-symmetry nature of the flow.

4.4 Effect of reduced thickness

We discuss here, the effect of the shell geometry through the study of the x-component of the velocity, which corresponds to the axial direction of shell deformation. We consider the temporal evolution of the averaged axial velocity during deflation* over the region illustrated in figure 4.16. Results are shown in figure 4.17.

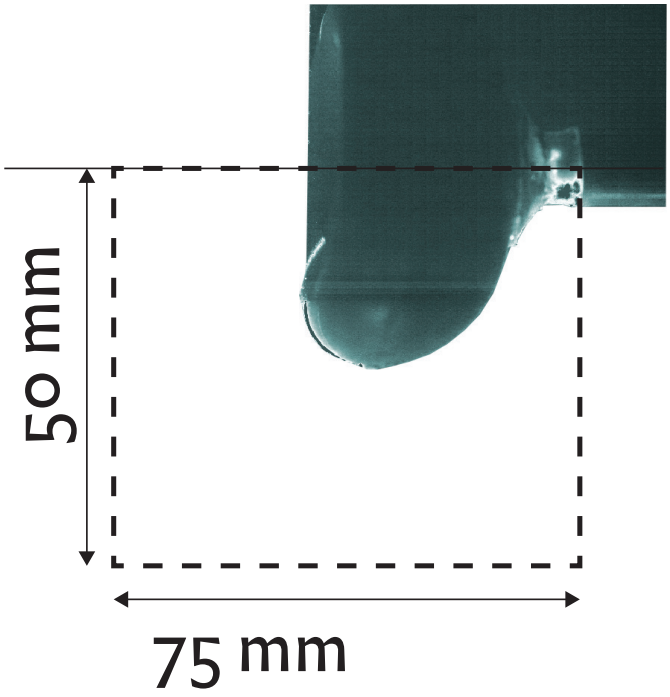

Figure 4.16: Frame where spatial averaging is performed.

*We will provide information on the temporal evolution of the averaged transverse velocity in the Appendix.

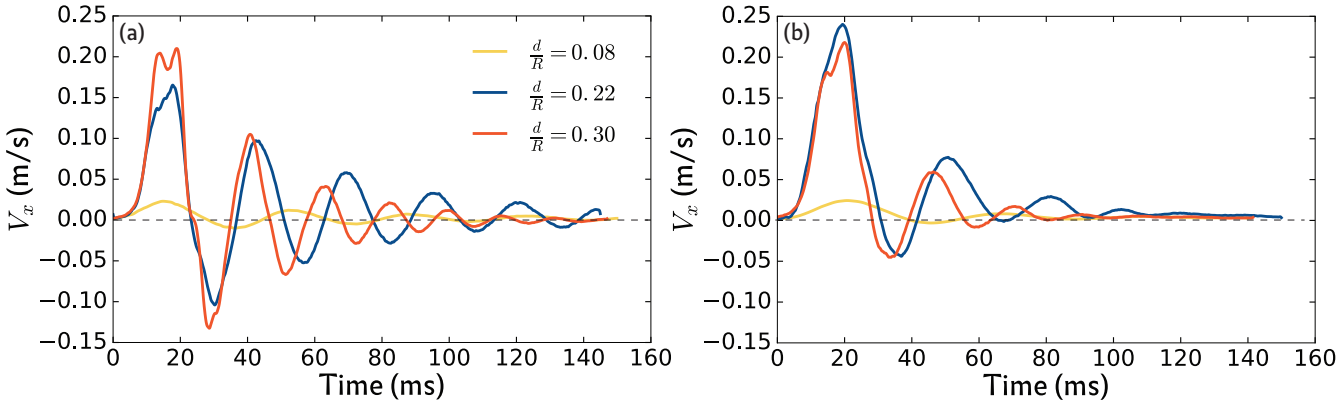

Figure 4.17: Temporal evolution of the x-component of velocity averaged spatially over a common area for different (d/R): (a) In water; (b) in glycerol. Dashed lines are a guide highlighting the zero value.

In water, we observe that the x-component of the velocity oscillates around 0 and damps toward this same value, with a period $\simeq$ 30 ms for (d/R)=0.22. The temporal value is similar to the period measured in shell dynamic study (see sec.3.3).We observe that the absolute values of the amplitude are comparable for (d/R)=0.22 and (d/R)=0.30. However, for (d/R)=0.08 the amplitude is $\simeq$ 8 times smaller compared to the two thicker shells. This ratio was also observed when looking at the maximum deformation rate ($|\frac{dH}{dt}|$) calculated in section 3.3.

In glycerol, we observe that the x-component of velocity signal first oscillates around zero and damps toward this value with a period $\simeq$ 40 ms for (d/R)=0.22, but we notice that after one period the signal is completely positive. We observe that the absolute values of the amplitude are comparable for (d/R)=0.22 and (d/R)=0.30. The amplitude of (d/R)=0.08 stays $\simeq$ 8 times smaller compared to the two thicker shells.

We evaluated the extent of the velocity signal asymmetry in glycerol compared to water by integrating the signal over time. Table 4.1 shows that in both cases more fluid converges axially toward the shell's concavity than escapes from it. More importantly, the overall positive contribution is twice as high in glycerol compared to water independently from (d/R). These results confirm the qualitative description we made earlier in section 4.2.

(d/R)	Water	Glycerol
(d/R)=0.08	0.7	1.3
(d/R)=0.22	2.3	5.0
(d/R)=0.30	1.9	3.6

Table 4.1: Values of integrated x-component of velocity over time (250 ms) in water and glycerol in (m).

What can be retained from these results is that increasing the shell reduced thickness increases the quantity of the average flow transported during the deflation phase. This quantity is twice higher in glycerol compared to water independently from (d/R).

4.5 Effect of loss tangent

We saw in chapter 3.3 that material properties play a role in the instability dynamics through Young modulus E' and material dissipation E''. The parameter that includes both parameters is the loss tangent $\tan\delta = \frac{E''}{E'}$. To explore the impact of this parameter on the flow dynamics, we performed time resolved PIV measurement on two shells made of materials that present comparable Young modulus E', but have different dissipation.

To do so, we also looked at the evolution of the x-component of the velocity, averaged on a domain with constant area in water and in glycerol. Results are shown in figure 4.18.

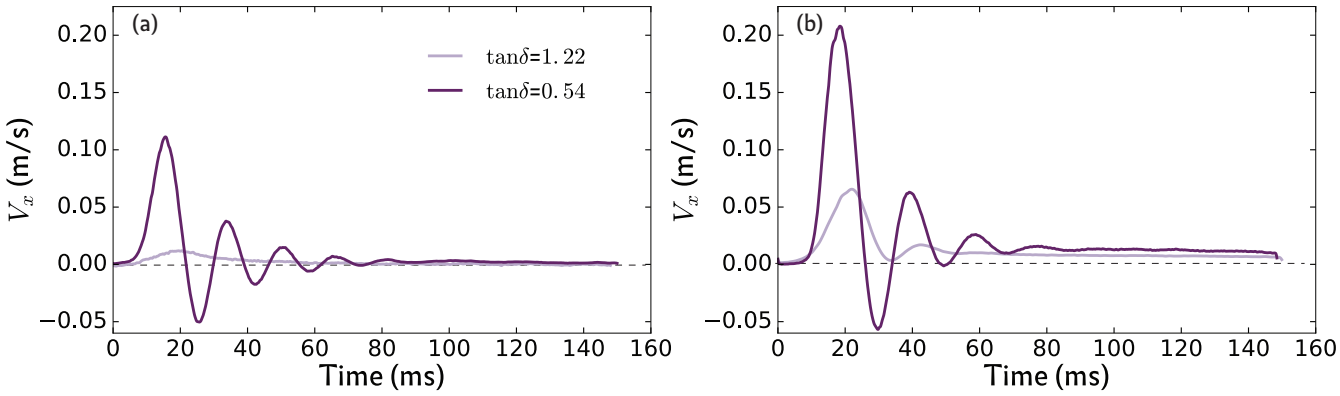

Figure 4.18: Temporal evolution of the x-component of velocity averaged spatially over a common area for different $\tan\delta$: (a) In water; (b) in glycerol. The dashed lines are a guide highlighting the zero value.

In water, we observe that the x-component of the velocity signal has a periodic nature, with oscillations around 0 for $\tan\delta = 0.54$, presenting a period $\leq$ 20 ms similar to the period measured in shell dynamic study (see sec.3.4.2). A qualitative difference lies in the heaving damping for $\tan\delta = 1.22$, no oscillations are observed, this is consistent with the observations done on the shell dynamics. The absolute values of the amplitude are significantly higher for $\tan\delta = 0.54$ than for $\tan\delta = 1.22$ with a ratio of the maxima $\simeq 6$ in favor of $\tan\delta = 0.54$. This ratio is almost two times higher that the one observed after calculating the maximum deformation rate ($|\frac{dH}{dt}|$) (see sec.3.4.2). The same observations can be made for the signals in glycerol except for an enhancement of the amplitude which is doubled for $\tan\delta = 1.22$ and for $\tan\delta = 0.54$. Integrals of the signals over time (see table 4.2) confirm the previous observations.

$\tan\delta$	Water	Glycerol
0.54	1.0	1.8
1.22	0.3	3.4

Table 4.2: Values of integrated x-component of velocity over time (150 ms) in water and glycerol in (m).

What can be retained from these results is that increasing the shell rebound resilience from 0.45 to 0.65 changes completely the nature of flow structures and speeds up the flow dynamics, which is illustrated by the increase by 400% of the maximum velocity.

4.6 Interaction ranges

4.6.1 Axial interaction range

An important information to extract from the PIV measurements is about the distance on which the instability impacts the surrounding fluid. This information provides an idea of the distance at which the flow structure could be disturbed and impacted by for example, the presence of an obstacle or another swimming shell.

In this purpose, we extracted the spatial evolution of the x component of the velocity along the symmetry axis of the concavity at the moment where it reaches its maximum amplitude, during the first inward deformation. Results are shown in figure 4.19.

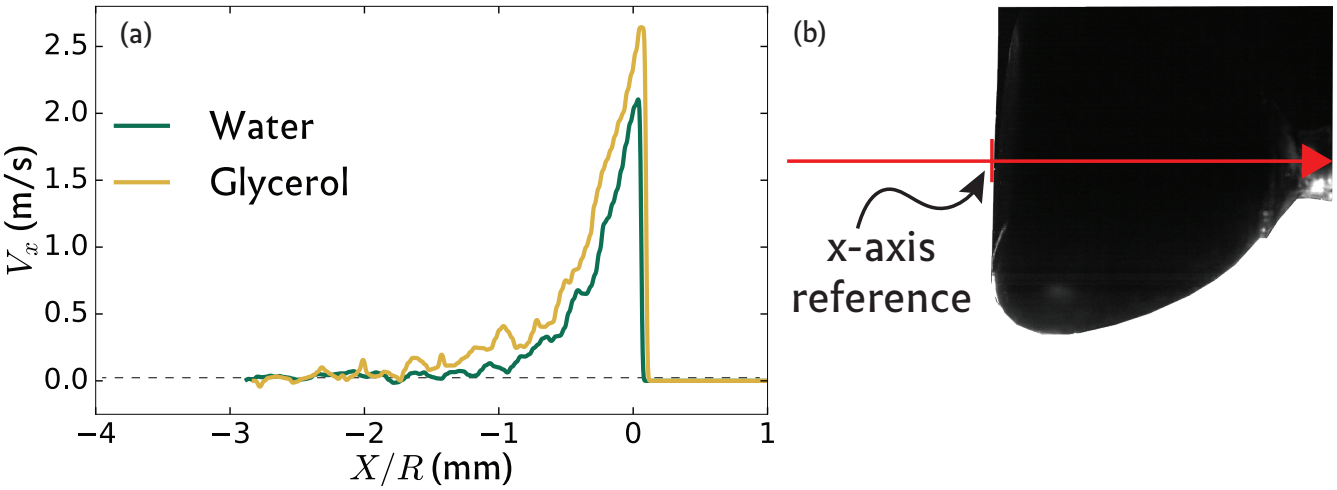

Figure 4.19: (a) Spatial profile of x-component of velocity along the axial direction in water and glycerol. Dashed lines are a guide highlighting the zero value. (b) Direction of the velocity profile with a zero reference that signals the limit of the fluid domain. Results using shell (d/R)=0.22.

We observe that independently from the liquid viscosity, the velocity profile decreases rapidly with X/R. This decrease is characterized by a typical length of $0.6R$ [*]. The flow is completely damped at a distance of $2R$. The fact that this distance is very similar between water and glycerol suggests that this interaction distance is determined purely from the shell deformation properties such as the depth of the concavity.

4.6.2 Transverse interaction range and shear wave

We iterated the same operation but this time along the vertical direction, passing through the flank. Results are shown in figure 4.20.

[*]determined as the intersection point of the x-axis with the curve maximum tangent line.

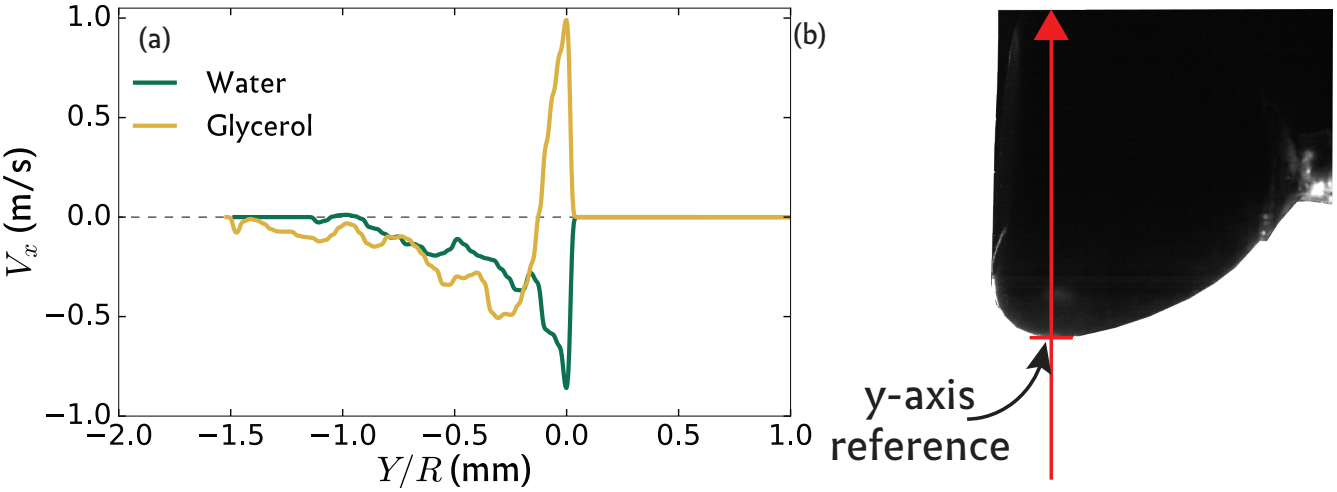

Figure 4.20: (a) Spatial profile of x-component of velocity along the vertical direction in water and glycerol, during first inward oscillation. Dashed lines are a guide highlighting the zero value. (b) Direction of the velocity profile with a zero reference that signals the limit of the fluid domain. Results using shell (d/R)=0.22.

In water, we observe that the velocity profile stays negative and converges toward zero, reached at a distance close to R. Meanwhile, in glycerol, velocity profile alternates between a positive and a negative value and converges to zero at a distance $\simeq \frac{3}{2}R$. When we looked at the evolution of this profile through time, we observed that the narrow positive peak widens and flattens during the inward deformation, and inverts during the outward deformation while keeping a positive and a negative contribution.

It may be useful at this point, to remind observations on the flow structures in water and glycerol: in glycerol, a vortex appears at the flank and moves toward the frontal concavity. From the results hold by fig.4.20, we can suggest that the axial motion of the flank shears the flow and is at the origin of this structure that we do not observe in water. This lead us to think that the vortex we observe is actually an indicator of a shear wave that is propagating away from the flank. This piece of information will be critical in the analysis of swimming results.

4.7 Summary

In this chapter, we described the flow structures created by the instabilities and how the viscosity of the surrounding fluid affects the flow. This generates a situation where the flow and the shell deformation are synchronous for water and asynchronous for glycerol.

We studied the effect of reduced thickness (d/R) and material properties on the flow dynamics. We concluded that both these parameters play a key role in determining the flow dynamics through their impact on shell dynamics.

We finished this chapter by studying the range for hydrodynamic interactions. We concluded that the typical characteristic length is R. We also illustrated the existence of a shear wave in glycerol that propagates away from the flank.

In the following chapter, we will consider both shell and flow aspects getting hints, about the swimming.

Experience is merely the name men gave to their mistakes.

Oscar Wilde

5 Swimming

5.1 Introduction

In the previous chapters, we showed how the shell dynamics is strongly influenced by the reduced thickness (d/R) and the loss tangent. We also showed that it is weakly dependent of the surrounding fluid viscosity. But when looking at the flow generated by the shell dynamics, we observed that the fluid viscosity plays an important role in determining the flow regime and the nature of the structures. We showed how history effects related to these structures modify qualitatively the flow during the shape oscillations.

In this chapter, we will see how these two dynamics interact in order to produce a non-zero displacement of a system composed of a shell (fully immersed) and a support (partially immersed) attached to a frictionless rail, over a cycle of pressure, as illustrated in figure 2.12.

When submitting the shell —attached to the system described in section 2.3 — to a series of internal pressure cycles, we observe displacements of the system during the phases of deflation and re-inflation that do not compensate on the whole cycle (see fig. 5.1). For a given shell, we show that the contribution of each phase depends on the viscosity of the medium, as illustrated in figure 5.1. In order to study this evolution, experiments were conducted in liquids with different viscosities spanning on 4 decades. In addition, the role of the reduced thickness d/R and of the loss tangent of the shell's material were investigated. In this chapter, the x axis direction is such that a positive displacement means a displacement of the buckling spot outward the shell.

To extract the displacement during the deflation, we calculated the difference between the position X_{ii} of the support after the deflation of a given cycle, and the position X_i preceding the deflation as highlighted in the zoomed region in figure 5.1. This operation is iterated through all cycles ($N_{cycles} \approx 20$), then the median of the sample is calculated, which defines the displacement after deflation in a given fluid viscosity. To estimate the error over the measurement, we took the maximum of the Median Absolute Deviation (MAD) of the displacement over all the viscosities explored. The same procedure was followed to determine the displacement during the re-inflation phase, but this time the displacement corresponds to the difference between the position of the support after the re-inflation X_{iii} and before it X_{ii} (see fig5.1).

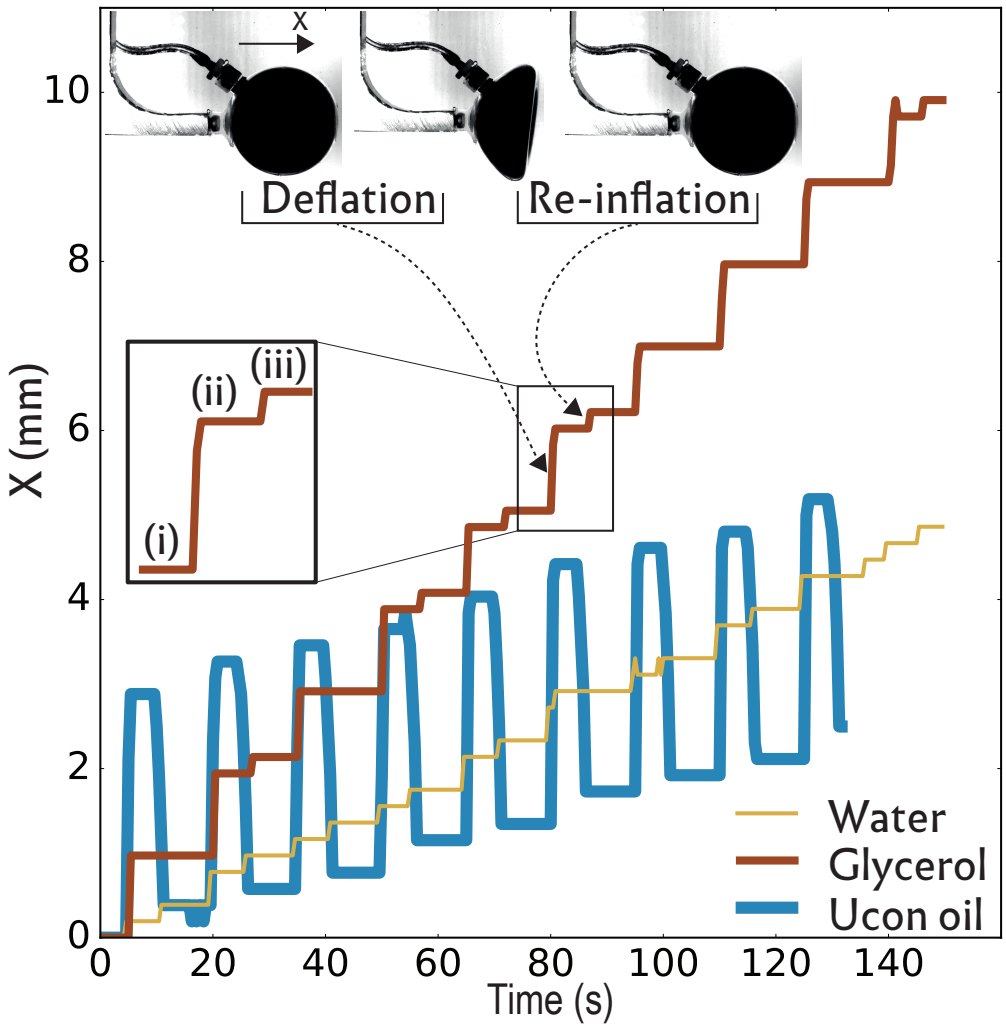

Figure 5.1: Displacement as a function of time of a shell with relative thickness d/R=0.22 in three liquids of different viscosities. Water ($\eta = 10^{-3}$ Pa.s), Glycerol ($\eta = 0.9$ Pa.s), Ucon© oil ($\eta = 37$ Pa.s). Pressure cycles of amplitude -600 to 0 mbar and period 15 s are applied. The zoomed region will be used later to explain the calculation of the displacement.

Note: These displacements are measured by tracking the edge of the support S to which the spherical shell is attached and do not correspond to the displacements of the center of mass of the system G, which varies during the deformation cycle.

The measure of the displacement at the point S and at the point G is equivalent when looking at the net displacement after a pressure cycle, but the displacement per phase (deflation/inflation) is different when taking the reference at the point S instead of the point G. The support and the truck to which the shell is attached weight $M{=}\approx$ 1.6 kg and constitute the rigid non-deformable part of the system

with a center of mass G_1.

In contrast, the shells have a mass M which lies between 11 g and 40 g, forty times less than the rigid part of the system. This means that the center of mass of the system is very close to G_1. When the shell is spherical, the system's center of mass is shifted by 1.4 mm at most. If we model the shell post-buckling as being half a hollow shell of a thickness of two times the shell before buckling—which overestimates the shell deformation—, the center of mass shifts closer to G_1 by at most 0.25 mm. This means the measure of the displacement after deflation is overestimated by at most 0.25 mm. The measure of displacement during after inflation is by opposition underestimated by 0.25 mm at most.

To extract the net displacement per cycle (displacement due to deflation and re-inflation), we calculated the difference between the initial position of the support and the final position of the support, divided by the number of cycles performed in-between. There are two contributions to the error over the measure of the net displacement, the first one is the edge detection error fixed at the pixel size and the second contribution is due to the precision of the horizontal alignment of the rail which may displace the truck. The sensitivity of the experimental setup to the horizontal alignment increases when the viscosity decreases, and special care was taken to cancel this effect by measuring the drift of the support at rest, and tuning the micro-metric slide until reaching a drift lower than 0.02 mm/s. Results of these experiments are summarized in figure 5.2.

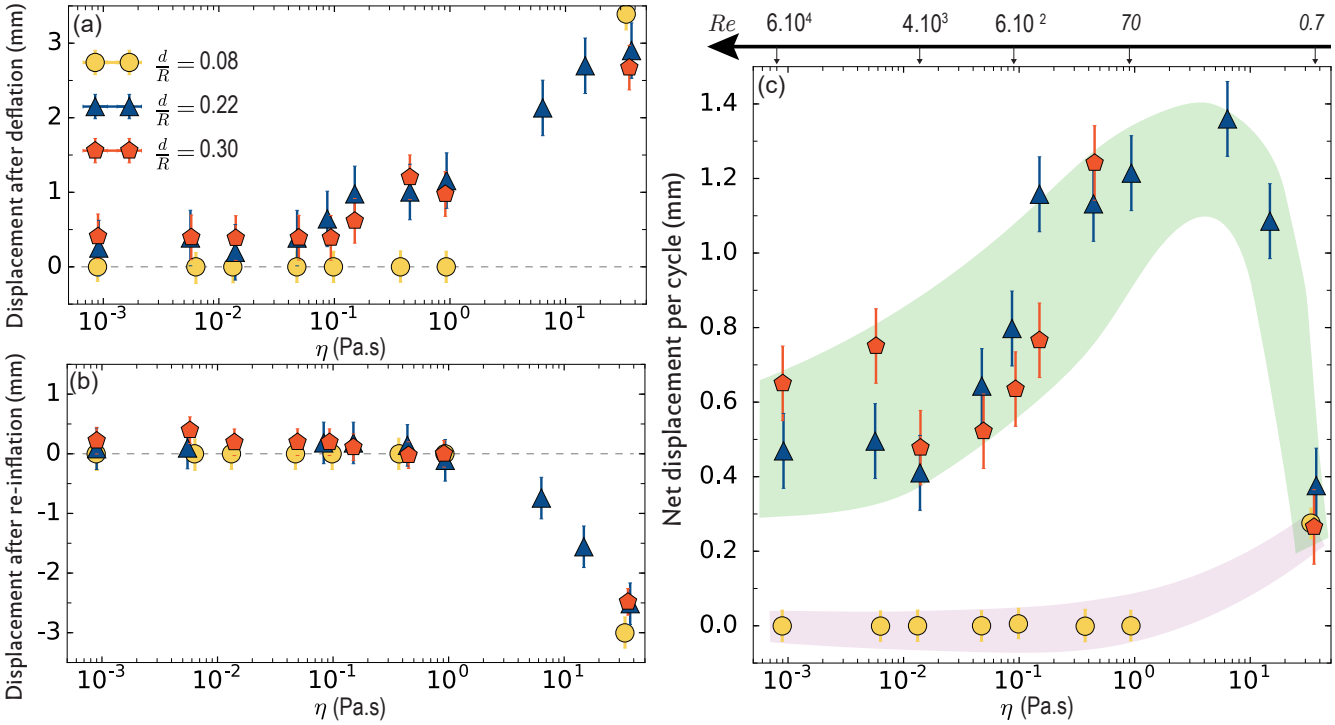

Figure 5.2: For 3 different (d/R) ratios: (a) Evolution with the fluid viscosity of the displacement of the shell support after one deflation sequence. (b) Displacement after re-inflation. (c) Total displacement after one deformation cycle. The indicated Reynolds numbers correspond to the $(d/R) = 0.22$ shell, Reynolds numbers for the shell of d/R= 0.3 are comparable, but Reynolds number corresponding to d/R=0.08 are 6 times smaller. Green (top) envelop highlights the high elastic energy regime while the low elastic energy regime is indicated by the pink (bottom) envelop.

5.2 Effect of the reduced thickness on the swimming

Deflation We observe that the displacement due to the deflation strongly increases when increasing the viscosity of the surrounding fluid. The displacement of thin shells is much smaller, when the viscosity is lower than 1 Pa.s, but when reaching a high viscosity, its displacement is similar to the displacement of shells with higher reduced thickness, denoting a transition in the swimming regime.

Re-inflation We observe that the displacement subsequent to the re-inflation is positive but small relatively to the one observed during deflation for low viscosities. It decreases when viscosity increases, and changes its sign for high viscosities. Furthermore, similarly to the deflation phase, we observe no

displacement due to re-inflation for the thin shell, until high viscosities are reached, where its displacement is comparable to shells with higher reduced thickness. In this regime, the re-inflation displacement —which contributes in the opposite way to displacement during deflation— is close in intensity to the displacement due to deflation.

Net displacement The consequence on the net displacement per cycle —shown in sub-figure (c)— is that its evolution in respect with the viscosity is not monotonous, *i.e* it presents a maximum at a viscosity around 1 Pa.s. In addition, we notice that the net displacement is always positive even at high viscosities.

In order to understand these results, we need to link together the shell dynamics to the fluid dynamics. We established in the previous chapters that the maximum fluid velocity V_b during the buckling is similar in water and glycerol, as is the deformation of the shell $H(t)$, and we noticed that:

$$V_b = 2\max(\frac{dH}{dt}) \tag{5.1}$$

Using this velocity, we define a fluid Reynolds number as:

$$Re = \frac{\rho_f V_b R_{ext}}{\eta} \tag{5.2}$$

Using the Reynolds number allows us to link previous observations with the flow regimes.

At low fluid Reynolds number ($Re = 0.7$ for Ucon oil of viscosity 37 Pa.s), when viscous effects outmatch inertia, displacements are important in both phases (deflation and re-inflation), but they almost compensate within one cycle, with a final displacement of around 1% of the radius. In this Stokes regime, the displacement is quite similar for all shell thicknesses, as is the sequence of shapes (as illustrated in fig. 3.10 of the chapter about shell dynamics).

On the opposite end of the viscosity range ($Re = 6.10^4$ for water), both phases induce a positive displacement, with a higher contribution from the deflation phase*.

The displacement is much smaller in the case of thinner shells. Both previous observations are qualitatively consistent in this regime with an inertial thrust due to the acceleration of the fluid in the vicinity of the buckling/unbuckling area. The accelerated fluid volume is linked to the size of the concavity. As we saw in the chapter about shell dynamics (see fig.3.13), the size of the concavity is much larger during the buckling compared to the unbuckling. In addition the size of the concavity increases strongly with the reduced thickness (d/R), which means that thinner shells accelerate a much smaller volume, explaining why it does not results in significant thrust at high Re.

Interestingly, the Stokes regime is the most efficient one for thin shells that are not able to store enough elastic energy to propel in the inertial regime. On the contrary, for thicker shells, a maximum net displacement is reached for an intermediate Reynolds number. This points to the need of understanding how the swimming of the system is linked to the fluid dynamics explored through particle imaging velocimetry. To do so, we measured the displacement of the system during the deflation with a high temporal resolution and compared it with the evolution of the fluid velocity field acquired through PIV measurement. Results are shown in figure 5.3.

*The reasons why re-inflation induces a positive displacement are still under investigation.

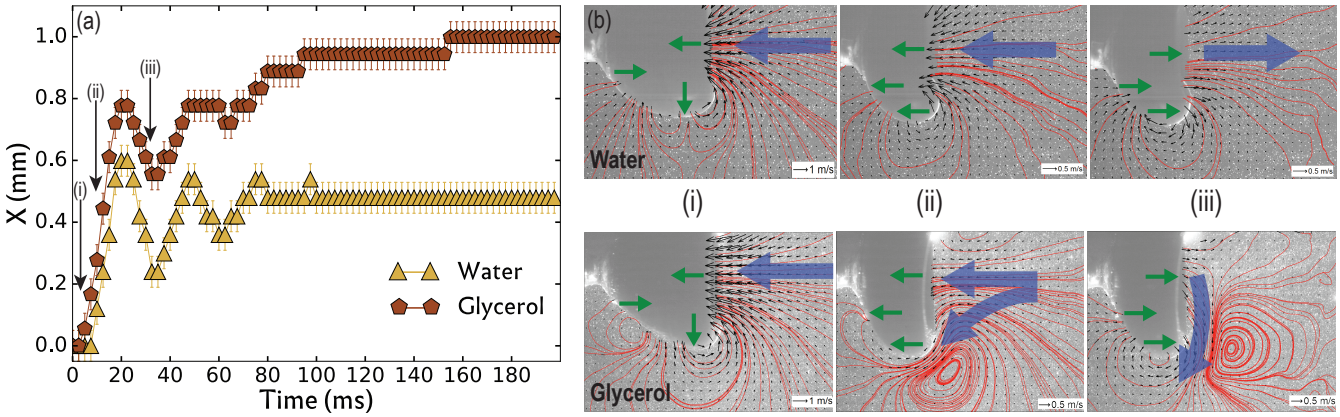

Figure 5.3: Shell with $d/R = 0.22$ undergoing deflation:(a) Displacement of the system as a function of time in water and glycerol; steps (i) to (iii) are indicated on the deformation curve of Fig. 3.16-b. (i) and (ii) correspond to the initial inwards collapse and (iii) to the first outward oscillation (b) Stream lines and velocity field during the shape oscillations, in water and in glycerol. Blue arrows indicate the main flow patterns. Arrows inside the ball indicate the main deformation direction at the front, the bottom and the flank.

The main observation we can extract from figure 5.3 is that, in water, the buckling induces a displacement of the moving support that oscillates in a synchronous way with the shape, and damps toward an average position. Whereas a different scenario is drawn in glycerol, the system moves forward even during shape oscillations until damping to a final position.

To understand this difference, we need to decompose the buckling phase into sub-phases, according to the shell deformation. Decomposition follows this thread:

First, during the nucleation of the concavity, *i.e* phase (i), the system moves in the positive direction at the same pace in both liquids. This similarity is also found when looking at flow patterns, which consist of two depressions created at the front and the bottom and a compression at the flank (as displayed by green arrows in fig.5.3). This configuration creates a flow converging from the flank towards the depression zones. Kinematic quantities *i.e* velocity and acceleration are also comparable in both liquids.

After 15 ms, the shell's concavity reaches its final width (introduced as C in 3.4). This marks the beginning of the phase (ii) where the shell starts an inward deformation. We observe an increase of the system's velocity in glycerol compared to the velocity of the system in water, leading ultimately to a displacement 20% larger in glycerol. To understand the reason of this difference, we need first to look

at the effect of shell deformation —common to both liquids— on the flow which consists of an inward deformation resulting in a frontal depression, a compression at the bottom and axial displacement at the flank (see green arrows on fig.5.3-(b)).

In water, the depression at the concavity sucks in liquid upfront. Liquid converges toward the concavity also from the bottom. The axial displacement which shears the flow locally does not appear to affect the global flow.

In glycerol, the flow upfront converges toward the concavity but a tangential flow near the flank escapes from the concavity and is tangential to the boundary condition (flank+bottom of the shell) during shell deformation. This latter shears the flow and cancels the converging flow from the rear that we see in the water sequence.

The latter flow configuration happens to be more efficient, since it accelerates more the flow axially.

In both liquids, the displacement reaches a first local maximum when the inward shell deformation stops. This local maximum corresponds to 150% of the final displacement in water, compared to 78% of the final displacement in glycerol.

During the outward deformation (phase (*iii*)): in water, the system moves backwards until reaching a minimum, with a peak-to-peak amplitude of 0.4 mm. In contrast, this amplitude is twice smaller in glycerol.

The displacement afterward keeps oscillating around an average position, while in glycerol, the displacement of the system does not follow anymore the oscillating nature of the shell deformation.

This difference can be understood from the flow structure during the first outward shell deformation (phase (*iii*)). We see that in water, the flow is reversed and is symmetrical to the configuration observable in phase (*ii*). This alternating behavior continues further during the remaining shape oscillations.

In opposition, in glycerol, the effect of the shear flow at the flank created in phase (*ii*) still has an effect during the outward deformation. As a result, the expelled fluid out of the concavity is not directed towards the x axis but is accelerated radially. It does not contribute to the inertial axial acceleration, which lowers the backward displacement (see phase (*iii*) in Fig. 5.3-(a)). Consequently, displacements

due to oscillations do not annihilate each other as in water, but contribute, thanks to the delay effect we identified, to a positive displacement that lasts more than 100 ms (Fig. 5.3-a).

Delay effect may be characterized by the Womersley number Wo, defined as $Wo^2 = R^2 \frac{\rho_f \omega}{\eta}$, that compares the oscillation period with the viscous damping time. In the classical Stokes problem of an oscillating plate with frequency ω in a viscous liquid shear waves propagates in the normal z direction with a wavenumber k and a damping e^{-kz}, where $k = \sqrt{\rho_f \omega/(2\eta)}$ [Batchelor, 1967]. At a given distance R, the shear waves are damped at high Wo due to a high wavenumber. On the opposite, they are in phase with the plate at low Wo where the damping tends toward 1 imposing the synchronicity of the shear wave with the displacement boundary condition. For intermediate values of $Wo \simeq 1$, the waves are nor damped nor synchronized. In our case, the phase shift gives rise to the complex pattern observed in glycerol. Indeed, in glycerol, $Wo \simeq 8$ while in water $Wo \simeq 300$. Furthermore, since $V_b! \simeq R\omega$, $Re \simeq Wo^2$ in our configuration, and we may conclude that the interplay between inertial non stationary dynamics and viscous damping of shear waves will always take place at an intermediate Reynolds number regime, and in this case results in an enhancement of the thrust during deflation.

5.3 Effects of the solid dissipation on the swimming

In the previous chapters, we showed how the shell dynamics is strongly influenced by the solid dissipation or loss tangent $\tan\delta = \frac{E''}{E'}$. Quantitatively, we showed that the tangential loss determines the deformation rate with a maximum value around 0.3 m/s for a shell with $\tan\delta = 1.22$ and 1.4 m/s for a shell with $\tan\delta = 0.54$. Buckling for a shell with $\tan\delta = 0.54$ is followed by damped oscillations whereas an over-damped regime is observed in the case of $\tan\delta = 1.22$. Such a different behavior, should have consequences on the swimming and its efficiency.

To study the impact of the loss tangent over the swimming, we performed frictionless rail experiments using the two shells previously introduced and we varied the surrounding fluid viscosity over 3 decades. Results are summarized in figure 5.4. The methodology previously presented was followed to extract displacement data and error estimation.

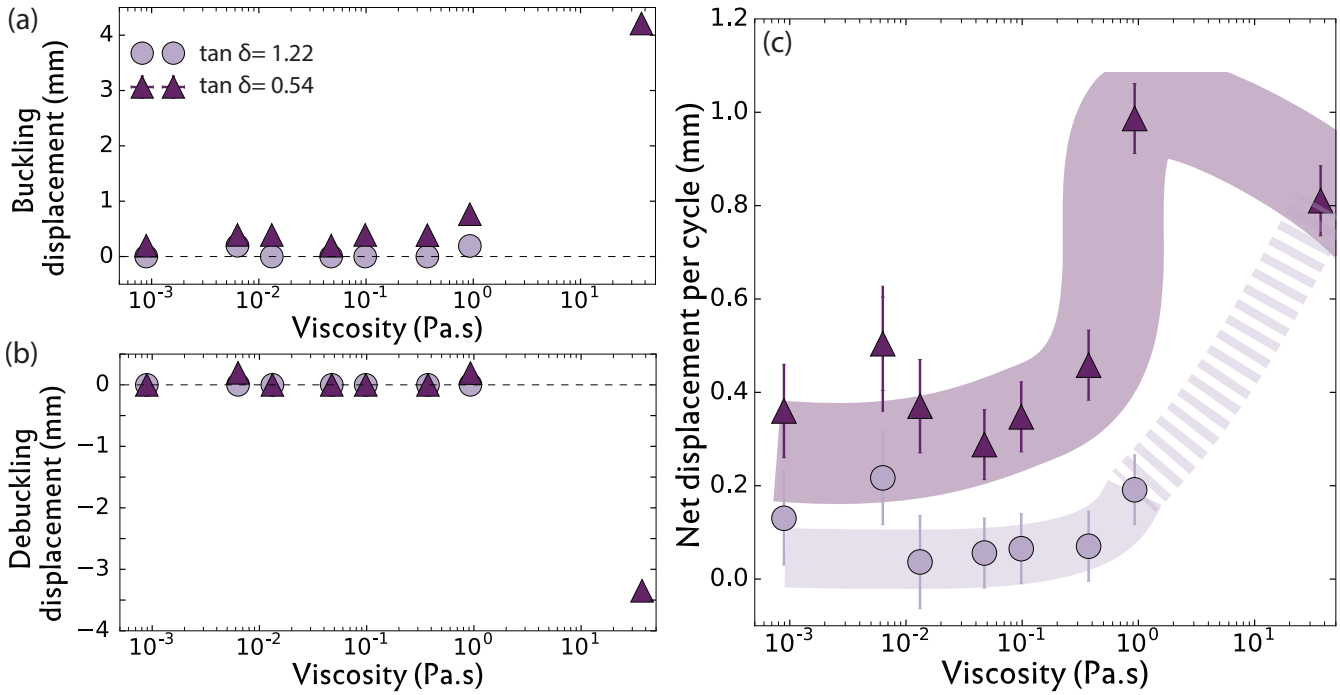

Figure 5.4: Displacements for different $\tan\delta$: (a) Evolution with the fluid viscosity of the displacement of the shell support after one deflation sequence. (b) Displacement after re-inflation. (c) Total displacement after one deformation cycle; dark violet (top) envelop highlights the low loss tangent net displacement while the high loss tangent net displacement is indicated by the light violet (bottom) envelop with an extrapolation of its value for η=37 Pa.s . Shells with a Young modulus $E \approx$2 MPa and $d/R = 0.08$; dashed lines represent the zero reference.

From figure 5.4-(a), we observe that the displacement induced by the buckling is positive and increases with viscosity, reaching a value 4 times higher in glycerol (η=1 Pa.s and $Re \approx$75) compared to water (η=10^{-3} Pa.s and $Re \approx 7.10^4$) and 20 times higher in Ucon oil (η=37 Pa.s and $Re \approx$1) compared to water.

The shell with higher loss tangent has a displacement that remains small until a viscosity of 1 Pa.s is reached which corresponds to $Re \approx 10$.

During unbuckling (see fig.5.4-(b)), we notice that for both shells no significant motion is produced on a wide range of viscosity and becomes important but negative at large viscosities.

Overall, a higher net displacement per cycle (see fig.5.4-(c)) is achieved by the shell with $\tan\delta = 0.54$. To illustrate this observation, we may focus our attention on the net displacement at η=1Pa.s: the ra-

tio between the displacement of the shell with $\tan\delta = 0.54$ is close to 6 compared to the shell with $\tan\delta = 1.22$, similar to the ratio of the mean axial velocities of the flow for these two parameters (see sec.4.5), while the ratio of tangential loss is around 0.45. This emphasizes the strong role of the loss tangent parameter on swimming efficiency.

5.4 Discussion

In order to propagate our comprehension of swimming through shell buckling from the restricted range of parameters explored above to a wider scale, we need to answer to this question: how do these parameters affect the swimming efficiency? In our case, shape deformations and their dynamics are mainly imposed by the reduced thickness and loss tangent and depend weakly on the surrounding fluid viscosity. The main kinematic quantities to be affected are: the buckling speed V_b, the frequency of shape oscillations ω, and their damping coefficient τ_f.

In chapter about the shell dynamics, we introduced a toy model (section 3.5) to get a full picture of how shell deformation and its dynamics evolve with these parameters, and we found that if the surrounding fluid does not influence the shell dynamics, the post-buckling frequency obeys:

$$\omega \simeq \zeta \frac{1}{R}\sqrt{\frac{\Delta P_C}{\rho}}\sqrt{\frac{E'(\omega)}{E}}, \tag{5.3}$$

with $0.3 < \zeta < 0.4$. ρ holds for the shell material volume mass. The buckling speed V_b obeys:

$$V_b \simeq \chi \sqrt{\frac{\Delta P_C}{\rho}}\sqrt{\frac{E'(\omega)}{E}}, \tag{5.4}$$

with $0.4 < \chi < 0.9$. Those narrow inequalities allow to estimate the buckling velocities and post buckling frequency from the sole knowledge of E' without that of E. This opens discussion for the possible scaling between microscopic systems and macroscopic ones without having to precise where the solutions ω and V lie exactly in the established ranges. Using these equations we determine the relevant dimensionless numbers: the Reynolds number, the quality factor $Q_f = \omega\tau_f$ which has been shown to

determine the shell dynamics in the fluid, and the Womersley number which is crucial to understand swimming enhancement during shape oscillations*.

Considering $\rho_f \simeq \rho$ and using Eq.(5.4) and (5.3), the scalings for these dimensionless numbers are:

$$Re \simeq 0.4 \frac{R}{\eta} (\rho \, \Delta P_C)^{1/2}$$

and

$$Q_f \simeq 0.1 \frac{d}{\eta} (\rho \, \Delta P_C)^{1/2}$$

with a prefactor $\simeq \sqrt{E'(\omega)/E}$. In addition, when $Q_f > 1$:

$$Wo^2 \simeq Re$$

Minimization Our ultimate purpose is to make artificial micro robots that achieve propulsion based on buckling mechanism. For this, we suggest to use colloidal armored bubbles as microswimmers activated by ultrasonic waves. To identify the regime in which such microswimmers would effectively lie, we use the three dimensionless numbers presented above.

For a shell of radius 10 μ m, and considering that at maximum $\Delta P_c = 1$ bar to avoid cavitation by the ± 1 bar pressure wave, Re can be as large as 40. Additionally, Eq. 5.3 shows that, as ω scales as R^{-1}, miniaturization down to the micron makes ω jump to the MHz. Usual values of compliance for elastomers [Lakes, 2009] indicate that the prefactor $\sqrt{E'(\omega)/E}$ raises Re by one order of magnitude. Microscopic shells then can swim in the intermediate Re (and Wo) regime where inertial thrust is enhanced by the coupling between flow and shape oscillations. Besides, this happens at frequencies compatible with sonographic devices that have already shown to induce repeated buckling on armored bubbles [Marmottant et al., 2011b].

*These quantities are derived from a toy model which assumes the existence of a damped oscillatory regime, and thus its usage is not relevant in the case of over-damped regime illustrated with the shell "'S121"'.

A microscopic shell would be controlled by variations of the external pressure while the macroscopic model used to obtain results shown previously relies on a an internal pressure control. In section 3.3, we compared quantitatively the shell deformation dynamics produced on the macroscopic model with a internal and an external pressure control, and we deduced that the main difference in the dynamics is the oscillation mode following the buckling instability (cf. see 3.3), which most probably changes the flow pattern during this phase. Apart from that, both ways of pressure control produce deformations with a similar order of magnitude in buckling velocity and oscillation frequencies. Based on these elements, we can extrapolate in the following, what would be the displacement at smaller scale.

At low Reynolds number, we saw that the motion is purely due to the sequence of shapes, which is quasi similar for both ways of controlling the pressure (Fig. 3.10-a). We may forecast that the result of 1% of R per cycle also holds for a microscopic shell.

At higher Reynolds number the inertial thrust due to fluid acceleration comes into play. The involved volume of fluid is given by the loss of shell volume $\Delta\mathcal{V}$ during buckling, which is limited by the resistance of the inner gas to compression. However, we showed that to the first three orders in d/R the volume loss in our macroscopic experiment can be considered as equal to the volume loss when the external pressure is controlled (see 3.2.3). This is due to the fastness of the buckling process, during which the enclosed gas has no time to escape so as to maintain the required pressure. Hence, our conclusions for the inertial regimes drawn from the macroscopic experiments should also apply when closed microscopic shells undergo deflation/re-inflation cycles with external pressure control.

A microswimmer submitted to an ultrasonic wave of amplitude ΔP_C and driving frequency ω_d will swim under the condition that $\omega_d < \omega$, where ω is the post buckling spontaneous frequency of the shape oscillations, so as to let time to the material to react to pressure variations. While the displacement per cycle is rather low, the high frequency that is allowed thanks to the fast activation due to the instability may lead to high velocities. We find that swimming velocity is at most equal to $U_s = 0.01R \times \omega/(2\pi)$ (the Stokes case). With $\omega_d \simeq \omega \simeq 1$ MHz, this potentially leads to a net velocity $\sim 1500R$ per second, that is 15 mm/s for a $R = 10$ μm shell, much faster than that of Janus particles

(10 μm/s [Paxton et al., 2004]), helicoidal microrobots (10 μm/s [Peyer et al., 2012]), microrobots with acoustically activated flagella (50 μm/s [Ahmed et al., 2016] to 1 mm/s but for much larger swimmers [Kaynak et al., 2017]), microrobots propelled by metachronal waves (3 μm/s [Palagi et al., 2013]), or living spherical microswimmers like Chlamydomonas Reinhardtii (50 μm/s [Garcia et al., 2011]). Recently, armored bubbles set into motion by acoustic streaming were found to swim at 1 mm/s [Bertin et al., 2015].

A microscopic shell designed in such a way that the buckling pressure is of order 1 bar (through an adequate choice of E and d) would even swim faster thanks to inertial effects amplified by the coupling between shape oscillations and flow patterns. In addition, we anticipate that this swimming amplification observed in the moderate Womersley number regime opens a path for active amplification by a fine tuning of the pressure cycle period, so as to make it comparable to the viscous decay time.

Active control in a compound of several spheres may be reached through playing on the wave amplitude (with strong non-linear on/off response depending on whether the buckling pressure is reached or not) and/or on the wave frequency, as discussed above. Two assembled spheres of different thickness may constitute a 1D robot. One swimming direction can be chosen by activating only the thin sphere at intermediate pressure, and the opposite direction will be activated by making the thick shell buckle at higher pressure, playing on the frequency in order to deaden for the thinner shell the delay effect that we saw to be the main point for swimming efficiency. Extension to 3D is straightforward: swimmers may be built using smart self-assembly properties of colloidal particles [Yang et al., 2008, Cademartiri et al., 2012, Yi et al., 2013], which opens promising possibilities for multi-directional remote control.

Swimming against buoyancy An interesting property to look at is the ability to swim against buoyancy in water. This amounts to estimate the swimmer critical size R at which the velocity due to buoyancy forces overcomes the swimming velocity.

In this situation, as Reynolds number associated to the swimmer would be small, we can estimate viscous forces following Stokes law. Viscous forces balance the buoyancy forces in the absence of swim-

ming thrust, which sets the maximum velocity as following:

$$U_{buoyancy} = \frac{2}{9}\frac{(\rho_f - \rho_s)g}{\eta}R^2 \tag{5.5}$$

where ρ_f and ρ_s correspond respectively to fluid density and swimmer density, g to the acceleration of gravity and R the swimmer radius.

If we take the minimum displacement that can be produced through a cycle of pressure, we can achieve a velocity $U_s = 0.01R \times \omega_d/(2\pi)$, with $\omega_d \leq \omega$ and $\omega \simeq \zeta R^{-1}\sqrt{\frac{\Delta P_C}{\rho}}\sqrt{\frac{E'(\omega)}{E}}$.

To evaluate at which size the crossover takes place, we need to make realistic assumptions on the different physical quantities: $\Delta\rho = (\rho_f - \rho_s) \simeq 500$ kg/m^3, and $\omega_d \simeq \frac{1}{3}\omega$ with $\omega \simeq 0.3R^{-1} \times 10$.

This allows to calculate a minor bound independent from R: $U_s = 0.01$ m/s.

We solve then:

$$R = \sqrt{\frac{9}{2}\frac{\eta}{\Delta\rho g}U_s} \tag{5.6}$$

Numerical application gives a minor bound crossover radius at $R \simeq 100$ μm, 10 times larger than the size of targeted microswimmers, which will most probably be able to swim against buoyancy.

5.5 Swimming near a wall

5.5.1 Introduction

In Nature, we can find multiple examples which illustrate the effect of the presence of a wall on the swimming of living organims that spans on a wide range of Reynolds number: from the circular orbit of *E. coli* [Lauga et al., 2006], or demersal fish and big water birds which use ground effect to increase the lift, decrease induced drag and even increase thrust in oscillating modes [Tanida, 2001, Fernandez-Prats et al., 2015].

In chapter 4.6, we showed that the frontal velocity field extends axially within a typical distance of $L \simeq \frac{R}{2}$. This implies that introducing an obstacle within this distance would disrupt the flow pattern and ultimately influence the swimming. Furthermore, understanding how the flow is influenced by the presence of obstacles, would *in fine* provide knowledge on how microscopic shells would behave inside pipes and how they would interact with each other in a compound.

5.5.2 Swimming results

To provide first insights, we performed a series of experiments using the frictionless rail setup and a shell of d/R=0.22 made in *Dragonskin*®30 material. We varied the distance between the shell and a wall and we measured the displacement during the deflation and re-inflation cycles. The shell was positioned such as to have its buckling spot facing the wall, which means that only the swimming direction normal to the wall was explored [*]. The reference for distance from the wall corresponds to the situation where the spherical shell is in contact with the wall as shown in figure 5.5-(a).

Figure 5.5-(b) shows that when a shell gets closer to the wall, the absolute value of the displacement induced by the deflation and re-inflation increases rapidly.

[*]Full study of the wall influence on swimming would require to vary the angle between the swimming axis and the wall, and ideally having 3 degrees of freedom (two translations and one rotation) in order to grasp this interaction. Such complex study would require another experimental setup.

The displacement is positive during deflation which means that the system moves toward the wall, and is negative during the re-inflation but keeps a smaller absolute value (at most, half the displacement during deflation).

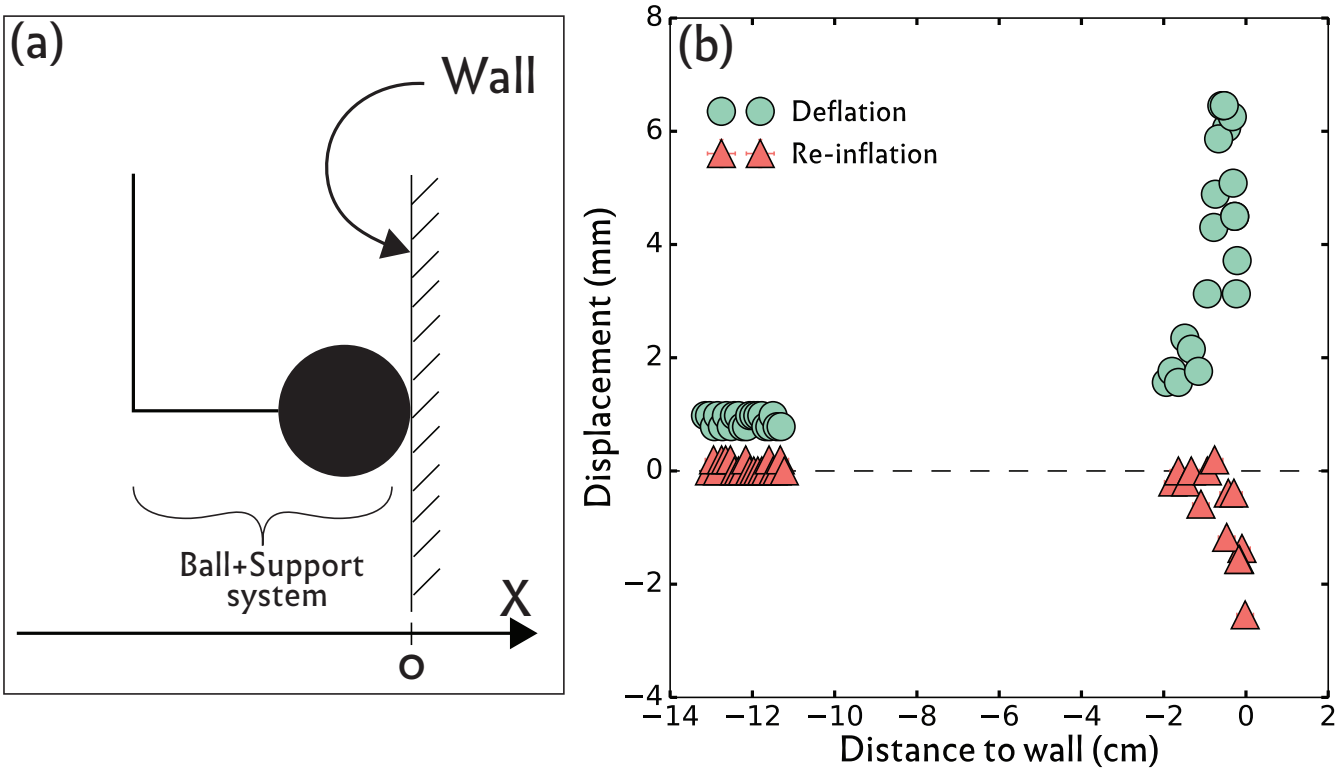

Figure 5.5: (a) Schematics explaining the reference choice for the distance from the wall which corresponds to the distance between the wall and the front tip of the shell in its spherical configuration. (b) Evolution of the displacement during deflation and re-inflation as a function of the distance from the wall for a shell of d/R=0.22 in glycerol.

This behavior is present on a wide range of viscosities as illustrated in figure 5.6, where we notice first, that independently from viscosity, the displacement during deflation begins to be influenced by the presence of the wall at a typical distance $X \simeq R$, as predicted from the flow pattern. The second observation we can make is that displacement amplification near the wall decreases with viscosity. Indeed displacement near the wall can reach almost 9 times the displacement far from the wall in water, whereas it is only 3 times at most for *Ucon*®oil.

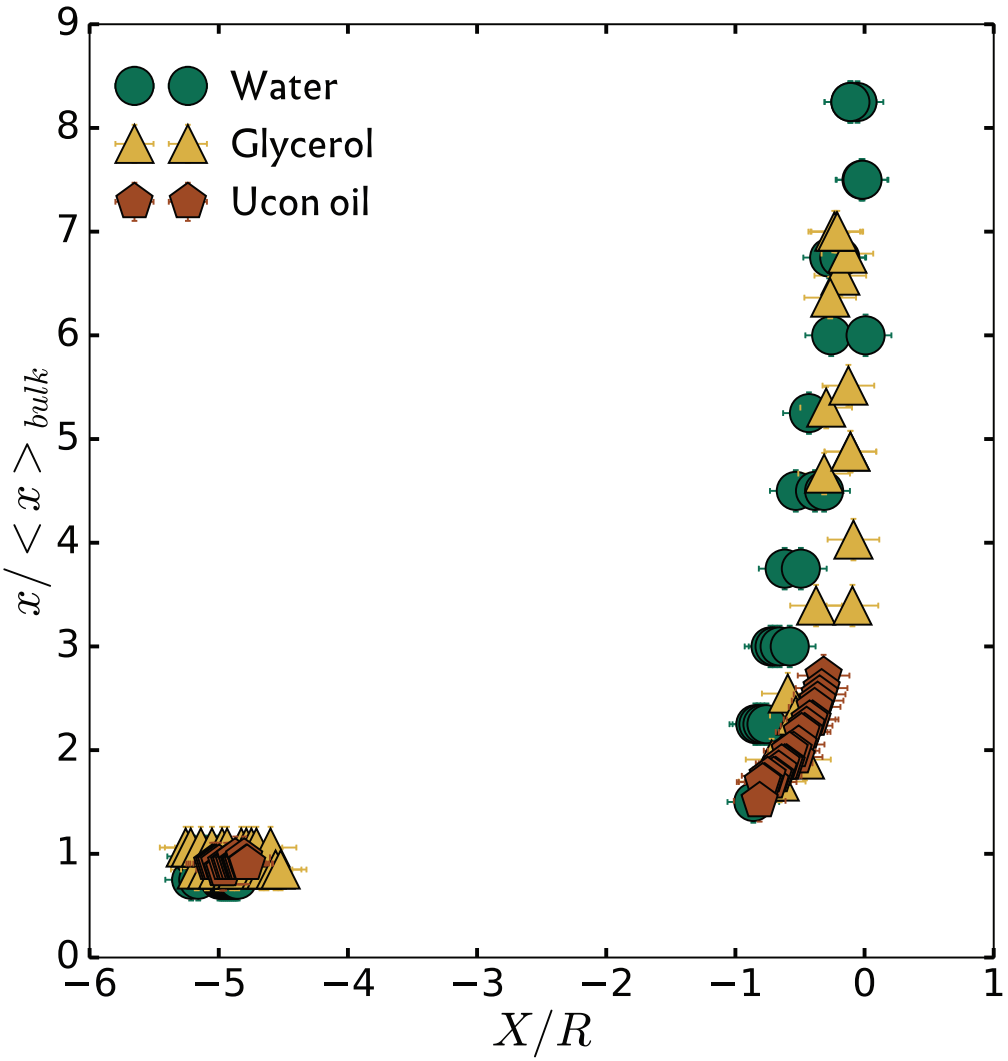

Figure 5.6: Displacement as a function of distance to wall during buckling in three different liquids with viscosities spanning over 4 decades. The displacement x is reduced by the mean displacement far from the wall called $< \quad x \quad >_{bulk}$, and the distance to wall is reduced by the shell external radius. The shell used is made of *DragonSkin*®30, and with a reduced thickness d/R=0.22.

To quantify this viscosity effect, we fitted the displacement as a function of the absolute value of distance to the wall as following:

$$x(X) = C \exp^{(-\frac{X}{L})} + < x >_{bulk} \tag{5.7}$$

To illustrate the observations above we plotted the evolution of the main fit quantities with respect to the viscosity as shown in figure 5.7. We observe that there is an amplification at high viscosities by a

factor of four. Swimming amplification increases with increasing inertial effects. The relaxation length L stays constant at $L \simeq 0.4R$ over a large interval of viscosity.

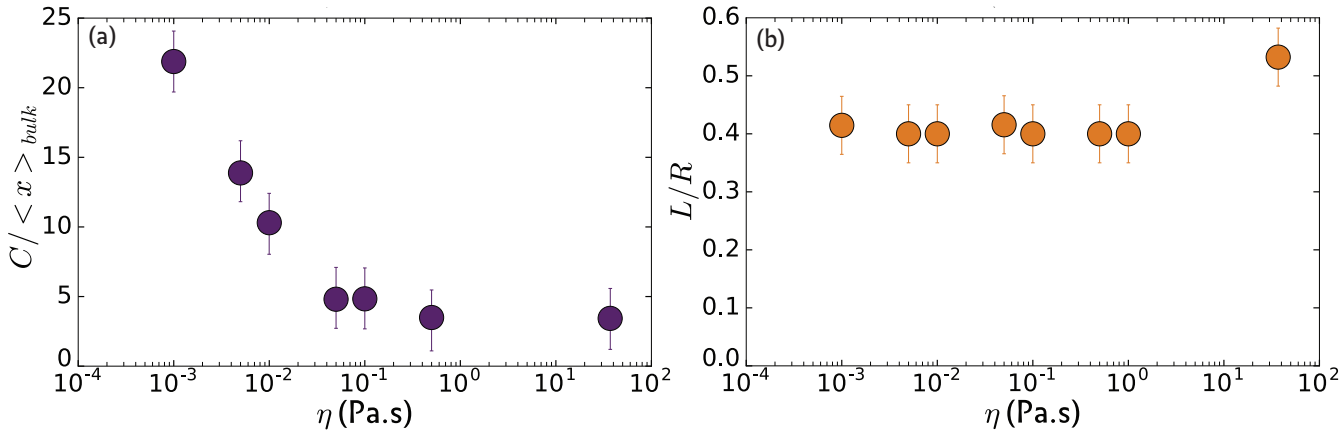

Figure 5.7: (a) Evolution of the leading fit coefficient C in respect with the fluid viscosity reduced by the mean displacement during deflation far from the wall. (b) Evolution of the fit relaxation length L reduced by the external radius of the shell R_{ext}=0.025 m. Measurement obtained with a shell of d/R=0.22.

5.5.3 Investigation of the flow near the wall

Previous results show that the presence of a wall in the vicinity of a shell swimming toward it enhances the displacement during deflation and re-inflation cycles. This paragraph aims at understanding the mechanism behind the amplification effect. The presence of a wall may increase the swimming efficiency by two means: either by increasing propulsion or by decreasing drag effects. This second hypothesis is probably not valid: a sphere sedimenting toward a wall is slowed down in its vicinity. We showed that enhancement is strong at high Re and decreases when Re decreases. We described the swimming mechanism at high Re as being pressure driven, which may lead to the conclusion that adding a wall enhances primarily pressure effects. To investigate the effect of the wall on the flow, we put a rigid wall at 5 mm in front of a spherical shell itself kept fixed to a support, which means no degree of freedom is allowed. We conducted time-resolved PIV measurements and extrac! ted the velocity field.

We show in figure 5.8 an illustration of how the flow induced by the buckling is affected by the presence of the wall. We observe that far from the wall the flow is mainly collected in the axial direction and this flow forms a uniform velocity front at the concavity entrance. Near the wall however, the flow is collected in the transverse direction mainly, with maximum velocity zones located at the flanks labeled as A and minimum velocity encountered on the axis of symmetry labeled as B.

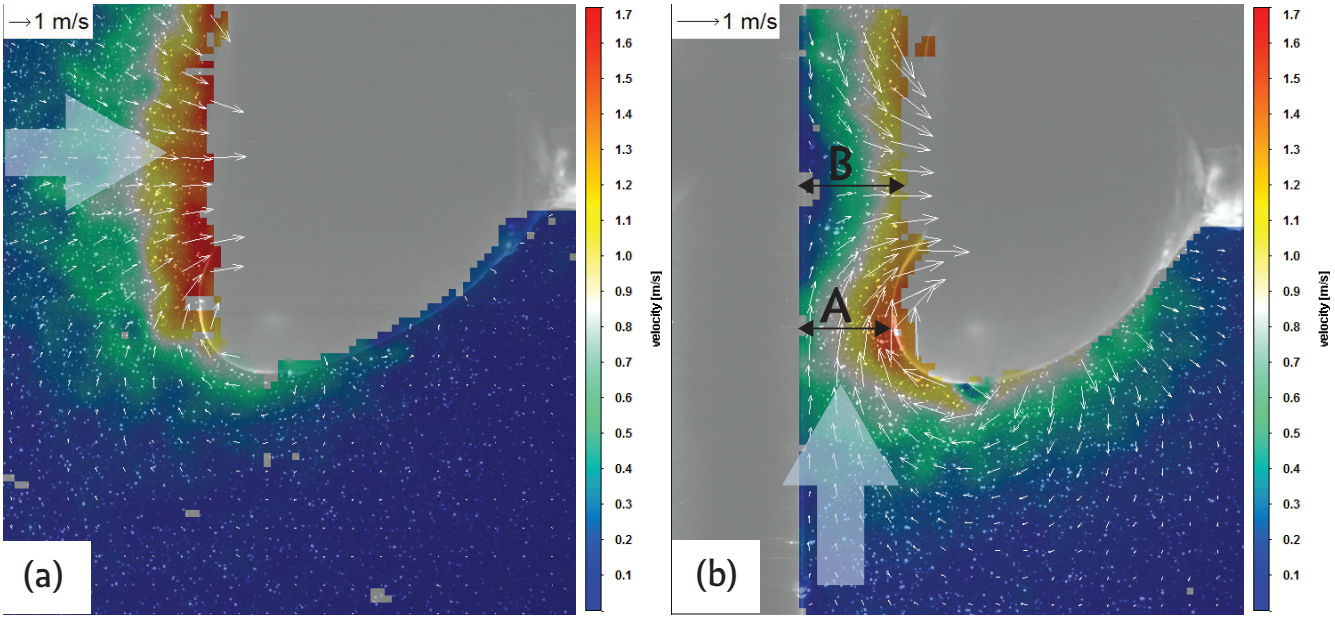

Figure 5.8: Typical velocity field in two configurations: (a) Velocity field in the bulk. (b) Velocity field near the wall, A and B regions are discussed in the text. PIV measurements in (b) are performed at 5 mm from the wall. PIV measurements in (a) and (b) are conducted in water.

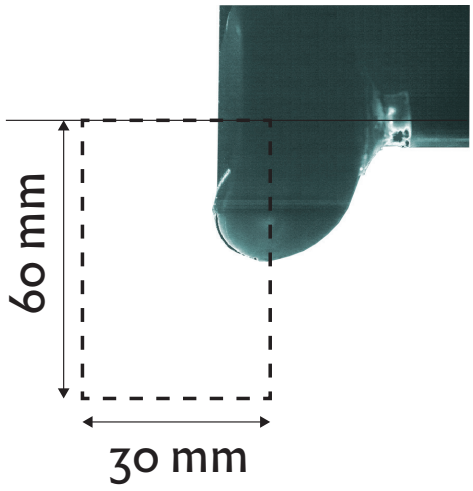

Figure 5.9: Illustration of the frame where spatial averaging is performed.

To quantify how the two velocity components of the flow evolve in both configurations (far from the wall and near the wall), we looked at the evolution in time of spatially averaged quantities on the region illustrated in figure 5.9. It clearly appears that the x-velocity component near the wall is smaller than its equivalent far from the wall (see fig 5.10-(a)). In opposition, the y-velocity component near the wall is larger than its equivalent far from the wall(see fig 5.10-(b)). When comparing the axial and transverse velocity components in the bulk we can see that they are comparable in intensity, but near the wall the axial velocity component of the flow is smaller than the y-velocity component by a factor four in terms of maximum amplitude [*].

To quantify these qualitative observations, we integrated the absolute value of the signal over time and results summarized in table 5.1 strongly confirm earlier observations.

position	Integral(V_x) (m/s)	Integral(V_y) (m/s)
Bulk	5.2	5.0
Wall	2.3	8.0

Table 5.1: Values of integrated velocity components over time.

[*]We notice that the oscillation period is comparable but near wall signals shift to the right compared to bulk signals, which means that the oscillation period increases over time. We still don't have a proper explanation for this effect.

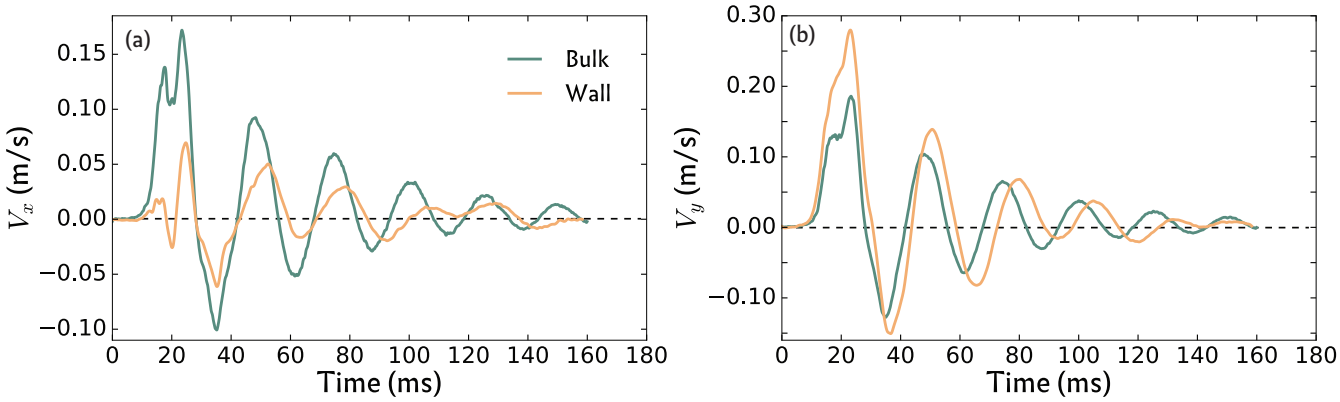

Figure 5.10: Spatial averaging of velocity components over time: (a) Evolution of x-velocity component over time. (b) Evolution of y-velocity component over time. Measurement far from the wall denoted by the the green line (dark) labeled *Bulk* and at 5 mm from the wall denoted by the the yellow line (light) labeled *Wall*

Once these puzzle pieces put all together, a physical interpretation to the displacement enhancement near the wall during the buckling emerges: when the buckling nucleates, available fluid upfront being limited, a strong transverse flow converges towards the concavity center by passing through the flanks where the section (labeled as A in figure 5.11) is the narrowest and the intensity of the velocity is maximum. This region should then correspond to a depression zone.

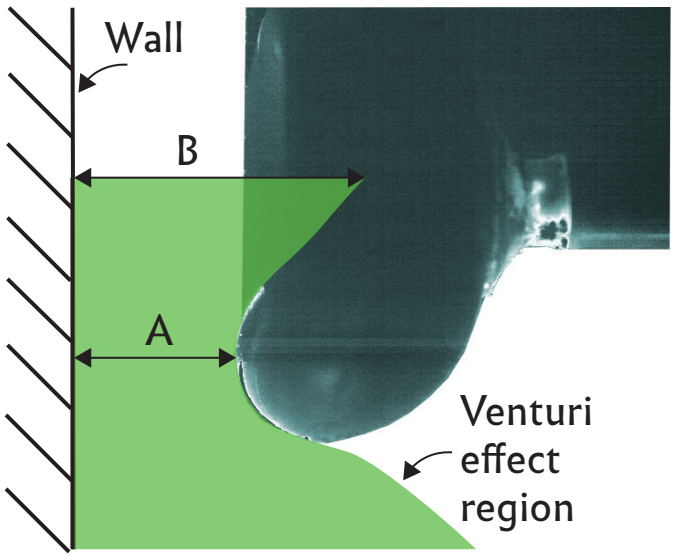

Figure 5.11: Illustration of the zone where Venturi effects take place.

To prove the presence of a strong depression between the wall and flanks, we calculated the pressure Laplacian to highlight the regions of high pressure and low pressure. It is obtained by taking the divergence of Navier-Stokes equation:

$$\partial_i \partial_t v_i + \partial_i v_j \partial_j v_i = -\frac{1}{\rho} \partial_i \partial_i p + \partial_i f_i + \nu \partial_i \partial_j \partial_j v_i \tag{5.8}$$

The first term on the left side of the equation and the last term on the right side of the equation are equal to zero due to the non-compressibility of the flow: $\partial_i v_i = 0$.

Since the flow is submitted to gravitational volume forces, the divergence of these forces has also a divergence equal to zero. Equation 5.8 the allows to calculate the pressure gradient from the knowledge of the velocity space derivatives.

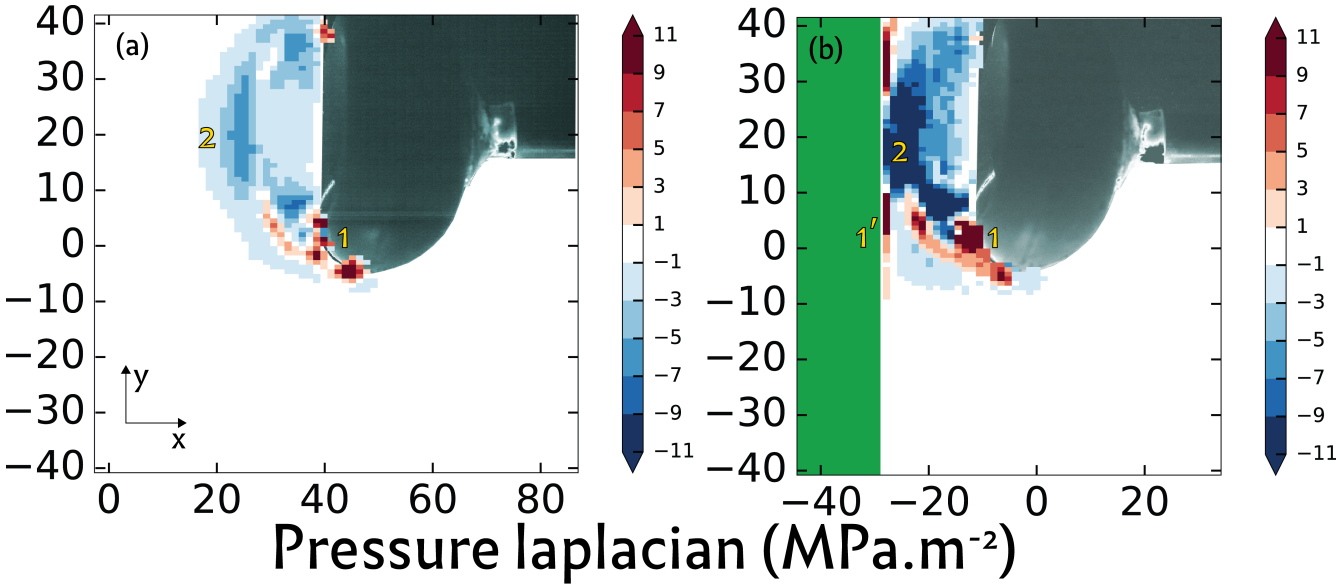

Figure 5.12: Pressure Laplacian averaged over buckling nucleation and first inward deformation: (a) In the bulk. (b) near the wall.

From the PIV measurements, we averaged the velocity field over the first stage of deflation (buckling nucleation and first inward deformation) and we calculated in both configurations the Laplacian of pressure from the measure of time averaged deformation and vorticity. Results are shown in figure 5.12.

We notice that in both configurations, a zone of low pressure is attached to the shell flanks (labeled by *1*). This depression is however stronger in the presence of the wall. Furthermore, another depression is attached to the wall at the narrowest section (labeled as *1'*). We also notice that in front of the concavity (labeled 2) a region of over-pressure attached to the wall is created due to the convergence there of opposite flows constituting a stagnation point. In the situation where the shell can move along the axial direction and is placed close enough from the wall, the strong depression at the flanks and wall has a *suction cup* effect which attracts the shell toward the wall. Then the closer it gets the more it "'feels"' the surpression attached to the wall, which *in fine* stops the shell at a given distance from the wall.

5.6 Summary

We showed in this chapter that shell buckling does indeed produce motion in liquids. This motion depends strongly on the reduced thickness (d/R) and on the loss tangent $\tan\delta$.

We also showed that swimming is influenced by the fluid viscosity which affects the flow pattern generated during the instability: swimming at high Reynolds number is dominated by pressure effects while shear effects dominates the swimming mechanism at intermediate Reynolds number which increase the efficiency due to history effects. Independently from reduced thickness or loss tangent, shells produce the same displacement at low Re; this is due to the fact that in this regime motion is governed by the sequence of deformations only, which do not depend much on shell parameters.

thanks to a toy model for the instability dynamics, we quantified the main quantities for the dynamics of buckling of microscopic shells actuated by ultrasound waves, and showed that we can expect reasonably high swimming velocities reaching 15mm/s for a shell of 10 μm radius.

Next, we showed that the presence of the wall in front of the buckling concavity enhances displacements during deflation and re-inflation. This phenomenon was then explained considering the Venturi

effect which creates depression zones between the shell's flanks and the wall. This pressure effect is therefore expected to be smaller in lower Reynolds regime, which is proved in figure 5.6.

All these results allow us to draft the profile of the optimal swimmer: it would be a shell made of a material that has a low loss tangent factor, whose dimensions are such that d/R is inferior to 1/3. The Young modulus has to be high enough to maximize elastic stored energy without exceeding a buckling critical pressure of 1 bar.

This seals the swimming chapter. We will present next thrust results from spring experiments and compare them to frictionless rail results.

One who treads a path in search of knowledge
has his path to Paradise made easy by God.

The Prophet Muhammad

6

Thrust

6.1 Introduction

After studying the swimming of shells submitted to internal pressure control, we want to compare these results to what we would obtain in the case of an external control of the pressure, which is the pressure control method closest to what should happen when ultrasound activates a microshell.

We showed in sec.3.3 similarities in terms of shell dynamics between both methods of pressure control, characterized by the deformation rate and frequency of the post-buckling oscillations. Still, for given material and (d/R), the instability produced through external pressure control has faster dynam-

ics. Since flow dynamics during buckling/unbuckling is closely related to shell dynamics, we can expect a higher efficiency with an external pressure control.

To settle this debate, we quantify experimentally the thrust obtained in both configurations during the whole deflation period in the case of viscous regimes. Then we estimate the thrust during the buckling phase where viscous efforts and drag are negligible compared to inertial efforts.

6.2 Integrated thrust during deflation

In the following, experiments were conducted in glycerol for three reasons: first, the inertial regime expected in swimming macroscopic experiments is not reachable, in water, at microscopic scale. Second, swimming in glycerol produced the highest net displacement, as shown in the chapter about swimming. Third, the viscous drag in glycerol is linear with the velocity. This will allow us to integrate analytically and determine the thrust. Results presented in the following concern a shell of (d/R)=0.22 made of *Dragonskin*®30.

6.2.1 Thrust with external pressure control

Performing frictionless rail experiments with an external pressure control is technically not achievable (as explained in sec.2.3.1). We used the spring experimental setup presented in sec.2.2.1 to extract the thrust during the buckling instability.

From images recorded during the deflation phase (at constant external pressure P=Pb), we extract the volume and the position of the center of mass of the shell and also the position of the connection point with the spring, at each time step.

Figure 6.1 shows the evolution in time of the displacement of the center of gravity $Y_g(t)$ relatively to its position when the shell is at rest($P = 0$).

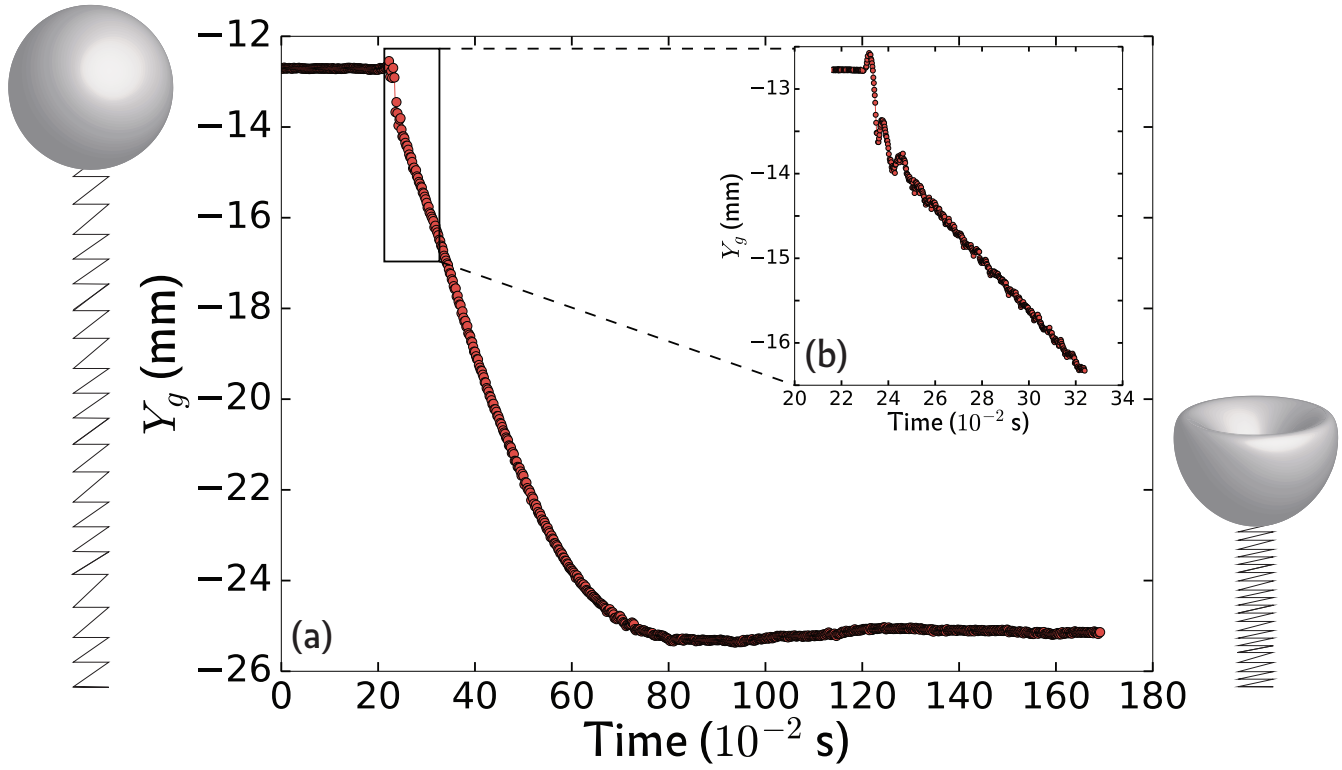

Figure 6.1: (a) Evolution in time of the center of mass of the shell during deflation. (b) Zoom over the framed region where buckling occurs. On the left side, an illustration of the shell-spring system before deflation. On the right side, the system state after deflation.

We observe that the system transits from one state of equilibrium to a lower state of equilibrium through damped oscillations. We observe in the zoomed region, that the center of mass goes up a for 5 ms achieving a displacement 0.25 mm before while it should be going down due to volume decrease and spring tension. Then, it oscillates shortly (30 ms) while decreasing steadily. These oscillations are induced by the shell pulsations following the buckling. During buckling, comparison between the displacement of the bottom of the shell Y_s —application point of the spring force— and the displacement of the mass center shows that the position of the center of mass has a frequency twice higher than the frequency of the bottom position, due to the deformation mode of the shell (see sec.2.2.1). Eventually, the center of mass continues decreasing after the end of shape oscillations until the new state of equilibrium.

The fact that the center of mass went up at the beginning of the instability shows the presence of a force pulling the shell up that lasts at least for few milliseconds, high enough to overcome the rapid

decrease in volume and the spring force. This is the force that we will quantify. We will call it $\vec{F_b}$. In order to do so, we need to quantify the remaining unknown force: the viscous friction force $\vec{F_v}$, since the spring force $\vec{F_s}$ and the volume forces $\vec{A}$ (weight and buoyancy force) are already known. In this purpose, we made the hypothesis that this viscous force is linear with the velocity. In section 3.3, we showed that there is a weak retro-action of the fluid dynamics on the shell dynamics when $Q_f = \omega\tau_f > 1$, which is the case in glycerol, for the shell used here. This assumption allows to decouple shell dynamics from fluid dynamics, and easily apply fundamental principle of dynamics to the shell:

$$\vec{F_b} + \vec{A} + \vec{F_v} + \vec{F_s} = m\vec{a_g} \tag{6.1}$$

By projecting on the y axis:

$$F_b + \rho g V(t) - \alpha \dot{Y_g} - kY_s = m\ddot{Y_g} \tag{6.2}$$

With m the effective mass of the shell*, k the spring stiffness, α the damping coefficient, ρ the fluid density, g the gravitational acceleration and $V(t)$ the shell's volume. $V(t)$, $Y_g(t)$ and $Y_s(t)$ are quantities relative to their absolute value at (P=0).

6.2.2 Extraction of the viscous force

We suppose that after the end of shell deformation, $\vec{F_b}$=$\vec{0}$. We re-write 6.2:

$$\rho g V(t) - \alpha \dot{Y_g} - kY_s = m\ddot{Y_g} \tag{6.3}$$

In order to obtain an analytical solution, we can re-write 6.3 as:

$$\rho g V(t) - \alpha \dot{Y_g} - k(Y_g - r(t)) = m\ddot{Y_g} \tag{6.4}$$

with $r(t) = Y_g(t) - Y_s(t)$.

*m does not correspond to the mass of the shell only, it takes into account an added mas relative to the fluid mass moving with the shell.

Equation 6.4 gives:

$$\ddot{Y_g} + 2\lambda\dot{Y_g} + \omega_0^2 Y_g = \frac{\rho}{m} g V(t) + \omega_0^2 r(t) \tag{6.5}$$

With ω_0=$\sqrt{\frac{k}{m}}$ and λ=$\frac{\alpha}{2m}$

$V(t)$ and $r(t)$ are obtained from the shell shape analysis. A good fit of the experimental data is obtained with the following expressions (see fig.6.2):

$$V(t) = V_{inf}\big(1 - (1 - \frac{V_0}{V_{inf}})\exp(\frac{-t}{\tau})\big) \tag{6.6}$$

$$r(t) = R_{inf}\big(1 - (1 - \frac{R_0}{R_{inf}})\exp(\frac{-t}{\tau})\big) \tag{6.7}$$

With V_{inf} and R_{inf} being asymptotic values when $t \to \infty$ of $V(t)$ and $r(t)$ respectively.

The quantity τ is the relaxation time of the shell's shape, which continues to evolve slowly even after the end of Post-buckling oscillations.

These simple expressions allow to solve analytically equation 6.5. For this, we first need to solve the homogeneous equation:

$$\ddot{Y_g} + 2\lambda\dot{Y_g} + \omega_0^2 Y_g = 0 \tag{6.8}$$

which yields a solution Y_{hom} that depends on the sign of the discriminant Δ':

$$\Delta' = \lambda^2 - \omega_0^2$$

The two particular solutions associated with the $V(t)$ and $r(t)$ terms are:

$$Y_{part_v}(t) = C_1 + C_2\exp(\frac{-t}{\tau}) \tag{6.9}$$

where: C_1=$\frac{\rho g V_{inf}}{m\omega_0^2}$, C_2=$\frac{\rho g \Delta V}{m((\frac{1}{\tau})^2 - 2\lambda\frac{1}{\tau} + \omega_0^2)}$ and ΔV=$V_{inf} - V_O$.

$$Y_{part_r}(t) = D_1 + D_2\exp(\frac{-t}{\tau}) \tag{6.10}$$

where D_1=R_{inf}, D_2=$\frac{\omega_0^2 \Delta R}{((\frac{1}{\tau})^2 - 2\lambda\frac{1}{\tau} + \omega_0^2)}$

We observe experimentally (fig.6.1) that the vibration mode of the spring-shell system is a damped oscillation regime, which implies that:

$$\Delta' < 0$$

This gives a homogeneous solution of the shape:

$$Y_{hom}(t) = L \exp(-\lambda t) \sin(\omega t + \phi) \tag{6.11}$$

with ω=$\omega_0\big(1 - (\frac{\lambda}{\omega_0})^2\big)^{\frac{1}{2}}$.

Combining the particular solutions 6.9 and 6.10 with the homogeneous solution 6.11, yields:

$$Y_{general}(t) = Y_{hom}(t) + Y_{part_v}(t) + Y_{part_r}(t) \tag{6.12}$$

Equation 6.12 describes the time evolution of the center of mass of the shell, after Post-buckling oscillations. We fit the experimental data for Yg after the Post-buckling oscillations by expressions 6.10 with four free parameters: L, ϕ, m and α. The last two parameters are the one we are interested in. The result is shown in figure 6.2.

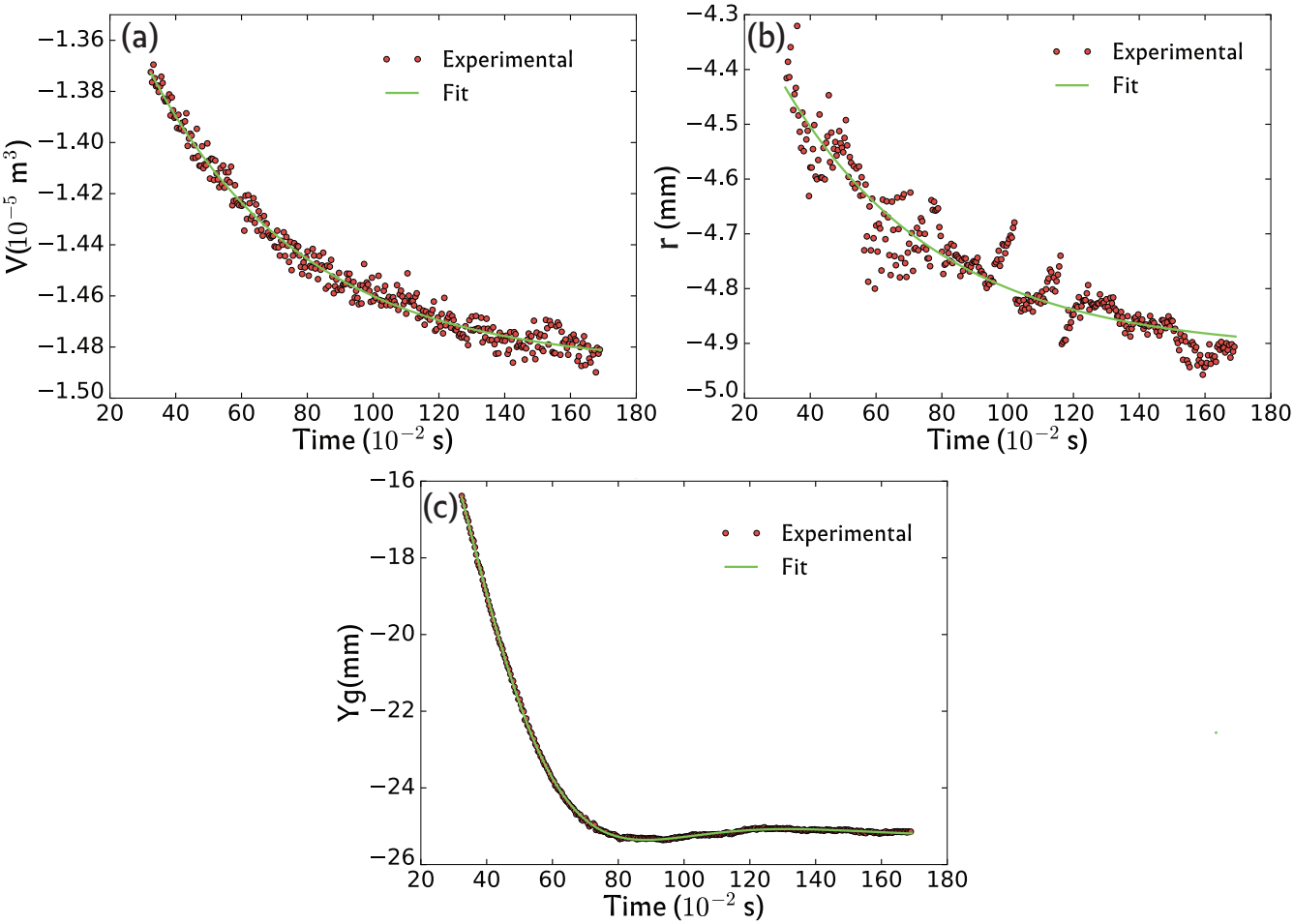

Figure 6.2: Fit of the quantities of interest after the end of post-buckling deformations: (a) Fit of the volume $V(t)$. (b) Fit of the deformation $r(t)$. (c) Fit of the displacement of the center of mass $Y_g(t)$, with $m \simeq 225$ g and $\lambda \simeq 3.9$ s^{-1}.

6.2.3 Extraction of the thrust during deformation phase

We assume that the damping coefficient α depends weakly on the shell shape and is thus equal to the coefficient determined in the previous section.

The thrust is determined by subtracting directly all the other forces as follows:

$$F_b = m\ddot{Y}_g - A + kY_s + \alpha\dot{Y}_g \tag{6.13}$$

Note During the transition between the convex shape and the concave shape, the exact shape is not known, a linear interpolation is performed to complete the experimental data.

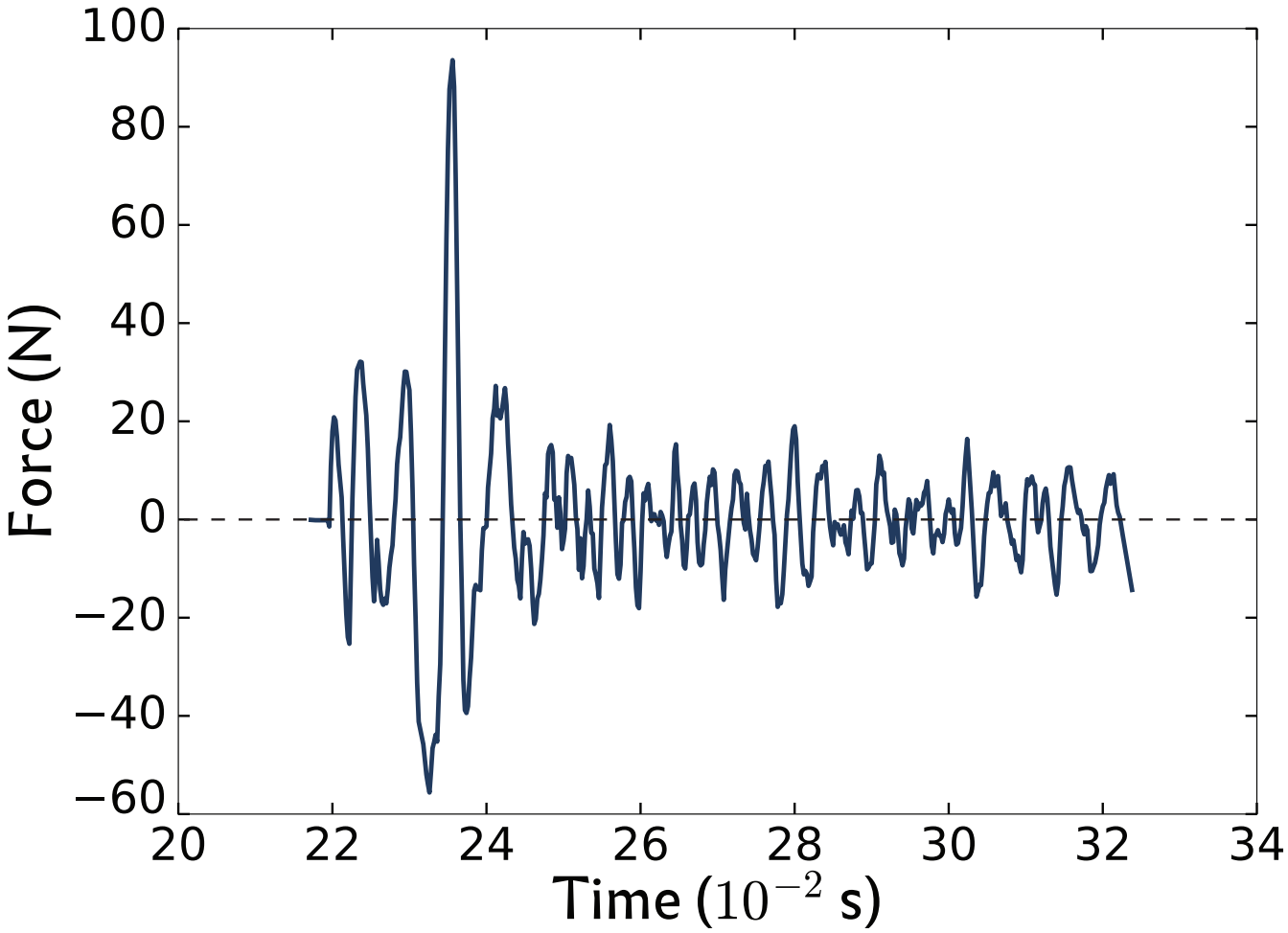

Figure 6.3: Evolution of the thrust $F_b(t)$ as a function of time

Figure 6.3 shows the evolution of the thrust. It shows a force oscillating with an amplitude that increases first then decreases to reach a noisy plateau. The maximum force reached during the buckling goes up to 80 N, with a period of 5 ms.

Now, we can define the integrated thrust as being the temporal integral of the thrust as follows:

$$\gamma(T) = \int_0^T F_b(t)\,\mathrm{d}t \tag{6.14}$$

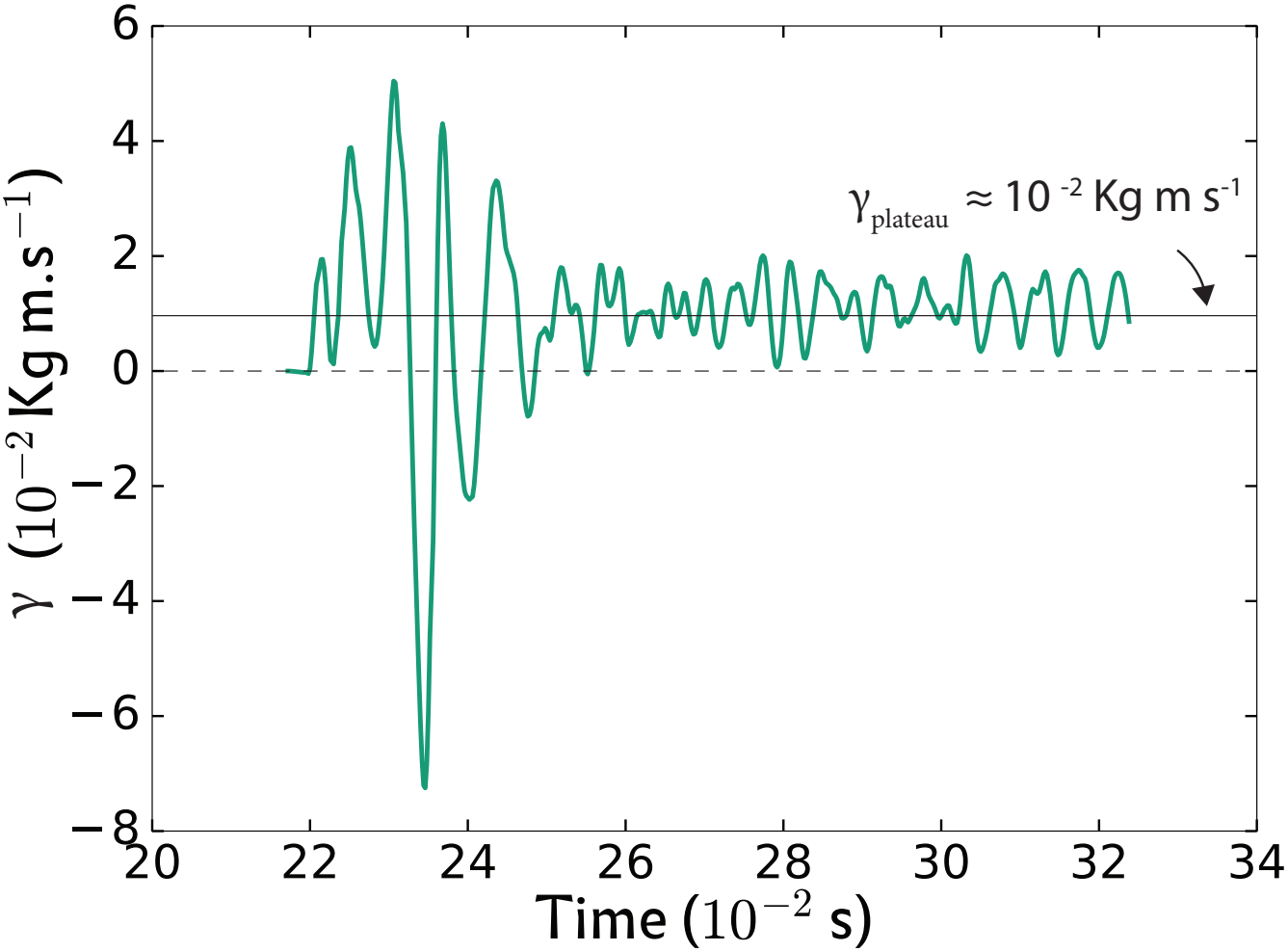

Figure 6.4: Evolution of the integrated thrust as a function of time, during buckling. Dashed black line shows the zero reference and light black line the mean value at the plateau.

As shown on figure 6.4, the integrated thrust oscillates and settles to a plateau with a positive value $\simeq 10^{-2}$ Kg.m/s. This means that the overall direction in which the swimming is produced, is toward the buckling direction (up).

6.2.4 Thrust with internal pressure control

In order to obtain the evolution over time of the thrust during deflation with internal pressure (frictionless rail experiment), it is necessary to measure the displacement of the mass center of the system (support+shell). As explained in the previous chapter, measurements of the displacement of the center

of mass of the whole system was not possible, due to the concave shape of the shell. We recall that the measurement of the displacement is overestimated by at most 0.25 mm (see sec.5.1). The value we measure corresponds in fact, to the motion of the support. The velocity extracted from such signal does not correspond to the velocity of the real center of mass during the buckling phase ($\approx$ 20 ms). But it is reasonable to consider that past this phase, the velocity extracted from the support motion is close to the velocity of the real center of mass. Furthermore, since the maximum velocity of the system is $\approx$ 5 cm/s, the R! eynolds number associated to the system in glycerol is $\approx$ 1, which means that postulating that viscous forces are linear with respect to the velocity, is a reasonable assumption.

Based on these hypotheses, we can write the fundamental principle of dynamics projected on the horizontal direction x:

$$F_b - \alpha \dot{X} = m\ddot{X} \tag{6.15}$$

With m being the mass of the system $\approx$ 1.6 Kg, and X the position of the (support) system. Both F_b generated during the deflation phase and α the dissipation coefficient (assumed constant and depending only on the geometry) are the unknown of equation 6.15.

In order to determine α, we performed an independent experiment where we gave an initial velocity to the system (support+shell) while the shell was maintained in a deflated state, and we recorded the displacement of the center of mass.

The evolution of the displacement over time is described by:

$$m\ddot{X} + \alpha \dot{X} = 0 \tag{6.16}$$

The solution of this differential equation is:

$$X(t) = -\frac{m}{\alpha} C_1 \exp(-\frac{\alpha}{m} t) + C_2 \tag{6.17}$$

With C_1=$\dot{X}(0)$, C_2=$\frac{m}{\alpha} C_1 + X(0)$ (determined from initial conditions) and α as fit parameters.

Fit results are shown in 6.5 and yield that α=4.13 Kg/s.

Figure 6.5: Results of the fit over the displacement of the (support+shell) system given an initial velocity, in glycerol.

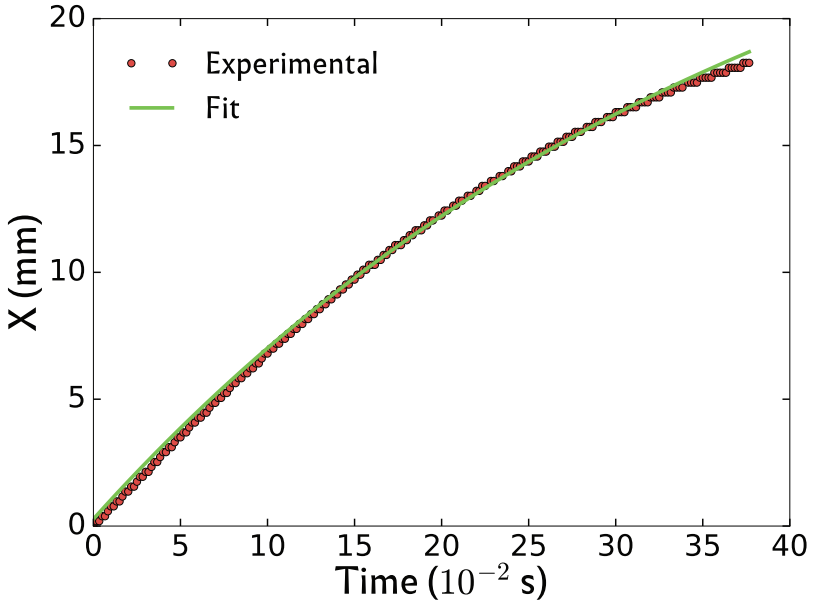

Once the dissipation coefficient determined, we extract the velocity from the displacement (see fig.6.6) of the (support) system during deflation. Integrated thrust is given by:

$$\gamma(T) = m\dot{X} + \alpha X \tag{6.18}$$

Velocity being zero after the deformation phase, we can estimate the integrated thrust with $\gamma(T \rightarrow \infty) = \alpha \Delta X \simeq 0.005$ Kg.m/s $\pm 10\%$.

The main observation we can make is that the value of thrust is similar to the plateau values obtained in the case of external pressure control [*].

[*]It is difficult to draw any other relevant observations because in the case of external pressure control, the experimental signal of displacement was derived twice to obtain the thrust which introduces errors inevitably, and in the case of internal pressure the displacement signal was derived once and value of the mass used in calculation did not take into account the added mass.

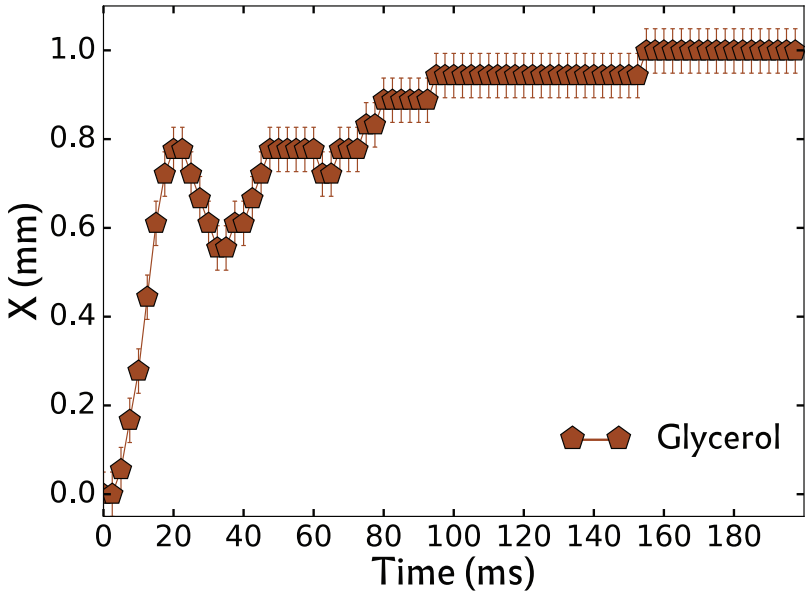

Figure 6.6: Evolution with time of the (support) system displacement, during deflation.

6.3 Inertial thrust during buckling phase

From the toy model, we expect the inertial thrust force F_b to scale like $\rho_f \Delta V \times V_b\omega$, where $\rho\Delta V$ is the mass of the accelerated fluid and $V_b\omega$ its typical acceleration. F_b scales to the first order like $R^{-1}Ed^3$ (see 3.2.3). This scaling explains the important gap in the displacement at high Re between the macroscopic shells with relative thickness $d/R = 0.08$ and $d/R = 0.22$.

In the macroscopic model, the effect of the inertial thrust first accelerates the whole system of mass $M \simeq 1.6$ kg (support+shell). For the $d/R = 0.22$ shell where ΔV is of order half of its total volume V_0 (see 3.2.3), this results in a typical swimming velocity $V_s = V_b \times \rho_f V_0/(2M) \simeq 0.05$ m/s, in very good agreement with the velocity measured during buckling $\simeq 0.03$ m/s (see motion of the system in water in Fig. 5.3). In the case of moderate values of Re, the equation of motion becomes more complicated since it should take the viscous drag into account, but we noticed when looking at the displacement of the system during deflation (Fig. 5.3) that the initial slope is quasi similar, in water and in glycerol. If we suppose that viscous drag is negligible compared to thrust during buckling phase, we can also write $V_s = V_b \times \rho_f V_0/(2M)$ with $\rho_f = 1250$ Kg/m^3 a! nd this gives $V_s \simeq 0.0625$ m/s in agreement with the system's velocity in glycerol $\simeq 0.04$ m/s (Fig. 6.6).

To complete this kinetic study, we can switch to an energetic perspective. From [Quilliet et al., 2008, Quilliet et al., 2010] we know that the elastic energy stored in the spherical configuration reads

$$E_{el} = 4\pi R^2 d \times \frac{E}{9(1-\nu)} \times (1 - \frac{V}{V_0})^2. \tag{6.19}$$

where $V = V_0 - \Delta V$ is the current volume and V_0 is the reference volume of the undeformed spherical shell.

Together with Eq. 3.2, this implies that right before buckling:

$$E_{el} = 4\pi \frac{\beta^2}{9(1-\nu)} \times E d^3. \tag{6.20}$$

Ignoring the prefactor, we note that Ed^3 in F_b is also the stored elastic energy right before buckling. At buckling, this elastic energy is then converted into work of F_T on a typical distance R.

A free shell whose mass will be comparable to (or even smaller than) the mass of the accelerated fluid will attain higher velocities, though drag forces will also come into play. The estimate we made for our heavy swimmer about the final displacement in the intermediate Re (and Wo) regime $1 < Re < 100$ is then obviously a minor bound. For slender bodies using undulation gaits, equilibrating thrust and drag force allows to determine the swimming velocity in a permanent regime [Gazzola et al., 2014]. Here the situation is more complex: the post-buckling oscillations and the buckling-debuckling alternance lead to succession of positive and negative thrusts because of which body acceleration cannot be fully neglected. As shown by our discussion for swimming at moderate Womersley numbers, the resulting actuation is a consequence of a subtle coupling of theses oscillations with the fluid flow. Determining the full force-velocity relation requires further investigations.

6.4 Summary

In this chapter, we measured the thrust when applying pressure externally and we showed that both pressure controls yield a very comparable integrated thrust. This important result validates the rele-

vance of the study with internal pressure control.

We also showed that thrust during the buckling stage has a major contribution at high Re and moderate Re. It is also expected to be similar in both cases of pressure control, since the volume variation and the buckling velocities are comparable.

This chapter concludes the presentation of the results obtained during my Ph.D work. In the next chapter, we will give a brief summary of the main results of this thesis and discuss about perspectives.

7

Conclusion

7.1 Global summary

The purpose of this thesis was to propose a new kind of artificial microswimmers using a mechanical instability as a novel propulsion mechanism. They consist in elastic hollow spherical shells which move through repeated buckling-unbuckling instability cycles. Such microswimmers would present undeniable advantages compared to already existing artificial microswimmers: first, the simplicity of their geometry makes it quite easy to manufacture with high throughput, using common physico-chemical methods such as emulsion-evaporation process. The second advantage comes from the actuation method; instability would be triggered using pressure waves which are easy to generate and to control, compared to

a vector field such as magnetic fields. Third, the major conceptual difficulty when operating at low *Re* regime (usually associated with microscopic scales), is that a non zero displacement may only occur via a nonreciprocal succession of shapes. This condition is fulfilled naturally by the instability mechanism due to the hysteresis shown to take place during a deflation-reinflation cycle. Furthermore, the swiftness of the deformation associated with buckling instability may produce inertial effects even at microscopic scale.

To investigate this proposition, we upscaled it to the macroscopic scale and performed experiments in a set of fluids with varying viscosity so that relevant dimensionless numbers (fluid flow, shell geometry, dynamics of the deformation...) can be kept unchanged from the microscopic scale. We realized centimetric shells through a fully controlled process and we developed three complementary experimental setups:

1. In the spring setup, pressure cycles are applied externally to a shell itself attached to a spring and immersed in a liquid, inside a pressurizeable tank. Using this setup, we were able to study the shell dynamics in a configuration close to the targeted microscopic application. We were also able to quantify the thrust generated during the instability.

2. In frictionless rail setup, pressure cycles were imposed to the air volume enclosed by the shell membrane. Thanks to this setup, we were able to quantify the swimming in a wide range of viscosity.

3. Time-resolved PIV measurements with internal pressure control allowed us to visualize flow structures and quantify flow dynamics in water and in glycerol.

Using these three experimental setups, we were able to draw a coherent picture of the shell dynamics. We showed that it depends strongly on a geometrical parameter which is the ratio between the thickness and the radius of spherical shell, and also on material properties which are the Young modulus that characterizes the capacity of the material to store elastic energy, and the loss tangent that denotes how much elastic energy is restored.

These parameters determine the deformation rate, the size of the depression and the frequency of the post-buckling oscillations. The way pressure cycles are applied influence the shell dynamics in a limited way, the main difference being the mode of deformation of the post-buckling pulsations.

We identified a dimensionless number Q_f that describes the dependency of shell dynamics with the viscosity of the surrounding fluid.

Flow dynamics is a direct consequence of shell dynamics but depends also on the viscosity of the surrounding fluid, which influences the flow structures encountered during the deformation.

This dependency is reflected by the displacement induced during a deflation and re-inflation cycle. Displacement induced by deflation increases when the viscosity of the surrounding fluid is increased, due to the existence of history effects whose origins are post-buckling oscillations. Displacement induced by re-inflation is additive to the displacement produced during deflation, but stays negligible in comparison, except for low Re regimes where the motion is sensitive to shape deformations only, in which case re-inflation phase contributes negatively to the net displacement. Consequently, the dependence of net displacement is not monotonous with respect to Re number and a maximum is reached for intermediate values of Re. Another important finding is that at any Re regime, the net displacement is positive: the shells swim in the direction of the depression formed during the buckling.

In terms of (d/R), increasing the shell thickness increases the net displacement up to a certain limit, that is associated to finite size effects. The Young modulus E increases the deformation rate and thus the flow acceleration during buckling phase, which increases the net displacement. The upper bound to the increase of both previous parameters is the critical buckling pressure, which needs to be in an operable range. As for the loss tangent $tan\delta$, increasing it decreases the swiftness of shell dynamics, which in turn decreases the flow acceleration and decreases the net displacement.

We highlighted the existence of interaction ranges, and studied the particular case of swimming toward a wall, in which case the displacement induced by deflation increases when the shell gets closer to the wall. The presence of the wall enhances pressure forces thanks to a Venturi effect.

Thrust generated during deflation with an external pressure control and an internal pressure control is similar. This validates the relevance of the results obtained with internal pressure control, and the expectations at small scale.

Based on these experimental results, we developed a toy model that describes the fundamentals of shell dynamics and we derived from this study three dimensionless numbers: Reynolds number, Womersley number and Quality factor. Using these numbers, we were able to predict in which regime would a microscopic shell swim and provided an estimation of swimming velocity.

7.2 What's next?

Now that we have the necessary experimental tools and the fundamental comprehension of the swimming mechanism, we can expand our knowledge through the following promising trails.

7.2.1 Coupled dynamics with driving frequency

During all the experimentation, the frequency of pressure cycles was around 0.1Hz. This choice was imposed by the slowness of the pressure controller we used, but it was not a handicap because we needed to uncouple the intrinsic shell dynamics from forced dynamics that would be induced by higher driving frequency. Now that we understand in an independent way the dynamics during deflation and reinflation, we can study the effect of driving frequency and its implication on the dynamics, especially on history effects which, as we saw, increase swimming efficiency.

Imposing shell deformation dynamics We postulated earlier that in order to trigger buckling instability, a spherical swimmer can only be submitted to pressure cycles with a frequency ω_d smaller than the post buckling spontaneous frequency ω of the shape oscillations which constitutes a high bound to driving frequencies. This limit was never reached experimentally due to slowness of the pressure controller we used (maximum frequency reached to achieve buckling being 0.4 Hz), and thus we cannot confirm nor refute this assumption.

A consequence is that if we submit the shell to a high amplitude pressure cycle which has a given frequency $\omega_d > \omega$, we might be able to force the dynamics of buckling and unbuckling. The limit being time necessary to propagate the pressure wave through the shell thickness defined as:

$$\tau_{prop} = \frac{d}{c} \tag{7.1}$$

with c being the the speed of sound (which represents the speed at which the pressure wave propagates inside the shell's material). For a shell used during experiments with a thickness of 5 mm, $\tau_{prop} \approx 3$ μs, setting a minimum driving frequency at 300kHz which is ten thousand times the post-buckling spontaneous frequency*.

If we can effectively overcome the post-buckling spontaneous frequency, we can optimize the driving frequency to reach higher swimming velocities, but more importantly we can introduce asymmetry of shell deformation during buckling and unbuckling. To illustrate this point, let us consider a configuration where we are at low *Reynolds* number. In this configuration, a *positive* displacement is induced by buckling and reaches 12% R, while a *negative* displacement is achieved during unbuckling which can reach 11% R. Taking into account that unbuckling at higher Re does not produce a significant displacement, we could impose an unbuckling deformation rate which would increase the Re during this phase through an asymmetric pressure signal, this would cancel the *negative* unbuckling displacement and we would reach a displacement per cycle at 12% R, increasing the swimming efficiency.

7.2.2 1-D robot

Swimmers arrangement In order to build a robot constituted of a combination of multiple swimmers, we suggest first to study the swimming efficiency of two swimmers in different configurations as displayed in figure 7.1. These swimmers can be either identical, with different (d/R) or made of different materials. The influence of the distance between swimmers will be studied and also the activation phase shift which can also play a role on flow dynamics, especially at close range.

*In the case of rubber-like materials c is typically around 1500 m/s.

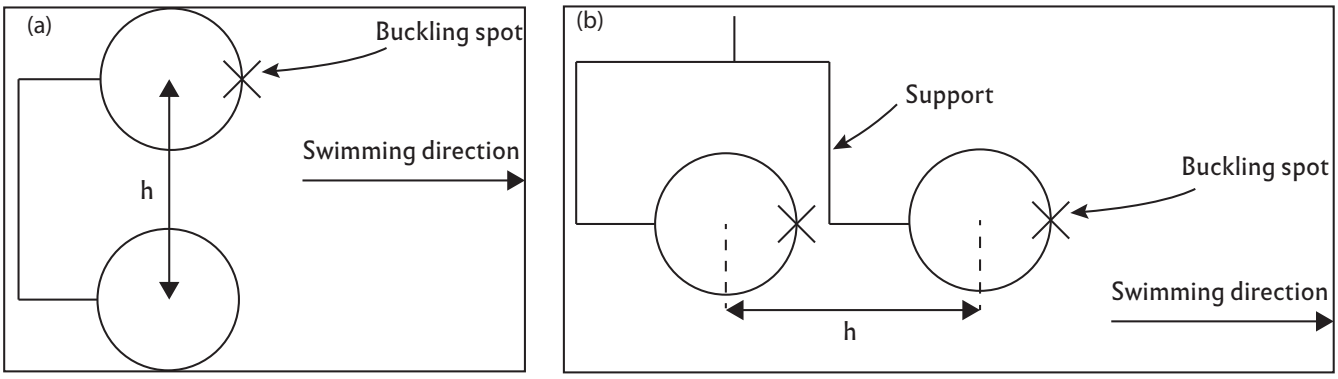

Figure 7.1: Schematics of two swimmers interaction: (a) Configuration of swimmers in parallel (view from above). (b) Configuration of swimmers in series (frontal view).

1D robot Building a fully free swimmer at macroscopic scale is hard to achieve due to buoyancy effects. In order to be in control, we are limited in terms of degrees of freedom to a translation, but that does not prevent us from building a robot that can move forward/backward as displayed in 7.2. Shell A and B have to be different, so we can activate one without the other which will favor one direction.

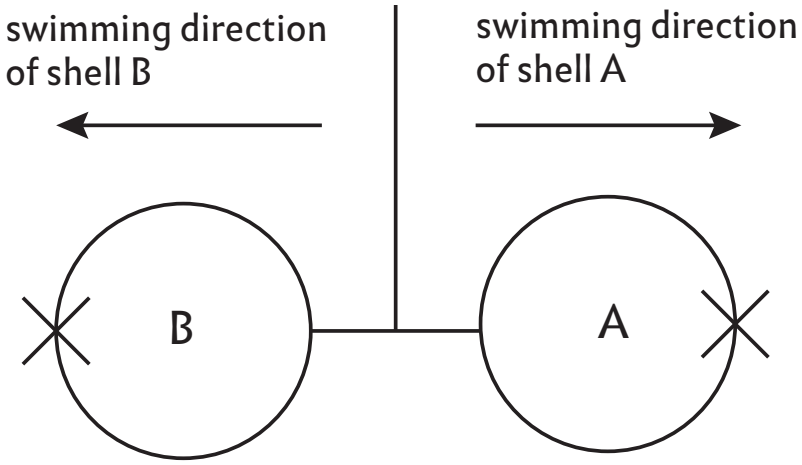

Figure 7.2: Schematics of a 1-D robot.

2D robot Buoyancy effects are a constraint if we want a fully immersed swimmer, but we can imagine a configuration where three different shells are linked together and floating at the interface (liquid/air) inside the pressurizeable tank (see fig.7.3). Such configuration would allow three degrees of freedom (two translations and one rotation). We could also trap the assembly at the interface of two non-miscible liquids with different densities, by playing on the weight of the linking support.

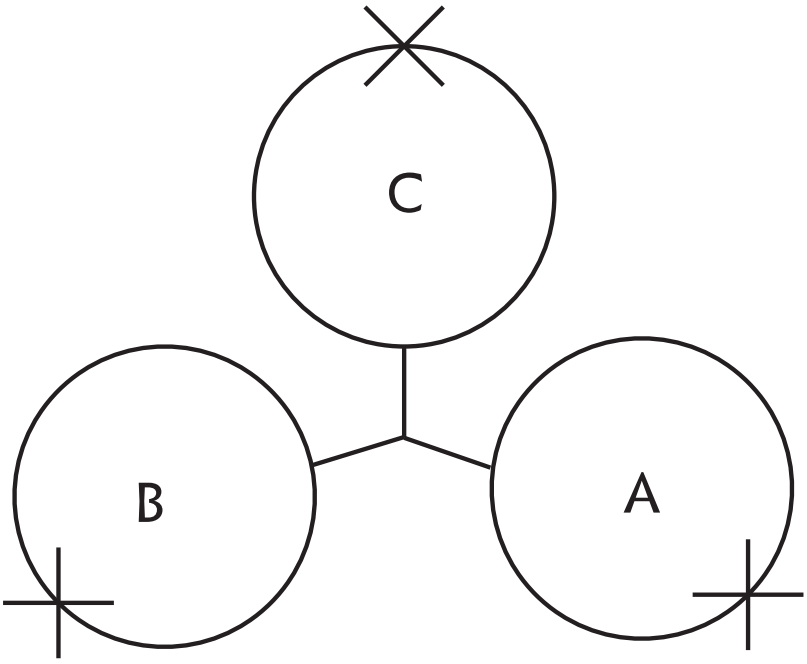

Figure 7.3: Schematics of a 2-D robot (view from above).

7.2.3 Swimming near a wall

In the chapter about swimming, we showed that the presence of a wall enhances the displacement during deflation and re-inflation, especially at high *Re*, due to an increase in pressure effects, but only one direction (swimming toward the wall in the normal direction) was explored. A thorough investigation should be lead in 1-D first varying the angle between the swimming direction and a wall equipped with pressure sensors. Then, in a second time, a 2-D study using the 2-D robot setup should take place. Rotation degree of freedom will allow for self arrangement near the wall.

7.2.4 Swimming in complex liquids

Non-Newtonian liquids We showed in the chapter about swimming, that swimming in low viscosity Newtonian liquids (high *Re*) is less efficient than swimming in intermediate viscosity liquids. We could produce however similar efficient regime by using a shear thickening fluid that would increase its viscosity during buckling and be at a lower viscosity during re-inflation where deformations are less brutal. This would most probably be an efficient configuration.

Visco-elastic liquids Another configuration would be to use a visco-elastic polymeric solution and explore the swimming dynamics. For now, we don't have any predictions on the swimming behavior in such a configuration.

7.2.5 Miniaturization

The main challenge we need to face is miniaturization. We built a fully experimental setup to test colloidal shells provided by our collaborator Nicolas Tsapis (see fig.7.4) from Institut Gallien in Paris. Unfortunately, the colloids were fragile and the Young modulus of the polymer used ($E_{min} \simeq$ 200 Mpa) places the critical buckling pressure(ΔP_c=5 bar) out of operable range, especially with acoustic pressure which induces cavitation. Now that we know what we are looking for, we can draft the requirements in terms of material properties and geometry of the colloids. This would allow to validate our findings and explore the physics at smaller scale with possibilities to study collective behavior.

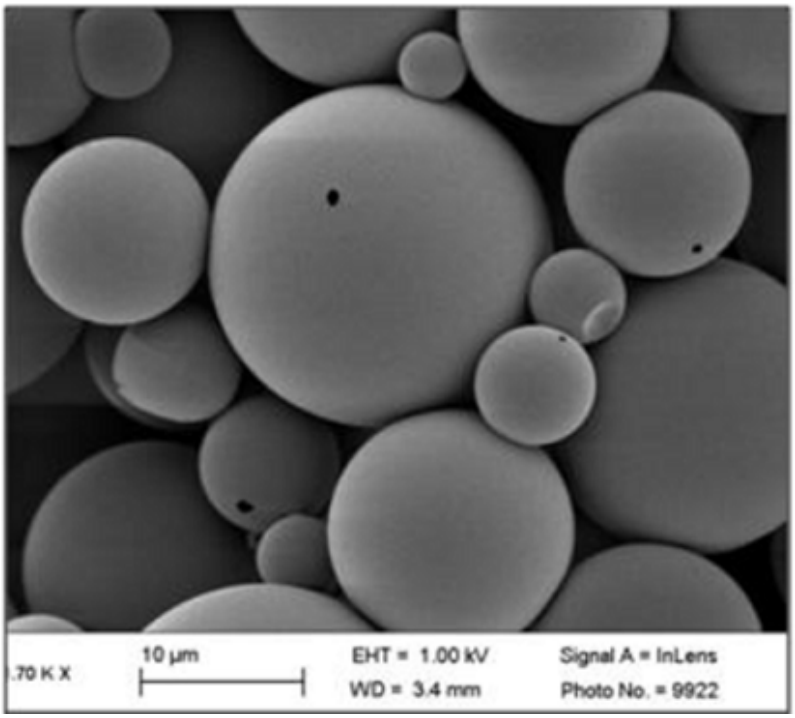

Figure 7.4: Poly-disperse spherical colloidal shell manufactured by emulsion-evaporation process. Provided by Nicolas Tsapis.

Temperature-driven swimming colloids If we can make such colloids, we could manage to maintain the air encapsulated inside the shell at low pressure. When preparing the solution, shells would be submitted to a pressure difference between external water pressure and inside pressure. If this difference is high enough, shells would spontaneously buckle. Using a laser source, we could point at the shell to heat it up rising the internal pressure and make it unbuckle and turn-off the heat source. After a certain cooling time it will buckle spontaneously again (decrease of internal pressure).

7.2.6 Numerical simulations

The nature of the instability, the complexity of the subsequent dynamics and fluid-solid coupling have proven to be challenging and discouraged us from trying direct numerical simulations. However, we saw that there are two regimes describing the influence of the fluid damping on the shell dynamics, characterized by Q_f. In the case $Q_f > 1$, we can consider that the dynamics are uncoupled. From the results obtained with the spring experimental setup, we extracted the evolution of the shape during the deflation. This set of shapes can be in turn implemented as a dynamic boundary condition to solve the flow dynamics.

In parallel, digital stereo-correlation measurements (DIC) at high temporal resolution can be performed during deflation to obtain the shell deformation, by putting markers on its surface. This would allow us to provide full boundary conditions (strain and stress) to the flow solver.

Thank you for reading my work.

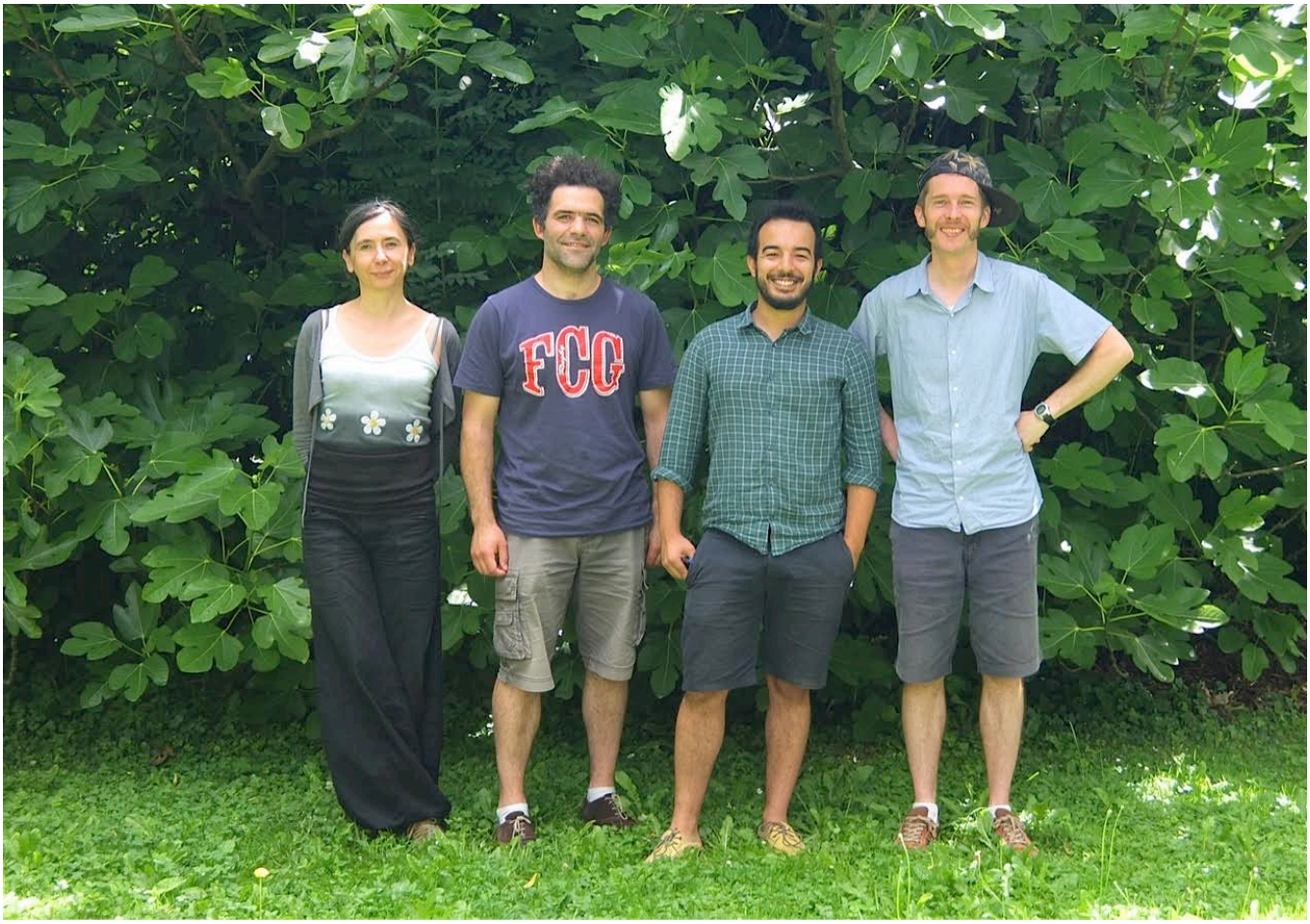

Figure 7.5: Ze dream team.

A

A.1 Molding equipments

Female mold: It consists of a cylinder of radius $R_{cylinder} = 30$ mm hollowed out to produce a half a sphere imprint of radius $R_{out} = 25$ mm and a height of $h = 30$ mm (see fig.A.1). The concavity is where the casting material is poured. A groove was added to store any potential material surplus. Two female molds are necessary for the casting operation.

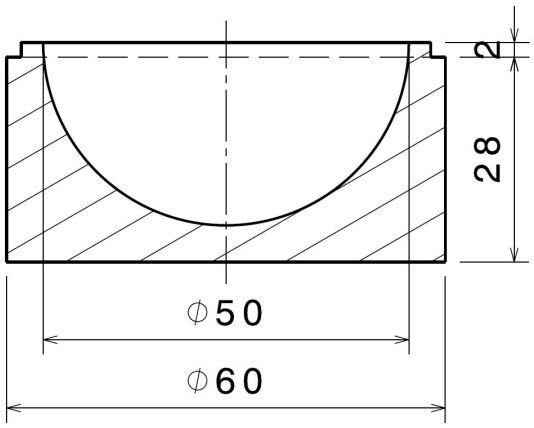

Figure A.1: Longitudinal section of the female mold

Translation guide sleeve: It is a hollow cylinder with an inner radius $R_{in} = R_{cylinder} = 30$ mm, and a thickness of 5 mm. where the female mold is slid in. It is slightly higher than the female mold by 5 mm. One extremity is provided with an inner chamfer of 5°which ensures the concentricity between the female mold and the male mold.

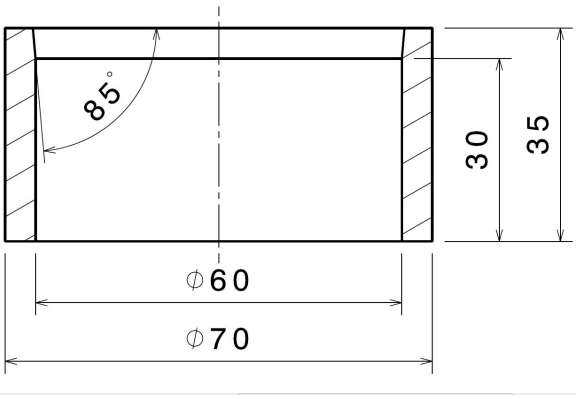

Figure A.2: longitudinal section of the sleeve

Male mold: Figure A.3 shows the design of the male mold which consists of half a sphere of radius $R_{int} < R_{out}$, which is changed to cast different thicknesses. It is supplied with a shouldering which acts as a travel stop, its flanks have a slight angle of 5 providing a translation guide and preventing an over-center locking in combination with the guiding sleeve previously presented. The cylindrical part over the shouldering helps manipulating the mold during the casting process. Three radii have been used:

$R_{int} = 18.5mm, 20mm, 23mm.$ *

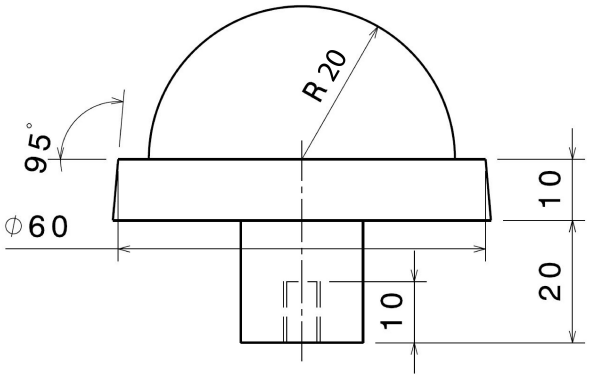

Figure A.3: Front view of an example of the male molds used

Gluing sleeve: It is a hollow cylinder with an inner radius $R_{in} = R_{cylinder} = 30$ mm, a thickness of 5 mm and a height of 50 mm. It is used during the gluing process where the female molds containing the two halves of the sphere, are faced to each other and slid inside the gluing sleeve, to ensure the concentricity.

Mechanical press: It's a simple press consisting of two metallic plates supplied with a set of threaded rods and hexagonal nuts used to apply pressure over female/male molds during the casting step, preventing air bubbles from getting trapped, during the casting step. It is also used during the gluing step on the female/female molds, to ensure the contact between the two half spheres to be glued together.

Pasta machine: This machine (figA.4) consists in two rotating cylinders, with an adjustable interspace. It was used to produce thin layers of a polymeric material.

*All the molding parts presented are made of Aluminum "'Fortal"'. The female and male molds were machined using a CNC (computerized numerical control) machine and with a precision of $tol = \pm 0.01$ mm. The surface roughness obtained was of $R_a = 0.04$ which indicates a very good finishing. This choice of manufacturing was unavoidable since no other alternative could produce spherical shapes with such a precision.

Figure A.4: Pasta maker

A.2 Dragon skin®30 molding protocol

Half shell casting To produce a shell with a certain thickness d, made of Dragon skin®30 material, these are the steps we followed:

1. Begin by determining the mass of a shell with a outer radius of $R_{out} = 25mm$ and a thickness d which gives an internal radius $R_{int} = R_{out} - d$

2. In a beaker, weigh 50% of the shell mass of component A which is the silicon polymer chain. We stir thoroughly and add 50% of the shell mass of component B, which constitutes the cross-linking agent, we stir thoroughly.

3. The mixture is then degassed using a vacuum pump.

4. The female and male are cleaned using acetone and 50% of the degassed mixture is poured in each one of the two female molds.

5. We degas again to make sure no air was entrapped during the previous step.

6. Each female mold is slid in the translation guide sleeve and the male mold with an internal radius R_{int} which corresponds to the desired thickness d defined as $d = R_{out} - R_{int}$, is gently slid inside the female mold to prevent air from getting trapped.

7. The female-male molds assembly is then pressed and locked using the press.*

8. The press is then put into an oven at 65°C to speed up the cross-linking process reducing it from 16 hours to only 20 minutes.

Half spheres gluing: Once the two halves of a hollow sphere of the desired thickness d, are cast. Next step is to glue the two halves together to obtain a complete hollow sphere. This part is critical: if the sewing is weak, it will tear apart during the buckling phase. if the sewing is thick, it means that the shape is no longer spherical. If the gluing material is not the same, we lose the homogeneity of the material and potentially create a weak zone at the sewing.

To efficiently glue the two halves and avoid the problems stated previously, we used the same material to perform the gluing, but for that it was necessary to decrease the viscosity of the mixture and enhance its wetting properties. For this purpose, we mixed Pentane which is an organic solvent [Ng Lee et al., 2003] with the highest solubility parameter for PDMS, assuming it would also work well for the Dragon skin®30 material . The following describes the protocol of gluing:

1. Prepare 10g of a mixture A+B of the Dragon skin®30 and degas it.

2. Add 5 ml of **Pentane** to the mixture and stir to obtain a diluted mixture that is neither too liquid nor too viscous and pump the resulting liquid inside a syringe.

3. Use an abrasive such as sandpaper over the gluing area of the two casts, to make the surface rougher.

4. Put back each cast in the female mold and align it correctly so that the gluing area is horizontal.

5. Pour uniformly a layer of the diluted mixture using the syringe needle on the gluing area of both casts.

6. Put one female mold inside the gluing sleeve, facing upward then slide the second one facing downward until the two gluing areas are in contact.

*This step is necessary to ensure that no bubbles get trapped during the assembly.

7. Ensure the contact by using the mechanical press and let the cross-linking happen at room temperature for 16 hours.*

8. After the curing time, the shell is produced and the last step is remove the residual thin skin circling around the sewing area.

A.3 AJO 121/122 molding protocol

Half shell casting: To produce a shell with a certain thickness d, made of *AJO 121* and *AJO 122*, these are the steps we followed:

1. We begin by determining the mass of a shell with a outer radius of $R_{out} = 50mm$ and a thickness th which gives an internal radius $R_{int} = R_{out} - th$, The mass of a hollow sphere is given by the following formula:
$$Mass_{shell} = \frac{4\pi}{3}\rho_{material}(R_{out}^3 - R_{int}^3)$$

2. We weigh the calculated mass from the paste-like material and divide it in two equal parts.

3. Press each part at the center of the female mold.

4. Each female mold is slid in the translation guide sleeve and the male mold corresponding to the desired R_{int} is slid inside the female mold.

5. The female-male molds assembly is then pressed and locked using the press.

6. The press is then put into an oven at 115°C to trigger the vulcanization process, during 10 minutes.

7. A post-curing at 200°C is needed to optimize the mechanical properties of the material, to evaporate remaining volatile substances (sub-products linked to the peroxide) and allow the sublimation of the 2,4 Dichlorobenzoic acid which manifests as a white powder at the surface of the material, at the end of the previous step.

*This time we don't use the oven to ensure that the pressure inside the spherical hollow shell is the atmospheric pressure.

Half spheres gluing: After casting the two halves of the spherical capsule, the next step is to glue them together, but the gluing using the AJO materials was very challenging for different reasons. First, the paste-like nature of the material which was not soluble in any organic solvent without compromising the vulcanization agent already mixed with the raw polymer. It also made manipulating it harder, contrary to the liquid nature of the "'Dragon Skin®30"'. Second, we were not able to glue together two flat surfaces, due to the fact that the cross-linking process reached a maximum with the prescribed time and temperature and leaving no room for an additional cross-linking. After several trials, we came up with a protocol which allows to glue the two half spheres, following these steps:

1. Two thin layers (0.1 mm) are prepared using the "'pasta maker"' machine (fig.A.4). Their width is set to 10 mm and the length to $2\pi R_{out} \approx 157mm$.

2. Sandpaper is used over the gluing area of the two casts to make the surface rougher.

3. Put back one cast in the female mold and align it correctly so that the gluing area is horizontal.

4. Put uniformly a first layer on the gluing area of one cast and make sure it adhered to the surface, cut the residual width using a scalpel.

5. Connect the remaining half (without the female mold) with the first and press to get and adhesion.

6. Remove the female mold gently and roll the second layer around the sewing perimeter, taking care not to disconnect the two halves while doing so.

7. Encapsulate the shell inside the two female molds and exert pressure using the mechanical press.

8. Put the press inside the oven at 115°C for 10 minutes. Remove it and let it cool at room temperature.*

9. The process ends by extracting the shell out of the female molds.

*The capsules produced using this protocol have an internal pressure close to 75% of the atmospheric pressure.

A.3.1 Material documentation

The commercial name for the is "'AJO 121"' material is "'Bluesil MF 360"', The commercial name for "'AJO 122"' material is is "'Bluesil MF 760"'.

A.3.1.1 Dragon skin 30

Dragon Skin® Series

Addition Cure Silicone Rubber Compounds

Cured Material Certified Skin Safe!

www.smooth-on.com

PRODUCT OVERVIEW

Dragon Skin® silicones are high performance platinum cure liquid silicone compounds that are used for a variety of applications ranging from creating skin effects and other movie special effects to making production molds for casting a variety of materials. Because of the **superior physical properties** and flexibility of Dragon Skin® rubbers, they are also used for medical prosthetics and cushioning applications. Dragon Skin® rubbers are also used for a variety of industrial applications and have a service temperature range of a constant -70°F to +400°F (-21°C to + 205°C).

Great for Making Molds for a Variety of Applications - Available in **Shore 10A, 20A and 30A**, Dragon Skin® silicones can be used to make exceptionally strong and tear resistant molds for casting plaster, wax, concrete (limited production run), resins and other materials.

Time Tested, Versatile Special Effects Material – Soft, super-strong and stretchy, Dragon Skin® 10 (**Very Fast, Fast, Medium and Slow speeds**) is used around the world to make spectacular skin and creature effects. An infinite number of color effects can be achieved by adding Silc Pig® silicone pigments or Cast Magic® effects powders. Cured rubber can also be painted with the Psycho Paint® system. Cured material is skin safe and certified by an independent laboratory to ISO 10993-10, Biological evaluation of medical devices, Part 10: Tests for irritation and skin sensitization.

Easy To Use – Dragon Skin® silicones are mixed 1A:1B by weight or volume. Liquid rubber can be thinned with Silicone Thinner® or thickened with THI-VEX®. Rubber cures at room temperature (73°F/23°C) with negligible shrinkage. ***Vacuum degassing is recommended to minimize air bubbles in cured rubber.***

TECHNICAL OVERVIEW

	Mixed Viscosity (ASTM D-2393)	Specific Gravity (g/cc) (ASTM D-1475)	Specific Volume (cu. in./lb.) (ASTM D-1475)	Pot Life (ASTM D-2471)	Cure Time	Shore A Hardness (ASTM D-2240)	Tensile Strength (ASTM D-412)	100% Modulus (ASTM D-412)	Elongation at Break % (ASTM D-412)	Die B Tear Strength (ASTM D-624)	Shrinkage (in./in.) (ASTM D-2566)
Dragon Skin® 10 Very Fast	23,000 cps	1.07	25.8	4 min.	30 min.	10A	475 psi	22 psi	1000%	102 pli	< .001 in./in.
Dragon Skin® 10 Fast	23,000 cps	1.07	25.8	8 min.	75 min.	10A	475 psi	22 psi	1000%	102 pli	< .001 in./in.
Dragon Skin® 10 Medium	23,000 cps	1.07	25.8	20 min.	5 hours	10A	475 psi	22 psi	1000%	102 pli	< .001 in./in.
Dragon Skin® 10 Slow	23,000 cps	1.07	25.8	45 min.	7 hours	10A	475 psi	22 psi	1000%	102 pli	< .001 in./in.
Dragon Skin® 20	20,000 cps	1.08	25.6	25 min.	4 hours	20A	550 psi	49 psi	620%	120 pli	< .001 in./in.
Dragon Skin® 30	30,000 cps	1.08	25.7	45 min.	16 hours	30A	500 psi	86 psi	364%	108 pli	< .001 in./in.

Mix Ratio: 1A:1B by volume or weight
Color: Translucent
Useful Temperature Range: -65°F to +450°F (-53°C to +232°C)
Dielectric Strength (ASTM D-147-97a)***:*** >350 volts/mil

*All values measured after 7 days at 73°F/23°C

PROCESSING RECOMMENDATIONS

PREPARATION... Safety – Use in a properly ventilated area ("room size" ventilation). Wear safety glasses, long sleeves and rubber gloves to minimize contamination risk. Wear vinyl gloves only. Latex gloves will inhibit the cure of the rubber.

Store and use material at room temperature (73°F/23°C). Warmer temperatures will drastically reduce working time and cure time. Storing material at warmer temperatures will also reduce the usable shelf life of unused material. These products have a limited shelf life and should be used as soon as possible.

Cure Inhibition – Addition-cure silicone rubber may be inhibited by certain contaminants in or on the pattern to be molded resulting in tackiness at the pattern interface or a total lack of cure throughout the mold. Latex, tin-cure silicone, sulfur clays, certain wood surfaces, newly cast polyester, epoxy, tin cure silicone rubber or urethane rubber may cause inhibition. If compatibility between the rubber and the surface is a concern, a small-scale test is recommended. Apply a small amount of rubber onto a non-critical area of the pattern. Inhibition has occurred if the rubber is gummy or uncured after the recommended cure time has passed.

Because no two applications are quite the same, a small test application to determine suitability for your project is recommended if performance of this material is in question.

A.3.1.2 AJO 121

Technical Data Sheet n° SIL 12 243 3 – June 2012
Cancels and replaces SIL 98 036 3

BLUESIL™ MF 360 U

High Tear Strength

Description

Silicone Master-Batch, vulcanizing after heating following addition of a vulcanizing agent (chosen according to the transformation procedure).

Examples of applications

Moulding, injection, extrusion of articles having good mechanical properties.

Advantages

- Slight replastifying.
- Easy proccessability.
- Short post-curing.
- Very good tear resistance.
- High stability up to 250°C.
- Highly transparent.
- Large possibilities of blending with other “Mix and Fix” masterbatches.
- Bright colours easily obtained with colour bases for silicone heat cure elastomers from Bluestar Silicones.

Characteristics

Type (in accordance with AFNOR T 40002) ..... MVQ
Density at 25°C, approx 1.16
Natural colour ..... Colourless, transparent

Properties after working:

- After addition of 1.25 % of 2,4-dichlorobenzoyl peroxide, (50% active ingredients), vulcanization for 8 min. at 115°C ***(1)***
- After addition of 0.6% of 2-5 bis (tertiobutylperoxy), 2,5 dimethyl hexane at 75%, and vulcanization for 10 min.at 170°C ***(2)***

1. Mechanical properties

1.1 Properties without post-curing

	(1)	*(2)*
Shore A hardness, approx.	60	62
Tensile strength, MPa, approx.	9.1	10
Secant modulus at 100% elongation. MPa, approx	2.2	2.1
Elongation at break, % approx.	560	640
Tear strength, kN/m, approx	38	39
Rebound resilience, (8 mm), % approx.	45	45
Linear shrinkage, % approx.	2.5	3.6

1.2 Properties after post-curing for 4 hours at 200°C

Shore A hardness, approx.	62	65
Tensile strength, MPa, approx.	9	10
Elongation at break, % approx.	430	510
Secant modulus at 100% elongation, MPa, approx	2.6	3
Tear strength, kN/m, approx	35	35
Compression set (22h/177°C/25%), %, approx	48	38
Rebound resilience, % approx.	47	48
Linear shrinkage, % approx.	3.4	4.3

BLUESIL™ MF 360 U

Characteristics *(cont')*

2. Heat stability

2.1 Properties after ageing 7 days at 177°C

Shore A hardness, approx.	67	73
Tensile strength, MPa, approx.	9	9.4
Elongation at break, % approx.	340	320
Tear strength, kN/m, approx	25	19

2.2 Properties after ageing 3 days at 200°C

Shore A hardness, approx.	69	73
Tensile strength, MPa, approx.	8.8	8.2
Elongation at break, % approx.	300	280

2.3 Properties after ageing 7 days at 200°C

Shore A hardness, approx.	70	77
Tensile strength, MPa, approx.	8.1	7.3
Elongation at break, % approx.	220	160

2.4 Properties after ageing 10 days at 200°C

Shore A hardness, approx.	74	79
Tensile strength, MPa, approx.	7.2	7.5
Elongation at break, % approx.	170	130

Packaging

BLUESIL MF 360 U is delivered in 25 kg reinforced cardboard boxes or in 500 kg containers.

Storage and shelf life

When stored in its original packaging at a temperature below +40°C, **BLUESIL MF 360 U** may be stored for up to 18 months from its date of manufacture.

Comply with the storage instructions and expiry date marked on the packaging.

Beyond this date, Bluestar Silicones no longer guarantees that the product meets the sales specifications.

Safety

Consult the Safety Data Sheet of **BLUESIL MF 360 U.**

A.3.1.3 AJO 122

Technical Data Sheet n° SIL 13 013 3 – January 2013
Cancels and replaces SIL 12 108 3

BLUESIL™ MF 760 U

General Purpose

Description

BLUESIL MF 760 U is a hot curing silicone rubber after addition of a vulcanization agent (chosen according to the transformation process).

Examples of applications

Moulding and injection moulding process for technical parts (sealing gaskets, grommets), extrusion profiles (windows profiles, sleeves, tubes) and calendering operations for manufactured hoses.

For extrusion applications, depending on processing conditions and geometry of the profile : the addition of 0,5 parts of BLUESIL ADD 916 improves the visual quality of profiles after vulcanization.

Advantages

- Only very slight re-plastifying occurring after prolonged storage.
- Easy working procedure.
- No post-curing, or with slight post-curing.
- Good heat stability, up to 225°C.
- Bright colour easily obtained.
- Good compromise between tear strength and compression set.
- Excellent rebound.

Characteristics

1. Physical properties

Properties	BLUESIL MF 760 U
Type *(AFNOR T 40002)*	MVQ
Natural colour	Translucent
Specific gravity *(g/cm^3)*	1.16

2. Mechanical properties

Below we give examples of the characteristics obtained using the following as a vulcanising agent:

- After addition of 1.25% of 2.4 dichloro benzoyl peroxide at 50% and curing for 8 minutes at 115°C *(1)*.
- After addition of 0.6% of 2.5 bis dimethyl 2,5 (peroxyde tertiobutyl) hexane at 75%, and curing for 10 minutes at 170°C *(2)*.

BLUESIL™ MF 760 U

Characteristics *(cont')*

2.1- Without post-curing	*(1)*	*(2)*
Shore A hardness, approx.	59	60
Tensile strength, MPa, approx.	8.2	8.0
Elongation at break, % approx.	366	449
Secant modulus at 100% approx.	2.3	1,9
Tear strength, KN/m, approx.	14	18
Rebound resilience, % approx.	61	59
Compression set (22h at 177°C, 25%)	25	20

2.2- With post-curing 4 hours at 200°C	*(1)*	*(2)*
Shore A hardness, approx.	63	60
Tensile strength, MPa, approx.	8.4	8.1
Elongation at break, % approx.	344	391
Secant modulus at 100% approx.	2.4	2.1
Tear strength, KN/m, approx.	15	17
Rebound resilience, % approx.	65	58
Compression set (22h at 177°C, 25%)	15	10

3. Heat stability

on cured slabs 4 hours at 200°C

3.1- Properties after ageing over 70 h at 225°C	*(1)*	*(2)*
Shore A hardness, approx.	61	64
Tensile strength, MPa, approx.	7.7	6.7
Elongation at break, % approx.	292	320
Secant modulus at 100% approx.	2.7	2.5
Tear strength, KN/m, approx.	12	14
Rebound resilience, (8 mm), % approx.	61	54

4. Oil resistance

Variation of properties after immersion for 70h at 150°C in ***IRM 903 oil***

Properties	*(1)*	*(2)*
Shore A hardness, approx.	-16	-18
Tensile strength, % of variation approx.	-27	-25
Elongation at break, % of variation approx.	-17	-21
Volume, %	37	38

BLUESIL™ MF 760 U

Characteristics *(cont')*

5. Liquid coolant resistance

5.1 Variation of properties after immersion during 500 hours at boiling point in ***Havoline XLC (50% vol.)***

Properties	*(1)*	*(2)*
Shore A hardness, approx.	-3	1
Tensile strength, % of variation approx.	-18	-22
Elongation at break, % of variation approx.	-14	-23
Volume, %	1	-2

5.2 Variation of properties after immersion during 7 days at boiling point in ***Coolelf (Railway coolant)***

Properties	*(1)*	*(2)*
Shore A hardness, approx.	-7	*I*
Tensile strength, % of variation approx.	-28	*I*
Elongation at break, % of variation approx.	-19	*I*
Volume, %	0	*I*

Packaging

BLUESIL MF 760 U is delivered in 500 kg containers.

Storage and shelf life

When stored in its original packaging at a temperature below +40°C, **BLUESIL MF 760 U** may be stored for up to 18 months from its date of manufacture.

Comply with the storage instructions and expiry date marked on the packaging.

Beyond this date, Bluestar Silicones no longer guarantees that the product meets the sales specifications.

Safety

Please consult the Safety Data Sheet of **BLUESIL MF 760 U .**

A.4 Algorithm for fitting the external shape of the shell

To fit the outer contour of the shell with a parametric curve, defined in the polar coordinates system, these operations were followed:

1. Define an initial center $M_{c0}(x_{c0}, y_{c0})$ to the polar coordinate system, as being the mean value of the experimental points constituting the ball shape.

$$x_{c0} = \frac{\sum_{i=1}^{N} x_i}{N}$$
$$y_{c0} = \frac{\sum_{i=1}^{N} y_i}{N}$$

   Where x_i and y_i are the coordinates of the experimental points, and N being the number of points.

2. Define an iterative process which minimizes the difference between a fitting parametric curve and the experimental points, where at each iteration, the following operations are performed:

   a) Transform every experimental point from the Cartesian coordinates system $M(x, y)$ to the polar coordinates system $M'(R, \theta)$ as follow:

$$R_{exp}(\theta)_i = \sqrt{(x_i - x_c)^2 + (y_i - y_c)^2}$$
$$\theta_{exp_i} = \arctan(\frac{y_i - y_c}{x_i - x_c})$$

   Where x_c and y_c are fitting parameters corresponding to the center of the polar coordinates, initialized by $M_{c0}(x_{c0}, y_{c0})$.

b) Evaluate the fitting parametric curve:

$$\tilde{R}(\theta)_i = \sum_{k=0}^{M} a_k \sin(\theta_{exp_i} - \theta_0)^k$$

for the fitting parameters θ_0* and a_k coefficients, with $k = 0, ..., M$, M being the degree of the polynomial.

c) Measure the distance $R_{exp}(\theta)_i - \tilde{R}_(\theta)_i$ and iterate.

The minimization is done using '$Levenberg - Marquardt'$ method, commonly known as '$least - squares'$ minimization method.

3. The iterative process stops when reaching a residual smaller than a given threshold.

*θ_0 represents the angle formed bet ween the symmetry axis of the experimental points and the y-axis.

A.5 PIV measurements

A.5.1 Davis image analysis parameters

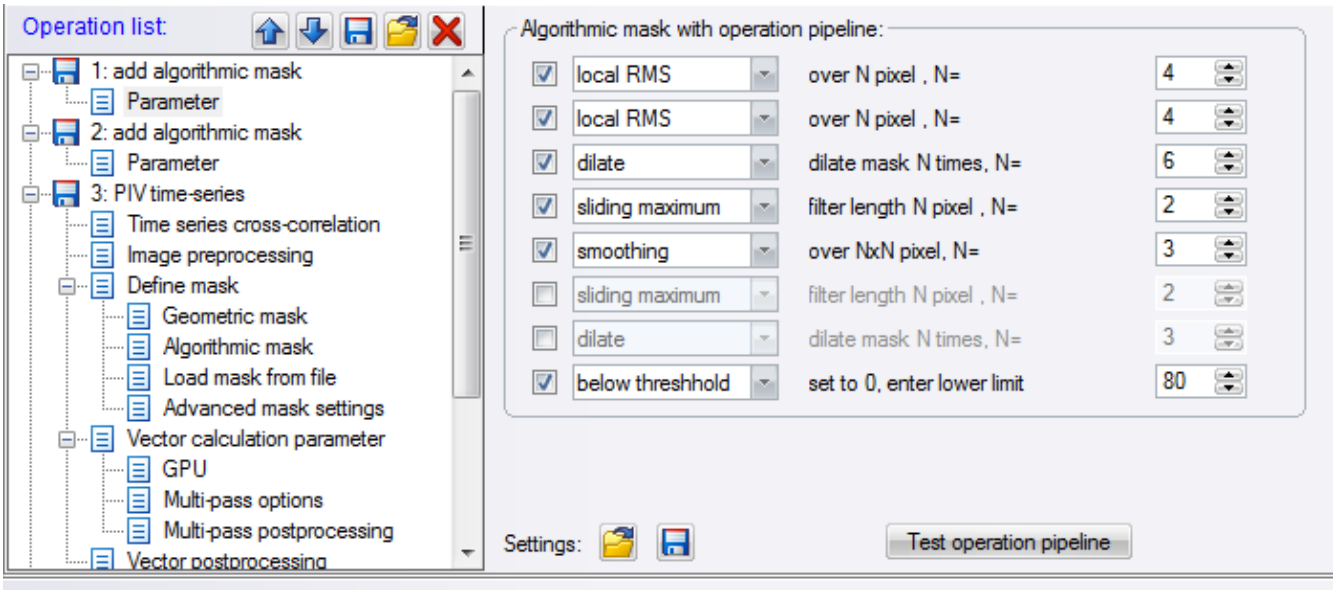

Figure A.5: Low intensity pixel dynamic masking

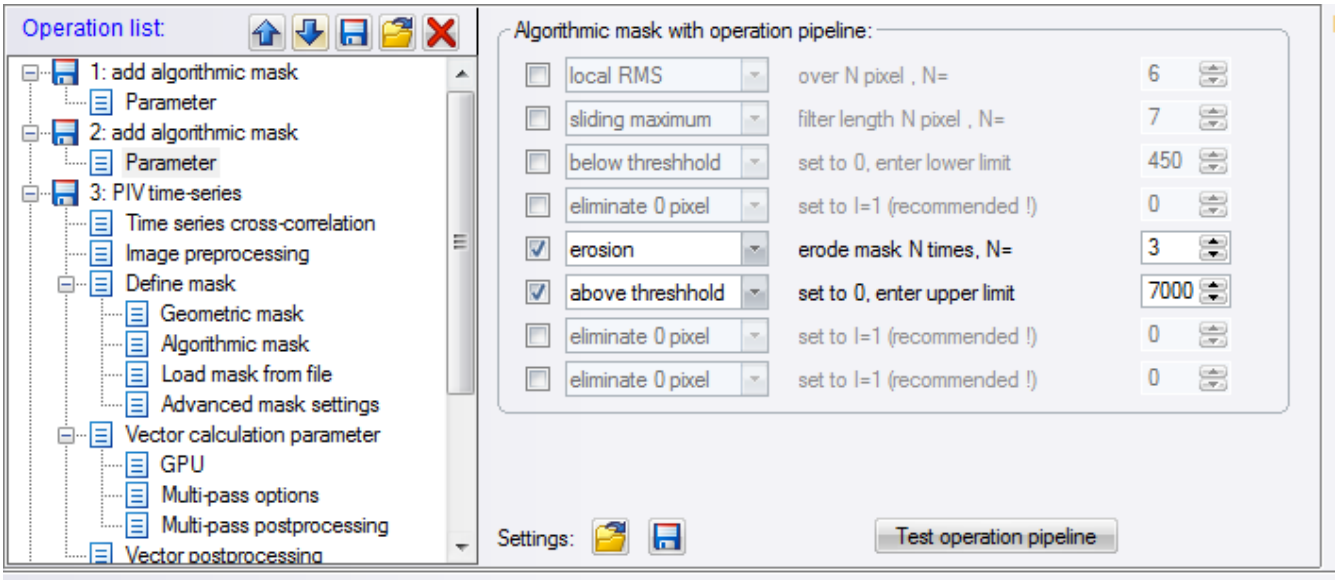

Figure A.6: High intensity pixel dynamic masking

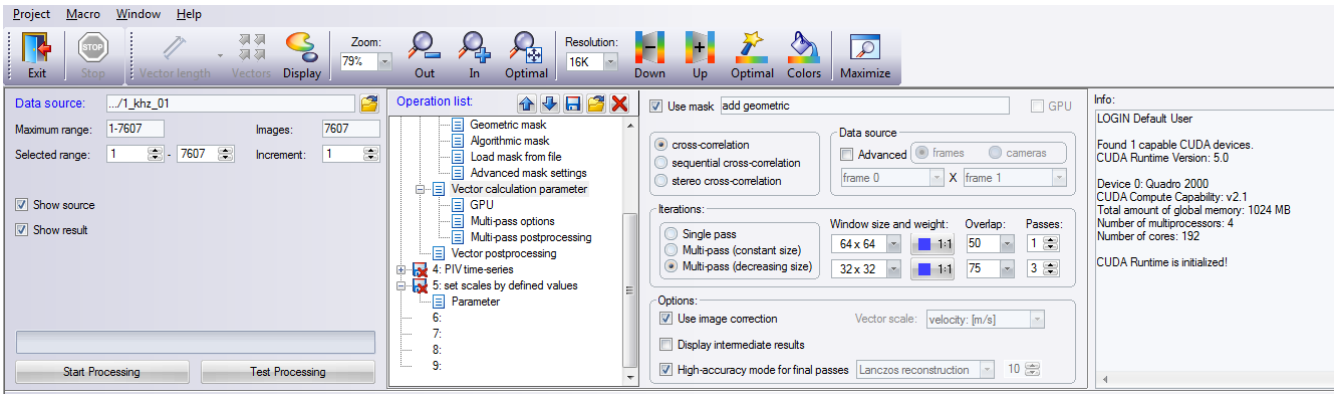

Figure A.7: Cross-correlation settings

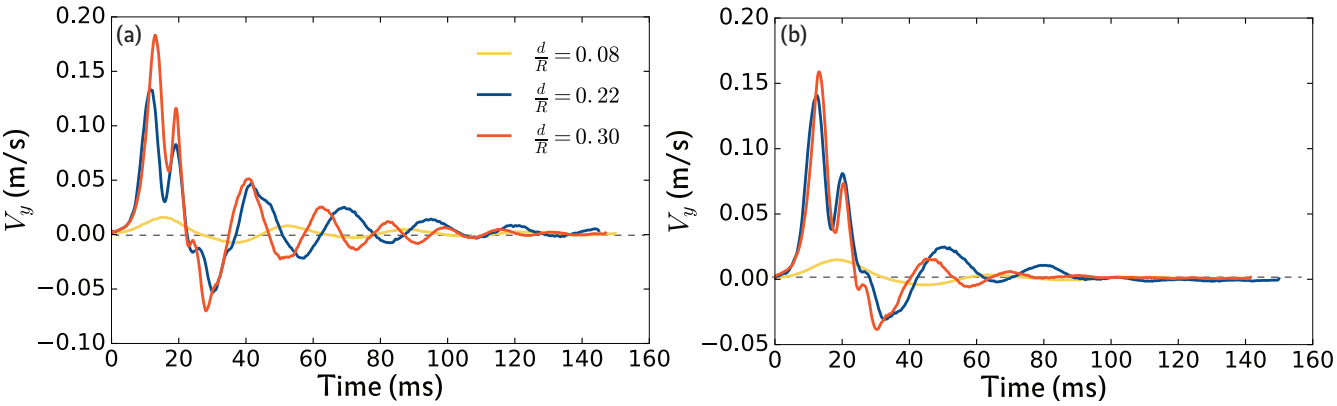

Figure A.8: Temporal evolution of the velocity y-component averaged spatially over a common area for different (d/R): (a) In water; (b) in glycerol. Dashed lines are a guide highlighting the zero value.

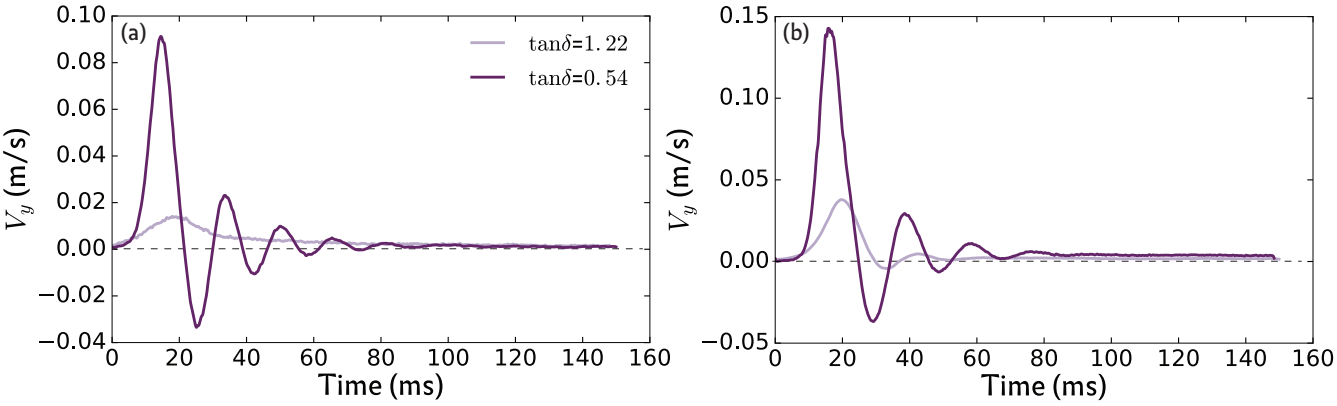

Figure A.9: Temporal evolution of the velocity y-component averaged spatially over a common area for different $(\tan\delta)$: (a) In water; (b) in glycerol. Dashed lines are a guide highlighting the zero value.

References

[Ahmed et al., 2016] Ahmed, D., Baasch, T., Jang, B., Pane, S., Dual, J., & Nelson, B. J. (2016). Artificial swimmers propelled by acoustically activated flagella. *Nano Lett.*, 16, 4968–4974.

[Ahmed et al., 2015] Ahmed, D., Lu, M., Nourhani, A., Lammert, P. E., Stratton, Z., Muddana, H. S., Crespi, V. H., & Huang, T. J. (2015). Selectively manipulable acoustic-powered microswimmers. *Scientific Reports*, 5, 9744.

[Arganda-Carreras et al., 2006] Arganda-Carreras, I., Sorzano, C. O. S., Marabini, R., Carazo, J.-M., Ortiz-de Solorzano, C., & Kybic, J. (2006). Consistent and elastic registration of histological sections using vector-spline regularization. *Computer Vision Approaches to Medical Image Analysis*, 4241, 85–95. Lecture Notes in Computer Science, Springer Berlin / Heidelberg.

[Baker et al., 1967] Baker, W. E., Woolam, W. E., & Young, D. (1967). Air and internal damping of thin cantilever beams. *Int. J. Mech. Sci.*, 9(743), 743–766.

[Batchelor, 1967] Batchelor, G. (1967). *An Introduction to Fluid Dynamics*. Cambridge University Press.

[Bertin et al., 2015] Bertin, N., Spelman, T. A., Stephan, O., Gredy, L., Bouriau, M., Lauga, E., & Marmottant, P. (2015). Propulsion of bubble-based acoustic microswimmers. *Phys. Rev. Applied*, 4, 064012.

[Boutier, 2013] Boutier, A., Ed. (2013). *Laser Metrology in Fluid Mechanics: Granulometry, Temperature and Concentration Measurements*. WILEY.

[Brennen, 1977] Brennen, C. (1977). Fluid mechanics of propulsion by cilia and flagella. *Annu. Rev.Fluid Mech.*, 9, 339.

[Cademartiri et al., 2012] Cademartiri, L., Bishop, K. J. M., Snyder, P. W., & Ozin, G. A. (2012). Using shape for self-assembly. *Philos. T. Roy. Soc. A*, 370, 2824–2847.

[Canny, 1986] Canny, J. (1986). A computational approach to edge detection. *IEEE Trans. Pattern Analysis and Machine Intelligence*, 8(6), 679–698.

[Cheng, 2008] Cheng, N. S. (2008). Formula for viscosity of glycerol-water mixture. *Industrial and Engineering Chemistry Research*, 47, 3285–3288.

[Childress, 1981] Childress, S. (1981). *Mechanics of swimming and flying.* Cambridge Studies.

[Dreyfus et al., 2005] Dreyfus, R., Baudry, J., Roper, M. L., Fermigier, M., Stone, H. A., & Bibette, J. (2005). Microscopic artificial swimmers. *Nature*, 437, 862.

[Drmota et al., 1987] Drmota, M., Scheidl, R., Troger, H., & Weinmüller, E. (1987). On the imperfection sensitivity of complete spherical shells. *Computational Mechanics*, 2, 63.

[Fernandez-Prats et al., 2015] Fernandez-Prats, R., Raspa, V., Thiria, B., Huera-Huarte, F., & Godoy-Diana, R. (2015). Large-amplitude undulatory swimming near a wall. *Bioinspiration and Biomimetics*, 10, 016003.

[Garcia et al., 2011] Garcia, M., Berti, S., Peyla, P., & Rafaï, S. (2011). The random walk of a low-Reynolds-number swimmer. *Phys. Rev. E*, 83, 035301(R).

[Gazzola et al., 2014] Gazzola, M., Argentina, M., & Mahadevan, L. (2014). Scaling macroscopic aquatic locomotion. *Nat. Phys.*, 10, 758–761.

[Golestanian et al., 2005] Golestanian, R., B., L. T., & A., A. (2005). Propulsion of a molecular machine by asymmetric distribution of reaction products. *Phys. Rev. Lett*, 94, 220801.

[Gräff et al., 1985] Gräff, R., Scheidel, R., Troger, H., & Weinmüller, E. (1985). An investigation of the complete post-buckling behavior of axisymmetric spherical shells. *ZAMP*, 36, 803.

[Hutchinson, 1967] Hutchinson, J. W. (1967). Imperfection sensitivity of externally pressurized spherical shells. *ASME. J. Appl. Mech.*, 34, 49–55.

[Kaynak et al., 2017] Kaynak, M., Ozcelik, A., Nourhani, A., Lammert, P. E., Crespi, V. H., & Huang, T. J. (2017). Acoustic actuation of bioinspired microswimmers. *Lab Chip*, 17, 395–400.

[Knoche & Kierfeld, 2011] Knoche, S. & Kierfeld, J. (2011). Buckling of spherical capsules. *Phys. Rev. E*, 84, 046608.

[Lakes, 2009] Lakes, R. S., Ed. (2009). *Viscoelastic Materials.* Cambridge University Press.

[Landau & Lifshitz, 1986] Landau, L. & Lifshitz, E. (1986). *Theory of elasticity.* Pergamon press.

[Lauga et al., 2006] Lauga, E., DiLuzio, W. R., Whitesides, G. M., & Stone, H. A. (2006). Swimming in circles: motion of bacteria near solid boundaries. *Biophys. J.*, 90, 400.

[Lauga & Powers, 2009] Lauga, E. & Powers, T. R. (2009). The hydrodynamics of swimming microorganisms. *Reports on Progress in Physics*, 72(9), 096601.

[Lee et al., 2016] Lee, A., López Jiménez, F., Marthelot, J., Hutchinson, J., & Reis, P. M. (2016). The geometric role of precisely engineered imperfections on the critical buckling load of spherical elastic shells. *ASME. J. Appl. Mech.*, 83, 111005–111005–11.

[Libai & Simmonds, 1998] Libai, A. & Simmonds, J. (1998). *The nonlinear theory of elastic shells*. Cambridge University Press.

[Lighthill, 1960] Lighthill, M. J. (1960). Note on the swimming of slender fish. *Journal of Fluid Mechanics*, 9, 305.

[Lopez Jimenez et al., 2017] Lopez Jimenez, F., Marthelot, J., Lee, A., Hutchinson, J., & Reis, P. (2017). Knockdown factor for the buckling of spherical shells containing large-amplitude geometric defects. *Journal of Applied Mechanics*, 84(034501).

[Marmottant et al., 2011a] Marmottant, P., Bouakaz, A., de Jong, N., & Quilliet, C. (2011a). Buckling resistance of solid shell bubbles under ultrasound. *J. Ac. Soc. Am.*, 129, 1231–1239.

[Marmottant et al., 2011b] Marmottant, P., Bouakaz, A., De Jong, N., & Quilliet, C. (2011b). Buckling resistance of solid shell bubbles with ultrasound. *Journal of Acoustical Society of America*, 129, 1231–1239.

[Ng Lee et al., 2003] Ng Lee, J., Park, C., & Whitesides, G. M. (2003). Solvent compatibility of poly(dimethylsiloxane)-based microfluidic devices. *Analytical Chemistry*, 75(23), 6544–6554.

[Palagi et al., 2013] Palagi, S., Jager, E. W. H., Mazzolai, B., & Beccai, L. (2013). Propulsion of swimming microrobots inspired by metachronal waves in ciliates: from biology to material specifications. *Bioinspir. Biomim.*, 8, 046004.

[Pande et al., 2017] Pande, J., Merchant, L., Krueger, T., Harting, J., & Smith, A.-S. (2017). Effect of body deformability on microswimming. *Soft Matter*, accepted.

[Paxton et al., 2004] Paxton, W. F., Kistler, K. C., Olmeda, C. C., Sen, A., St. Angelo, S. K., Cao, Y., Mallouk, T. E., Lammert, P. E., & Crespi, V. H. (2004). Catalytic nanomotors: Autonomous movement of striped nanorods. *J. Am. Chem. Soc.*, 126, 13424–13431.

[Peyer et al., 2012] Peyer, K., Mahoney, A., Zhang, L., Abbott, J., & Nelson, B. (2012). *Bacteria-Inspired Microrobots*, (pp. 165–199). Elsevier Inc.

[Pisani et al., 2009] Pisani, E., Ringard, C., Nicolas, V., Raphaël, E., Rosilio, V., Moine, L., Fattal, E., & Tsapis, N. (2009). Tuning microcapsules surface morphology using blends of homo and copolymers of plga and plga-peg. *Soft Matt.*, 5, 3054–3060.

[Pogorelov, 1988] Pogorelov, A. (1988). *Bendings of surfaces and stability of shells*. American Mathemathical Society.

[Purcell, 1977] Purcell, E. M. (1977). Life at low reynolds number. *Am. J. Phys*, 45, 3.

[Qiu et al., 2014] Qiu, T., Lee, T.-C., Mark, A. G., Morozov, K. I., Münster, R., Mierka, O., Turek, S., Leshansky, A. M., & Fischer, P. (2014). Swimming by reciprocal motion at low reynolds number. *Nature communications*, 5, 5119.

[Quilliet, 2012] Quilliet, C. (2012). Numerical deflation of beach balls with various poisson's ratios: from sphere to bowl's shape. *Eur. Phys. J. E*, 35, 48.

[Quilliet et al., 2008] Quilliet, C., Zoldesi, C., Riera, C., van Blaaderen, A., & Imhof, A. (2008). Anisotropic colloids through non-trivial buckling. *Eur. Phys. J. E*, 27, 13–20.

[Quilliet et al., 2010] Quilliet, C., Zoldesi, C., Riera, C., van Blaaderen, A., & Imhof, A. (2010). Erratum to: Anisotropic colloids through non-trivial buckling. *Eur. Phys. J. E*, 32, 419–420.

[R, 2009] R, G. (2009). Anomalous diffusion of symmetric and asymmetric active colloids. *Phys. Rev. Lett.*

[Sorzano et al., 2005] Sorzano, C. O. S., Thévenaz, P., & Unser, M. (2005). Elastic registration of biological images using vector-spline regularization. *IEEE Transactions on Biomedical Engineering*, 52(4), 652–663.

[Tamm & Horridge, 1970] Tamm, S. L. & Horridge, G. A. (1970). The relation between the orientation of the central fibrils and the direction of beat in cilia of opalina. *Proc. R. Soc. Lond.*, 175, 219–233.

[Tanida, 2001] Tanida, Y. (2001). Groud effect in flight (birds, fishes and high-speed vehicles). *JSME International Journal Series B*, 44, 481.

[Triantafyllou, 2002] Triantafyllou, M. S. (2002). Vorticity control in fish-like propulsion and maneuvering. In *Integrative and Comparative Biology*.

[Tropea et al., 2007] Tropea, C., Yarin, A. L., & Foss, J. F. (2007). *Handbook of experimental fluid mechanics*. Springer.

[Vincent et al., 2011] Vincent, O., Roditchev, I., & Marmottant, P. (2011). Spontaneous firings of carnivorous aquatic utricularia traps: Temporal patterns and mechanical oscillations. *PLoS ONE*, 6, e20205.

[Walker, 2002] Walker, J. A. (2002). Functional morphology and virtual models: physical constraints on the design of oscillating wings, fins, legs, and feet at intermediate reynolds numbers. *Integr. Comp. Biol.*, 42, 232.

[Yang et al., 2008] Yang, S.-M., Kim, S.-H., Lim, J.-M., & Yi, G.-R. (2008). Synthesis and assembly of structured colloidal particles. *J. Mater. Chem.*, 18, 2177–2190.

[Yi et al., 2013] Yi, G.-R., Pine, D. J., & Sacanna, S. (2013). Recent progress on patchy colloids and their self-assembly. *J. Phys.: Cond. Matt.*, 25, 193101.

[Zhang et al., 2009] Zhang, L., Abbott, J. J., Dong, L. X., Kratochvil, B. E., Bell, D. J., & Nelson, B. J. (2009). Artificial bacterial flagella: fabrication and magnetic control. *Applied Physics Letters*, 94, 064107.

[Zhang & Ru, 2016] Zhang, L. & Ru, C. Q. (2016). Imperfection sensitivity of pressured buckling of biopolymer spherical shells. *Phys. Rev. E*, 93, 062403.

[Zoldesi & Imhof, 2005] Zoldesi, C. & Imhof, A. (2005). Synthesis of monodisperse colloidal spheres, capsules, and microballoons by emulsion templating. *Adv. Mat.*, 17, 924.

This thesis was typeset using LaTeX, originally developed by Leslie Lamport and based on Donald Knuth's TeX. The body text is set in 11 point Egenolff-Berner Garamond, a revival of Claude Garamont's humanist typeface. The above illustration, *Science Experiment 02*, was created by Ben Schlitter and released under CC BY-NC-ND 3.0. A template that can be used to format a PhD dissertation with this look & feel has been released under the permissive AGPL license, and can be found online at github.com/suchow/Dissertate or from its lead author, Jordan Suchow, at suchow@post.harvard.edu.